BIOLOGICAL AND FUNCTIONAL RESTORATION OF MECHANO- AND ELECTRO CONDUCTIVE TISSUES AND ORGANS: A REGENERATIVE APPROACH

EDITED BY: Yun Qian, Xuqing Liu, Gonzalo Rosso and Peisheng Xu
PUBLISHED IN: Frontiers in Bioengineering and Biotechnology

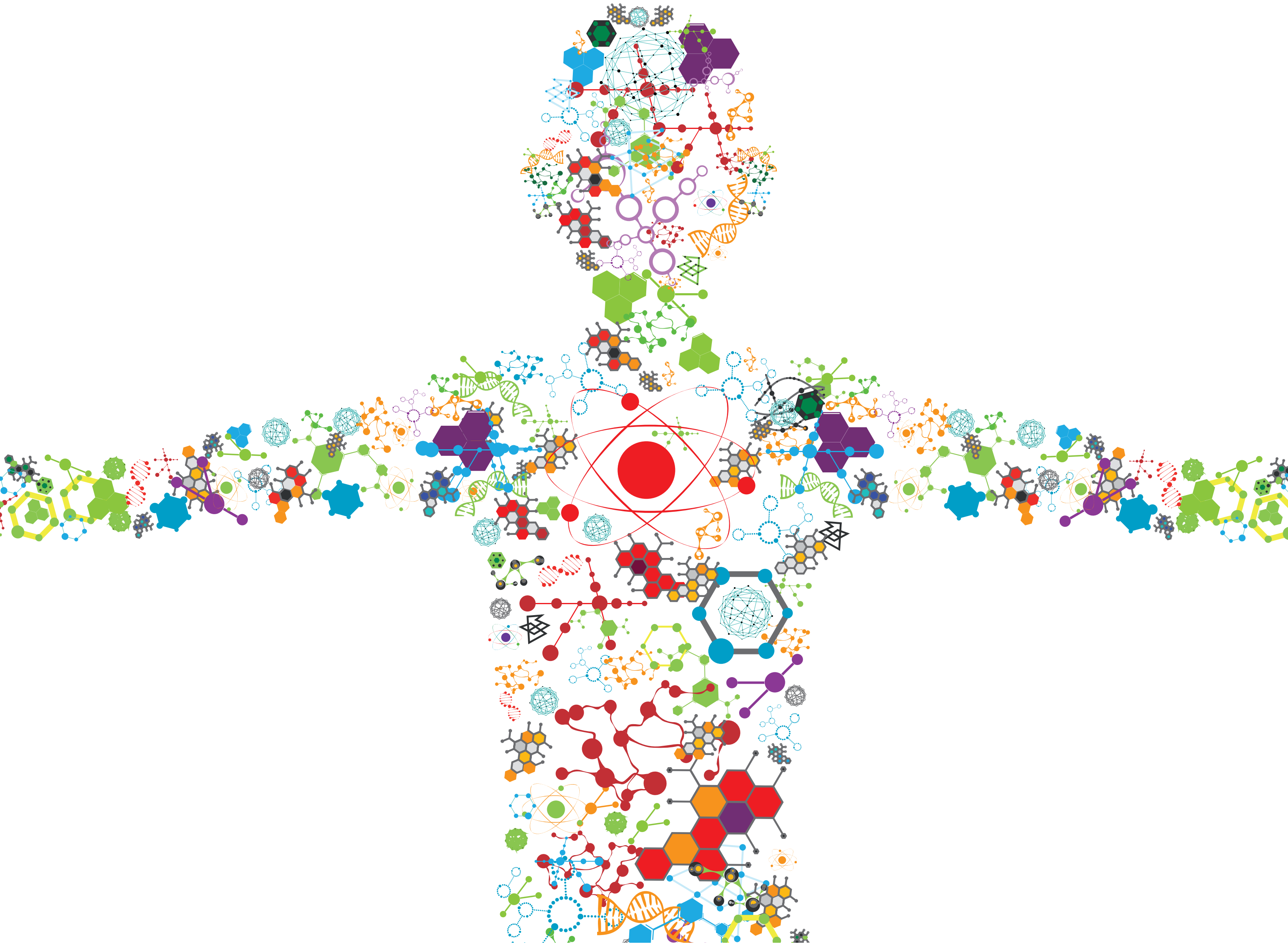

frontiers Research Topics

ISSN 1664-8714
ISBN 978-2-83250-806-0
DOI 10.3389/978-2-83250-806-0

About Frontiers

Frontiers is more than just an open-access publisher of scholarly articles: it is a pioneering approach to the world of academia, radically improving the way scholarly research is managed. The grand vision of Frontiers is a world where all people have an equal opportunity to seek, share and generate knowledge. Frontiers provides immediate and permanent online open access to all its publications, but this alone is not enough to realize our grand goals.

Frontiers Journal Series

The Frontiers Journal Series is a multi-tier and interdisciplinary set of open-access, online journals, promising a paradigm shift from the current review, selection and dissemination processes in academic publishing. All Frontiers journals are driven by researchers for researchers; therefore, they constitute a service to the scholarly community. At the same time, the Frontiers Journal Series operates on a revolutionary invention, the tiered publishing system, initially addressing specific communities of scholars, and gradually climbing up to broader public understanding, thus serving the interests of the lay society, too.

Dedication to Quality

Each Frontiers article is a landmark of the highest quality, thanks to genuinely collaborative interactions between authors and review editors, who include some of the world's best academicians. Research must be certified by peers before entering a stream of knowledge that may eventually reach the public - and shape society; therefore, Frontiers only applies the most rigorous and unbiased reviews.
Frontiers revolutionizes research publishing by freely delivering the most outstanding research, evaluated with no bias from both the academic and social point of view. By applying the most advanced information technologies, Frontiers is catapulting scholarly publishing into a new generation.

What are Frontiers Research Topics?

Frontiers Research Topics are very popular trademarks of the Frontiers Journals Series: they are collections of at least ten articles, all centered on a particular subject. With their unique mix of varied contributions from Original Research to Review Articles, Frontiers Research Topics unify the most influential researchers, the latest key findings and historical advances in a hot research area! Find out more on how to host your own Frontiers Research Topic or contribute to one as an author by contacting the Frontiers Editorial Office: frontiersin.org/about/contact

BIOLOGICAL AND FUNCTIONAL RESTORATION OF MECHANO- AND ELECTRO CONDUCTIVE TISSUES AND ORGANS: A REGENERATIVE APPROACH

Topic Editors:
Yun Qian, Shanghai Jiao Tong University, China
Xuqing Liu, The University of Manchester, United Kingdom
Gonzalo Rosso, Max Planck Institute for the Science of Light, Germany
Peisheng Xu, University of South Carolina, United States

Citation: Qian, Y., Liu, X., Rosso, G., Xu, P., eds. (2022). Biological and Functional Restoration of Mechano- and Electro Conductive Tissues and Organs: A Regenerative Approach. Lausanne: Frontiers Media SA.
doi: 10.3389/978-2-83250-806-0

Table of Contents

frontiers | Frontiers in Bioengineering and Biotechnology

TYPE Editorial
PUBLISHED 03 November 2022
DOI 10.3389/fbioe.2022.1070888

OPEN ACCESS

EDITED AND REVIEWED BY
Hasan Uludag,
University of Alberta, Canada

*CORRESPONDENCE
Yun Qian,
lollipopcloudland@foxmail.com

SPECIALTY SECTION
This article was submitted to Biomaterials,
a section of the journal Frontiers in Bioengineering and Biotechnology

RECEIVED 15 October 2022
ACCEPTED 21 October 2022
PUBLISHED 03 November 2022

CITATION
Qian Y, Liu X, Rosso G and Xu P (2022), Editorial: Biological and functional restoration of mechano- and electro conductive tissues and organs: A regenerative approach.
Front. Bioeng. Biotechnol. 10:1070888.
doi: 10.3389/fbioe.2022.1070888

Editorial: Biological and functional restoration of mechano- and electro conductive tissues and organs: A regenerative approach

Yun Qian[1]*, Xuqing Liu[2], Gonzalo Rosso[3] and Peisheng Xu[4]

[1]Department of Orthopedics, Shanghai Sixth People's Hospital Affiliated to Shanghai Jiao Tong University School of Medicine, Shanghai, China, [2]Department of Materials, University of Manchester, Manchester, United Kingdom, [3]Max Planck Institute for the Science of Light and Max-Planck-Zentrum für Physik und Medizin, Erlangen, Germany, [4]Department of Drug Discovery and Biomedical Sciences, University of South Carolina, Columbia, SC, United States

KEYWORDS

pharmacological therapy, mechanical and electrical stimuli, conductive materials, tissue engineering, regenerative medicine

Editorial on the Research Topic
Biological and functional restoration of mechano-and electro conductive tissues and organs: A regenerative approach

The primary mission of tissue engineering and regenerative medicine (TERM) is to mimic the architectural and functional nature of impaired tissues (Berthiaume et al., 2011). TERM has made up significantly for the shortage of organs and tissues after severe trauma or terminal illness. Nevertheless, the complete functional and biological recovery of tissues and organs is still limited due to failure to restore *in vitro* and *in vivo* biomimetic scenarios based on tissue engineering. Among various regenerative cues, including chemical, biological, optical, magnetic and mechanical factors, the implementation of advanced pharmacological approaches, electrical and mechanical stimuli have long been underestimated in regard to their potential for the development and improvement of bioengineered and biological tissues, such as the bone, cartilage, muscle, heart, and nerve.

Mechanical and electrical activities play a crucial role in a series of physiological phenomena in the living body and are important for the functionality of mechano- and electro-active tissues, such as bone, cartilage, muscle, heart, brain, spinal cord, and peripheral nerve. Therefore, it is vital to focus on the application of conductive scaffolds and their regulation on endogenous electrical activities in the process of tissue regeneration, with or without exogenous mechanical and electrical stimuli of different paradigms (e.g., intensity, frequency, and wave type). Positive outcomes have been reported in previous literature, but it is poorly understood how electrical phenomena affect cell physiological function-behavior, metabolism, signaling transduction, and gene expression, or how the combination of engineered conductive scaffolds with the specific delivery of therapeutic drugs boosts the regenerative capacity of tissues. For instance, the inter-cellular communication between neurons or glial cells influenced by electrically conductive scaffolds is not well elucidated in nerve tissue engineering. Some preliminary findings were obtained from *in vitro* studies. Long-term evaluation on the reparative potential of mechanically and electrically conductive biomaterials is the key to identifying a translational approach to advance the field of mechano- and electro-active tissue regeneration therapies.

In this Research Topic, we have covered the latest advances in the modulation of electrophysiological activities of cells, tissues, and organs by conductive biomaterials and their regenerative signaling mechanisms. This has ultimately led to a comprehensive display of papers (10 articles from China, the United Kingdom, Germany, and Australia).

Some papers focused on physiological and metabolic response of excitable and non-excitable cells and tissues on electrically active substrates under mechanical and electrical stimuli in normal and tissue injury environments. Liu et al. stressed the involvement of osteoclasts and osteoblasts in the activation of various mechanical transduction pathways and discussed changes in the differentiation, formation, and functional mechanisms under multiple forms of mechanical stress to bone tissues. Mei et al. designed a mesoporous bioactive glass biomimetic scaffold to enhance cellular adhesion and to improve osteogenic/cementogenic differentiation in human periodontal ligament cells.

Wang F et al. proposed a conductive adhesive and anti-bacterial Zwitterionic hydrogel dressing to repair full-thickness skin wounds. In their study, modulation of electrical paradigms facilitated intercellular communication and transcriptional signaling, mechanical stimulation for angiogenesis and skin development and function supported by conductive scaffolds. Tian Y et al. claimed pro-healing effects of mechanically conductive tissue engineering strategy with bardoxolone methyl on nucleus pulposus cells and tissues by inhibiting extracellular matrix (ECM) catabolism and promoting ECM anabolism. In addition to traditional electrical stimuli, *in vitro* and *in vivo* evaluation of wound healing and tissue regeneration technologies of combined electrical stimulation and smart materials also yielded some promising results, including novel electroactive scaffold design and user-friendly application (Nan et al.; Xiong et al.).

Jiang Y et al. reported the Netrin-1 modified adipose-derived stem cells and the combined application of such *in vitro* and *in vivo* tissue engineering strategies to accelerate or improve the development and function of bioengineered endovascular tissues. In addition, there are some research papers concerning novel biomaterial design, fabrication and application for mechanobiology/electrobiology and interfacial characterization of these biomedical materials in bone and nerve regeneration (Liu et al.; Yan et al.; Gao et al.).

The improvement in tissue regeneration, either in functionality or morphology, largely depends on the increasing knowledge of the properties of mechano- and electro conductive tissues and organs. The purpose of physical stimulation is generally to simulate the nature of the living tissue and organ itself. For instance, microenvironmental remodeling in nerve repair is essential and influenced by the spatial and temporal changes after nerve injury. This also greatly affects the scaffold design and physiochemical factors of the nano- and micro-scale biomaterials (Qian et al., 2021). The recent progress from this Research Topic provides novel insights into the regenerative approach from a physical or mechanical perspective for various cells and tissues. Some of the exciting techniques and advanced concepts may be valuable for inspiring more applications for potential clinical translation in the near future.

Author contributions

All authors listed have made a substantial, direct, and intellectual contribution to the work and approved it for publication.

Conflict of interest

The authors declare that the research was conducted in the absence of any commercial or financial relationships that could be construed as a potential conflict of interest.

Publisher's note

References

Berthiaume, F., Maguire, T. J., and Yarmush, M. L. (2011). Tissue engineering and regenerative medicine: History, progress, and challenges. *Annu. Rev. Chem. Biomol. Eng.* 2, 403–430. doi:10.1146/annurev-chembioeng-061010-114257

Qian, Y., Lin, H., Yan, Z., Shi, J., and Fan, C. (2021). Functional nanomaterials in peripheral nerve regeneration: Scaffold design, chemical principles and microenvironmental remodeling. *Materials Today* 51, 165–187. doi:10.1016/j.mattod.2021.09.014

frontiers
in Bioengineering and Biotechnology

ORIGINAL RESEARCH
published: 13 September 2021
doi: 10.3389/fbioe.2021.736063

Determination of an Initial Stage of the Bone Tissue Ingrowth Into Titanium Matrix by Cell Adhesion Model

Ziyu Liu[1,2,3], Maryam Tamaddon[1], Shen-Mao Chen[1], Haoyu Wang[1], Vee San Cheong[4], Fangli Gang[2,3], Xiaodan Sun[3]* and Chaozong Liu[1]*

[1]Division of Surgery & Interventional Science, University College London, Royal National Orthopaedic Hospital, London, United Kingdom, [2]School of Engineering Medicine, Beihang University, Beijing, China, [3]Key Laboratory of Advanced Materials of Ministry of Education of China, School of Materials Science and Engineering, Tsinghua University, Beijing, China, [4]Insigno Institute of in Silico Medicine and Department of Automatic Control and Systems Engineering, University of Sheffield, Sheffield, United Kingdom

Edited by:
Yun Qian,
Shanghai Jiao Tong University, China

Reviewed by:
Peng Gao,
Beijing University of Technology, China
Hui Tan,
Shenzhen Second People's Hospital, China
Feiyan Zhu,
University of Chinese Academy of Sciences, China

***Correspondence:**
Xiaodan Sun
sunxiaodan@mail.tsinghua.edu.cn
Chaozong Liu
chaozong.liu@ucl.ac.uk

Specialty section:
This article was submitted to Biomaterials, a section of the journal Frontiers in Bioengineering and Biotechnology

Received: *04 July 2021*
Accepted: *21 July 2021*
Published: *13 September 2021*

Citation:
Liu Z, Tamaddon M, Chen S-M, Wang H, San Cheong V, Gang F, Sun X and Liu C (2021) Determination of an Initial Stage of the Bone Tissue Ingrowth Into Titanium Matrix by Cell Adhesion Model. Front. Bioeng. Biotechnol. 9:736063. doi: 10.3389/fbioe.2021.736063

For achieving early intervention treatment to help patients delay or avoid joint replacement surgery, a personalized scaffold should be designed coupling the effects of mechanical, fluid mechanical, chemical, and biological factors on tissue regeneration, which results in time- and cost-consuming trial-and-error analyses to investigate the *in vivo* test and related experimental tests. To optimize the fluid mechanical and material properties to predict osteogenesis and cartilage regeneration for the *in vivo* and clinical trial, a simulation approach is developed for scaffold design, which is composed of a volume of a fluid model for simulating the bone marrow filling process of the bone marrow and air, as well as a discrete phase model and a cell impingement model for tracking cell movement during bone marrow fillings. The bone marrow is treated as a non-Newtonian fluid, rather than a Newtonian fluid, because of its viscoelastic property. The simulation results indicated that the biofunctional bionic scaffold with a dense layer to prevent the bone marrow flow to the cartilage layer and synovia to flow into the trabecular bone area guarantee good osteogenesis and cartilage regeneration, which leads to high-accuracy *in vivo* tests in sheep . This approach not only predicts the final bioperformance of the scaffold but also could optimize the scaffold structure and materials by their biochemical, biological, and biomechanical properties.

Keywords: osteochondral scaffold, gradient design, volume of fluid model, discrete phase model, cell adhesion

INTRODUCTION

Knee osteoarthritis is a common and frequently occurring disease in the middle-aged and elderly population, including cartilage destruction and subchondral bone thickening (Peat et al., 2001). It ranks first in causing disability in the elderly and seriously affects the quality of life. Large-area cartilage defects can only be treated by joint replacement surgery. In the tissue engineering field, scaffolds play a pivotal role in tissue engineering, which provide a three-dimensional template for cell seeding, temporary mechanical function, and an extracellular matrix environment for tissue regeneration (Karageorgiou and Kaplan, 2005; Hollister, 2006). Osteochondral scaffolds act as an osteoconductive part and serve as delivery vehicles for cytokines like bone morphogenetic proteins (BMPs), thus providing osteoinduction (Groeneveld et al., 1999). Osteogenesis and bone mesenchymal stem cell (BMSC) attachment occur after the implantation of the scaffolds.

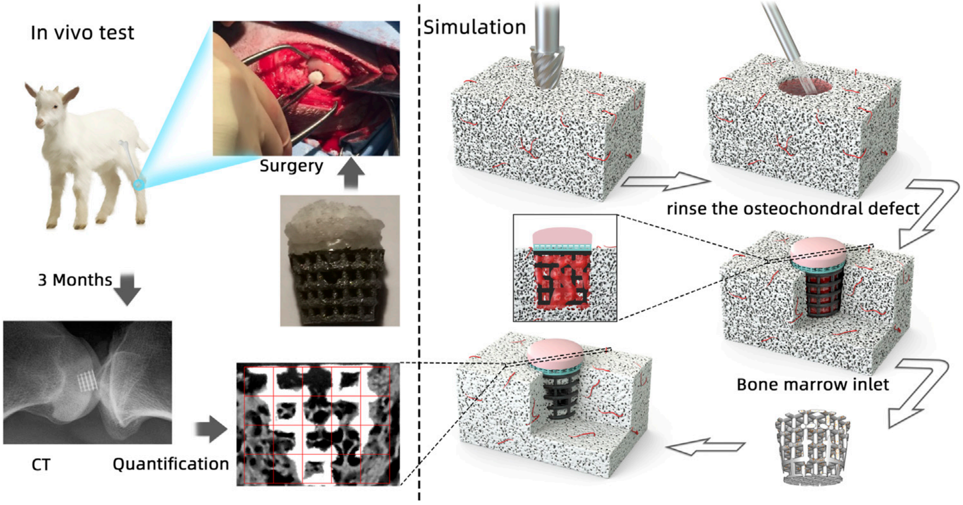

GRAPHICAL ABSTRACT |

Aiming for osteogenesis and cartilage regeneration, an ideal scaffold is needed to provide suitable biomimetic mechanical and biological environments having similar morphology and function like natural osteochondral bone which could optimize integration into neighboring tissues (Healy, 1999; Hubbell, 1999; Sakiyama-Elbert and Hubbell, 2001; Lin et al., 2004; Karageorgiou and Kaplan, 2005; Wu et al., 2017). In general, *in vitro* and *in vivo* tests are used to evaluate scaffold bioperformance with high funding cost. An ethical and economical method is needed to evaluate scaffold bioperformance which considers the influence of the material (surface tension and material kinds) and its geometry (pore size, porosity, geometry, and surface area).

Computational analysis is seen as a promising method for scaffold evaluation. Sanz-Herrera et al. analyzed bone growth and formation in a two-dimensional (2D) scaffold by bone remodeling theories which assumed that it is driven by a mechanical stimulus (Beaupré et al., 1990; Adachi et al., 2001; Sanz-Herrera et al., 2008). With the same assumption, Adachi et al. also used the bone remodeling theory with uniform stress hypothesis to express how new bone tissues formed (Cowin, 1993; Adachi et al., 1998; Adachi et al., 2006). However, neither of them involved fluid stimuli in the simulation, which plays an important role in bone tissue regeneration when using an osteochondral scaffold. Moreover, recruiting BMSCs, as the first step of tissue engineering, and simulating BMSC attachment on the scaffold and their distribution is a really significant step in predicting the final bioperformance (Byrne et al., 2007).

Prendergast et al. proposed a theory that mechanical and fluid mechanical stimuli caused stem cell differentiation (Prendergast et al., 1996). And this mechano-regulation method successfully validated tissue differentiation by experimentally surrounding implants (Huiskes et al., 1997). Damian P.B. et al. explored various design parameters of the scaffold in tissue regeneration, and by this method modeling, cell proliferation, migration, and differentiation, he assumed that cells were randomly seeded on the lattice scaffold. However, cells distributed on the scaffold are not random, and it is determined by a lot of complex influence factors—material, surface roughness, geometry, and bone marrow flow speed. After recruiting the scaffold, BMSCs would start proliferating and migrating until they are mature enough to undergo differentiation. The position of cells would finally influence the final tissue formation (Wendt et al., 2006; Santoro et al., 2010). Till now, few researchers have studied cell distribution in the scaffold at the initial stage of the tissue engineering process after surgery since it is impossible to sacrifice animals at the initial stage to observe cell distribution ethically and economically. In that case, computational analysis provided an important solution to investigate this postsurgery process. As it is impossible to observe cell distribution using *in vivo* tests to validate simulation results, our previous work (Liu et al., 2020) used a numerical cell attachment model with a volume of fluid (VOF) model and discrete phase model (DPM) to investigate the cell seeding process and validated using *in vitro* tests.

To explore the relationship between BMSC distribution at the postsurgery initial stage and bone formation on the scaffold, the novel model is developed in a more real environment for cell attachment. The bone marrow is set as non-Newtonian fluid calculated by the power law for non-Newtonian viscosity, rather than normal Newtonian fluid like the solution for cell seeding. The model is validated by using *in vivo* tests in which bone formation and distribution are quantified by a self-designed MATLAB program by analyzing the Micro-CT–scanned image by threshold-based operation. The information of osteogenesis could be obtained not only on the outside of the scaffold but also within the pores of the scaffold. This model is aiming to decrease both *in vivo* and *in vitro* tests for optimizing the scaffold design and material properties which could avoid unnecessary time and money investment.

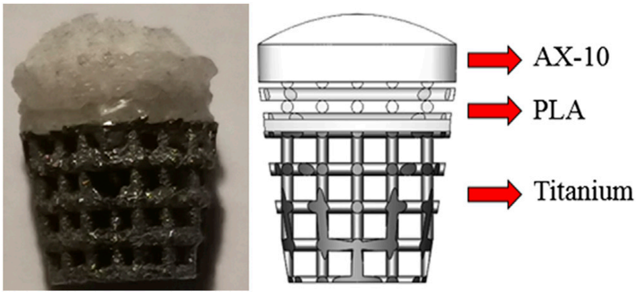

FIGURE 1 | Biomimetic multi-layer gradient osteochondral scaffold (**left:** real structure; **right:** schematic structure).

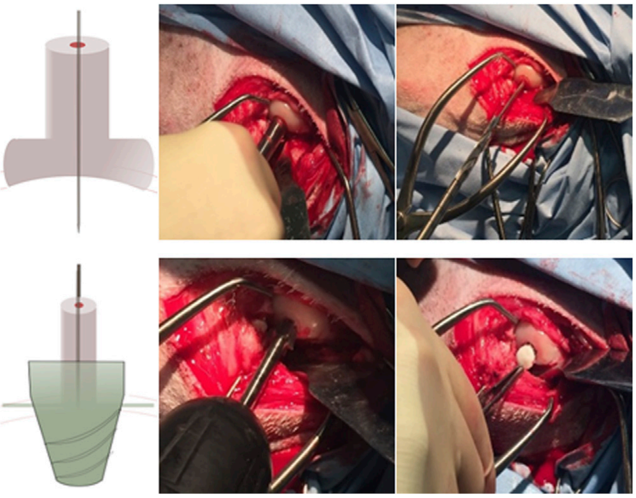

FIGURE 2 | Presurgical operation procedure: 1–3. Drill the small hole located by a drill sleeve and insert a pin guide into the hole; 4–5. Access the driller bite to create a larger hole, and use special design roam to create a truncated cone hole; and 6. Place the mountain scaffold into the osteochondral defect.

MATERIALS AND METHODS

Bionic Scaffold and Manufacturing

The bionic scaffold has 3 layers shown in **Figure 1**. The top layer is produced by 10% poly(lactic-co-glycolic acid) (PLGA) solutions in acetone pipetted into 90% freeze-dried collagen scaffold which is called AX-10. The cone structure is combined with an 8.5-mm-diameter and 1.2-mm-height spherical cap on the top and an 8.5-mm-diameter and 1.5-mm-height column at the bottom. The medium layer is 3D-printed with polylactic acid (PLA) composited by one solid dense layer at the bottom and one high porosity truncated cone structure. The high-porosity structure has 4 small layers, and each layer's column beam has the same direction but perpendicular to the close layer's beam direction. The column size is 0.5 mm diameter. The PLA scaffold was plasma-treated at 50–60 Hz frequency and with 60% power-oxygen for 3 min on two sides (top and bottom). The samples were then sterilized with 70% ethanol for 15 min. The bottom layer with a high-porosity and high interconnected pore network was printed by an EOS M270 machine with titanium powder. The high-porosity and interconnected structure aims to provide enough routes for nutrient transport like porous trabecular bones.

For large osteochondral defect repair, the PLGA layer is a column design with 8.5 diameter and 1.5 mm height. Below the porous structure, the dense PLA layer is designed as a 0.5-mm-height column with 8 mm diameter. The Ti layer is designed as a truncated cone with 8 mm diameter on the top surface and 5.9 mm on the bottom surface manufactured by an EOS 290 3D printer. To combine three layers together, the PLA layer was melted and pressed into a titanium matrix and fused together by hot fusion. And then, these two layers were submerged into the cross-linked collagen suspension and then freeze-dried.

In Vivo Test

Ethical Aspects and Animals

Five young female sheep with a mean weight of 81.6 ± 6.4 kg were operated in the Royal Veterinary College (RVC). All sheep were treated according to Animals (Scientific Procedures) Act (ASPA). Animal examinations, housing, feeding, and veterinary care were conducted using established procedures. The sheep were housed in a free land with sufficient food and water. Furthermore, sheep can freely move in the outside during the research period.

Surgical Procedure

Under anesthetics, the sheep were bedded carefully on their right side, exposing their left knee. A truncated critical-sized osteochondral defect of 9 mm diameter was created using two surgical drills on the load-bearing area medial to the femoral condyle up to a depth of 10 mm.

According to the surgical operation procedure (**Figure 2**), first, a small hole was created by using a drill sleeve on the load-bearing area medial to the femoral condyle, and then a nail guide was put into the bone with a 9.3-mm-deep hole. After that, the cartilage of 9.45 mm diameter was removed using a circular cylindrical cutter. Then, a critical-sized, truncated cone-shaped osteochondral defect was drilled up to 8.8 mm depth by using two surgical drills . The truncated cone defect was scoured by water until the biomimic multi-layer gradient scaffold was inserted into the defect.

After the surgery, they were housed in individual places for five days restricting their activities at the initial stage of the healing process. In these five postsurgery days, they were treated with analgesia (carprofen 5 mg/kg) and antibiotics (enrofloxacin 10 mg/kg) subcutaneously twice daily. After 3 months, the animals were euthanized under anesthesia. Both legs' condyles were fixed with paraformaldehyde at room temperature for further analysis.

Micro-Computed Tomography (Micro-CT) and X-Ray Analysis

The X-ray micrographs of limbs were used to look at the stability of scaffolds in the joint. The X-ray scan of pre-euthanized and the postoperative tissue scaffold was performed by using a Nikon XT

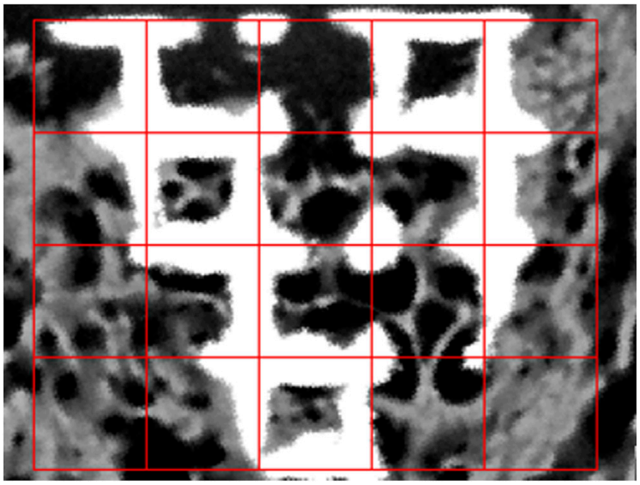

FIGURE 3 | MATLAB program image analysis of osteogenesis.

H 225 machine which offers a powerful 225 kV micro-focus source with real-time X-ray visualization. And the tissue with the scaffold inside was scanned in a small-scale slice-by-slice manner with great resolution. Three-dimensional reconstruction was solved by CTvox and CTan (Bruker, United States) software. The knee joint of the animal was scanned using X-ray immediately after euthanasia to look at the position of the scaffolds within the joint after 3 months.

X-Ray–Based Bone Analysis for Quantification of Osteogenesis and Bone–Scaffold Interaction

2D images from X-ray–scanned objects were utilized to determine the amount of the newly formed bone in the scaffold and bone–scaffold surface interaction values. Due to the high resolution of the scanner, the information within the pores of the scaffolds could be obtained with certainty. Thus, not only the outer but also the inner regions of the scaffolds were taken into account for the determination of osteogenesis.

MATLAB R2017a is used to translate images to binary images at first and then to divide images into the same length grids (**Figure 3**). As binary images store an unsigned one-byte integer to describe the area between 0 (representing black) and 255 (maximum value—representing white), we defined three threshold values to identify the scaffold and bone structure. As the images are composed of pixels, 10 pixels of the bone and scaffold were selected to define the pixel's threshold range in the program. To define both ranges accurately, scaffold thresholds are calculated by selecting 10 pixels on the edge of the image (white area) as the pixel in the middle of the scaffold threshold is definitely larger than that in the edge. As for bone threshold definition, 5 pixels with dim color that represent the bone tissue were selected to find the lowest value, and 5 pixels with the lightest color were selected to find the highest value. After careful selection, the thresholds of the scaffold which were seen as white are all beyond 250. And the threshold of the bone could be set between 60 and 180. The thresholding operation is defined as follows:

$$Area\ defination = \begin{cases} Titanium\ scaffold & , intensity > 250 \\ Bone & , 60 \leq intensity < 180 \end{cases}$$

The pixel is seen as bone if the intensity is larger than 60 and smaller than 180. As for the scaffold area percentage, the intensity should be greater than 250. The percentage is defined as follows:

$$P_b = \frac{S_{bone}}{S_{all} - S_s}$$

where P_b represents the bone percentage of each grid, S_{all} is the whole image area of each grid, and S_{bone} and S_s are defined as the bone and scaffold area occupied in each grid, respectively.

There are two different conventions that are used to decide whether pixels (titanium scaffold and bone tissue) are connected or not in two-dimensional images—4-connected and 8-connected neighborhoods. As for the 4-connected neighborhood, pixels are seen as connected when their edges touch. In other words, the pixels, which are along the diagonals, are not considered connected. As for the 8-connected neighborhood, adjoining pixels are connected along not only horizontal and vertical directions but also the diagonal direction. Both are shown in **Figure 4**.

Physical Model and Computational Framework

A column model with a truncated cone hole in the bulk was developed to simulate the scaffold as the same geometry as the osteochondral defect. The osteochondral defect was set as 8.2 mm diameter on the top and 5.88 mm diameter at the bottom which could just fit the bottom of the scaffold but little bit larger than the scaffold's top surface size (8 mm) because this 0.1-mm hole is used for air outlet after the bone marrow flowed into the void space of the defect. To further investigate the relationship between osteogenesis in the scaffold and simulation results of cell distribution, only the titanium scaffold layer is set as a physical model for recruiting BMSCs. This is because only in the titanium layer osteogenesis occurs.

The bone marrow is considered as a continuity fluid, which could carry BMSCs to attach on the scaffold. The volume of fluid (VOF) model is used to control the movements of these two immiscible fluids. Considering BMSCs as discrete particles, cell attachment is governed by the discrete phase model (DPM) with the Stanton–Rutland model through the Eularian–Lagrangian approach. The interaction of the cell with the scaffold is simulated by the cell impingement model (CIM), which is governed not only by cell physical properties (viscosity, surface tension, and density) but also by the impingement conditions (cells velocity and diameter).

In the DPM, discrete particles representing the BMSCs were carried by the fluid phase, and trajectories of cells were predicted by integrating the force balance on the cell written in a Lagrangian reference frame. All particles (BMSCs) are set as non-rotating. Particle impingement causes energy loss because of the inelastic collision.

In the CIM, the cell impingement model for simulating cell adhesion on the scaffold is defined as three regimes, including stick, rebound, and spread, when cells impinge the scaffold wall. The detailed descriptions are in our previous article.

In VOF model, the bone marrow is seen as a non-Newtonian fluid, which was chosen to simulate the fluid of the bone marrow. Air and the bone marrow are governed by the continuity equation and Navier–Stokes equations as follows:

$$\nabla \cdot \vec{\boldsymbol{u}} = 0$$

$$\rho\left(\frac{\partial \boldsymbol{u}}{\partial t} + \boldsymbol{u} \cdot \nabla \boldsymbol{u}\right) = -\nabla \boldsymbol{p} + \boldsymbol{p}\vec{\boldsymbol{g}} + \mu \nabla^2 \boldsymbol{u}$$

Non-Newtonian fluids will be calculated by the power law for non-Newtonian viscosity as follows:

$$\boldsymbol{\eta} = \mathbf{k}\,\dot{\boldsymbol{\gamma}}^{n-1}\boldsymbol{H}(\boldsymbol{T})$$

where $\dot{\gamma}$ is defined as the shear stress rate-of-deformation tensor $\overline{\overline{\mathrm{D}}}$:

$$\dot{\boldsymbol{\gamma}} = \sqrt{\frac{1}{2}\overline{\overline{\mathbf{D}}}:\overline{\overline{\mathbf{D}}}}$$

$$\overline{\overline{\mathbf{D}}} = \left(\frac{\partial \mathbf{u_j}}{\partial \mathbf{x_i}} + \frac{\partial \mathbf{u_i}}{\partial \mathbf{x_j}}\right)$$

H(T), known as the Arrhenius law (Wendt et al., 2006; Santoro et al., 2010), is temperature-dependent. As the bone marrow is non-isothermal, H(T) is set to 1.

$$\boldsymbol{H}(\mathbf{T}) = \mathbf{exp}\left[\boldsymbol{\alpha}\left(\frac{1}{\mathbf{T}-\mathbf{T}_0} - \frac{1}{\mathbf{T}_{\alpha}-\mathbf{T}_0}\right)\right]$$

BMSCs were treated as spherical particles with non-rotating movement during the calculation and carried by fluid phase (bone marrow). Trajectories of particles were predicted by intergrating force balance on the particles through the Lagrangian frame.

Solving Process and Boundary Conditions

As the scaffold was pushed into the defect after the osteochondral defect was continuously washed, the simulation process is set as the bone marrow starts to flow into the defect when the scaffold is already stably put into the defect (**Figure 5**). In this model, as the scaffold roughness height is in the micro scale, the roughness height is set as 0. Nonslip and non-adherence conditions occurred on the wall and scaffold. Furthermore, as the scaffold manufacturing process is the same as our previous work, the surface and material settings are the same as the previous simulation model (Liu et al., 2020). To validate the cell distribution simulation by the *in vivo* test (osteogenesis on the scaffold), in this simulation, we assumed that BMSCs prefer to proliferate and differentiate on the scaffold surface.

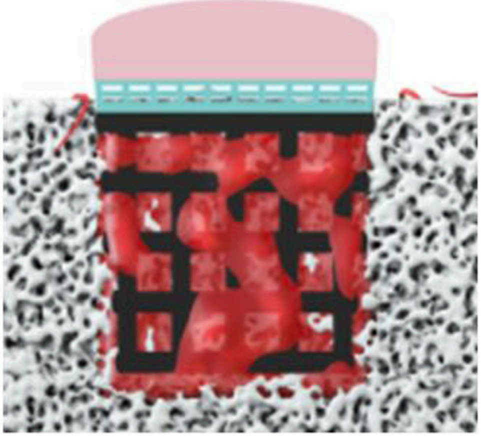

FIGURE 5 | Boundary conditions of simulation (the bone marrow injected from the surrounding and bottom faces).

This process is simplified to simulate the attaching process in which the bone marrow was set as coming from the surrounding and bottom faces for 2.5 s for filling the empty space. After that, two simulation working conditions are set to discover which boundary condition is more suitable for predicting cell attachment. One is that the scaffold starts to absorb cells after 2.5 s, and no more cells would be injected from the sides. The other one is to set at 1 mm/s injection speed of cells after 2.5 s.

The bone marrow is set as a non-Newtonian fluid governed by non-Newtonian power law. Consistency and power law index are set at k = 0.017 and n = 0.708, respectively, with 0.01 and 0.001 as their maximum and minimum viscosity limits. The bone marrow

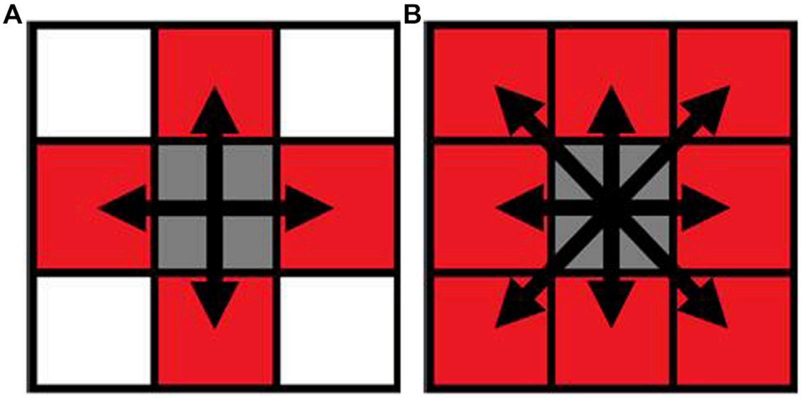

FIGURE 4 | Pixel neighborhood analysis for bone-scaffold connection percentage (**(A)** 4-connected neighborhood; **(B)** 8-connected neighborhood). Simulation of scaffold recruitment for bone marrow mesenchymal stem cells.

TABLE 1 | Characterization of the scaffold and bone.

	Pore size (mm)	*Porosity*	*Surface area (mm^2)*	*Young's modulus (MPa)*
AX-10	**—**	**—**	**157.95**	**1–2**
Cartilage	**—**	**—**	**—**	**0.3–1.5** Mow et al. (1984), Jurvelin et al. (1988), Arokoski et al. (1999), and Nieminen et al. (2000)
PLA dense	**—**	**—**	**112.68**	**2,200**
Subchondral bone plate	**—**	**—**	**—**	**635** ± **94** Wu et al. (2008)
Titanium	**1*1 mm**	**78.6%**	**411.67**	**70–100**
Trabecular bone	**1 mm** Kaplan et al. (1994), Keaveny et al. (2001), and Marks and Odgren (2002)	**50–90%** Kaplan et al. (1994), Keaveny et al. (2001), and Marks and Odgren (2002)	**—**	**19** ± **7** Mittra et al. (2005)

flowing speed is set at 1 mm/s, and the density is 1050 kg/m3. 50,000 spherical cells of 25 μm diameter are injected to the system for 2.5 s uniformly with 1,000 kg/m3 density and 0.03 N/s surface tension. Furthermore, cells could be attached on the boundary faces during the whole calculation period.

RESULTS

Bionic Structural and Mechanical Performance of the Osteochondral Scaffold

As normal joints are formed by three parts, namely, the cartilage, subchondral bone plate, and trabecular bone, scaffolds were designed to mimic three layers of the bone in compliance with structural and mechanical properties. Considering only osteogenesis of the scaffold, the layer made by PLGA for cartilage regeneration would not be well-discussed in this article.

The bionic scaffold is designed with the PLA dense layer on the top and the titanium layer at the bottom which aims to mimic the osteochondral bone structure and mechanical property. The PLA dense layer plays the same role like the subchondral bone which could not only separate the synovial fluid and bone marrow but also connect the trabecular bone (the titanium layer of the scaffold). With high-porosity and interconnected holes, the titanium layer provides a structure for the tissue to attach and proliferate. Moreover, this 3D-printed titanium scaffold is characterized by a flexible design to match the requirement of the pore size, porosity, and surface area, which is used for supporting the mechanical loading from the sheep and provide a spatial structure for bone growth. The pore sizes larger than 100 μm are good for osteogenesis (Karageorgiou and Kaplan, 2005), and 100–400 μm are optimal for bone tissue regeneration (Hulbert et al., 1970; Schliephake et al., 1991; Bloebaum et al., 1994; Hofmann et al., 1997). According to a 3D printing machine's accuracy and the residual stress after the printing, the beams of the scaffold were set at 0.5 mm in diameter, and pore sizes were set at 1 mm^2.

The characterizations of the scaffold and bone are listed as follows (**Table 1**): To combine the PLA layer and titanium layer together, heat treatment was used to make these two layers stick together stably. As BMSC regeneration is hard to control *in vivo* or even the clinical trial and subchondral bone plate is hard to form as prospect, we

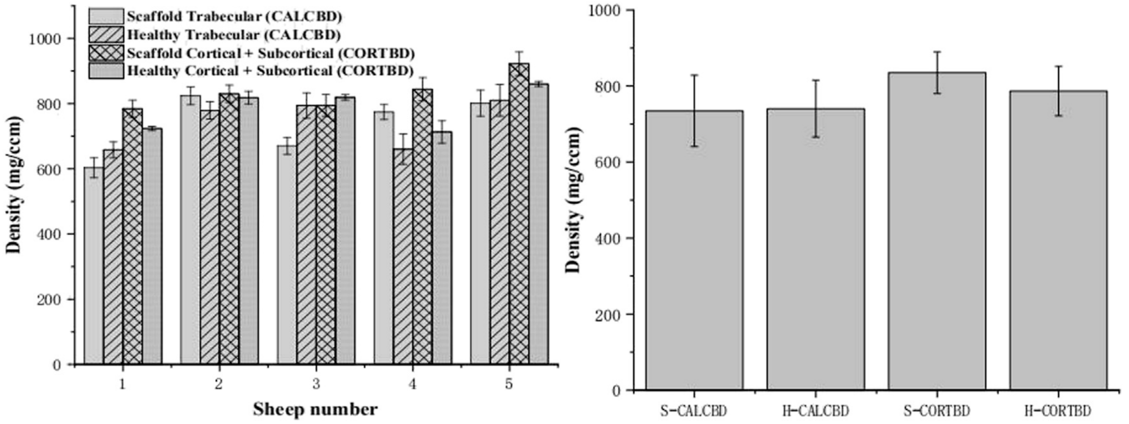

FIGURE 6 | PQCT analysis of the trabecular and cortical BMD of the scaffold and healthy sheep condyle (**left:** each sheep; **right:** in total).

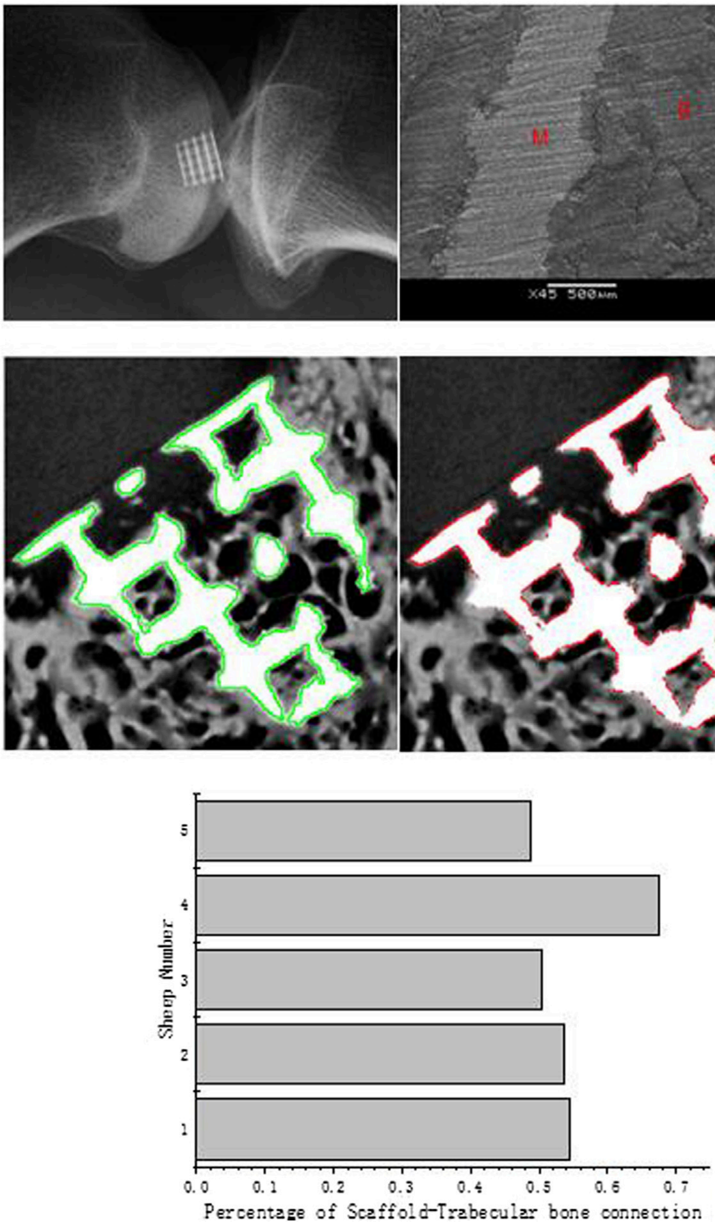

FIGURE 7 | X-ray micrographs of the scaffold in the sheep condyle **(top left)**; an SEM image of scaffold–bone tissue connection **(top right;** M represents the metal alloy scaffold; B represents regenerated bone); the scaffold edge is identified by the green line **(medium left)**; bone–scaffold connection is identified by the red line **(medium right)**; percentage of scaffold–bone tissue connection **(bottom)**.

believe that a dense layer of PLA could substitute biological and mechanical functions of the subchondral bone plate.

The layer for osteogenesis could not achieve the trabecular bone tissue structure as this kind of structure lacks mechanical properties and is easy to break. This layer is made of 3D-printed titanium layer cross-section. As some researchers mentioned that the synovial fluid inhibits bone formation (Andrish and Holmes, 1979; Hazelton et al., 1990), the biofunctional design that uses a PLA dense layer to avoid the synovial fluid flow into the trabecular bone section provides a reliable design for tissue regeneration.

In Vivo Test

After being implanted into the sheep condyle, the bioperformance of the bionic osteochondral scaffold has been evaluated by consequent osteogenesis and tissue quality.

Quantification of Bone–Scaffold Contact

During the *in vivo* test, the 3D scaffold will be affected as the fixation becomes weakening by loading. Such weakening would sometimes occur during the implantation procedure (Knecht et al., 2007). After the surgery, four sheep gaits were normal, and only one sheep had a slight limping, but it

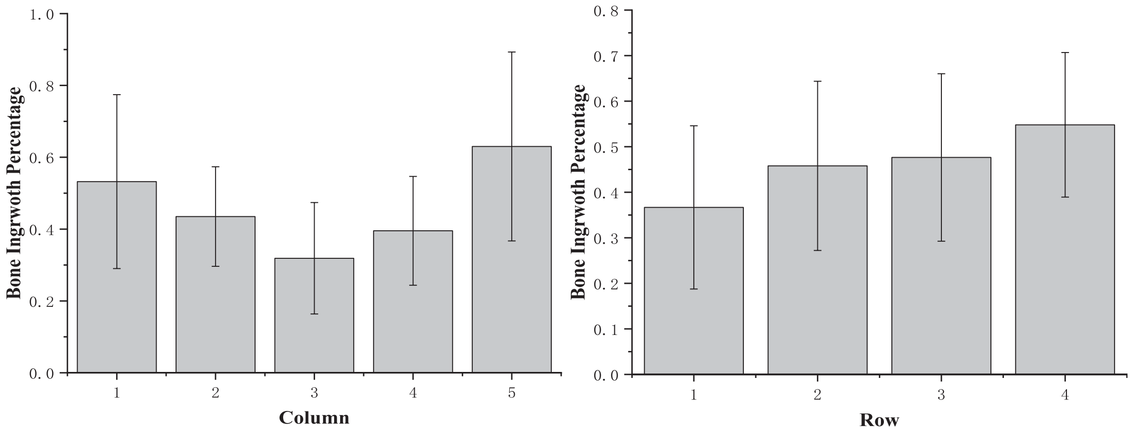

FIGURE 8 | Osteogenesis of scaffold vertical and horizontal analysis.

recovered after several days. After a 3-month recovery period, all five sheep recovered well, and no postoperative complications were found during this period. The X-ray micrographs of the sheep condyle (**Figure 6**. left) showed that scaffold's surrounding tissue connected well with the scaffold, and no loosening was seen in the image. According to the scanning electron microscope (SEM) image, it clearly illustrated that regenerated bone growth based on the metal surface connected well. To quantify and qualify the mechanical fixation, one of the most important things is to investigate tissue–scaffold interactions. Higher tissue–scaffold connection could provide higher skeletal integrity. It is shown that all the sheep's tissue–scaffold connections reached 50% and more after the 3-month healing process using the scaffold. One of them even nearly reached 70%. Because of the high-resolution X-ray image, some printing defects on the scaffold edge (powder with air) were identified, but it is hard to define whether it is the bone or scaffold. To make data more convincible, the real value of the connection of the bone and scaffold should be larger than it is shown in **Figure 7**.

According to the image analysis, we found that new bone tissues prefer to regenerate on the scaffold surface. Similar to the simulation boundary condition, the assumption has been proved by this analysis as the cells and tissues grew based on the scaffold surface.

Quantification of Osteogenesis

To analyze the bone growth preference position in the scaffold, the grids were combined together as columns (horizontal) or rows (vertical). According to the results from the micro-CT and X-ray image analysis (**Figure 8**), in horizontal, compared with column groups 2 and 4, the side edge of the scaffold column group has more bone ingrowths (p1-2 = 0.457; p5-4 = 0.122). Also, the sub-mid area of column groups 2 and 4 is significantly larger than the middle area, with p values 0.247 and 0.452, respectively. No significant difference was found between columns 1–5 and 2–4. In the middle, more than 30% of the void space was occupied by the new regenerative bone tissue; around 40% on the subside of the scaffold and more than 50% of regenerative bone tissue occupied the space. Although the trabecular bone was regenerated more on the side of the scaffold than in the middle, it is believed that the decreasing trend from the side to middle is very slight. Vertically, a slightly decreasing trend was observed from the bottom to top surface. Nearly no difference of the regenerative bone formation was observed between two middle rows. Although the regenerated bone tissue showed a gradual growth trend from the scaffold edge to the middle, the growth rate in the scaffold middle is considerable.

Bone Mineral Density

At 3 months, bone mineral density (BMD) of the cortical bone for the scaffold group and healthy group was 835.04 ± 87.46 and 784.98 ± 72.32 mg/cm^3, respectively. The trabecular bone density of the scaffold and healthy groups was 734.44 ± 131.01 and 740.18 ± 81.98 mg/cm^3, respectively, as shown in **Figure 6**. There were no significant interactions between scaffold and healthy groups' BMD on either the trabecular bone or cortical bone density. Mean trabecular BMD was not significantly different between the healthy knee and experimental knee ($p = 0.92$). And also, no significant difference was found in mean cortical and subcortical BMD ($p = 0.24$).

Simulation of Bone Mesenchymal Stem Cell Attachment on the Scaffold

This simulation aims to investigate the cell attachment process and the final cell distribution after scaffolds are put into the defect, and the bone marrow flows into the defect void space through combining DPM and VOF model. According to the boundary conditions, cells are not attached to the scaffold at the first 2.5 s to mimic the real circumstance of the *in vivo* test. Then, the cell attachment mass counts every integer time from 3 to 5 s. For the whole osteochondral defect system, cell density of scaffolds in two boundary conditions with or without cell inlet after 2.5 s showed a steady increase (**Figure 9** top left). However, as for boundary faces' (trabecular bone) cell density, it showed a

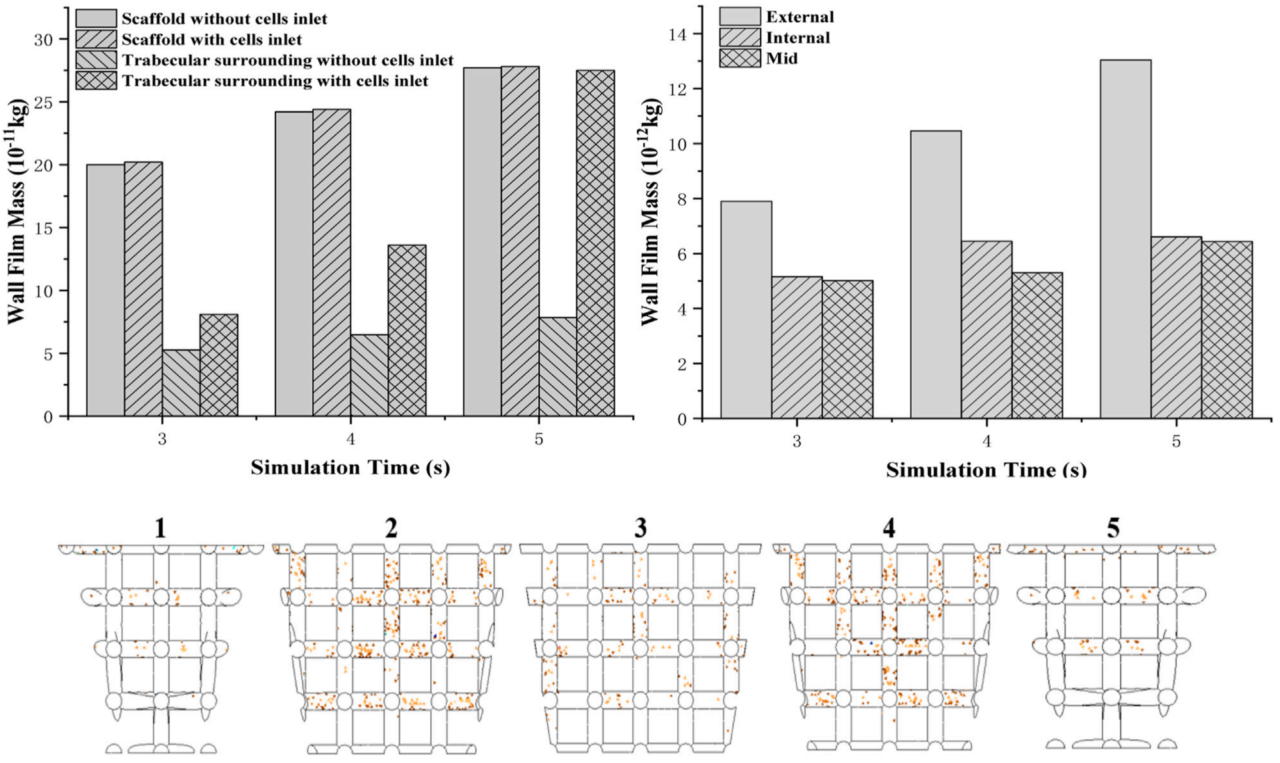

FIGURE 9 | Two different boundary conditions of cells attached to a mass of scaffold and boundary wall **(top left)**; cell (density) distribution in the scaffold from the edge to the middle **(top right)**; simulation of cell attachment at 3 s—boundary conditions: no cells injection **(bottom)**.

rapid growth when cells were still coming to the system after 2.5 s. At 5 s, the cell density of surroundings even reached the same value as the scaffold.

To validate the *in vivo* test more accurately, the scaffold is separated to five parts from one side to the other. Cell attached mass is accounted by averaging the mass on each beam. It is found that from the external to the middle of the scaffold, the cell attached mass showed a decreasing trend (**Figure 9** top right). Compared to the external's cell density which increased rapidly when time goes by, only a little increase in cell density for the internal and middle areas is shown in the graph.

Separating into five parts to investigate cell distribution thoroughly (**Figure 9** bottom), it is found that fewer cells attached at the bottom beam even though they were closer to the bottom injection face. Moreover, sub-closer to edge parts 2 and 4 have more cells attached than 1 and 5.

DISCUSSION

In recent years, cell-based repairing therapeutics has been proved not successful enough for patients who have OA or cartilage defects (Fellows et al., 2016). Lack of blood vessels, low chondrocyte density, and migration ability make cartilage hard to repair (Henrotin et al., 2005). Compared to the autologous chondrocyte implantation (ACI) technology, using scaffolds to recruit BM-MSCs is seen as an effective way for cartilage regeneration and repair.

An ideal three-dimensional scaffold needs to have the same geometrical, mechanical, and biological properties with the host tissue. Our novel bionic osteochondral scaffold is designed by mimicking three main parts of the osteochondral bone which are cartilage, subchondral bone plate, and trabecular bone (Burr and Gallant, 2012). To mimic cartilage's mechanical and biofunctional properties, we combined PLGA and collagen together with a 1–2 MPa elastic modulus. Although the peak stresses *in vivo* could be reached 18 MPa in joints during dynamic loads (Hodge et al., 1986), the elastic modulus is typically 0.3–1.5 MPa (Mow et al., 1984; Jurvelin et al., 1988; Arokoski et al., 1999; Nieminen et al., 2000).This phenomenon is caused by highly pressurized interstitial water during dynamic loading as it cannot be squeezed out during the loading process, which could cause high physiological stresses (Jurvelin et al., 1997; Laasanen et al., 2003). The high-porosity inner structure could also achieve the same function. As for the subchondral plate, it plays an important role in supporting the cartilage and also separating the synovial fluid and trabecular bone because osteogenesis could be inhibited by the synovial fluid (Andrish and Holmes, 1979; Hazelton et al., 1990). The PLA layer design is able to prevent the synovial fluid flow into the trabecular bone defect during the surgery and healing process and also provide sufficient mechanical support. The

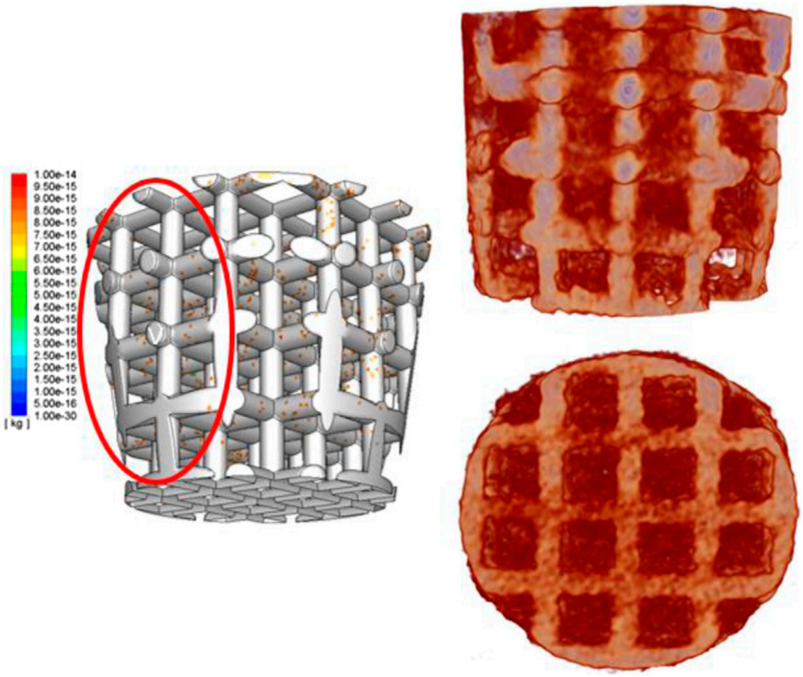

FIGURE 10 | Simulation results of cell distribution in a 3D structure **(left)**; 3D-reconstructed image of the scaffold and bone tissue ingrowth **(right)**.

bottom layer mimicking the trabecular bone is made by 3D-printed titanium which is widely used for trabecular bone regeneration because of its excellent biocompability, mechanical property, chemical stability, and suitability to mimic the biomimetic geometry (Long and Rack, 1998). The trabecular bone, with lower resistance to stress (50 MPa) and high resistance to strain (50%), has 50–90% porosity (Kaplan et al., 1994) and 1 mm diameter pore size (Keaveny et al., 2001). As 100–400 µm pore size is seen as optimal for bone regeneration (Hulbert et al., 1970; Schliephake et al., 1991; Bloebaum et al., 1994; Hofmann et al., 1997), a scaffold with 78.6% porosity and nearly 500 µm is designed.

As the porous design could result in diminished mechanical properties, the design needs to have an adequate mechanical stability to enable initial fixation with the host tissue during implantation as well as surface loading after surgery (Knecht et al., 2007). If the implantation detached partially or even completely fails *in vivo*, patients would feel serious locking or catching at the target area (Nehrer et al., 1999; Peterson et al., 2000). According to the *in vivo* test analysis by X-ray and SEM, it is found that new regenerated tissue connected to the scaffold with high porosity with similar mechanical property to natural bone tissue is really stable.

Interestingly, we found that even the regenerated bone tissue does not fill the void space of the bone defect after 3 months; more than 50% of the scaffolds' whole structure is surrounded by new bone tissue, and there is only a slight decrease in osteogenesis from the side to the middle. This phenomenon illustrates that tissues and cells grow based on the scaffold surface which also points out that cell and tissue distribution is really important as good osteogenesis provides high-quality cartilage.

To further investigate cell distribution in the scaffold for *in vivo* tests, as it is impossible to sacrifice animals at the initial stage (Keaveny et al., 2001), a novel numerical model has been developed to predict cell distribution after the surgery process. For validating the model, we compared the cell distribution results from simulation in 5 s and the regenerated bone distribution of the sheep after 3 months together. According to previous research of Byrne et al., cell proliferation, differentiation, and migration just occur in neighboring areas (Keaveny et al., 2001), and it is found that cell migration does not influence a lot in cell distribution, especially in macroscale (Keaveny et al., 2001). In that case, it is believed that cell distribution at the initial stage is really related to the final bioperformance—regenerated tissue distribution (Keaveny et al., 2001). In other words, it is found that cells remain in their position on the scaffold when they work together and form tissues, as shown in **Figure 10**. As for the bone tissue distribution, horizontally, the trabecular bone occupied more percentage of the void volume at an external place than in the middle, which showed a same trend as external beams have more cell density after cell attachment. But the simulation results did not show that all external areas have really high cell density as *in vivo* tests showed. The reason is that cells attaching to the previous defect hole surfaces cannot be avoided. The cells attaching on the surroundings would proliferate and differentiate to build up the tissues. That is why the external place showed a more intensive cell density. In addition, comparing the cell distribution vertically between the experiment and simulation did not show that the bottom area has higher trabecular bone growth than the top. However, the cell density of the simulation only shows the same trend of the experiment results after the second titanium junction layer. It is clearly seen that not many cells were attached to the lower beam during the attaching process. But, a lot of cells were attached to the bottom surface of the hole. The bone percentage of the bottom is larger than that of the top because the bottom surface has much cell attachment, and they can absorb nutrients more easily as their position is much more close to the bottom and surrounding surfaces (nutrients injection position). In that case, the boundary condition that cells still come to the system after the bone marrow fills the void volume is more accurate to simulate the initial stage of tissue engineering—recruiting cells.

After validation and finding the best boundary condition to simulate the cell attachment process, we found that during the whole attachment process, the external area's cell density was increasing rapidly, but the cell density of internal and middle areas increased extremely slowly. The reason is that initially (first 2.5 s), cells distribute more uniformly as the bone marrow already fills the void space and become steady at that time. When the scaffold starts to absorb cells (after 2.5 s), at the beginning, the cells attaches to the scaffold uniformly. After that, the balance of the cell density in the fluid breaks down, and cells start to move. As there are many beams in the middle providing drags for cells to move in, cells prefer to move outside to somewhere with less drags. That is why the cell density at external beams increases quicker than in the middle.

This novel numerical method for predicting tissue distribution is also available to provide rehabilitation guidance for patients after the surgery as the inner environment of the knee joint like flow speed and temperature could be influenced by rehabilitation devices. By this model, the optimized flow speed and temperature could be explored, and some special medical device should be designed to achieve this environment.

There are some drawbacks to the experiments. First, it is impossible to recognize whether the surrounding areas' bone tissue is a new regenerate bone tissue or old ones according to the X-ray images. Although the external bone tissue growth is well, we cannot identify whether its growth is mainly based on the scaffold influence or it is just the surrounding bones' remodeling and regeneration.

Although we could only ensure that the bone tissue in the internal scaffold's pores are the new tissues, the biomimic scaffold still showed good-quality bioperformance. Second, during the drilling osteochondral defect process, it is unavoidable that the old bone's powder created by the driller in the surroundings may be pushed into the bottom when the scaffold is pushed into the hole. In that case, the bone percentage in the bottom is higher than the other areas, which may not only be influenced by the cell attachment. Bone resorption and remodeling would also affect the final results.

CONCLUSION

This study develops a numerical model which could help researchers to optimize scaffold material property and geometry and could also avoid unnecessary *in vivo* and *in vitro* tests. As the initial healing process of the sheep could not be observed accurately, this model provides an opportunity for researchers to understand how the cell attached and distributed influenced by the scaffold structure and a proper mechanical and biological environment. The simulation results of cell distribution in the scaffold matched well with the regenerated bone tissue distribution in the *in vivo* test. The regenerated bone tissue on the surroundings (scaffold–material interface) is only around 15% more than that in the inner structure. This model could achieve an application to design a personalized scaffold and provide a proper mechanical and biological environment for recovery. It is also useful to help surgeons provide rehabilitation guidance for patients after implantation considering their knee joint inner environment.

DATA AVAILABILITY STATEMENT

The original contributions presented in the study are included in the article/Supplementary Material. Further inquiries can be directed to the corresponding authors.

ETHICS STATEMENT

The animal study was reviewed and approved by Royal Veterinary College. Written informed consent was obtained from the owners for the participation of their animals in this study.

AUTHOR CONTRIBUTIONS

CL and XS are the funders for this publication, and they both revised it critically for important intellectual content. MT and S-MC did the *in vivo* tests. VS, FG, and HW helped analyze the data of both *in vivo* tests and simulation results. I am the main writer for this manuscript and also made the scaffold design and did the simulation work.

FUNDING

This work was supported by the Versus Arthritis Research United Kingdom (Grant No. 21977), European Commission via a H2020-MSCA-RISE programme (BAMOS, Grant No. 734156), Innovative United Kingdom via Newton Fund (Grant No. 102872), Engineering and Physical Science Research Council (EPSRC) via DTP case programme (Grant No. EP/T517793/1) and the Intergovernmental cooperation in science and technology of China (No. 2016YFE0125300).

REFERENCES

Adachi, T., Osako, Y., Tanaka, M., Hojo, M., and Hollister, S. J. (2006). Framework for Optimal Design of Porous Scaffold Microstructure by Computational Simulation of Bone Regeneration. *Biomaterials* 27, 3964–3972. doi:10.1016/j.biomaterials.2006.02.039

Adachi, T., Tsubota, K.-i., Tomita, Y., and Hollister, S. J. (2001). Trabecular Surface Remodeling Simulation for Cancellous Bone Using Microstructural Voxel Finite Element Models. *J. biomechanical Eng.* 123, 403–409. doi:10.1115/1.1392315

Andrish, J., and Holmes, R. (1979). Effects of Synovial Fluid on Fibroblasts in Tissue Culture. *Clin. Orthop. Relat. Res.*, 279–283.

Arokoski, J. P., Hyttinen, M. M., Helminen, H. J., and Jurvelin, J. S. (1999). Biomechanical and Structural Characteristics of Canine Femoral and Tibial Cartilage. *J. Biomed. Mater. Res.* 48, 99–107. doi:10.1002/(sici)1097-4636(1999)48:2<99:aid-jbm1>3.0.co;2-n

Beaupré, G. S., Orr, T. E., and Carter, D. R. (1990). An Approach for Time-dependent Bone Modeling and Remodeling-Theoretical Development. *J. Orthop. Res.* 8, 651–661. doi:10.1002/jor.1100080506

Bloebaum, R. D., Bachus, K. N., Momberger, N. G., and Hofmann, A. A. (1994). Mineral Apposition Rates of Human Cancellous Bone at the Interface of Porous Coated Implants. *J. Biomed. Mater. Res.* 28, 537–544. doi:10.1002/jbm.820280503

Burr, D. B., and Gallant, M. A. (2012). Bone Remodelling in Osteoarthritis. *Nat. Rev. Rheumatol.* 8, 665–673. doi:10.1038/nrrheum.2012.130

Byrne, D. P., Lacroix, D., Planell, J. A., Kelly, D. J., and Prendergast, P. J. (2007). Simulation of Tissue Differentiation in a Scaffold as a Function of Porosity, Young's Modulus and Dissolution Rate: Application of Mechanobiological Models in Tissue Engineering. *Biomaterials* 28, 5544–5554. doi:10.1016/j.biomaterials.2007.09.003

Cowin, S. C. (1993). Bone Stress Adaptation Models. *J. Biomechanical Eng.* 115, 528–533. doi:10.1115/1.2895535

Fellows, C. R., Matta, C., Zakany, R., Khan, I. M., and Mobasheri, A. (2016). Adipose, Bone Marrow and Synovial Joint-Derived Mesenchymal Stem Cells for Cartilage Repair. *Front. Genet.* 7, 213. doi:10.3389/fgene.2016.00213

Groeneveld, E. H. J., van den Bergh, J. P. A., Holzmann, P., ten Bruggenkate, C. M., Tuinzing, D. B., and Burger, E. H. (1999). Mineralization Processes in Demineralized Bone Matrix Grafts in Human Maxillary Sinus Floor Elevations. *J. Biomed. Mater. Res.* 48, 393–402. doi:10.1002/(sici)1097-4636(1999)48:4<393:aid-jbm1>3.0.co;2-c

Hazelton, R. A., Vedam, R., Masci, P. P., and Whitaker, A. N. (1990). Partial Purification and Characterisation of a Synovial Fluid Inhibitor of Osteoblasts. *Ann. Rheum. Dis.* 49, 121–124. doi:10.1136/ard.49.2.121

Healy, K. E. (1999). Molecular Engineering of Materials for Bioreactivity. *Curr. Opin. Solid State. Mater. Sci.* 4, 381–387. doi:10.1016/s1359-0286(99)00038-8

Henrotin, Y., Kurz, B., and Aigner, T. (2005). Oxygen and Reactive Oxygen Species in Cartilage Degradation: Friends or Foes? *Osteoarthritis and Cartilage* 13, 643–654. doi:10.1016/j.joca.2005.04.002

Hodge, W. A., Fijan, R. S., Carlson, K. L., Burgess, R. G., Harris, W. H., and Mann, R. W. (1986). Contact Pressures in the Human Hip Joint Measured *In Vivo*. *Proc. Natl. Acad. Sci.* 83, 2879–2883. doi:10.1073/pnas.83.9.2879

Hofmann, A. A., Bloebaum, R. D., and Bachus, K. N. (1997). Progression of Human Bone Ingrowth into Porous-Coated Implants: Rate of Bone Ingrowth in Humans. *Acta Orthopaedica Scand.* 68, 161–166. doi:10.3109/17453679709004000

Hollister, S. J. (2006). Erratum: Porous Scaffold Design for Tissue Engineering. *Nat. Mater* 5, 590. doi:10.1016/j.cad.2013.05.00510.1038/nmat1683

Hubbell, J. (1999). Bioactive Biomaterials. *Curr. Opin. Biotechnol.* 10, 123–129. doi:10.1016/s0958-1669(99)80021-4

Huiskes, R., Driel, W. D. V., Prendergast, P. J., and Søballe, K. (1997). A Biomechanical Regulatory Model for Periprosthetic Fibrous-Tissue Differentiation. *J. Mater. Sci. Mater. Med.* 8, 785–788. doi:10.17816/vto202027224-29-2180210.1023/a:1018520914512

Hulbert, S. F., Young, F. A., Mathews, R. S., Klawitter, J. J., Talbert, C. D., and Stelling, F. H. (1970). Potential of Ceramic Materials as Permanently Implantable Skeletal Prostheses. *J. Biomed. Mater. Res.* 4, 433–456. doi:10.1002/jbm.820040309

Jurvelin, J., Säämänen, A.-M., Arokoski, J., Helminen, H. J., Kiviranta, I., and Tammi, M. (1988). Biomechanical Properties of the Canine Knee Articular Cartilage as Related to Matrix Proteoglycans and Collagen. *Eng. Med.* 17, 157–162. doi:10.1243/emed_jour_1988_017_042_02

Jurvelin, J. S., Buschmann, M. D., and Hunziker, E. B. (1997). Optical and Mechanical Determination of Poisson's Ratio of Adult Bovine Humeral Articular Cartilage. *J. Biomech.* 30, 235–241. doi:10.1016/s0021-9290(96)00133-9

Kaplan, F. S., Hayes, W. C., Keaveny, T. M., Boskey, A., Einhorn, T. A., and Iannotti, J. P. (1994). Form and Function of Bone. *Orthopaedic Basic Sci.*, 127–185.

Karageorgiou, V., and Kaplan, D. (2005). Porosity of 3D Biomaterial Scaffolds and Osteogenesis. *Biomaterials* 26, 5474–5491. doi:10.1016/j.biomaterials.2005.02.002

Keaveny, T. M., Morgan, E. F., Niebur, G. L., and Yeh, O. C. (2001). Biomechanics of Trabecular Bone. *Annu. Rev. Biomed. Eng.* 3, 307–333. doi:10.1146/annurev.bioeng.3.1.307

Knecht, S., Erggelet, C., Endres, M., Sittinger, M., Kaps, C., and Stüssi, E. (2007). Mechanical Testing of Fixation Techniques for Scaffold-Based Tissue-Engineered Grafts. *J. Biomed. Mater. Res.* 83B, 50–57. doi:10.1002/jbm.b.30765

Laasanen, M. S., Töyräs, J., Korhonen, R. K., Rieppo, J., Saarakkala, S., Nieminen, M. T., et al. (2003). Biomechanical Properties of Knee Articular Cartilage. *Biorheology* 40, 133–140.

Lin, C. Y., Kikuchi, N., and Hollister, S. J. (2004). A Novel Method for Biomaterial Scaffold Internal Architecture Design to Match Bone Elastic Properties with Desired Porosity. *J. Biomech.* 37, 623–636. doi:10.1016/j.jbiomech.2003.09.029

Liu, Z., Tamaddon, M., Gu, Y., Yu, J., Xu, N., Gang, F., et al. (2020). Cell Seeding Process experiment and Simulation on Three-Dimensional Polyhedron and Cross-Link Design Scaffolds. *Front. Bioeng. Biotechnol.* 8, 104–4185. doi:10.3389/fbioe.2020.00104

Long, M., and Rack, H. J. (1998). Titanium Alloys in Total Joint Replacement-A Materials Science Perspective. *Biomaterials* 19, 1621–1639. doi:10.1016/s0142-9612(97)00146-4

Marks, S. C., Jr, and Odgren, P. R. (2002). Structure and Development of the Skeleton. *Principles bone Biol.*, 3–15. doi:10.1016/b978-012098652-1.50103-7

Mittra, E., Rubin, C., and Qin, Y.-X. (2005). Interrelationship of Trabecular Mechanical and Microstructural Properties in Sheep Trabecular Bone. *J. Biomech.* 38, 1229–1237. doi:10.1016/j.jbiomech.2004.06.007

Mow, V. C., Holmes, M. H., and Michael Lai, W. (1984). Fluid Transport and Mechanical Properties of Articular Cartilage: a Review. *J. Biomech.* 17, 377–394. doi:10.1016/0021-9290(84)90031-9

Nehrer, S., Spector, M., and Minas, T. (1999). Histologic Analysis of Tissue after Failed Cartilage Repair Procedures. *Clin. Orthopaedics Relat. Res.* 365, 149–162. doi:10.1097/00003086-199908000-00020

Nieminen, M. T., Toyras, J., Rieppo, J., Hakumaki, J. M., Silvennoinen, J., Helminen, H. J., et al. (2000). Quantitative MR Microscopy of Enzymatically Degraded Articular Cartilage. *Magn. Reson. Med.* 43, 676–681. doi:10.1002/(sici)1522-2594(200005)43:5<676:aid-mrm9>3.0.co;2-x

Peat, G., McCarney, R., and Croft, P. (2001). Knee Pain and Osteoarthritis in Older Adults: a Review of Community burden and Current Use of Primary Health Care. *Ann. Rheum. Dis.* 60, 91–97. doi:10.1136/ard.60.2.91

Peterson, L., Minas, T., Brittberg, M., Nilsson, A., Sj??gren-Jansson, E., and Lindahl, A. (2000). Two- to 9-year Outcome after Autologous Chondrocyte Transplantation of the Knee. *Clin. Orthopaedics Relat. Res.* 374, 212–234. doi:10.1007/978-1-4471-5451-8_4010.1097/00003086-200005000-00020

Prendergast, P. J., Huiskes, R., and Søballe, K.ESB Research Award (1996). ESB Research Award 1996. Biophysical Stimuli on Cells during Tissue Differentiation at Implant Interfaces. *J. Biomech.* 30 (1997), 539–548. doi:10.1016/s0021-9290(96)00140-6

Sakiyama-Elbert, S., and Hubbell, J. (2001). Functional Biomaterials: Design of Novel Biomaterials. *Annu. Rev. Mater. Res.* 31, 183–201. doi:10.1146/annurev.matsci.31.1.183

Santoro, R., Olivares, A. L., Brans, G., Wirz, D., Longinotti, C., Lacroix, D., et al. (2010). Bioreactor Based Engineering of Large-Scale Human Cartilage Grafts for Joint Resurfacing. *Biomaterials* 31, 8946–8952. doi:10.1016/j.biomaterials.2010.08.009

Sanz-Herrera, J. A., Garcia-Aznar, J. M., and Doblare, M. (2008). A Mathematical Model for Bone Tissue Regeneration inside a Specific Type of Scaffold. *Biomech. Model. Mechanobiol* 7, 355–366. doi:10.1007/s10237-007-0089-7

Schliephake, H., Neukam, F. W., and Klosa, D. (1991). Influence of Pore Dimensions on Bone Ingrowth into Porous Hydroxylapatite Blocks Used as Bone Graft Substitutes. *Int. J. Oral Maxillofac. Surg.* 20, 53–58. doi:10.1016/s0901-5027(05)80698-8

Adachi, T., Tanaka, M., and Tomita, Y., (1998, Uniform Stress State in Bone Structure with Residual Stress, *J. Biomech. Eng.*, 120) 342–347. doi:10.1115/1.2798000

Wendt, D., Stroebel, S., Jakob, M., John, G. T., and Martin, I. (2006). Uniform Tissues Engineered by Seeding and Culturing Cells in 3D Scaffolds under Perfusion at Defined Oxygen Tensions. *Biorheology* 43, 481–488. doi:10.1101/815621

Wu, T., Yu, S., Chen, D., and Wang, Y. (2017). Bionic Design, Materials and Performance of Bone Tissue Scaffolds. *Materials* 10, 1187. doi:10.3390/ma10101187

Wu, Z.-x., Lei, W., Hu, Y.-y., Wang, H.-q., Wan, S.-y., Ma, Z.-s., et al. (2008). Effect of Ovariectomy on BMD, Micro-architecture and Biomechanics of Cortical and Cancellous Bones in a Sheep Model. *Med. Eng. Phys.* 30, 1112–1118. doi:10.1016/j.medengphy.2008.01.007

Conflict of Interest: The authors declare that the research was conducted in the absence of any commercial or financial relationships that could be construed as a potential conflict of interest.

frontiers
in Bioengineering and Biotechnology

MINI REVIEW
published: 08 November 2021
doi: 10.3389/fbioe.2021.746074

Two-Dimensional Nanomaterials for Peripheral Nerve Engineering: Recent Advances and Potential Mechanisms

Zhiwen Yan[1,2,3†], *Cheng Chen*[1†], *Gonzalo Rosso*[4,5,6*], *Yun Qian*[1,2,3*] *and Cunyi Fan*[1,2,3*]

[1]Department of Orthopedics, Shanghai Jiao Tong University Affiliated Sixth People's Hospital, Shanghai, China, [2]Shanghai Engineering Research Center for Orthopaedic Material Innovation and Tissue Regeneration, Shanghai, China, [3]Youth Science and Technology Innovation Studio, Shanghai Jiao Tong University School of Medicine, Shanghai, China, [4]Max Planck Institute for the Science of Light, Erlangen, Germany, [5]Max-Planck-Zentrum für Physik und Medizin, Erlangen, Germany, [6]Institute of Physiology II, University of Münster, Münster, Germany

Edited by:
Jianxun Ding,
Changchun Institute of Applied Chemistry (CAS), China

Reviewed by:
Francesco Baino,
Politecnico di Torino, Italy
Wen Shi,
University of Nebraska Medical Center, United States

***Correspondence:**
Gonzalo Rosso
gonzalo.rosso@mpl.mpg.de
Yun Qian
lollipopcloudland@foxmail.com
Cunyi Fan
cyfan@sjtu.edu.cn

†These authors have contributed equally to this work

Specialty section:
This article was submitted to Biomaterials, a section of the journal Frontiers in Bioengineering and Biotechnology

Received: 23 July 2021
Accepted: 19 October 2021
Published: 08 November 2021

Citation:
Yan Z, Chen C, Rosso G, Qian Y and Fan C (2021) Two-Dimensional Nanomaterials for Peripheral Nerve Engineering: Recent Advances and Potential Mechanisms. Front. Bioeng. Biotechnol. 9:746074. doi: 10.3389/fbioe.2021.746074

Peripheral nerve tissues possess the ability to regenerate within artificial nerve scaffolds, however, despite the advance of biomaterials that support nerve regeneration, the functional nerve recovery remains unsatisfactory. Importantly, the incorporation of two-dimensional nanomaterials has shown to significantly improve the therapeutic effect of conventional nerve scaffolds. In this review, we examine whether two-dimensional nanomaterials facilitate angiogenesis and thereby promote peripheral nerve regeneration. First, we summarize the major events occurring after peripheral nerve injury. Second, we discuss that the application of two-dimensional nanomaterials for peripheral nerve regeneration strategies by facilitating the formation of new vessels. Then, we analyze the mechanism that the newly-formed capillaries directionally and metabolically support neuronal regeneration. Finally, we prospect that the two-dimensional nanomaterials should be a potential solution to long range peripheral nerve defect. To further enhance the therapeutic effects of two-dimensional nanomaterial, strategies which help remedy the energy deficiency after peripheral nerve injury could be a viable solution.

Keywords: two-dimensional nanomaterial, peripheral nerve regeneration, nerve scaffold, nerve tissue engineering, angiogenesis, nanomedicine

TWO-DIMENSIONAL NANOMATERIALS AND PERIPHERAL NERVE ENGINEERING

Two-dimensional (2D) nanomaterials have received great interest by the whole research community due to their exceptional electrochemical properties, based on the special character of atom-scale thickness, which allows for the free transfer of electrons on the material surface. Furthermore, 2D nanomaterials exhibit enhanced and tunable electronic, physical and chemical properties due to their distinctive phase, crystallinity, degree of exfoliation, stability and fundamental limitation of thickness (Rohaizad et al., 2021). In addition, as it is the case for the well-known electroactive nature of peripheral nerve tissue (Yao et al., 2021), 2D nanomaterials possess remarkable electrical properties making them ideal candidates for improving the outcomes of peripheral nerve injuries (PNI) (Qian et al., 2019d). Although there are several exciting studies demonstrating that the 2D nanomaterial-based neural regeneration devices could improve the efficiency of peripheral nerve regeneration (PNR) (**Table 1**) the exact mechanisms underlying this phenomenon remains elusive.

TABLE 1 | Therapeutic effects of the 2D nanomaterial functionalized nerve scaffold *in vivo*.

2D Nano-material	Concentration (%)	Nerve defect range (mm)	Time after implantation (weeks)	NCV (ms^{-1})	DCMAP (mV)	Angiogenesis marker	Ref.
Graphene oxide	1	15	18	33.4	25.1	CD31, CD34	Qian et al. (2018b)
Graphene oxide	/	10	8	24.8	9.9	/	Zhang et al. (2020)
Carboxylic graphene oxide	/	10	12	39	3.8	/	Chen et al. (2019)
Reduced graphene oxide	1.14	10	12	25.0	/	/	Wang et al. (2019)
Reduced graphene oxide	0.5	10	12	25	2.5	/	Fang et al. (2020)
Graphene	4	18	18 (months)	42.9	34.5	CD34, VEGF	Qian et al. (2021a)
Graphene	5	10	6	/	5.6	Histology	Lee et al. (2020)
Black phosphorus	0.5	20	16	29.5	22.1	VEGF, CD34	Qian et al. (2019b)
Zinc oxide	10	15	18	45.4	22.6	VEGF, CD34	Qian et al. (2020)
Boron nitride	10	15	18	48.2	30.2	CD34	Qian et al. (2021b)

NVC, Nerve conduction velocity; DCMAP, Distal compound motor action potential; VEGF, Vascular endothelial growth factor; CD, Cluster differentiation; /: Not applicable.

In this review, we summarize the applications of 2D nanomaterials in aiding PNR and focus on the mechanism of new-vessel guided regeneration. First, we summarize the major physiological events occurring after PNI. Second, we describe the application of 2D nanomaterials in peripheral nerve engineering and the corresponding therapeutic effects. Third, we analyze the mechanism by that the newly-formed capillaries provide directionality and metabolic support for neural regeneration. Finally, we discuss the use of 2D nanomaterial-based neural regeneration devices as a potential biomedical strategy to improve long range peripheral nerve defects, and how that could help to remedy the energy deficiency after PNI.

PERIPHERAL NERVE DAMAGE AND REGENERATION

The peripheral nerve acts as a real-time information transmitter between human brain and the rest body. Compared to the well-protected brain and spinal cord in the central nervous system by the skull and vertebrates, peripheral nerves are not surrounded by hard structures, making them extremely vulnerable to different physical damage. Normally, PNIs result in numbness, locomotor dysfunction and even life-long disabilities for individuals (**Figure 1A**), causing huge social and economic burdens (Taylor et al., 2008). The gold standard treatment to PNI (anastomosis and autograft transplanting) have intrinsic limitations such as donor site morbidity and size mismatch (Ray and Mackinnon, 2010). Despite researchers have developed various neural regeneration devices as alternative therapies to PNIs, these products fail to guarantee satisfactory functional nerve recovery.

The peripheral nervous system (PNS) is among the very few tissues in adult mammals which possess remarkable regeneration capabilities after injury. After PNI, Schwann cells–the myelin forming cells in the PNS–dedifferentiate and transform into a repair phenotype that play key roles in the nerve regeneration process (Jessen and Mirsky, 2016; Clements et al., 2017). However, such regeneration process is often mistakenly thought to occur robustly and successfully (Scheib and Höke, 2013). Hence, the complex biological events induced by the injury lead to changes in the biochemical and mechanical properties of the nerve tissue microenvironment, impairing the restoration of nerve function (Yan and Qian, 2020; Qian et al., 2021c). Therefore, it is of tremendous biomedical interest to improve current strategies to regenerate peripheral nerves more efficiently, especially in nerve defect models.

PNIs are characterized by the retraction of two nerve stumps or the direct loss of a nerve segment. During the regeneration process, a natural bridge forms between the two nerve stumps (Min et al., 2021) where damaged axons need to grow through in order to reach the distal nerve trunk and their designated target effectors. The distal trunk, usually referred to as Bands of Büngner, provides a pro-regenerative environment for the outgrowth of axons across the lesion site. However, the environment within the nerve bridge is rather hostile for Schwann cell and axons to travel through. Endothelial cells, which help form new vessels, help remodel the hostile environment and play an essential and inevitable role in the regeneration process (Cattin and Lloyd, 2016). The degree of vascularization determines the success of PNR, i.e., the higher degree of vascularization within the nerve bridge contributes to better PNI outcomes while the inhibition of vascularization destroys normal PNR.

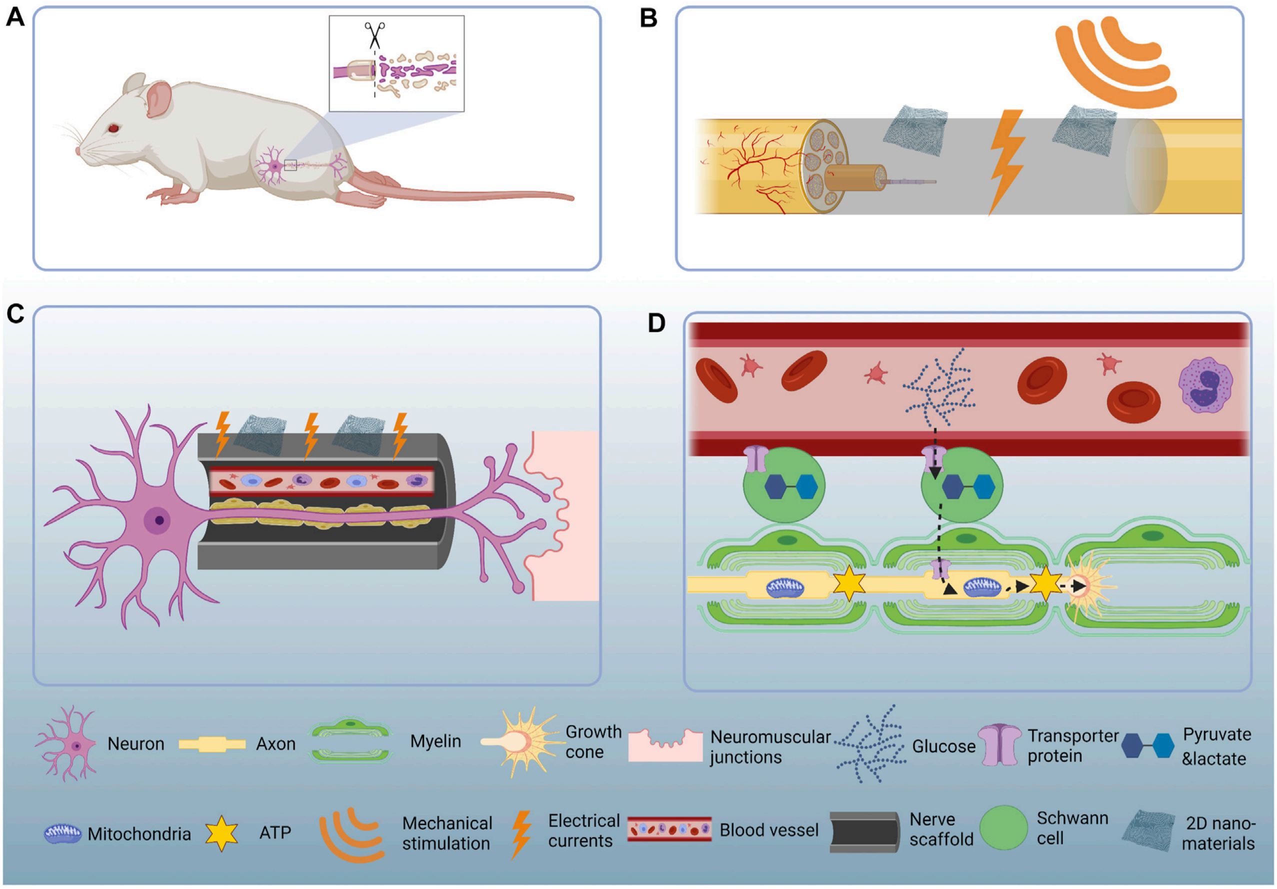

FIGURE 1 | Schematic illustration of the 2D nanomaterial mediated PNR. **(A)** PNI causes sensory and locomotor dysfunction. **(B)** Two-dimensional nanomaterials convert mechanical energy to electrical currents and thereby stimulate PNR. **(C)** Two-dimensional nanomaterials help rebuild the micro-vessels and guide the regenerating nerves back to their original targets. **(D)** Glucose in the reconstructed capillaries get transported to the Schwann cells and then get processed into pyruvate and lactate. The pyruvate and lactate get transported to the regenerating axons and serve as metabolic substrate. The mitochondria accumulate at the axonal growth cone and consume pyruvate and lactate to produce ATP which could be directly used as cellular energy.

APPLICATIONS OF 2D NANOMATERIALS IN PNR AND THE UNDERLYING MECHANISMS

In this subsection, we update the applications of 2D nanomaterials for the fabrication of nerve scaffolds, and focus on the mechanism that the 2D nanomaterials could facilitate the formation of new blood-vessels and discuss their pro-regenerative effects for PNR (**Figure 1B**).

Graphene

Graphene is the most representative material of the 2D nanomaterial family. The unique nano-scale honeycomb planar structure formed by carbon sp^2 hybridization, provides graphene with outstanding electrical conductivity, surface area and mechanical properties (Qian et al., 2018c). Convertino et al. observed that dorsal root ganglion (DRG) neurons elongate more when cultured on graphene surfaces compared to glass *in vitro* (Convertino et al., 2020). The authors attribute this effect to the decreased retrograde transport of nerve growth factor (NGF), and suggested that the increased NGF concentration in axons cultured on graphene is responsible for the improved regenerative capacity of peripheral neurons. Furthermore, when encountered with graphene, neurons show hyperpolarized resting membrane potentials detected by patch-clamp technology, indicating that graphene is able to modulate neuron excitability. Furthermore, the decreased neuron membrane charge could be due to the increase of the local hole doping of graphene. An independent study presented by Pampaloni et al. also supports the notion that single-layered graphene could modulate neuron behavior by influencing membrane functions (Pampaloni et al., 2018). Our group fabricated a graphene-based nerve guide to repair a lengthy peripheral nerve gap (Qian et al., 2021a). Results obtained from *in vivo* measurement showed that the vascular endothelial growth factor (VEGF) protein expression within the graphene-based scaffold was higher when compared to the autograft transplantation 18 months after PNI. Interestingly, the robustly formed capillaries provide the regenerating axons with a microenvironment rich in nutrients. The cell soma of peripheral axons resides in spinal cords and DRGs, so we dissected the spinal cords and DRGs of the rats implanted with graphene-based scaffolds 18 months after injury. We found that the expression level of nestin, a protein specifically expressed in neural stem cells that plays essential roles in neural stem cell differentiation, were upregulated. These results indicate that the presence of graphene accelerates axonal regrowth by creating a pro-angiogenesis microenvironment and increase the stemness of neurons. Interestingly, the high VEGF concentration within the graphene scaffold chamber is also responsible for the increased neuronal activity after PNI. The receptors of VEGF are not only expressed on endothelial cells but also present on the axons and growth cones. The conditional knockdown of hypoxia-inducible factor 1a (HIF-1a) in mice DRG leads to impaired neuronal regenerative ability and the local administration of VEGF could partly remedy this (Cho et al., 2015). Sondell et al. also pointed out VEGF stimulates PNR by acting both on the growing axons and cell bodies (Sondell et al., 2000). Therefore, the graphene induced VEGF expression is responsible for both local angiogenesis and neuronal regeneration.

Graphene Oxide

The incorporation of graphene oxide, an extremely oxidized graphene derivative, elevated the electrical conductivity of a polymeric conduit to 4.55×10^4 S cm^{-1} while the non-oxidized single-layered graphene conduit is 8.92×10^{-3} S cm^{-1}. We have tested the neural functional recovery from the aspect of electrophysical regain, remyelination degree and morphological regeneration at 6, 12, 18 weeks after implantation (Qian et al., 2018a). Interestingly, the graphene oxide embedded nerve guide shows superior regenerative potential compared to the polymeric counterparts at various time points. Of note, after 18 weeks, the regeneration outcome of graphene oxide containing scaffold was similar to that of the clinical "gold standard" autograft transplantation. Then we proposed that this phenomenon could be due to the pro-angiogenesis effects of graphene oxide. As expected, the micro-vessel density and vessel-like structure area significantly elevated in the graphene oxide containing conduit. Further, the CD34, a transmembrane phosphor-glycoprotein, widely used as biomarker of hematopoietic progenitor cells, significantly increased by the controlled release of graphene oxide (Sidney et al., 2014). Additional results showed that AKT-eNOS-VEGF signaling pathway involved in the increase in endothelial cell proliferation may provide new insights for the underlying physiological mechanisms of graphene function in nerve regeneration.

Black Phosphorus

Another promising 2D nanomaterials that has recently received tremendous attention is the black phosphorus for its thickness-dependent bandgap, high charge-carrier mobility, in-plane anisotropic structure, and biodegradable properties (Tao et al., 2015). As a new star of the 2D materials family, black phosphorus exhibited huge potential in aiding peripheral nerve regrowth. For example, the incorporation of 0.5% black phosphorus into polymers elevates the electrical conductivity to 9.81×10^{-3} S cm^{-1}. Hence, a black phosphorus containing nerve scaffold restores the bioelectrical continuity of damaged nerves and promotes the expression of VEGF, thereby contributing to successful formation of new vessels (Qian et al., 2019b). VEGF, as described above, specifically targets endothelial cells and is essential for vasculogenesis. In a rat long-range nerve defect model (20 mm), the incorporation of black phosphorus into a nerve guide has shown to successfully enhance the formation of vessels compared to the polymeric counterparts. The elevated vessel density is responsible for faster neural regeneration. Therefore, the function of target muscle measured by the distal compound motor action potential (DCMAP) increased from 10.1 to 22.1 mV in the polymer group compared to the black phosphorus group 4 months after implantation.

Moreover, mounting evidence suggest that 2D nanomaterials could facilitate PNR by generating electrical currents. Conversely, the process of angiogenesis has also been linked to these 2D materials. Electrical currents that enhance axonal growth combined with the formation of new vessels are two promising outcomes with tremendous potential for the advancement of nerve regeneration strategies. Electrical stimulation has long been proved to be a valid therapeutic strategy for accelerating nerve regrowth (Qian et al., 2019a) and researchers have developed artificial electrical stimulators to facilitate nerve regeneration (Koo et al., 2018). However, such equipment is usually cumbersome to use because it requires external power sources and the implantation of electrodes is also prone to trigger neuroinflammation and gliosis (Cheng et al., 2020). Back in 1991, Fine et al. proposed the application of vinylidenefluoride-trifluoroethylene, a conventional piezoelectrical active material utilized in the engineering of neural regeneration devices (Fine et al., 1991). The piezoelectrical active material possesses the ability to transform the mechanic energy into electrical stimulation. Basically, when the piezoelectrical active neural scaffold gets mechanically deformed by an internal stimulation (e.g., muscle compression) or an external stimulation (e.g., ultrasound), the electrical currents are generated on the scaffold's surface, thereby providing a wireless and self-powered nerve electrical stimulation therapy. Unfortunately, this innovative experiment encountered some difficulties. The polymeric piezoelectric material was hard to degrade *in vivo* and some fibrous capsules formed around the scaffold (Reis et al., 2012). From a crystallography point of view, except for the cubic class 432, all non-centrosymmetric point groups possess the piezoelectric effect. With the fast development of 2D material synthesis technology, the reduced 2D dimensionality embodies spontaneous breakdown of three-dimensional (3D) symmetry. Therefore, some non-piezoelectric bulk materials may become piezoelectric when thinned to single atomic layer (Lin et al., 2018). In addition, the 2D piezoelectric nanomaterials have the advantage of possessing ultra-high piezoelectric coefficients and the ability to degraded by human enzymes (Fei et al., 2015; Lin et al., 2017).

Zinc Oxide

Interestingly, it has been shown that the incorporation of 2D zinc oxide embedded in a polymeric conduit is able to bridge a sciatic nerve defect (Qian et al., 2020a). Qian and colleagues took advantage of a treadmill to trigger electrical activity of the zinc oxide nerve implants in rats. Results from these experiments showed that after 30 min running exercise per day during 18 weeks, the zinc oxide group showed significantly improved nerve regeneration outcomes compared to controls animals. Hence, the zinc oxide nerve scaffold promoted the expression of S100 and myelin basic protein (MBP) in regenerated nerve tissues, indicating a higher number of Schwann cells and myelinated axons. In addition, the β3-tubulin and NF160 levels were also elevated, indicating an increased density of regrowing axons. The cellular and molecular mechanisms underlying nerve regeneration in zinc oxide nerve implants remains still poorly understood. However, an *in vitro* study showed that the ultrasonic activated piezoelectric scaffold increased the VEGF secretion in Schwann cells. On the other hand, an *in vivo* study demonstrated that the exercise activated piezoelectric therapy up-regulates the VEGF and CD34 expression levels within the scaffold chamber (Qian et al., 2020).

Boron Nitride

The incorporation of 2D boron nitride into nerve scaffolds has also shown promising results for the treatment of PNIs. Structured boron nitride possesses unique properties, such as an atomically flat surface, free of dangling bonds, charged impurities, highly chemical stability, superior elastic modulus and outstanding mechanical flexibility (Zhang et al., 2021). Owing to the polarization of the B–N chemical bond, the 2D boron nitride exhibits piezoelectrical activity. Qian et al. incorporated boron nitride into a nerve scaffold to test the neuronal regeneration ability of this 2D nanomaterial (Qian et al., 2021b). The authors first validated that the 2D boron nitride scaffold possessed excellent piezoelectric property measured by piezo-response force microscopy. Then, they applied a treadmill running protocol to induce mechanical deformation on the 2D boron nitride scaffold, thereby generated electrical currents. 18 weeks post implantation, the morphology of regenerated nerve tissues was analyzed by transmission electron microscopy and found a fully regenerated peripheral nerve comprised of axons and myelin sheaths. Specifically, the axons inside the 2D boron nitride scaffold showed an increase of axonal areas, myelin sheath thickness, diameter of myelinated axons, and number of myelinated axons. Furthermore, the locomotor function restoration measured by walking track analysis and DCMAP was improved. The motor function restoration is a challenge for artificial nerve scaffold due to the denervation induced muscle atrophy. The 2D boron nitride scaffold preserved the endplate function and promoted the muscle fiber phenotype shift from slow muscle fiber to fast muscle fiber. The faster axonal regeneration was responsible for this phenomenon and as the micro vessel-reconstruction was the premise for axonal regeneration. As expected, CD34, the indicator of neo-vessel formation, was significantly increased in the 2D boron nitride scaffold group.

2D NANOMATERIALS FACILITATE MICRO-VESSEL FORMATION AND PROVIDE GUIDANCE FOR MIGRATING SCHWANN CELLS

It remains controversial whether 2D nanomaterials could enhance the angiogenesis ability of endothelial cells. Cibecchini et al. reported that the 2D graphene oxide compromised the angiogenic potential of primary human endothelial cells *in vitro* when administered at high concentration (50 μg ml^{-1}) (Cibecchini et al., 2020). The excessive amount of graphene oxide internalized into the cells forms aggregates and affects the consumption of niacinamide. Excessive graphene oxide hindered angiogenesis of human endothelial cells by altering the distribution of mitochondria and disturbing several metabolic pathways. Contrary to *in vitro* results, *in vivo* data showed that 2D nanomaterials stimulate the formation new vessels in different disease models (Qian et al., 2019d; Norahan et al., 2019; Wierzbicki et al., 2020). One possible explanation for this phenomenon could be that *in vivo* studies utilized scaffolds which allow for the controlled release of 2D nanomaterials. But more importantly, *in vivo* environment possesses the multi-cellular complexity. Macrophages, as the important line of defense in human body, are extremely sensitive to foreign implants such as 2D nanomaterials. Xue et al. pointed out that 2D graphene oxide nanosheets could be phagocytosed by macrophages and activate the toll-like receptors (TLR)/myeloid differentiation factor 88 (MyD88)/nuclear factor kappa-B (NF-κB) pathway, thereby excrete VEGF (Xue et al., 2018). The human umbilical vein endothelial cells (HUVEC) treated with graphene oxide conditioned macrophage culture supernatant exhibited enhanced tube formation ability. Overall, the incorporation of 2D nanomaterials could increase new vessel formation *in vivo*. In the following section we discuss the mechanism behind the micro-vessel mediated PNR.

Back in the 1990s, researchers started to observe the relevance between capillary number and nerve regeneration outcomes. Hobson et al. visualized the interactions between RECA-1 positive endothelial cells, S100 positive Schwann cells and axons at different time points after PNI (Hobson et al., 1997). They found first the sprouted of newly formed blood vessels, followed by the migration of Schwann cells and regenerating axons. Of note, the position of Schwann cells and axons within the nerve bridge never exceed the sprouting vessels. In a different work, the incorporation of the proliferative marker EdU in endothelial cells has been used to prove that the vessels are newly formed (Cattin et al., 2015) and observed that the EdU positive endothelial cells only existed within the regenerating nerves.

How does the endothelial cells respond to the nerve injury? In intact nerve tissues, blood vessels go along with nerve fascicles and supply oxygen and nutrients to maintain the normal physiology of nerve function. However, after traumatic nerve injury, both the nerves and the accompanied blood vessels are severely damaged and eventually completely transected causing a hypoxic microenvironment within the injured site. 2 days after nerve dissection, the injury site undergoes severe hypoxia (Cattin et al., 2015). Interestingly, among the diverse cell components of peripheral nerves, macrophages are extremely sensitive to hypoxia. Over 98% hypooxyprobe-1 positive cells are macrophages and over 80% macrophages are hypoxic. Then, the hypoxic microenvironment stabilizes transcriptional factor HIF-1α and initiates the expression of downstream protein VEGF. The VEGF binds to its receptor on endothelial cells and stimulates endothelial cell proliferation which triggers the formation of new vessels and sprouts from the two ends of dissected nerves to form a vessel bridge.

What is the cellular mechanism behind the blood vessel guided nerve regeneration? Schwann cells, a key cell type that plays a major role in the orchestration of PNR, get attracted by the vessel bridge (Clements et al., 2017). The Schwann cells directly migrate along the vessel bridge in an amoeboid-like mode. The actomyosin cytoskeleton is responsible for this behavior, which is impaired by the application of Rho-kinase inhibitor. Besides, the aligned blood vessels provide directionality for Schwann cell migration and intentionally misdirection (implantation of VEGF releasing beads into the surrounding muscle beds) of endothelial cells results in completely failed PNR. Schwann cells follow the vessel track to form a permissive corridor for regenerating axons to travel through (Cattin et al., 2015). It has been shown that Netrin1/DCC signal acts as a critical cue for regenerating axons to grow alongside the migrating Schwann cells (Webber et al., 2011). Only after the regenerating axons reach their final targets, the peripheral nerve damage could be repaired and the denervation induced atrophy of target organs could be remedied.

Where are the newly formed vessels from? Cattin et al. suggested that the new vessels originate from both the proximal and distal nerve stumps, whereas Hobson et al. pointed out that new vessels originate from the adjacent muscle beds (Hobson et al., 1997; Cattin et al., 2015). The differences in the origin of vessels' formation could be explained by the different injury models utilized. Cattin et al. used the simple nerve dissection surgery while Hobson et al. implanted a 10 mm fibronectin graft.

In summary, newly formed vessel is the premise for successful PNR. The capillaries directly guide Schwann cell migration and indirectly contribute to axonal regeneration. The ability of angiogenesis modulation should be taken into account when designing a neural regeneration device (**Figure 1C**).

THE 2D NANOMATERIAL FACILITATED MICRO-VESSEL FORMATION PROVIDES ENERGY FOR PROLIFERATING SCHWANN CELLS

It remains an open question whether 2D nanomaterials facilitate micro-vessel formation and guidance to migrating Schwann cells. In this subsection, we propose a new mechanism which suggests that the newly-formed capillaries may provide nutrients necessary for the proliferation Schwann cells, and metabolically support neuronal regeneration.

Tissue regeneration is a highly energy-demanding process and energy deficiency happens during PNR as well (Han et al., 2016). In response to injury, the PNS adapts a series of metabolic changes to initiate the regeneration process. Recent studies revealed bioenergetically compensatory processes in neuronal axons and Schwann cells. Mitochondria, the cell power-house in mammalian cells, accumulate at the site of injury in axons by microtubule-based mitochondrial transport from the neuronal soma (Han et al., 2016; Patrón and Zinsmaier, 2016). On the other hand, after nerve injury Schwann cells undergo a glycolysis shift to synthesize excessive amount of pyruvate and lactate (Babetto et al., 2020; Trimarco and Taveggia, 2020). The pyruvate and lactate get transferred to the injured axons, serving as metabolic substrate to support the mitochondrial ATP synthesis (Patrón and Zinsmaier, 2016; Trimarco and Taveggia, 2020). In short, Schwann cells metabolically support axonal regeneration, however, where do Schwann cells get metabolic substrate is not completely understood A similar phenomenon occurs in the central nervous system (CNS) where astrocytes and oligodendrocytes - the glial cells in CNS - transfer lactate to neuronal axons and the lactate is used to generate metabolic energy in the form of ATP, thereby supporting the high energy consumption of neuronal axons (Lee et al., 2012; Rinholm and Bergersen, 2012). Of note, the astrocytes and oligodendrocytes break up blood glucose to generate lactate. In other words, blood vessels energetically support axons through glial cells. As mentioned in *2D Nanomaterials Facilitate Micro-Vessel Formation and Provide Guidance for Migrating Schwann Cells*, the newly formed blood vessel is the premise for neural regeneration in PNS where the capillaries serve as tracks for Schwann cells to migrate along and indirectly guide axonal regeneration (Cattin et al., 2015). It remains open whether the newly formed vessels support axonal regeneration in other ways, for instance, by directly providing energy necessary for axonal regeneration. The latter t is highly possible if we consider that the expression levels of glucose transporter 1 (GLUT1) is upregulated during the glycolysis shift in Schwann cells after PNI (Babetto et al., 2020). The GLUT1 is widely accepted as a protein that help glucose transfer between blood vessels and organs (Veys et al., 2020). Thus, the metabolic substrate Schwann cells use may possibly originated from the nearby blood vessels and angiogenesis supports neurogenesis not only by providing directionality but also by supplying nutrients (**Figure 1D**).

Therefore, apart from angiogenesis, attention should also be paid upon the metabolic process during PNR. However, several studies pointed out that the 2D nanomaterials pose threat on endothelial cells by disturbing the metabolic pathways. In this regard, Chen et al. performed transcriptional sequencing on 2D black phosphorus exposed aortic artery and identified metabolic disturbance (Chen et al., 2021). Furthermore, Luo et al. also reported that 2D graphene oxide impaired HUVEC viability by compromising lipid droplet biogenesis (Luo et al., 2021). Lipid, as an integral part of cellular membrane, is essential for endothelial cell proliferation. Importantly, the researchers found the addition of oleic acid and α-linolenic acid, metabolic substrate in lipid biosynthesis, could alleviate the 2D graphene oxide induced cytotoxicity in HUVEC and restore the lipid biosynthesis. Overall, 2D nanomaterials facilitate angiogenesis, the newly formed vessels nourish sprouting axons *via* Schwann cells. However, the 2D nanomaterial itself potentially harms the cellular metabolism, while the incorporation of a bio-metabolic active substrate could remedy this and further enhance the therapeutic effects of 2D nanomaterials.

FINAL REMARKS

Artificial nerve scaffolds hold great promise for the biomedical treatment of injured nerves by connecting the damaged stumps and new nerve tissues form within the scaffold chamber (Liu et al., 2019; Jiang et al., 2020; Yan et al., 2020; Li et al., 2021). However, the functional restoration of PNIs still remains unsatisfactory (Qian et al., 2018b; Qian et al., 2019b; Qian et al., 2019c). The formation of new vessels is the premise for successful PNR, and augmentation of angiogenesis could significantly advance the quality of regenerated nerves and nerve repair strategies. 2D nanomaterials exhibit huge potential in aiding PNR. They not only promote axonal growth *via* electric stimulation, but also facilitate angiogenesis within the regenerating nerve tissue, which directly stimulates Schwann cell proliferation and enhance axonal outgrowth. In this review, we summarize the updates on the mechanism underlying this phenomenon and point out that the 2D nanomaterial promotes PNR *via* facilitating angiogenesis.

Despite there are strong evidences to support that 2D nanomaterials modulate the angiogenesis ability to aid PNR, there are still questions to be answered. What is the target cell of 2D nanomaterials? Whether the 2D nanomaterials directly interact with endothelial cells to drive the proliferation and capillary-forming responses? Or macrophages internalize the 2D nanomaterials to initiate the HIF-1α/VEGF signaling axis, and thereby attract endothelial cell migration? Whether the 2D nanomaterials need to be released from the scaffold to facilitate angiogenesis, or do they take effect *in situ*? Whether the protein within the regeneration microenvironment envelop the 2D nanomaterials to form the “protein corona” and whether the protein-adsorbed nanomaterials change their original biological activities (Wan et al., 2015)?

Moreover, the concentration of 2D nanomaterials should be taken into consideration when fabricating artificial nerve scaffolds. Many nanostructures can facilitate angiogenesis when administered at low dose, but at high dose, they will inhibit new vessel formation (Kargozar et al., 2020). This bimodal effect could be explained by that the low dose nanomaterial triggers moderate level of reactive oxygen species and thereby activates the downstream pro-angiogenesis signaling. However, high dose nanomaterial causes cytotoxicity and compromises cell activity, thereby contributes to the anti-angiogenesis effects.

PERSPECTIVE

Although researchers developed various neural regeneration devices to treat PNI, long-range nerve defect remains a huge challenge (Qian et al., 2018a; Zhao et al., 2018; Chen et al., 2020; Qian et al., 2020b; Yan et al., 2021). The possibility for axons to travel through the chamber of a non-functionalized nerve scaffold is under 50% when the nerve defect exceeds 1 cm in rodents (Wieringa et al., 2018). Insufficient vascularization is observed in the long-range nerve defect model and it contributes to poor regeneration outcomes (Farber et al., 2016). With the development of 2D nanomaterials, the compromised vasculature formation could be remedied. Thus, 2D nanomaterials serve as a potential solution to long-range nerve defects.

Apart from angiogenesis, emphasis should also be placed upon the metabolic disturbance after peripheral nerve injury. Recent studies revealed the metabolically regulatory effects of certain biomaterials and the bioenergetic-active materials substantially accelerated tissue regeneration (Liu et al., 2020; Ma et al., 2019). Thus, the incorporation of bioenergetic active substrate into 2D nanomaterial nerve scaffold is poised to be an efficient and effective way to enhance the performance of conventional nerve scaffolds.

PNIs result in over 8.5 million restricted activity days and almost five million bed or disability days per year. In the US alone, over 200,000 peripheral nerve repair procedures are performed annually (Kehoe et al., 2012). So there is a great need for nerve regeneration devices. Since the mid-1980s, the FDA have approved several devices based on natural and synthetic materials to repair nerve defects, however, the therapeutic efficiency remains unsatisfactory. A preclinical assessment was carried out to examine the long-term biosafety and pro-regeneration effects of the graphene loaded nerve conduits (Qian et al., 2021a). The successful translation of these functionalized nerve conduits can meet the huge clinical demand and indirectly relieve the social and economic burden caused by PNIs.

AUTHOR CONTRIBUTIONS

YQ conceptualized the study. CC, CF, and ZY reviewed the literature and designed the figure and table. ZY drafted the manuscript. YQ, GR, and CF revised the manuscript. All authors read and approved the final version.

FUNDING

The study was sponsored by the Projects of National Natural Science Foundation of China (grant nos. 82002290, and 81830076), the Shanghai Sailing Program (no. 20YF1436000), Shanghai Engineering Research Center for Orthopaedic Material Innovation and Tissue Regeneration (no. 20DZ2254100), Municipal Hospital Newly-developing Cutting-edge Technologies Joint Research Program of Shanghai Shenkang

Hospital Development Center (no. SHDC12018130), Special Fund for Research on People's Livelihood (Medical Treatment and Public Health) of Shanghai Pudong Science, Technology and Economic Commission Scientific and Technological Development Fund (no. PKJ2018-Y52), and Shanghai Pudong Health Commission Special Program for Clinical Research in the Health Industry (no. PW2018E-01).

ACKNOWLEDGMENTS

The authors appreciate the support from Base for Interdisciplinary Innovative Talent Training, Shanghai Jiao Tong University and Youth Science and Technology Innovation Studio of Shanghai Jiao Tong University School of Medicine.

REFERENCES

Babetto, E., Wong, K. M., and Beirowski, B. (2020). A Glycolytic Shift in Schwann Cells Supports Injured Axons. *Nat. Neurosci.* 23 (10), 1215–1228. doi:10.1038/s41593-020-0689-4

Cattin, A.-L., and Lloyd, A. C. (2016). The Multicellular Complexity of Peripheral Nerve Regeneration. *Curr. Opin. Neurobiol.* 39, 38–46. doi:10.1016/j.conb.2016.04.005

Cattin, A.-L., Burden, J. J., Van Emmenis, L., Mackenzie, F. E., Hoving, J. J. A., Garcia Calavia, N., et al. (2015). Macrophage-Induced Blood Vessels Guide Schwann Cell-Mediated Regeneration of Peripheral Nerves. *Cell* 162 (5), 1127–1139. doi:10.1016/j.cell.2015.07.021

Chen, X., Ge, X., Qian, Y., Tang, H., Song, J., Qu, X, et al. (2020). Electrospinning Multilayered Scaffolds Loaded with Melatonin and Fe_3O_4 Magnetic Nanoparticles for Peripheral Nerve Regeneration. *Adv. Funct. Mater.* 30, 2004537. doi:10.1002/adfm.202004537

Chen, X., Liu, C., Huang, Z., Pu, X., Shang, L., Yin, G., et al. (2019). Preparation of Carboxylic Graphene Oxide-composited Polypyrrole Conduits and Their Effect on Sciatic Nerve Repair under Electrical Stimulation. *J. Biomed. Mater. Res.* 107 (12), 2784–2795. doi:10.1002/jbm.a.36781

Chen, J., Lu, L., Zhang, C., Zhu, X., and Zhuang, S. (2021). Endothelial Dysfunction and Transcriptome Aberration in Mouse Aortas Induced by Black Phosphorus Quantum Dots and Nanosheets. *Nanoscale* 13 (19), 9018–9030. doi:10.1039/d1nr01965a

Cheng, Y., Xu, Y., Qian, Y., Chen, X., Ouyang, Y., and Yuan, W.-E. (2020). 3D Structured Self-Powered PVDF/PCL Scaffolds for Peripheral Nerve Regeneration. *Nano Energy* 69**,** 104411. doi:10.1016/j.nanoen.2019.104411

Cho, Y., Shin, J. E., Ewan, E. E., Oh, Y. M., Pita-Thomas, W., and Cavalli, V. (2015). Activating Injury-Responsive Genes with Hypoxia Enhances Axon Regeneration through Neuronal HIF-1α. *Neuron* 88 (4), 720–734. doi:10.1016/j.neuron.2015.09.050

Cibecchini, G., Veronesi, M., Catelani, T., Bandiera, T., Guarnieri, D., and Pompa, P. P. (2020). Antiangiogenic Effect of Graphene Oxide in Primary Human Endothelial Cells. *ACS Appl. Mater. Inter.* 12 (20), 22507–22518. doi:10.1021/acsami.0c03404

Clements, M. P., Byrne, E., Camarillo Guerrero, L. F., Cattin, A.-L., Zakka, L., Ashraf, A., et al. (2017). The Wound Microenvironment Reprograms Schwann Cells to Invasive Mesenchymal-like Cells to Drive Peripheral Nerve Regeneration. *Neuron* 96 (1), 98–114.e7. doi:10.1016/j.neuron.2017.09.008

Convertino, D., Fabbri, F., Mishra, N., Mainardi, M., Cappello, V., Testa, G., et al. (2020). Graphene Promotes Axon Elongation through Local Stall of Nerve Growth Factor Signaling Endosomes. *Nano Lett.* 20 (5), 3633–3641. doi:10.1021/acs.nanolett.0c00571

Fang, X., Guo, H., Zhang, W., Fang, H., Li, Q., Bai, S., et al. (2020). Reduced Graphene Oxide-GelMA-PCL Hybrid Nanofibers for Peripheral Nerve Regeneration. *J. Mater. Chem. B* 8 (46), 10593–10601. doi:10.1039/d0tb00779j

Farber, S. J., Hoben, G. M., Hunter, D. A., Yan, Y., Johnson, P. J., Mackinnon, S. E., et al. (2016). Vascularization is Delayed in Long Nerve Constructs Compared with Nerve Grafts. *Muscle Nerve* 54, 319–321. doi:10.1002/mus.25173

Fei, R., Li, W., Li, J., and Yang, L. (2015). Giant Piezoelectricity of Monolayer Group IV Monochalcogenides: SnSe, SnS, GeSe, and GeS. *Appl. Phys. Lett.* 107 (17), 173104. doi:10.1063/1.4934750

Fine, E. G., Valentini, R. F., Bellamkonda, R., and Aebischer, P. (1991). Improved Nerve Regeneration through Piezoelectric Vinylidenefluoride-Trifluoroethylene Copolymer Guidance Channels. *Biomaterials* 12 (8), 775–780. doi:10.1016/0142-9612(91)90029-a

Han, S. M., Baig, H. S., and Hammarlund, M. (2016). Mitochondria Localize to Injured Axons to Support Regeneration. *Neuron* 92 (6), 1308–1323. doi:10.1016/j.neuron.2016.11.025

Hobson, M. I., Brown, R., Green, C. J., and Terenghi, G. (1997). Inter-relationships between Angiogenesis and Nerve Regeneration: a Histochemical Study. *Br. J. Plast. Surg.* 50 (2), 125–131. doi:10.1016/s0007-1226(97)91325-4

Jessen, K. R., and Mirsky, R. (2016). The Repair Schwann Cell and its Function in Regenerating Nerves. *J. Physiol.* 594 (13), 3521–3531. doi:10.1113/JP270874

Jiang, H., Qian, Y., Fan, C., and Ouyang, Y. (2020). Polymeric Guide Conduits for Peripheral Nerve Tissue Engineering. *Front. Bioeng. Biotechnol.* 8, 582646. doi:10.3389/fbioe.2020.582646

Kargozar, S., Baino, F., Hamzehlou, S., Hamblin, M. R., and Mozafari, M. (2020). Nanotechnology for Angiogenesis: Opportunities and Challenges. *Chem. Soc. Rev.* 49 (14), 5008–5057. doi:10.1039/c8cs01021h

Kehoe, S., Zhang, X. F., and Boyd, D. (2012). FDA Approved Guidance Conduits and Wraps for Peripheral Nerve Injury: a Review of Materials and Efficacy. *Injury* 43 (5), 553–572. doi:10.1016/j.injury.2010.12.030

Koo, J., MacEwan, M. R., Kang, S.-K., Won, S. M., Stephen, M., Gamble, P., et al. (2018). Wireless Bioresorbable Electronic System Enables Sustained Nonpharmacological Neuroregenerative Therapy. *Nat. Med.* 24 (12), 1830–1836. doi:10.1038/s41591-018-0196-2

Lee, Y., Morrison, B. M., Li, Y., Lengacher, S., Farah, M. H., Hoffman, P. N., et al. (2012). Oligodendroglia Metabolically Support Axons and Contribute to Neurodegeneration. *Nature* 487 (7408), 443–448. doi:10.1038/nature11314

Lee, T.-H., Yen, C.-T., and Hsu, S.-h. (2020). Preparation of Polyurethane-Graphene Nanocomposite and Evaluation of Neurovascular Regeneration. *ACS Biomater. Sci. Eng.* 6 (1), 597–609. doi:10.1021/acsbiomaterials.9b01473

Li, Y., Shen, Q., Shen, J., Ding, X., Liu, T., He, J., et al. (2021). Multifunctional Fibroblasts Enhanced *via* Thermal and Freeze-Drying Post-treatments of Aligned Electrospun Nanofiber Membranes. *Adv. Fiber Mater.* 3 (1), 26–37. doi:10.1007/s42765-020-00059-3

Lin, H., Gao, S., Dai, C., Chen, Y., and Shi, J. (2017). A Two-Dimensional Biodegradable Niobium Carbide (MXene) for Photothermal Tumor Eradication in NIR-I and NIR-II Biowindows. *J. Am. Chem. Soc.* 139 (45), 16235–16247. doi:10.1021/jacs.7b07818

Lin, P., Pan, C., and Wang, Z. L. (2018). Two-dimensional Nanomaterials for Novel Piezotronics and Piezophototronics. *Mater. Today Nano* 4, 17–31. doi:10.1016/j.mtnano.2018.11.006

Liu, H., Du, Y., St-Pierre, J. P., Bergholt, M. S., Autefage, H., and Wang, J. (2020). Bioenergetic-Active Materials Enhance Tissue Regeneration by Modulating Cellular Metabolic State. *Sci. Adv.* 6 (13), eaay7608. doi:10.1126/sciadv.aay7608

Liu, Y., Wu, F., Ding, Y., Zhu, B., Su, Y., and Zhu, X. (2019). Preparation and Characterization of Paclitaxel/Chitosan Nanosuspensions for Drug Delivery System and Cytotoxicity Evaluation *In Vitro*. *Adv. Fiber Mater.* 1 (2), 152–162. doi:10.1007/s42765-019-00012-z

Luo, Y., Wang, X., and Cao, Y. (2021). Transcriptomic Analysis Suggested the Involvement of Impaired Lipid Droplet Biogenesis in Graphene Oxide-Induced Cytotoxicity in Human Umbilical Vein Endothelial Cells. *Chemico-Biol. Interact.* 333, 109325. doi:10.1016/j.cbi.2020.109325

Ma, C., Kuzma, M. L., Bai, X., and Yang, J. (2019). Biomaterial-Based Metabolic Regulation in Regenerative Engineering. *Adv. Sci.* 6 (19), 1900819. doi:10.1002/advs.201900819

Min, Q., Parkinson, D. B., and Dun, X. P. (2021). Migrating Schwann Cells Direct Axon Regeneration within the Peripheral Nerve Bridge. *Glia* 69 (2), 235–254. doi:10.1002/glia.23892

Norahan, M. H., Amroon, M., Ghahremanzadeh, R., Mahmoodi, M., and Baheiraei, N. (2019). Electroactive Graphene Oxide-Incorporated Collagen Assisting Vascularization for Cardiac Tissue Engineering. *J. Biomed. Mater. Res.* 107 (1), 204–219. doi:10.1002/jbm.a.36555

Pampaloni, N. P., Lottner, M., Giugliano, M., Matruglio, A., D'Amico, F., Prato, M., et al. (2018). Single-layer Graphene Modulates Neuronal Communication and Augments Membrane Ion Currents. *Nat. Nanotech* 13 (8), 755–764. doi:10.1038/s41565-018-0163-6

Patrón, L. A., and Zinsmaier, K. E. (2016). Mitochondria on the Road to Power Axonal Regeneration. *Neuron* 92 (6), 1152–1154. doi:10.1016/j.neuron.2016.12.007

Qian, Y., Song, J., Zhao, X., Chen, W., Ouyang, Y., Yuan, W., et al. (2018a). 3D Fabrication with Integration Molding of a Graphene Oxide/Polycaprolactone Nanoscaffold for Neurite Regeneration and Angiogenesis. *Adv. Sci.* 5 (4), 1700499. doi:10.1002/advs.201700499

Qian, Y., Song, J., Zheng, W., Zhao, X., Ouyang, Y., Yuan, W., et al. (2018b). 3D Manufacture of Gold Nanocomposite Channels Facilitates Neural Differentiation and Regeneration. *Adv. Funct. Mater.* 28 (14), 1707077. doi:10.1002/adfm.201707077

Qian, Y., Zhao, X., Han, Q., Chen, W., Li, H., and Yuan, W. (2018c). An Integrated Multi-Layer 3D-Fabrication of PDA/RGD Coated Graphene Loaded PCL Nanoscaffold for Peripheral Nerve Restoration. *Nat. Commun.* 9 (1), 323. doi:10.1038/s41467-017-02598-7

Qian, Y., Cheng, Y., Cai, J., Zhao, X., Ouyang, Y., Yuan, W.-E., et al. (2019a). Advances in Electrical and Magnetic Stimulation on Nerve Regeneration. *Regener. Med.* 14 (10), 969–979. doi:10.2217/rme-2018-0079

Qian, Y., Cheng, Y., Ouyang, Y., Yuan, W.-E., and Fan, C. (2019b). Multilayered Spraying and Gradient Dotting of Nanodiamond-Polycaprolactone Guidance Channels for Restoration of Immune Homeostasis. *NPG Asia Mater.* 11 (1), 36. doi:10.1038/s41427-019-0136-8

Qian, Y., Han, Q., Zhao, X., Li, H., Yuan, W.-E., and Fan, C. (2019c). Asymmetrical 3D Nanoceria Channel for Severe Neurological Defect Regeneration. *iScience* 12, 216–231. doi:10.1016/j.isci.2019.01.013

Qian, Y., Yuan, W.-E., Cheng, Y., Yang, Y., Qu, X., and Fan, C. (2019d). Concentrically Integrative Bioassembly of a Three-Dimensional Black Phosphorus Nanoscaffold for Restoring Neurogenesis, Angiogenesis, and Immune Homeostasis. *Nano Lett.* 19 (12), 8990–9001. doi:10.1021/acs.nanolett.9b03980

Qian, Y., Cheng, Y., Song, J., Xu, Y., Yuan, W. E., Fan, C., et al. (2020). Mechano-Informed Biomimetic Polymer Scaffolds by Incorporating Self-Powered Zinc Oxide Nanogenerators Enhance Motor Recovery and Neural Function. *Small* 16 (32), 2000796. doi:10.1002/smll.202000796

Qian, Y., Wang, X., Song, J., Chen, W., Chen, S., Jin, Y., et al. (2021a). Preclinical Assessment on Neuronal Regeneration in the Injury-Related Microenvironment of Graphene-Based Scaffolds. *NPJ Regen. Med.* 6 (1), 31. doi:10.1038/s41536-021-00142-2

Qian, Y., Xu, Y., Yan, Z., Jin, Y., Chen, X., Yuan, W.-E., et al. (2021b). Boron Nitride Nanosheets Functionalized Channel Scaffold Favors Microenvironment Rebalance Cocktail Therapy for Piezocatalytic Neuronal Repair. *Nano Energy* 83, 105779. doi:10.1016/j.nanoen.2021.105779

Qian, Y., Lin, H., Yan, Z., Shi, J., and Fan, C. (2021c). Functional Nanomaterials in Peripheral Nerve Regeneration: Scaffold Design, Chemical Principles and Microenvironmental Remodeling. *Mater. Today*. doi:10.1016/j.mattod.2021.09.014

Qian, Y., Yao, Z., Wang, X., Cheng, Y., Fang, Z., Yuan, W. E, et al. (2020b). (-)-Epigallocatechin Gallate-Loaded Polycaprolactone Scaffolds Fabricated Using a 3D Integrated Moulding Method Alleviate Immune Stress and Induce Neurogenesis. *Cell Prolif.* 53, e12730. doi:10.1111/cpr.12730

Ray, W. Z., and Mackinnon, S. E. (2010). Management of Nerve Gaps: Autografts, Allografts, Nerve Transfers, and End-To-Side Neurorrhaphy. *Exp. Neurol.* 223 (1), 77–85. doi:10.1016/j.expneurol.2009.03.031

Reis, J., Frias, C., Canto e Castro, C., Botelho, M. L., Marques, A. T., Simões, J. A. O., et al. (2012). A New Piezoelectric Actuator Induces Bone Formation *in Vivo*: A Preliminary Study. *J. Biomed. Biotechnol.* 2012, 613403. doi:10.1155/2012/613403

Rinholm, J. E., and Bergersen, L. H. (2012). Neuroscience: The Wrap that Feeds Neurons. *Nature* 487 (7408), 435–436. doi:10.1038/487435a

Rohaizad, N., Mayorga-Martinez, C. C., Fojtů, M., Latiff, N. M., and Pumera, M. (2021). Two-dimensional Materials in Biomedical, Biosensing and Sensing Applications. *Chem. Soc. Rev.* 50 (1), 619–657. doi:10.1039/d0cs00150c

Scheib, J., and Höke, A. (2013). Advances in Peripheral Nerve Regeneration. *Nat. Rev. Neurol.* 9 (12), 668–676. doi:10.1038/nrneurol.2013.227

Sidney, L. E., Branch, M. J., Dunphy, S. E., Dua, H. S., and Hopkinson, A. (2014). Concise Review: Evidence for CD34 as a Common Marker for Diverse Progenitors. *Stem Cells* 32 (6), 1380–1389. doi:10.1002/stem.1661

Sondell, M., Sundler, F., and Kanje, M. (2000). Vascular Endothelial Growth Factor Is a Neurotrophic Factor Which Stimulates Axonal Outgrowth through the Flk-1 Receptor. *Eur. J. Neurosci.* 12 (12), 4243–4254. doi:10.1046/j.0953-816x.2000.01326.x

Tao, J., Shen, W., Wu, S., Liu, L., Feng, Z., Wang, C., et al. (2015). Mechanical and Electrical Anisotropy of Few-Layer Black Phosphorus. *ACS Nano* 9 (11), 11362–11370. doi:10.1021/acsnano.5b05151

Taylor, C. A., Braza, D., Rice, J. B., and Dillingham, T. (2008). The Incidence of Peripheral Nerve Injury in Extremity Trauma. *Am. J. Phys. Med. Rehabil.* 87 (5), 381–385. doi:10.1097/PHM.0b013e31815e6370

Trimarco, A., and Taveggia, C. (2020). Schwann cell energy to die for. *Nat. Neurosci.* 23 (10), 1179–1181. doi:10.1038/s41593-020-00707-2

Veys, K., Fan, Z., Ghobrial, M., Bouché, A., García-Caballero, M., Vriens, K., et al. (2020). Role of the GLUT1 Glucose Transporter in Postnatal CNS Angiogenesis and Blood-Brain Barrier Integrity. *Circ. Res.* 127 (4), 466–482. doi:10.1161/circresaha.119.316463

Wan, S., Kelly, P. M., Mahon, E., Stöckmann, H., Rudd, P. M., Caruso, F., et al. (2015). The "sweet" Side of the Protein corona: Effects of Glycosylation on Nanoparticle-Cell Interactions. *ACS Nano* 9 (2), 2157–2166. doi:10.1021/nn506060q

Wang, J., Cheng, Y., Chen, L., Zhu, T., Ye, K., Jia, C., et al. (2019). *In Vitro* and *In Vivo* Studies of Electroactive Reduced Graphene Oxide-Modified Nanofiber Scaffolds for Peripheral Nerve Regeneration. *Acta Biomater.* 84, 98–113. doi:10.1016/j.actbio.2018.11.032

Webber, C. A., Christie, K. J., Cheng, C., Martinez, J. A., Singh, B., Singh, V., et al. (2011). Schwann Cells Direct Peripheral Nerve Regeneration through the Netrin-1 Receptors, DCC and Unc5H2. *Glia* 59 (10), 1503–1517. doi:10.1002/glia.21194

Wieringa, P. A., Gonçalves de Pinho, A. R., Micera, S., van Wezel, R. J. A., and Moroni, L. (2018). Biomimetic Architectures for Peripheral Nerve Repair: A Review of Biofabrication Strategies. *Adv. Healthc. Mater.* 7, 1701164. doi:10.1002/adhm.201701164

Wierzbicki, M., Hotowy, A., Kutwin, M., Jaworski, S., Bałaban, J., Sosnowska, M., et al. (2020). Graphene Oxide Scaffold Stimulates Differentiation and Proangiogenic Activities of Myogenic Progenitor Cells. *Ijms* 21 (11), 4173. doi:10.3390/ijms21114173

Xue, D., Chen, E., Zhong, H., Zhang, W., Wang, S., Joomun, M. U., et al. (2018). Immunomodulatory Properties of Graphene Oxide for Osteogenesis and Angiogenesis. *Int. J. Nanomed.* 13, 5799–5810. doi:10.2147/ijn.S170305

Yan, Z., and Qian, Y. (2020). Rectify the Injury-Induced Microenvironment Imbalance in Peripheral Nerve Repair. *Aml* 11 (10), 20101562. doi:10.5185/amlett.2020.101562

Yan, Z., Qian, Y., and Fan, C. (2021). Biomimicry in 3D Printing Design: Implications for Peripheral Nerve Regeneration. *Regen. Med.* 16 (7), 683–701. doi:10.2217/rme-2020-0182

Yan, J., Wu, R., Liao, S., Jiang, M., and Qian, Y. (2020). Applications of Polydopamine-Modified Scaffolds in the Peripheral Nerve Tissue Engineering. *Front. Bioeng. Biotechnol.* 8, 590998. doi:10.3389/fbioe.2020.590998

Yao, X., Qian, Y., and Fan, C. (2021). Electroactive Nanomaterials in the Peripheral Nerve Regeneration. *J. Mater. Chem. B* 9 (35), 6958–6972. doi:10.1039/d1tb00686j

Zhang, D., Yao, Y., Duan, Y., Yu, X., Shi, H., Nakkala, J. R., et al. (2020). Surface-Anchored Graphene Oxide Nanosheets on Cell-Scale Micropatterned Poly(d,l-Lactide-Co-Caprolactone) Conduits Promote Peripheral Nerve Regeneration. *ACS Appl. Mater. Inter.* 12 (7), 7915–7930. doi:10.1021/acsami.9b20321

Zhang, J., Tan, B., Zhang, X., Gao, F., Hu, Y., Wang, L., et al. (2021). Atomically Thin Hexagonal Boron Nitride and its Heterostructures. *Adv. Mater.* 33 (6), 2000769. doi:10.1002/adma.202000769

Zhao, X., Qian, Y., Cheng, Y., Guo, X., and Yuan, W. E. (2018). One-Pot Construction of a Twice-Condensed pDNA Polyplex System for Peripheral Nerve Crush Injury Therapy. *Biomater. Sci.* 6 (8), 2059–2072. doi:10.1039/c8bm00356d

Conflict of Interest: The authors declare that the research was conducted in the absence of any commercial or financial relationships that could be construed as a potential conflict of interest.

frontiers
in Bioengineering and Biotechnology

ORIGINAL RESEARCH
published: 01 February 2022
doi: 10.3389/fbioe.2021.814040

Bardoxolone Methyl Ameliorates Compression-Induced Oxidative Stress Damage of Nucleus Pulposus Cells and Intervertebral Disc Degeneration *Ex Vivo*

*Yueyang Tian[1]†, Jiaqi Duan[2]†, Yang Cao[3], Huichao Zhou[1], Ashish D Diwan[4] and Ji Tu[4]**

[1]*School of Medicine, Nankai University, Tianjin, China,* [2]*Queen Mary College, Nanchang University, Nanchang, China,* [3]*Zhengzhou University of Light Industry, Zhengzhou, China,* [4]*Spine Labs, St.George and Sutherland Clinical School, University of New South Wales, Sydney, NSW, Australia*

Intervertebral disc degeneration (IDD) is the main cause of low back pain, and little is known about its molecular and pathological mechanisms. According to reports, excessive compression is a high-risk factor for IDD; compressive stress can induce oxidative stress in nucleus pulposus (NP) cells during IDD progression that, in turn, promotes cell apoptosis and extracellular matrix (ECM) degradation. Currently, NP tissue engineering is considered a potential method for IDD treatment. However, after transplantation, NP cells may experience oxidative stress and induce apoptosis and ECM degradation due to compressive stress. Therefore, the development of strategies to protect NP cells under excessive compressive stress, including pretreatment of NP cells with antioxidants, has important clinical significance. Among the various antioxidants, bardoxolone methyl (BARD) is used to protect NP cells from damage caused by compressive stress. Our results showed that BARD can protect the viability of NP cells under compression. BARD inhibits compression-induced oxidative stress in NP cells by reducing compression-induced overproduction of reactive oxygen species (ROS) and malondialdehyde. Thus, BARD has a protective effect on the compression-induced apoptosis of NP cells. This is also supported by changes in the expression levels of proteins related to the mitochondrial apoptosis pathway. In addition, BARD can inhibit ECM catabolism and promote ECM anabolism in NP cells. Finally, the experimental results of the mechanism show that the activation of the Nrf2 signaling pathway participates in the protection induced by BARD in compressed NP cells. Therefore, to improve the viability and biological functions of NP cells under compression, BARD should be used during transplantation.

Keywords: intervertebral disc degeneration, tissue engineering, compression, oxidative stress, bardoxolone methyl, Nrf2

Edited by:
Yun Qian,
Shanghai Jiao Tong University, China

Reviewed by:
Baoshan Xu,
Tianjin Hospital, China
Weishi Li,
Peking University Third Hospital, China

***Correspondence:**
Ji Tu
ji.tu@unsw.edu.au

†These authors have contributed equally to this work and share first authorship.

Specialty section:
This article was submitted to Biomaterials,
a section of the journal
Frontiers in Bioengineering and Biotechnology

Received: *12 November 2021*
Accepted: *20 December 2021*
Published: *01 February 2022*

Citation:
Tian Y, Duan J, Cao Y, Zhou H, Diwan AD and Tu J (2022) Bardoxolone Methyl Ameliorates Compression-Induced Oxidative Stress Damage of Nucleus Pulposus Cells and Intervertebral Disc Degeneration Ex Vivo.
Front. Bioeng. Biotechnol. 9:814040.
doi: 10.3389/fbioe.2021.814040

INTRODUCTION

The main cause of low back pain (LBP) is intervertebral disc (IVD) degeneration (IDD) (Anderson et al., 2005). LBP is a common, chronic, and expensive musculoskeletal disease that places a huge economic burden on the world (Maniadakis and Gray, 2000). Nucleus pulposus (NP), cartilage endplate, and annulus fibrosus (AF) are interconnected to form IVDs (Fernandez-Moure et al., 2018). The central NP tissue is an important unit for the normal physiological function of the IVD that allows the IVD to maintain a high water content to withstand mechanical stress from all directions (Hutton et al., 1997). There is still no clear explanation for the molecular mechanism of IDD. Many researchers have found that in the harsh environment of IDD, oxidative stress can cause excessive apoptosis of NP cells and disorder of NP extracellular matrix (ECM) metabolism, induce the destruction of normal IVD physiological function and structure, and, finally, lead to the development of IDD (Roughley, 2004; Zhang et al., 2020). Therefore, inhibiting NP cell apoptosis and ECM degradation induced by oxidative stress is of great significance for the treatment of IDD.

At present, the treatment of IDD generally involves discectomy combined with spinal fusion, which can only alleviate the clinical symptoms to a certain extent and cannot completely restore the biological function of IVD. Following the procedure, patients eventually experience recurrence or symptom aggravation (Iatridis et al., 2013). In recent years, NP tissue engineering technology has become a new method for repairing degenerative IVD (Yang and Li, 2009). The goal of NP tissue engineering is to reconstruct the complex structure, including materials and cells, and to replace the degenerative NP tissue. The survival of cells in the harsh environment of IDD is very important (Nomura et al., 2001). In daily life, the spine is subjected to varying degrees of mechanical pressure, and the excessive compression of the IVD, the load-absorbing structure of the spine, is a major cause of IDD (Kang et al., 2020). Therefore, IDD compression models allow investigators to study the pathogenesis of IDD. In the degenerative disc environment, NP cell survival needs to overcome compression-induced injury (Wang et al., 2020c). A previous study has shown that when the pressure reaches 1.0 MPa, mitochondrial dysfunction, excessive ROS production, and apoptosis are observed NP cells (Hutton et al., 1999).

Bardoxolone methyl (BARD) is a synthetic triterpenoid. In studies of diabetic nephropathy and acute lung injury, it has been confirmed that BARD can exert an antioxidant effect by activating the Nrf2/ARE pathway (Nagasu et al., 2019; Pei et al., 2019; Rossing et al., 2019; Kanda and Yamawaki, 2020). However, it is unclear whether BARD can inhibit compression-induced oxidative stress, apoptosis, and ECM degradation in NP cells. Therefore, we investigated the effect of BARD on NP cell injury induced by compression and the underlying molecular mechanism. This experiment is of great significance for optimizing the application of NP tissue engineering in the treatment of IDD.

MATERIALS AND METHODS

Human NP Cell Acquisition and Culture

Human NP cells, derived from human IVD NP, were purchased from ScienCell Research Laboratory (ScienCell). NP cells were cultured as described below (Kang et al., 2017).

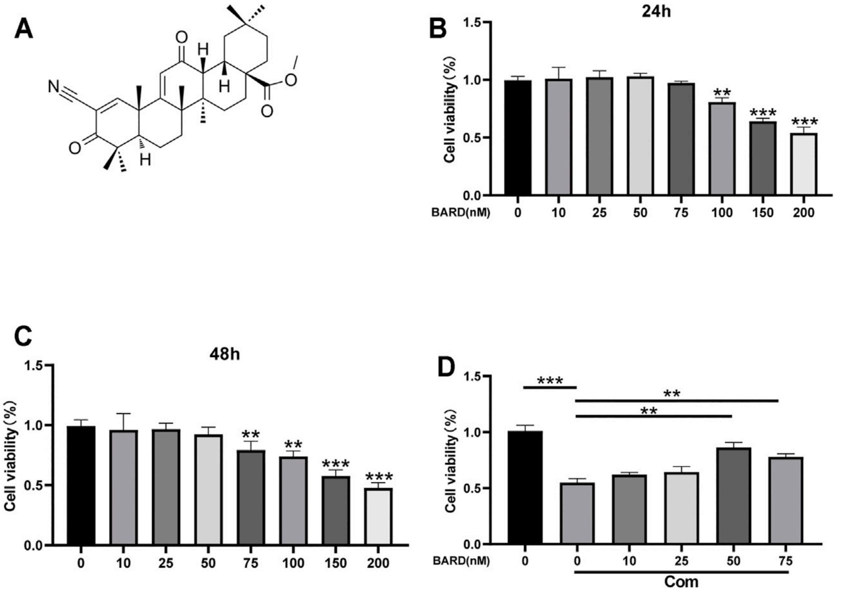

FIGURE 1 | The effect of BARD on NP cell viability. **(A)** Molecular structure of BARD. CCK-8 assay is used to detect changes in the viability of NP cells treated with different concentrations of BARD for 24 h **(B)** and 48 h **(C)**. **(D)** 50 and 75 nM BARD significantly improve NP cell viability under compression. Data are expressed as mean ± SD. ***$p < 0.001$, **$p < 0.01$, n = 3.

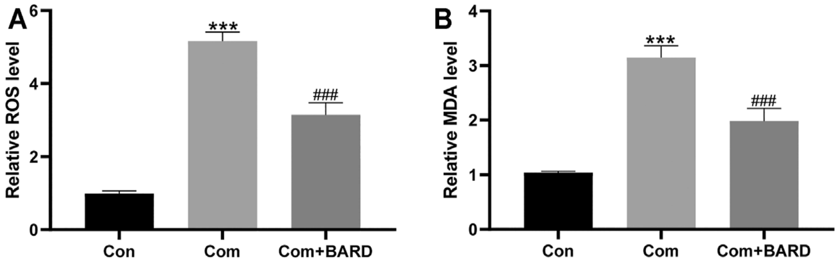

FIGURE 2 | The effect of BARD ROS and MDA accumulation in NP cells caused by compression. **(A–B)** The ROS and MDA contents of NP cells were detected with a fluorescence microplate reader. Data are expressed as mean ± SD. *** indicates $p < 0.001$ when data are compared to those for the control (Con) group. ### indicates $p < 0.001$ when data are compared to those for the compression (Com) group. n = 3.

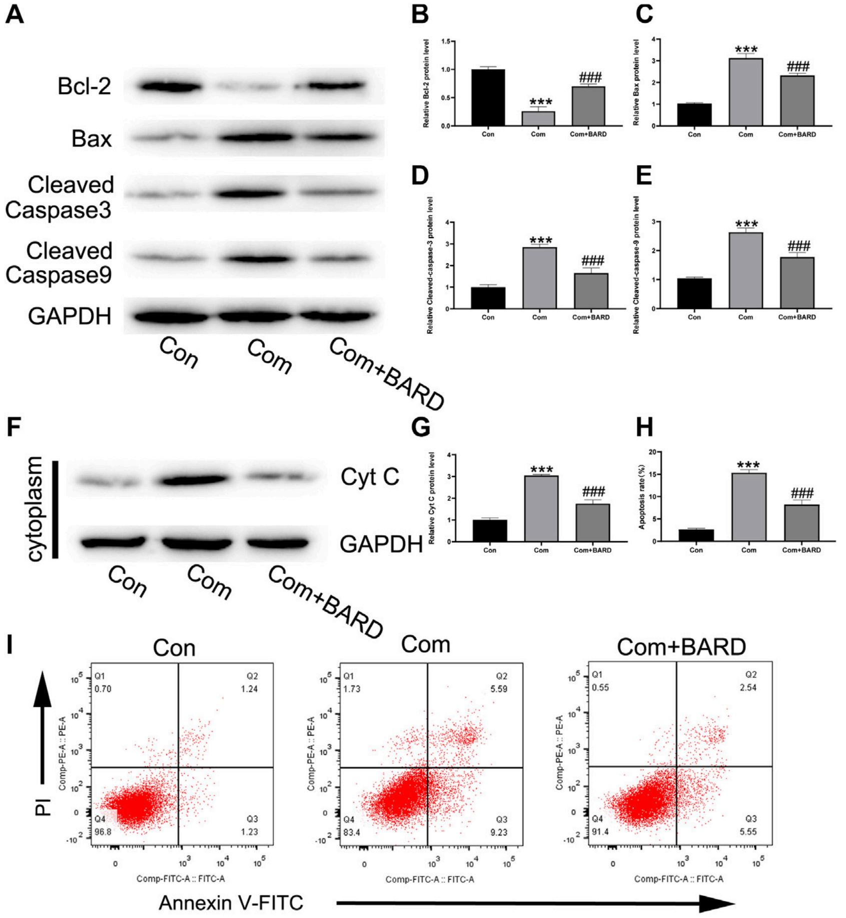

FIGURE 3 | BARD prevents nucleus pulposus cell apoptosis caused by compression. **(A–E)** The expression of BCL2, BAX, cleaved caspase-3, and cleaved caspase-9 in NP cells after BARD treatment was detected by Western blotting. **(F–G)** The expression of cytochrome c (cyt c) in the cytoplasm decreased after BARD treatment, indicating that BARD relieves NP cell apoptosis through the mitochondrial apoptotic pathway. **(H–I)** Flow cytometry results show the apoptosis rate of NP cells. Data are expressed as mean ± SD. *** indicates $p < 0.001$ when data are compared to those for the control (Con) group. ### indicates $p < 0.001$ when data are compared to those for the compression (Com) group. n = 3.

Briefly, NP cells were maintained in a mixed medium containing DMEM/F12 (Gibco), supplemented with 15% fetal bovine serum (FBS) and 1% penicillin/streptomycin (P/S) (Invitrogen), and placed in a 5% CO_2 incubator at 37°C. In order to keep the phenotype stable, we used second-generation cells for the experiments.

Cell Viability Assay

According to the manufacturer's instructions, a cell counting kit (CCK-8; Biosharp) was used for cell viability analysis. Briefly, after treatment with different concentrations of BARD (MCE; 99.72%) treatment or compression treatment, the cells were seeded in a 96-well plate and subjected to different conditions. Then, 10 µl of CCK-8 solution was added, and the samples were incubated at 37°C for 2 h. Finally, a spectrophotometer was used to measure absorbance at 450 nm.

Compression Treatment

The tissue or cells were placed, in cell culture plates, at the bottom of the compression device, which was then placed in a 37°C incubator. The compression device is pressurized until the pressure reaches 1.0 MPa (Kang et al., 2020). The control samples were not placed in the compression device during culture. The specific operation was performed as described previously (Iatridis et al., 2013).

Western Blotting

According to the manufacturer's instructions, a nuclear and cytoplasmic protein extraction kit (Beyotime) was used to extract total protein, cytoplasmic protein, and nuclear protein from NP cells and tissues. The BCA protein analysis kit (Beyotime) was used to determine the protein concentration. Equal amounts of protein from each sample were separated using SDS-PAGE and transferred to a PVDF membrane. Non-fat milk (5%) was used to block the membranes at room temperature for 2 h. Then, the membranes were incubated overnight at 4°C with the following primary antibodies: Bax (Abcam), Bcl-2 (Abcam), cleaved caspase-9 (Abcam), cleaved caspase-3 (Cell Signaling Technology), cytochrome c (Abcam), collagen II (Abcam), MMP-13 (Thermo Fisher), Nrf2 (Abcam), and HO-1 (Proteintech). Histone (Abcam) and GAPDH (Cell Signaling Technology) were used as the internal controls. Subsequently, the membrane was washed with TBST and incubated with the respective secondary antibodies (Abcam) for 1 h at room temperature, and then, the membranes were washed with TBST again. Protein bands were observed by enhanced chemiluminescence (Thermo Fisher) according to the manufacturer's instructions. ImageJ software (NIH) was used to quantify band intensity.

Flow Cytometry

The cells were digested with trypsin (Solarbio) without EDTA, washed twice with PBS, and stained with Annexin V–FITC and PI for 20 min (Keygen, China). Then, they were immediately analyzed using a FACSCalibur flow cytometer (BD Biosciences).

Measurements of ROS and Malondialdehyde Levels

The cells were processed according to the experimental design using ROS (Beyotime) and MDA (Beyotime) kits to determine the content of ROS and MDA, respectively, in human NPCs according to the manufacturer's instructions.

Immunofluorescence

The immunofluorescence assay was performed following different cells, according to a previously described procedure. The assay was performed through incubating the samples with antibodies against MMP-13 (Thermo Fisher) overnight at 4°C, followed by incubation with Alexa Fluor® 488-conjugated secondary antibodies for 1 h at 37°C. The nuclei were stained with 4′,6-diamidino-2-phenylindole (Beyotime). Finally, each slide was observed under a fluorescence microscope, and the fluorescence intensity was quantified using ImageJ software.

siRNA Transfection

Small interfering RNA (siRNA) that was against Nrf2 (si-Nrf2) mRNA was produced by Gene Pharma. According to the manufacturer's instructions, Lipofectamine® 2000 (Invitrogen) was used to transfect NP cells with 100 nmol/L of each siRNA for 6 h. After 48 h, the cells were used for the experiments.

Ex Vivo IVD Organ Culture

12-week-old Sprague–Dawley (SD) rats were used for the IVD. The tail disc was separated and cultivated with a complete endplate structure in DMEM containing 15% FBS (Gibco) and 1% P/S (Invitrogen). The specific operation was as described previously (Wu et al., 2019).

Assessments of the *Ex Vivo* IVD Compression Model

After treatment, the IVD tissues of SD rats were fixed in formaldehyde, decalcified, dehydrated, embedded in paraffin, and cut into slices, with a thickness of 4 µm. These sections were stained with hematoxylin and eosin (HE) and safranin O-fast green (SO). According to previously described methods, the histological score was used to assess the degree of IVD injury (Han et al., 2008). For immunohistochemical analysis, sections were incubated with Nrf2 primary antibodies at 4°C overnight and then incubated with appropriate horseradish peroxidase-conjugated secondary antibodies and counterstained with hematoxylin. Images were captured using an optical microscope (Olympus).

Statistical Analyses

The results are expressed as mean ± standard deviation (SD). At least three independent experiments were performed for each test. SPSS software (version 20.0; IBM Corporation) was used to analyze the data. Student's t-test or analysis of variance was used, followed by Tukey's test, to assess the differences between the results of each group. Statistical significance was set at $p < 0.05$.

RESULTS

The Protective Effect of BARD on the Viability of NP Cells Induced by Compression

Compression (Com) was used to establish an IDD model *in vitro*. **Figure 1A** shows the BARD structural formula. The results of the

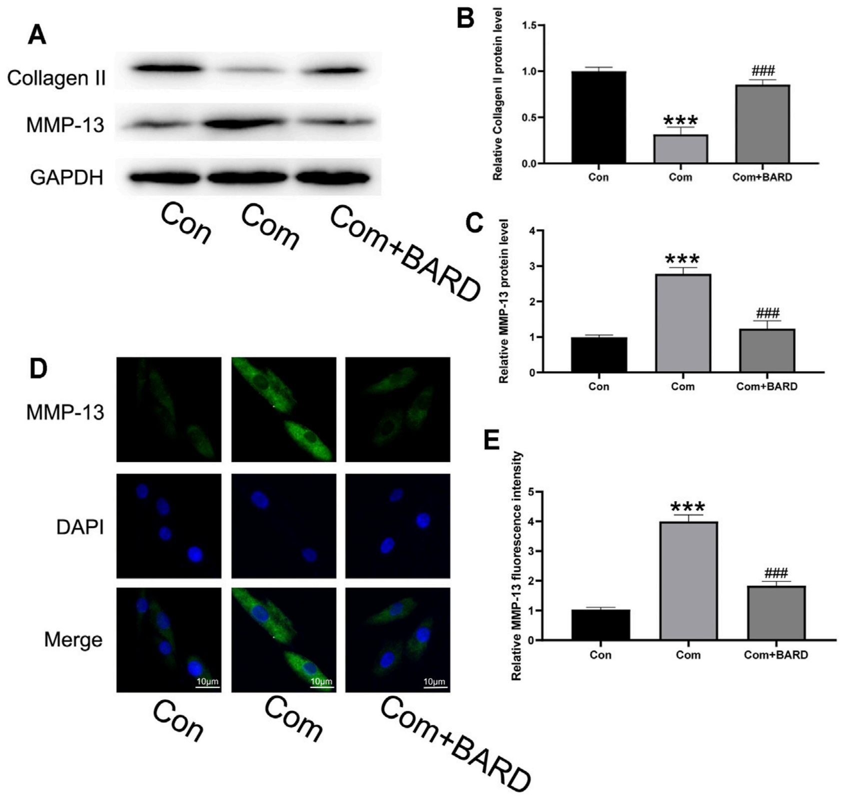

FIGURE 4 | BARD prevents nucleus pulposus cell ECM degeneration caused by compression. **(A–C)** Western blotting was used to detect collagen II and MMP-13 expression. **(D–E)** Immunofluorescence was used to observe the expression of MMP-13. Data are expressed as mean ± SD. *** indicates $p < 0.001$ when data are compared to those for the control (Con) group. ### indicates $p < 0.001$ when data are compared to those for the compression (Com) group. n = 3.

CCK-8 assay showed that at ≤50 nM, BARD was not cytotoxic to human NP cells for 24 and 48 h treatment times (**Figures 1B,C**). Subsequently, we observed that under compression conditions, 50 nM BARD showed the best cytoprotective effect (**Figure 1D**). Therefore, BARD was used at a dose of 50 nM in subsequent experiments.

The Protective Effect of BARD on Compression-Induced Oxidative Stress in NP Cells

To assess the level of oxidative damage, we tested the levels of ROS and MDA, which are commonly used indicators of oxidative stress. Compression increased the levels of ROS and MDA in NP cells compared to the control (Con) group (**Figures 2A,B**). Compared with compression treatment alone, BARD treatment significantly reduced ROS and MDA levels, which suggests that BARD protects NP cells from oxidative stress.

The Protective Effect of BARD on Compression-Induced Apoptosis in NP Cells

Western blotting was used to detect changes in apoptosis-related proteins in the mitochondrial pathway after BARD treatment (**Figure 3A**). The results showed that after BARD treatment, the expression of the anti-apoptotic protein Bcl-2 increased, while that of the pro-apoptotic protein Bax decreased (**Figures 3B,C**). In addition, the expression of cleaved caspase-3 and cleaved caspase-9 in the BARD treatment group was lower than that in the compression group (**Figures 3D,E**). In addition, the level of cytochrome c in the cytoplasm changed significantly due to BARD treatment (**Figures 3F,G**). As shown in **Figures 3H,I**, we used Annexin V–FITC/PI staining to detect the apoptosis of NP cells. The flow cytometry results showed that compression significantly increased the number of apoptotic NP cells. However, BARD treatment significantly alleviated this trend.

The Protective Effect of BARD on Compression-Induced ECM Degradation in NP Cells

Because the imbalance between ECM synthesis and degradation is also an important feature of IDD, we evaluated collagen II (main ECM component) and MMP-13 (ECM catabolism factor) protein expression levels. As shown in **Figures 4A–C**, compression treatment decreased collagen II and increased MMP-13 protein levels, and these compression-induced alterations were significantly ameliorated by BARD pretreatment. The

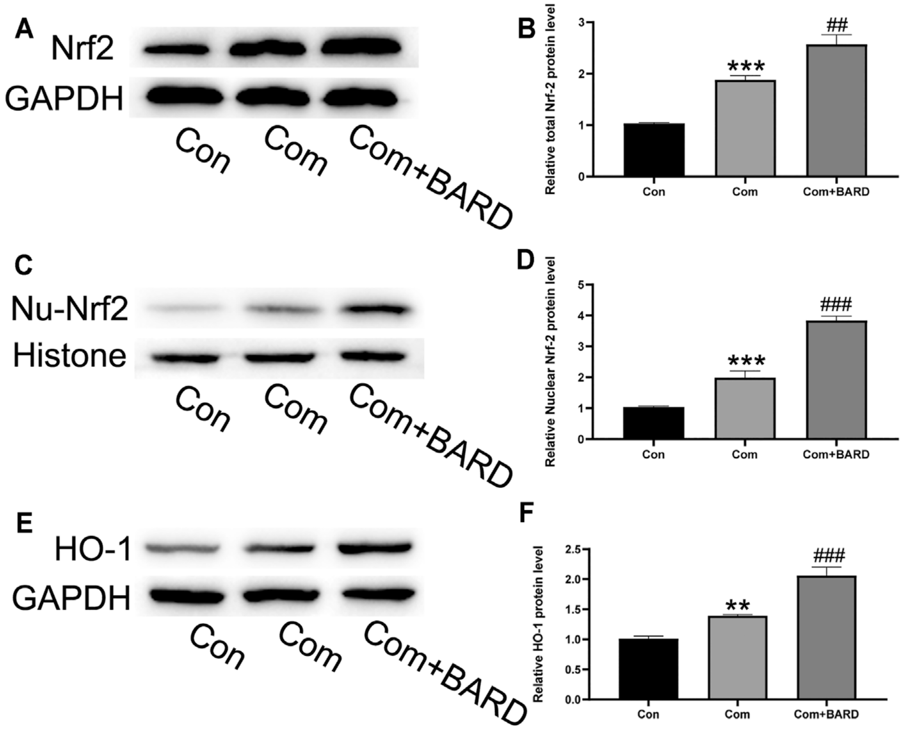

FIGURE 5 | The effect of BARD on the Nrf2 pathway in compression-exposed NP cells. **(A–B)** Western blotting was used to detect Nrf2 expression. **(C–D)** Western blotting was used to detect nuclear Nrf2 (Nu-Nrf2) expression. **(E–F)** Western blotting was used to detect HO-1 expression. Data are expressed as mean ± SD. *** indicates $p < 0.001$ and ** indicates $p < 0.01$ when data are compared to those for the control (Con) group. $^{###}$ indicates $p < 0.001$ and $^{##}$ indicates $p < 0.01$ when data are compared to those for the compression (Com) group. n = 3.

immunofluorescence staining results showed that MMP-13 levels significantly increased under compression and BARD ameliorated this trend (**Figures 4D,E**). These results suggest that BARD protects against compression-induced ECM degeneration.

The Protective Effect of BARD on the Nrf2 Pathway in Compression-Treated NP Cells

As shown in the above results, oxidative stress, apoptosis, and ECM degeneration in NP cells caused by compression were all significantly alleviated after BARD treatment. BARD has been found to activate the Nrf2 pathway in many studies, and as a classic antioxidative stress-related pathway, the Nrf2 pathway plays an important role in compression-induced NP cell damage. Therefore, it is reasonable to assume that the Nrf2 pathway is involved in the protection of BARD against compression-induced NP cell damage. To verify our hypothesis, we evaluated Nrf2 signaling pathway activation under different processing conditions. Compression increased Nrf2 expression (**Figures 5A,B**) and nuclear translocation of Nrf2 (**Figures 5C,D**), and the expression of its downstream target protein HO-1 also increased (**Figures 5E,F**). BARD treatment further increased Nrf2 pathway activation in NP cells induced by compression. Thus, the Nrf2 pathway is implicated in the protective effect of BARD on NP cells.

Nrf2 Activation is Required for BARD-Induced NP Cell Protection Against Compression

The present results show that BARD activates the Nrf2 cascade and protects human NP cells from compression-induced cell injury. We further studied the link between Nrf2 activation and BARD-induced cytoprotection in NP cells. As shown in **Figures 6A,B**, si-Nrf2 significantly knocked down the expression level of Nrf2 in NP cells. Furthermore, the expression of Nrf2-dependent genes (HO-1) was significantly blocked by Nrf2 knockdown (**Figure 6C**). Importantly, the protection of BARD against compression-induced oxidative injury in human NP cells was reversed through Nrf2 knockdown, as indicated by collagen II, MMP-13, cleaved caspase-3, apoptosis, and ROS levels (**Figures 6D–K**). These results suggest that Nrf2 activation is required for BARD-induced cytoprotection in compression-treated NP cells.

BARD Ameliorates NP Tissue Degeneration in an *Ex Vivo* IDD Model

We used the compressed isolated rat tail disc degeneration model to further confirm the results of the above *in vitro* experiments. After 2 weeks of compression treatment, the

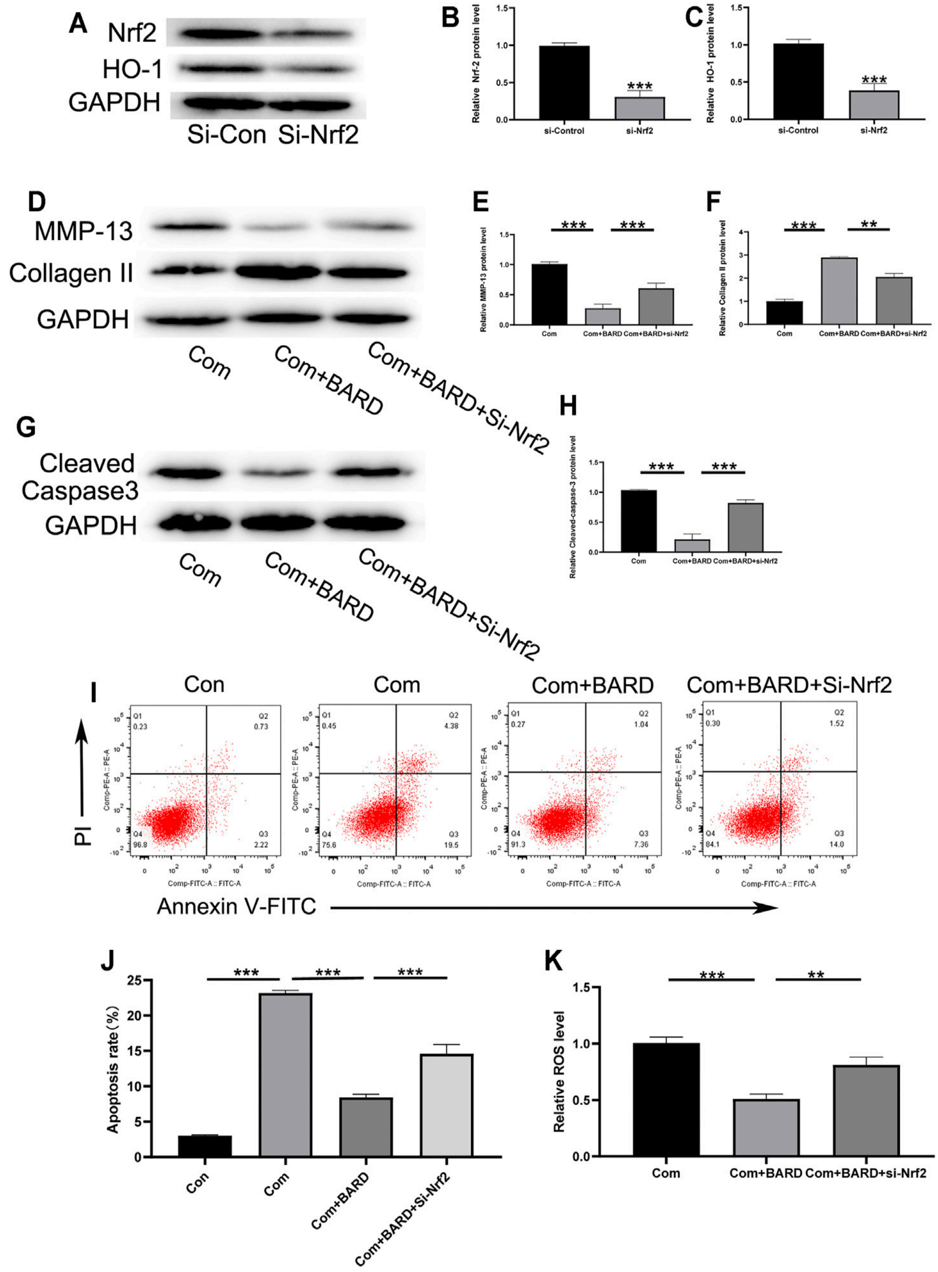

FIGURE 6 | Nrf2 signaling plays a role in the BARD antioxidative stress response in compressed-exposed NP cells. **(A–C)** Western blotting was used to detect the expression of Nrf2 and HO-1. **(D–F)** Western blotting was used to detect the expression of MMP-13 and collagen II. **(G–H)** Western blotting was used to detect the expression of cleaved caspase-3. **(I–J)** Flow cytometry results show the apoptosis rate of NP cells. **(K)** The ROS content of NP cells was detected with a fluorescence microplate reader. ***$p < 0.001$, **$p < 0.01$. n = 3.

collected disc tissues were stained with HE and SO to evaluate morphological changes (**Figure 7A**). The compression treatment group showed severe degenerative changes, but the BARD treatment group significantly alleviated this process. The histological score further proved that BARD could prevent the IDD process (**Figure 7C**). Based on the results of the *in vitro* studies, *ex vivo* Nrf2 activation by BARD was further verified. Consistent with the results of the *in vitro* studies, the immunohistological staining (**Figure 7B**) and Western blotting (**Figures 7D,E**) results showed that BARD promoted Nrf2 expression in NP tissues. These results indicate that BARD ameliorated rat tail disc degeneration caused by compression. At the same time, the protective effect of BARD may be mediated by Nrf2 upregulation.

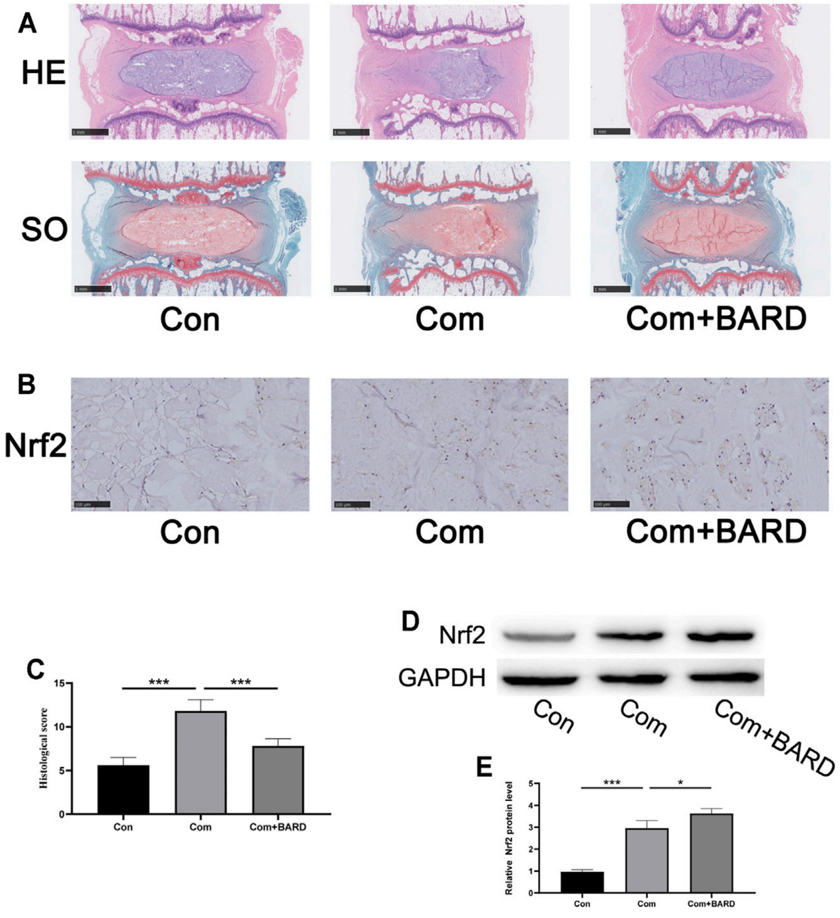

FIGURE 7 | BARD improves the development of IDD in an *ex vitro* compression model. **(A)** HE and SO staining of the rat IVD tissues. Scale bar: 1 mm. **(B)** Immunohistochemical staining showing Nrf2 protein expression in NP tissues. Scale bar: 100 μm. **(C)** The histological score of SD rat IVD tissue was based on histological grading scale. **(D–E)** Western blotting was used to detect Nrf2 expression. Data are expressed as mean ± SD. *** indicates $p < 0.001$ when data are compared to those for the control (Con) group. ### indicates $p < 0.001$ when data are compared to those for the compression (Com) group. n = 5.

DISCUSSION

Previous studies have shown that excessive compression plays an important role in the development of IDD (Cheng et al., 2021; Lyu et al., 2021). Compression induces oxidative stress, apoptosis, and ECM degradation in NP cells (Li et al., 2018). Oxidative damage can promote apoptosis and ECM degradation, which contribute to the development of IDD (Chen et al., 2019; Xu et al., 2021). Therefore, for the successful application of NP tissue engineering, we focused on preventing compression-induced oxidative stress and subsequent NP cell apoptosis and ECM degradation (Sun et al., 2015). This may be a valuable method for alleviating and reversing IDD progression. Our study showed that BARD effectively increased the viability of NP cells treated with compression. In terms of indicators of oxidative stress, BARD prevented the production of excessive ROS and MDA in NP cells induced by compression. This study also showed that BARD could prevent compression-induced mitochondrial apoptosis in NP cells. In terms of ECM metabolism, BARD can inhibit ECM degradation and promote ECM synthesis. In terms of molecular mechanisms, BARD can promote the nuclear transfer of Nrf2 proteins and the overexpression of Nrf2 target proteins, which may reflect the molecular basis of the antioxidant effect of BARD. The *ex vivo* compression model also showed that BARD could reduce progressive damage of the IVD structure induced by compression.

Intracellular oxidative stress is precisely regulated and slightly biased toward oxidative processes (Balaban et al., 2005). Due to the transfer of electrons during oxidative phosphorylation, ROS are inevitably produced. As a by-product of aerobic catalysis, ROS levels are often used as an indicator of oxidative stress (Giorgio et al., 2005). The main forms of ROS include hydrogen peroxide (H_2O_2), superoxide anions (O_2^-), and free radicals. Lower concentrations of ROS act as signaling molecules to activate specific physiological pathways that control multiple life processes (Finkel and Holbrook, 2000; Quarrie and Riabowol, 2004). When the balance between the production and removal of ROS in the body is disrupted, the increase in ROS levels destroys DNA, proteins, and lipids, eventually triggering oxidative stress and leading to cell damage (Glasauer and Chandel, 2013;

Tsukahara, 2007). Recent studies have shown that the occurrence and development of IDD is closely related to ROS and oxidative stress (Dimozi et al., 2015; Hou et al., 2014; Suzuki et al., 2015). Oxidative stress can accelerate the process of IDD in many ways, including through apoptosis, ECM degeneration, senescence, and autophagy (Feng et al., 2017). Many reports have shown that BARD has a strong antioxidative effect (Khurana et al., 2020; Pang et al., 2021; Snijders et al., 2021). However, whether BARD can alleviate IVD degeneration caused by compression has not been studied. This experiment proved that BARD can significantly reduce the increase in ROS and MDA levels caused by compression.

Under normal conditions, apoptosis plays an important role in maintaining tissue homeostasis. Apoptosis is a self-programmed cell destruction process. Its purpose is to remove unwanted cells and remodel development (Zhang et al., 2021). A major cause of IDD is the excessive apoptosis of IVD cells (Ding et al., 2013; Zhang et al., 2021). Excessive ROS increase the permeability of the outer mitochondrial membrane and the release of the pro-apoptotic factor, cytochrome c, which leads to cell apoptosis (Pervaiz et al., 2009). The important physiological function of IVD cells is to secrete ECM components (Tsingas et al., 2020). The ECM surrounds the IVD cells, maintains their normal physiological functions and characteristics, and, ultimately, maintains the normal physiological structure and tissue stability of the IVD. The ECM also provides buffering capacity to resist compressive mechanical loads on the spine from all directions (Li et al., 2021). However, during the IDD process, many factors, such as aging, inflammation, oxidative stress, and abnormal pressure load, lead to imbalances in the synthesis and degradation of the ECM components in the IVD tissue, and eventually, the IVD irreversibly degenerates (Wang et al., 2020b). In particular, the NP tissue is located at the center of the IVD, and compression leads to the destruction of the IVD tissue, which causes the ability of the IVD to withstand mechanical loads to weaken. Furthermore, the physiological stress structure of the spine changes, leading to a series of spinal degenerative diseases (Wang et al., 2020b; Kim et al., 2021; Zhang et al., 2021). Therefore, preventing NP cell apoptosis and ECM degradation induced by oxidative stress may be effective methods for the treatment of IDD.

Nrf2 is a transcription factor that plays an important role in the cell response to oxidative stress. Nrf2 activation represents the initiation of the oxidative stress defense system. In the non-stimulated state, Nrf2 exists in the cytoplasm, and the Nrf2 protein contains two Keap1 protein-binding motifs (Tu et al., 2019). ETGE and DLG enable Nrf2 to bind to the inhibitory protein Keap1 in the cytoplasm. Keap1 functions as an adaptor for cullin 3 (CUL3) E3 ubiquitination ligase-mediated Nrf2 proteasomal degradation. The cysteine residues on Keap1 can be modified by oxidants or electrophiles, which cause the protein to undergo conformational changes, leading to the dissociation of Keap1–Nrf2, the termination of Nrf2 polyubiquitination, and the translocation of Nrf2 into the nucleus (Ferrándiz et al., 2018). Nrf2 combines with the sMaf (small musculoaponeurotic fibrosarcoma) protein to form a heterodimer, which can then combine with antioxidant response elements to initiate the transcription of multiple target genes that are involved in redox balance, metabolic response, inflammatory response, etc. (Alcaraz and Ferrándiz, 2020). The antioxidative stress effect of Nrf2 has been reported in many studies of IDD, and Nrf2 in NP cells can directly act through its downstream target regulated antioxidant proteins (Kang et al., 2020; Wang Y. et al., 2019). On the other hand, the mitochondrion is the body's energy factory, and it is also the main source of ROS (Fukai and Ushio-Fukai, 2020; Zhang and Wong, 2021). Nrf2 can reduce the production of ROS from the source by maintaining mitochondrial homeostasis, thereby maintaining the redox balance in NP cells (Tang et al., 2019; Wang K. et al., 2019). Various drugs can inhibit IDD by activating the Nrf2 signaling pathway (Gu et al., 2019; Song et al., 2021; Wang K. et al., 2019; Wang et al., 2020a; Zhong et al., 2021). In this study, we confirmed that BARD increased the expression and nuclear translocation of Nrf2 and downstream HO-1 expression also significantly increased. In addition, inhibition of Nrf2 attenuated the protective effect of BARD on oxidative stress damage in NP cells.

There were several limitations associated with our study. It is well known that NP cells are in a hypoxic state *in vivo*. However, the oxygen concentration of cells cultured *in vitro* in this experiment was normal, which caused excessive ROS production. Second, this experiment only explored the effect of BARD on Nrf2 activation. Whether BARD affects the activation of other pathways has yet to be determined.

In conclusion, this study provides evidence that BARD protects NP cells from apoptosis and ECM degradation under compression-induced oxidative stress. Its protective effect is, at least partially, mediated by the Nrf2 signaling pathway. Therefore, to improve the effectiveness of NP tissue engineering, BARD has been proposed as a supplement for minimizing the destructive effect of compression on engineered NP tissue.

DATA AVAILABILITY STATEMENT

The raw data supporting the conclusions of this article will be made available by the authors, without undue reservation.

ETHICS STATEMENT

The animal study was reviewed and approved by the Laboratory Animal Ethics Committee of Institute of Radiation Medicine, Chinese Academy of Medical Sciences.

AUTHOR CONTRIBUTIONS

JT and YYT designed the study. YYT, JT, JQD, YC, and HCZ performed the study. JT, YYT, and JQD wrote the paper. ADD revised the manuscript and provide critical comments for the study. All authors approved the final version of the paper.

REFERENCES

Alcaraz, M. J., and Ferrándiz, M. L. (2020). Relevance of Nrf2 and Heme Oxygenase-1 in Articular Diseases. *Free Radic. Biol. Med.* 157, 83–93. doi:10.1016/j.freeradbiomed.2019.12.007

Anderson, D. G., Albert, T. J., Fraser, J. K., Risbud, M., Wuisman, P., Meisel, H.-J., et al. (2005). Cellular Therapy for Disc Degeneration. *Spine* 30 (Supplement), S14–S19. doi:10.1097/01.brs.0000175174.50235.ba

Balaban, R. S., Nemoto, S., and Finkel, T. (2005). Mitochondria, Oxidants, and Aging. *Cell* 120, 483–495. doi:10.1016/j.cell.2005.02.001

Chen, Y., Wu, Y., Shi, H., Wang, J., Zheng, Z., Chen, J., et al. (2019). Melatonin Ameliorates Intervertebral Disc Degeneration via the Potential Mechanisms of Mitophagy Induction and Apoptosis Inhibition. *J. Cel. Mol. Med.* 23, 2136–2148. doi:10.1111/jcmm.14125

Cheng, Z., Xiang, Q., Wang, J., and Zhang, Y. (2021). The Potential Role of Melatonin in Retarding Intervertebral Disc Ageing and Degeneration: A Systematic Review. *Ageing Res. Rev.* 70, 101394. doi:10.1016/j.arr.2021.101394

Dimozi, A., Mavrogonatou, E., Mavrogonatou, E., Sklirou, A., and Kletsas, D. (2015). Oxidative Stress Inhibits the Proliferation, Induces Premature Senescence and Promotes a Catabolic Phenotype in Human Nucleus Pulposus Intervertebral Disc Cells. *eCM* 30, 89–103. doi:10.22203/ecm.v030a07

Ding, F., Shao, Z.-w., and Xiong, L.-m. (2013). Cell Death in Intervertebral Disc Degeneration. *Apoptosis* 18, 777–785. doi:10.1007/s10495-013-0839-1

Feng, C., Yang, M., Lan, M., Liu, C., Zhang, Y., Huang, B., et al. (2017). ROS: Crucial Intermediators in the Pathogenesis of Intervertebral Disc Degeneration. *Oxidative Med. Cell Longevity* 2017, 1–12. doi:10.1155/2017/5601593

Fernandez-Moure, J., Moore, C. A., Kim, K., Karim, A., Smith, K., Barbosa, Z., et al. (2018). Novel Therapeutic Strategies for Degenerative Disc Disease: Review of Cell Biology and Intervertebral Disc Cell Therapy. *SAGE Open Med.* 6, 205031211876167. doi:10.1177/2050312118761674

Ferrándiz, M. L., Nacher-Juan, J., and Alcaraz, M. J. (2018). Nrf2 as a Therapeutic Target for Rheumatic Diseases. *Biochem. Pharmacol.* 152, 338–346. doi:10.1016/j.bcp.2018.04.010

Finkel, T., and Holbrook, N. J. (2000). Oxidants, Oxidative Stress and the Biology of Ageing. *Nature* 408, 239–247. doi:10.1038/35041687

Fukai, T., and Ushio-Fukai, M. (2020). Cross-talk between NADPH Oxidase and Mitochondria: Role in ROS Signaling and Angiogenesis. *Cells* 9, 1849. doi:10.3390/cells9081849

Giorgio, M., Migliaccio, E., Orsini, F., Paolucci, D., Moroni, M., Contursi, C., et al. (2005). Electron Transfer between Cytochrome C and p66Shc Generates Reactive Oxygen Species that Trigger Mitochondrial Apoptosis. *Cell* 122, 221–233. doi:10.1016/j.cell.2005.05.011

Glasauer, A., and Chandel, N. S. (2013). ROS. *Curr. Biol.* 23, R100–R102. doi:10.1016/j.cub.2012.12.011

Gu, R., Huang, Z., Liu, H., Qing, Q., Zhuan, Z., Yang, L., et al. (2019). Moracin Attenuates LPS-Induced Inflammation in Nucleus Pulposus Cells via Nrf2/HO-1 and NF-κB/TGF-β Pathway. *Biosci. Rep.* 39 (9). doi:10.1042/BSR20191673

Han, B., Zhu, K., Li, F.-c., Xiao, Y.-x., Feng, J., Shi, Z.-l., et al. (2008). A Simple Disc Degeneration Model Induced by Percutaneous Needle Puncture in the Rat Tail. *Spine* 33, 1925–1934. doi:10.1097/BRS.0b013e31817c64a9

Hou, G., Lu, H., Chen, M., Yao, H., and Zhao, H. (2014). Oxidative Stress Participates in Age-Related Changes in Rat Lumbar Intervertebral Discs. *Arch. Gerontol. Geriatr.* 59, 665–669. doi:10.1016/j.archger.2014.07.002

Hutton, W. C., Elmer, W. A., Boden, S. D., Horton, W. C., and Carr, K. (1997). Analysis of Chondroitin Sulfate in Lumbar Intervertebral Discs at Two Different Stages of Degeneration as Assessed by Discogram. *J. Spinal Disord.* 10, 47–54. doi:10.1097/00002517-199702000-00007

Hutton, W. C., Elmer, W. A., Boden, S. D., Hyon, S., Toribatake, Y., Tomita, K., et al. (1999). The Effect of Hydrostatic Pressure on Intervertebral Disc Metabolism. *Spine* 24, 1507–1515. doi:10.1097/00007632-199908010-00002

Iatridis, J. C., Nicoll, S. B., Michalek, A. J., Walter, B. A., and Gupta, M. S. (2013). Role of Biomechanics in Intervertebral Disc Degeneration and Regenerative Therapies: what Needs Repairing in the Disc and what Are Promising Biomaterials for its Repair? *Spine J.* 13, 243–262. doi:10.1016/j.spinee.2012.12.002

Kanda, H., and Yamawaki, K. (2020). Bardoxolone Methyl: Drug Development for Diabetic Kidney Disease. *Clin. Exp. Nephrol.* 24, 857–864. doi:10.1007/s10157-020-01917-5

Kang, L., Hu, J., Weng, Y., Jia, J., and Zhang, Y. (2017). Sirtuin 6 Prevents Matrix Degradation through Inhibition of the NF-κB Pathway in Intervertebral Disc Degeneration. *Exp. Cel Res.* 352, 322–332. doi:10.1016/j.yexcr.2017.02.023

Kang, L., Liu, S., Li, J., Tian, Y., Xue, Y., and Liu, X. (2020). The Mitochondria-targeted Anti-oxidant MitoQ Protects against Intervertebral Disc Degeneration by Ameliorating Mitochondrial Dysfunction and Redox Imbalance. *Cell Prolif* 53, e12779. doi:10.1111/cpr.12779

Khurana, N., Chandra, P. K., Kim, H., Abdel-Mageed, A. B., Mondal, D., and Sikka, S. C. (2020). Bardoxolone-methyl (CDDO-Me) Suppresses Androgen Receptor and its Splice-Variant AR-V7 and Enhances Efficacy of Enzalutamide in Prostate Cancer Cells. *Antioxidants* 9, 68. doi:10.3390/antiox9010068

Kim, J.-W., Jeon, N., Shin, D.-E., Lee, S.-Y., Kim, M., Han, D. H., et al. (2021). Regeneration in Spinal Disease: Therapeutic Role of Hypoxia-Inducible Factor-1 Alpha in Regeneration of Degenerative Intervertebral Disc. *Ijms* 22, 5281. doi:10.3390/ijms22105281

Li, L., Wei, K., Ding, Y., Ahati, P., Xu, H., Fang, H., et al. (2021). M2a Macrophage-Secreted CHI3L1 Promotes Extracellular Matrix Metabolic Imbalances via Activation of IL-13Rα2/MAPK Pathway in Rat Intervertebral Disc Degeneration. *Front. Immunol.* 12, 666361. doi:10.3389/fimmu.2021.666361

Li, Z., Chen, S., Ma, K., Lv, X., Lin, H., Hu, B., et al. (2018). CsA Attenuates Compression-Induced Nucleus Pulposus Mesenchymal Stem Cells Apoptosis via Alleviating Mitochondrial Dysfunction and Oxidative Stress. *Life Sci.* 205, 26–37. doi:10.1016/j.lfs.2018.05.014

Lyu, F.-J., Cui, H., Pan, H., Mc Cheung, K., Cao, X., Iatridis, J. C., et al. (2021). Painful Intervertebral Disc Degeneration and Inflammation: from Laboratory Evidence to Clinical Interventions. *Bone Res.* 9, 7. doi:10.1038/s41413-020-00125-x

Maniadakis, N., and Gray, A. (2000). The Economic burden of Back Pain in the UK. *Pain* 84, 95–103. doi:10.1016/S0304-3959(99)00187-6

Nagasu, H., Sogawa, Y., Kidokoro, K., Itano, S., Yamamoto, T., Satoh, M., et al. (2019). Bardoxolone Methyl Analog Attenuates Proteinuria-induced Tubular Damage by Modulating Mitochondrial Function. *FASEB j.* 33, 12253–12263. doi:10.1096/fj.201900217R

Nomura, T., Mochida, J., Okuma, M., Nishimura, K., and Sakabe, K. (2001). Nucleus Pulposus Allograft Retards Intervertebral Disc Degeneration. *Clin. Orthopaedics Relat. Res.* 389, 94–101. doi:10.1097/00003086-200108000-00015

Pang, Z., Jiang, Z., Zhu, R., Song, C., Tang, H., Cao, L., et al. (2021). Bardoxolone-methyl Prevents Oxidative Stress-Mediated Apoptosis and Extracellular Matrix Degradation *In Vitro* and Alleviates Osteoarthritis *In Vivo*. *Dddt* Vol. 15, 3735–3747. doi:10.2147/DDDT.S314767

Pei, X., Zhang, X.-J., and Chen, H.-M. (2019). Bardoxolone Treatment Alleviates Lipopolysaccharide (LPS)-induced Acute Lung Injury through Suppressing Inflammation and Oxidative Stress Regulated by Nrf2 Signaling. *Biochem. Biophysical Res. Commun.* 516, 270–277. doi:10.1016/j.bbrc.2019.06.006

Pervaiz, S., Taneja, R., and Ghaffari, S. (2009). Oxidative Stress Regulation of Stem and Progenitor Cells. *Antioxid. Redox Signaling* 11, 2777–2789. doi:10.1089/ars.2009.2804

Quarrie, J. K., and Riabowol, K. (2004). Murine Models of Life Span Extension. *Sci. Aging Knowledge Environ.* 2004, re5. doi:10.1126/sageke.2004.31.re5

Rossing, P., Block, G. A., Chin, M. P., Goldsberry, A., Heerspink, H. J. L., McCullough, P. A., et al. (2019). Effect of Bardoxolone Methyl on the Urine Albumin-To-Creatinine Ratio in Patients with Type 2 Diabetes and Stage 4 Chronic Kidney Disease. *Kidney Int.* 96, 1030–1036. doi:10.1016/j.kint.2019.04.027

Roughley, P. J. (2004). Biology of Intervertebral Disc Aging and Degeneration. *Spine* 29, 2691–2699. doi:10.1097/01.brs.0000146101.53784.b1

Snijders, K. E., Fehér, A., Táncos, Z., Bock, I., Téglási, A., van den Berk, L., et al. (2021). Fluorescent Tagging of Endogenous Heme Oxygenase-1 in Human Induced Pluripotent Stem Cells for High Content Imaging of Oxidative Stress in Various Differentiated Lineages. *Arch. Toxicol.* 95, 3285–3302. doi:10.1007/s00204-021-03127-8

Song, D., Ge, J., Wang, Y., Yan, Q., Wu, C., Yu, H., et al. (2021). Tea Polyphenol Attenuates Oxidative Stress-Induced Degeneration of Intervertebral Discs by Regulating the Keap1/Nrf2/ARE Pathway. *Oxidative Med. Cell Longevity* 2021, 1–13. doi:10.1155/2021/6684147

Sun, Z., Luo, B., Liu, Z.-H., Samartzis, D., Liu, Z., Gao, B., et al. (2015). Adipose-derived Stromal Cells Protect Intervertebral Disc Cells in Compression: Implications for Stem Cell Regenerative Disc Therapy. *Int. J. Biol. Sci.* 11, 133–143. doi:10.7150/ijbs.10598

Suzuki, S., Fujita, N., Hosogane, N., Watanabe, K., Ishii, K., Toyama, Y., et al. (2015). Excessive Reactive Oxygen Species Are Therapeutic Targets for Intervertebral Disc Degeneration. *Arthritis Res. Ther.* 17, 316. doi:10.1186/s13075-015-0834-8

Tang, Z., Hu, B., Zang, F., Wang, J., Zhang, X., and Chen, H. (2019). Nrf2 Drives Oxidative Stress-Induced Autophagy in Nucleus Pulposus Cells via a Keap1/Nrf2/p62 Feedback Loop to Protect Intervertebral Disc from Degeneration. *Cell Death Dis* 10, 510. doi:10.1038/s41419-019-1701-3

Tsingas, M., Ottone, O. K., Haseeb, A., Barve, R. A., Shapiro, I. M., Lefebvre, V., et al. (2020). Sox9 Deletion Causes Severe Intervertebral Disc Degeneration Characterized by Apoptosis, Matrix Remodeling, and Compartment-specific Transcriptomic Changes. *Matrix Biol.* 94, 110–133. doi:10.1016/j.matbio.2020.09.003

Tsukahara, H. (2007). Biomarkers for Oxidative Stress: Clinical Application in Pediatric Medicine. *Cmc* 14, 339–351. doi:10.2174/092986707779941177

Tu, W., Wang, H., Li, S., Liu, Q., and Sha, H. (2019). The Anti-inflammatory and Anti-oxidant Mechanisms of the Keap1/Nrf2/ARE Signaling Pathway in Chronic Diseases. *Aging Dis.* 10, 637–651. doi:10.14336/AD.2018.0513

Wang, H., Jiang, Z., Pang, Z., Zhou, T., and Gu, Y. (2020a). Acacetin Alleviates Inflammation and Matrix Degradation in Nucleus Pulposus Cells and Ameliorates Intervertebral Disc Degeneration *In Vivo*. *Drug. Des. Devel. Ther.* Vol. 14, 4801–4813. doi:10.2147/DDDT.S274812

Wang, K., Hu, S., Wang, B., Wang, J., Wang, X., and Xu, C. (2019). Genistein Protects Intervertebral Discs from Degeneration via Nrf2-mediated Antioxidant Defense System: An *In Vitro* and *In Vivo* Study. *J. Cel. Physiol.* 234, 16348–16356. doi:10.1002/jcp.28301

Wang, Y., Che, M., Xin, J., Zheng, Z., Li, J., and Zhang, S. (2020b). The Role of IL-1β and TNF-α in Intervertebral Disc Degeneration. *Biomed. Pharmacother.* 131, 110660. doi:10.1016/j.biopha.2020.110660

Wang, Y., Wang, H., Zhuo, Y., Hu, Y., Zhang, Z., Ye, J., et al. (2020c). SIRT1 Alleviates High-Magnitude Compression-Induced Senescence in Nucleus Pulposus Cells via PINK1-dependent Mitophagy. *Aging* 12, 16126–16141. doi:10.18632/aging.103587

Wang, Y., Zuo, R., Wang, Z., Luo, L., Wu, J., Zhang, C., et al. (2019). Kinsenoside Ameliorates Intervertebral Disc Degeneration through the Activation of AKT-ERK1/2-Nrf2 Signaling Pathway. *Aging* 11, 7961–7977. doi:10.18632/aging.102302

Wu, X., Liao, Z., Wang, K., Hua, W., Liu, X., Song, Y., et al. (2019). Targeting the IL-1β/IL-1Ra Pathways for the Aggregation of Human Islet Amyloid Polypeptide in an *Ex Vivo* Organ Culture System of the Intervertebral Disc. *Exp. Mol. Med.* 51, 1–16. doi:10.1038/s12276-019-0310-7

Xu, Z., Zheng, J., Zhang, Y., Wu, H., Sun, B., Zhang, K., et al. (2021). Increased Expression of Integrin Alpha 6 in Nucleus Pulposus Cells in Response to High Oxygen Tension Protects against Intervertebral Disc Degeneration. *Oxidative Med. Cell Longevity* 2021, 1–16. doi:10.1155/2021/8632823

Yang, X., and Li, X. (2009). Nucleus Pulposus Tissue Engineering: a Brief Review. *Eur. Spine J.* 18, 1564–1572. doi:10.1007/s00586-009-1092-8

Zhang, G.-Z., Deng, Y.-J., Xie, Q.-Q., Ren, E.-H., Ma, Z.-J., He, X.-G., et al. (2020). Sirtuins and Intervertebral Disc Degeneration: Roles in Inflammation, Oxidative Stress, and Mitochondrial Function. *Clinica Chim. Acta* 508, 33–42. doi:10.1016/j.cca.2020.04.016

Zhang, X.-b., Hu, Y.-c., Cheng, P., Zhou, H.-y., Chen, X.-y., Wu, D., et al. (2021). Targeted Therapy for Intervertebral Disc Degeneration: Inhibiting Apoptosis Is a Promising Treatment Strategy. *Int. J. Med. Sci.* 18, 2799–2813. doi:10.7150/ijms.59171

Zhang, Y., and Wong, H. S. (2021). Are Mitochondria the Main Contributor of Reactive Oxygen Species in Cells? *J. Exp. Biol.* 224. doi:10.1242/jeb.221606

Zhong, W. X., Zhang, G. S., and Tang, J. (2021). The Effect of Nrf2 Activators tBHQ and 4-octyl Itaconate on the Nucleus Pulposus Cell Degeneration. *Eur. Rev. Med. Pharmacol. Sci.* 25, 5189–5198. doi:10.26355/eurrev_202108_26532

Conflict of Interest: The authors declare that the research was conducted in the absence of any commercial or financial relationships that could be construed as a potential conflict of interest.

frontiers
in Bioengineering and Biotechnology

REVIEW
published: 17 February 2022
doi: 10.3389/fbioe.2022.830722

Effects of Mechanical Stress Stimulation on Function and Expression Mechanism of Osteoblasts

Pan Liu[1,2†], *Ji Tu*[3†], *Wenzhao Wang*[4], *Zheng Li*[5], *Yao Li*[1,2], *Xiaoping Yu*[6,7*] *and Zhengdong Zhang*[1,2,8*]

[1]School of Clinical Medicine, Chengdu Medical College, Chengdu, China, [2]The First Affiliated Hospital of Chengdu Medical College, Chengdu, China, [3]Spine Labs, St. George & Sutherland Clinical School, University of New South Wales, Sydney, NSW, Australia, [4]Department of Orthopedics, West China Hospital of Sichuan University, Chengdu, China, [5]People's Hospital of Jiulongpo District, Chongqing, China, [6]School of Public Health, Chengdu Medical College, Chengdu, China, [7]Basic Medical College of Chengdu University, Chengdu, China, [8]Department of Orthopedics, The First Affiliated Hospital of Chengdu Medical College, Chengdu, China

Edited by:
Yun Qian,
Shanghai Jiao Tong University, China

Reviewed by:
Christian Hellmich,
Vienna University of Technology, Austria
Chuandong Wang,
Shanghai Jiaotong University, China

***Correspondence:**
Xiaoping Yu
cyggwsyxp@sina.com
Zhengdong Zhang
doctorzzd@vip.qq.com

†These authors have contributed equally to this work and share first authorship

Specialty section:
This article was submitted to Biomaterials, a section of the journal Frontiers in Bioengineering and Biotechnology

Received: *07 December 2021*
Accepted: *10 January 2022*
Published: *17 February 2022*

Citation:
Liu P, Tu J, Wang W, Li Z, Li Y, Yu X and Zhang Z (2022) Effects of Mechanical Stress Stimulation on Function and Expression Mechanism of Osteoblasts.
Front. Bioeng. Biotechnol. 10:830722.
doi: 10.3389/fbioe.2022.830722

Osteoclasts and osteoblasts play a major role in bone tissue homeostasis. The homeostasis and integrity of bone tissue are maintained by ensuring a balance between osteoclastic and osteogenic activities. The remodeling of bone tissue is a continuous ongoing process. Osteoclasts mainly play a role in bone resorption, whereas osteoblasts are mainly involved in bone remodeling processes, such as bone cell formation, mineralization, and secretion. These cell types balance and restrict each other to maintain bone tissue metabolism. Bone tissue is very sensitive to mechanical stress stimulation. Unloading and loading of mechanical stress are closely related to the differentiation and formation of osteoclasts and bone resorption function as well as the differentiation and formation of osteoblasts and bone formation function. Consequently, mechanical stress exerts an important influence on the bone microenvironment and bone metabolism. This review focuses on the effects of different forms of mechanical stress stimulation (including gravity, continuously compressive pressure, tensile strain, and fluid shear stress) on osteoclast and osteoblast function and expression mechanism. This article highlights the involvement of osteoclasts and osteoblasts in activating different mechanical transduction pathways and reports changings in their differentiation, formation, and functional mechanism induced by the application of different types of mechanical stress to bone tissue. This review could provide new ideas for further microscopic studies of bone health, disease, and tissue damage reconstruction.

Keywords: mechanical stress, stimulation, function, expression mechanism, osteoblasts

1 INTRODUCTION

Mechanical forces affect almost every sphere of various life processes of living organisms, such as the perception of external hearing and touch, fluid flow and deformation during embryonic development, changes in cell osmotic pressure, pressure on blood vessel walls, and the movement of individual animals regulated by the earth's gravitational environment. These forces range from mechanical stress signal generation, induction, and transduction to the final response, which involves the cell membrane, cytoderm, cytoskeleton, and other structures.

Bone tissue is very sensitive to mechanical stress stimulation. Unloading and loading of mechanical stress are closely involved in the differentiation and formation of osteoclasts and osteoblasts, and their bone resorption and formation functions, respectively (Robling and Turner, 2009; Li et al., 2020a). Consequently, mechanical stress exerts an important influence on the bone microenvironment and metabolism. Wolff's Law points out that the lack of mechanical stress would lead to bone microstructure degeneration, mass loss and metabolism disorders, and would ultimately lead to osteoporosis (Brand, 2010). The absence of mechanical stress, such as with limb casts fixation, bed-rest, reduced exercise, and the weightlessness of astronauts in space, can lead to significant bone loss (Berg et al., 2007; Ragnarsson, 2015). In contrast, the mechanical load caused by exercise can restore bone mass and reverse these effects in most situations (Iura et al., 2015; Suniaga et al., 2018).

Exposure of tissues and cells to external mechanical stress transforms the external mechanical force into local mechanical signals in the body, triggering responses of cellular sensors. Subsequently, cellular mechanical signals are coupled to biochemical signaling molecules such as the nitric oxide produced and prostaglandins (PGs) (Duncan and Turner, 1995; Johnson et al., 1996; Klein-Nulend et al., 1997). Osteoblasts, osteocytes, bone lining cells, osteoclasts, and macrophages can sense mechanical stimulation and respond directly or indirectly (Dong et al., 2021). Mechanical transduction in bone tissue cells is a complex but precise regulatory process between cells and the microenvironment, between adjacent cells, and between mechanical sensors with different functions in a single cell. Ion channels, integrins, gap junction proteins, focal adhesion kinase, the extracellular matrix, the cellular skeletal components (such as intermediate filaments, microtubules, and actin filaments), and primary cilia are mechanical sensors that have been proven to regulate intracellular signaling pathways (Qin et al., 2020).

In vitro studies often use peripheral blood mononuclear cells, monocyte cells, bone marrow derived precursors and RAW264.7 cells induced to exhibit osteoclast formation (Owen and Reilly, 2018; Xiang et al., 2020). Bone mesenchymal stem cells (BMSCs), Human periodontal ligament cells (hPDLCs) and mouse embryo osteoblast precursor (MC3T3-E1) cells were induced to form osteoblasts (Rutkovskiy et al., 2016). The metabolic characteristics and mechanism of bone formation and remodeling have been explored by observing and studying the process of bone differentiation and formation. Osteocytes, osteoclasts and osteoblasts play major roles in bone tissue homeostasis. Bone tissue remodeling is a continuous process in which the role of osteoclasts is mainly in bone resorption, whereas that of osteoblasts is mainly bone remodeling, such as bone cell formation, mineralization, and secretion (Hardy and Fernandez-Patron, 2020). RANKL secreted by osteocytes binds to the receptor RANK on the precursor surface of osteoclasts to promote the differentiation and maturation of osteoclasts. Osteocytes also secrete OPG, which acts as the decoy receptor of RANKL and negatively regulates RANK signal to prevent osteoclast differentiation. When the ratio of RANKL/OPG increases, bone resorption increases; when the ratio of RANKL/OPG decreases, bone formation increases. In addition, osteocytes secrete sclerotin, which is a negative regulator of bone formation (Bonucci, 2009; Prideaux et al., 2016). These cell types balance and restrict each other to maintain bone tissue metabolism and homeostasis.

Previous studies have shown that appropriate mechanical stress stimulation can reduce the number and activity of osteoclasts and inhibit bone resorption, promote the differentiation and osteogenic function of osteoblasts, inhibit the differentiation of BMSCs into adipocytes, and prevent the loss of bone mass (Uzbekov et al., 2012). This effect also critically influences the regulation of bone metabolism signaling pathways (Uzbekov et al., 2012; Kameyama et al., 2013). However, the exact mechanism is not entirely clear. Numerous studies have further investigated the mechanism underlying the effects of mechanical stress on bone metabolism by examining mechanical stress stimulation in osteoclasts and osteoblasts (involving different species such as humans, mice and zebrafish,etc.) (Nomura and Takano-Yamamoto, 2000; Ho et al., 2005; Wittkowske et al., 2016). In this review, we review the mechanisms of mechanical stress stimulation on the function and expression of osteoblasts. Through this review, we attempt to provide a theoretical basis for the microscopic study of bone health, diseases, and injury reconstruction.

2 MECHANORECEPTOR

2.1 Ion Channels

Appropriate mechanical stimulation can activate calcium channels on the cell membrane to promote the transport of extracellular calcium into the cell, increasing the intracellular calcium concentration and promoting bone mass increase. Piezo1 and Piezo2 have been identified as important mechanosensitive channels. Piezo1 is a mechanosensitive ion channel through which osteoblasts sense and respond to changes in mechanical load and are required for gene expression changes caused by fluid shear stress (FSS) (Li et al., 2019; Zhou et al., 2020). Piezo1 expression in osteoblasts may also be promoted by mechanical tensile force (Wang et al., 2020a) and its deficiency in osteoblasts promotes bone resorption and contributes to osteoporosis in mice, but does not affect bone mass (Wang et al., 2020b).

Li et al. (Li et al., 2019) reported that the removal of Piezo1 from osteoblasts and bone cells does not completely eliminate the response of bones to mechanical stimuli. Furthermore, Piezo1 is not the only mechanosensor in osteoblasts and bone cells. Although Piezo1 and Piezo2 mRNA expression was detected in bone tissues, Piezo1 expression was significantly higher in bone cells and osteoblasts than that of Piezo2 (Sugisawa et al., 2020). Piezo2 is more involved in the development of the nervous system and the perception of touch and pain, than Piezo 1 is, including through molecules such as Merkel cells, outer hair cells and somatosensory ganglia (Woo et al., 2014). Other channels, such as the transient receptor potential (TRP) vanilloid (TRPV) and certain members of the epithelial Na^+ channel (ENaC) protein family, can guide cation influx under a hypertonic environment or membrane tension, converting mechanical force signals into electrical and chemical signals (Gu and Gu, 2014; Kefauver et al., 2020).

2.2 Cytoskeleton

The cytoskeleton is a network structure in cells that is mainly composed of protein fiber (Kounakis and Tavernarakis, 2019), and mainly consists of microtubules, actin fibers, and intermediate filaments (Sandbo et al., 2016). It plays an important role in maintaining cell morphology, bearing external forces, and maintaining the internal cellular structure. The cytoskeletal structure is highly nonlinear, enabling cells to sense deformation and change and the complete cytoskeleton contributes to maintaining tight adhesion between cells and the extracellular matrix (ECM). The integrin glycoprotein family located on the cell membrane senses mechanical signals through interactions between the ECM and intracellular signals (Aisha et al., 2015). Human MSCs (hMSCs) can be gradually remodeled through cell recombination and arrangement and the regulation of smooth muscle cells by the cytoskeleton (Parandakh et al., 2017). Microtubule actin cross-linking factor 1 (MACF1) is a regulator of cytoskeletal dynamics that is necessary for maintaining bone tissue integrity (Wang et al., 2021a), whereas actin in the cytoskeleton is mainly involved in mechanical stress (Zhou et al., 2018). The link between mechanical stimulation, integrin/cytoskeleton/Scr/extracellular signal-regulated protein kinase (ERK) signaling pathway activation, and osteocyte survival provides a mechanical basis for the role of mechanical forces in the bone (Plotkin et al., 2005).

2.3 Integrin

Integrins are heterodimers formed by the non-covalent binding of α and β subunits and presently, mammals are known to express18 α and 8 β subunits, which combine to form 24 integrins (Selvakumarasamy et al., 2019). Integrin senses physical or biochemical stimulation of the ECM by binding to its ligands (including fibonectin, collagen, and laminin) in the extracellular region. Furthermore, through conformational changes, integrin mediates the transmission of signals to cells to induce their adhesion, migration, proliferation, and differentiation. Moreover, intracellular signal changes also affect the conformational changes of integrin, alter the affinity of ligand binding, and affect the biological behavior of cells. This integrin-dependent bidirectional signal transduction mechanism plays an important role in bone remodeling (Uda et al., 2017; Kong et al., 2020; Michael and Parsons, 2020). Recent studies have shown that osteoclasts express integrin α2 and αV and play an important role in bone resorption (Kong et al., 2020). Subsequent studies should focus on further clarifying the important role of integrin in mechanical stimulation and bone metabolism.

2.4 Primary Cilia

Primary cilia is widely found in osteocytes, MC3T3-E1 cells, murine long bone osteocyte-Y4 (MLO-Y4) osteoid cells, cranial osteoblasts, and hMSCs, and it is an important mechanoreceptor that responds to mechanical stimulation and coordinated load induction in these cells (Xiao et al., 2006; Malone et al., 2007; Hoey et al., 2012). However, the existence of primary cilia in osteoclasts has not been reported in existing studies (Yuan et al., 2015). The exposure of osteoblasts and hMSCs to suitable FSS upregulated the expression levels of runt-related transcription factor 2 (RUNX2), bone morphogenetic protein 2 (BMP2), alkaline phosphatase (ALP), and osteopontin (Sonam et al., 2016). In bone cells, primary cilia act as mechanosensors that respond to and flex extracellular fluid impulses generated by the body during walking and running. When primary cilia bend, the increased tension on the membrane opens mechanosensitive ion channels, which leads to intracellular Ca^{2+} influx, membrane depolarization, and activation of nerve fibers and then, the cell experiences mechanical stimulation (Whitfield, 2003). Studies have shown that a simulated microgravity environment eliminates the formation of primary cilia, inhibits the formation and mineralization of rat skull osteoblasts, and significantly shortens the residual cilia (Shi et al., 2020). However, the specific mechanism underlying the action of primary cilia in the bone under mechanical stress has cannot be fully explained by current studies, and further elucidation is needed in future studies.

3 MECHANICAL STIMULATION WITH OSTEOBLASTS

3.1 Gravity

The force through which objects are attracted to each other on earth is called gravity, which is exerted by the earth, and the direction of gravity is always straight down.

3.1.1 Hypergravity and Osteoblasts

MC3T3-E1 cells as osteoblast precursors are commonly used for mechanical sensing and gravity studies, which often use different methods or stimulatory interventions to observe the effects of osteoblast differentiation. Hypergravity (a force of 5, 10, 20, and 40 × g) was shown to promote the proliferation of MC3T3-E1 and osteoblast-like cells through a PGE2-mediated mechanism *in vitro* (Miwa et al., 1991), increase ALP activity, and was positively correlated with the duration of hypergravity (Nakajima, 1991). Similarly, hypergravity of 3 × g stimulates bone formation by enhancing the activity of osteopontin and RUNX2 in osteoblasts (Zhou et al., 2015). Kawao et al. (Kawao et al., 2020) found increased mRNA levels of RUNX2, osterix, ALP, and osteocalcin; ALP activity; and mineralization *in vivo* in osteoblasts from mice exposed to 3 ×g hypergravity. In addition, Woodcock et al. (Woodcock et al., 2019) found that high gravity effectively increased the intracellular viscosity of MC3T3-E1 cells and promoted the maturation and differentiation of osteoblasts, whereas higher levels (10, 15, and 20 × g) had a more significant effect.

3.1.2 Microgravity

The force of gravity in space is one millionth that on earth (9.8 m/s^2). Microgravity can lead to osteoblast and osteoclast interaction disorders, resulting in bone loss, muscle relaxation, and the development of osteoporosis. Space microgravity and simulated microgravity (such as in plaster splintage, tail suspension test, sciatic denervation, and hindlimb unloading are commonly used in studies of bone metabolism *in vivo* and *in vitro* (Globus and Morey-Holton, 2016).

3.1.2.1 Microgravity and Osteoblasts

In space microgravity and simulated microgravity, sclerostin (SOST) enhances osteoclast formation by decreasing the production of osteoprotegerin (OPG) in osteoblasts and increasing the secretion of receptor activator of nuclear factor (NF)-κB ligand (RANKL) (Saxena et al., 2011; Chatani et al., 2016). Similar studies have shown that microgravity reduced osteoblast production and enhanced that of osteoclasts by decreasing OPG secretion by osteoblasts (increasing the RANKL/OPG ratio) (Rucci et al., 2007). Serum glucocorticoid levels increased significantly on day 3 in an animal model of hindlimb unloading that simulated microgravity. High glucocorticoid levels inhibited the expression of Wnt/β-catenin signaling pathway molecules and upregulated the expression of SOST in bone cells (Yang et al., 2020). Therefore, enhanced secretion of glucocorticoid may be an important factor for bone loss in the hindlimb unloading model (Yang et al., 2020). A recent study showed that the leukemia inhibitory factor (LIF) enhanced signal transducer and activator of transcription 3 (STAT3) phosphorylation in BMSCs and increased the expression of ALP and osteogenic genes. However, in the *in vitro* microgravity environment, the secretion of LIF by bone cells was inhibited, which weakened the osteogenic effect (Du et al., 2020). Microgravity also increases the level of oxidative damage markers in the body and weakens the total antioxidant capacity.

Reactive oxygen species (ROS) inhibit the function of osteoblasts (Manolagas, 2010; Steller et al., 2018), promote MC3T3-E1 cell apoptosis, and downregulate the expression of MAF BZIP transcription factor G (MafG) (Wang et al., 2021b). Therefore, increased ROS expression in microgravity is also one of the key factors for bone loss. In addition, microRNA (miR)-494 inhibits BMP2-induced osteoblast differentiation by downregulating BMPR2 and RUNX2 under microgravity simulation (Qin et al., 2019). An increasing number of studies have shown that the inhibition of osteogenic differentiation in microgravity can be regulated by multiple non-coding RNAs (ncRNAs) (Wang et al., 2018; Wang et al., 2020c; Cao et al., 2021).

Although resistance training for astronauts can effectively prevent bone loss (Stein, 2013), the adverse effects of the space microgravity environment on the bones of astronauts can last for several years, which highlights the importance of studying bone metabolism under microgravity conditions. The huge cost of *in vivo* and *in vitro* experiments on space flight has necessitated the development of a variety of experimental platforms to simulate ground microgravity environments (Bonnefoy et al., 2021; Iordachescu et al., 2021). However, fully replicating the changes induced by space microgravity exposure is challenging and, therefore, the develop of more reliable and accurate ground microgravity simulation environments for in-depth research is necessary.

3.1.3 Continuously Applied Compressive Pressure

The force perpendicular to the surface of a fluid per unit area is called the static pressure of the fluid, and continuous action for a specified period of time is called the continuously applied compressive pressure (CCP) (Xing et al., 2004). As a form of stress stimulated by mechanical stress, CCP is an effective condition for stimulating bone tissue growth. However, when CCP is too high or insufficient, it can reduce bone mass and lead to bone loss.

3.1.3.1 Continuously Applied Compressive Pressure and Osteoblasts

Imamura et al. (Imamura et al., 1990) Found that CCP inhibits osteoblast differentiation of MC3T3-E1 cells through production of PGE2. Their further study found that applying continuous static pressure (3 atm, ATM) to MC3T3-E1 cells inhibited the ALP activity of the osteoblasts and promoted PGE2 secretion. When MC3T3-E1 cells were transferred to a CO_2 incubator at 1 ATM, the inhibition of ALP activity was rapidly reversed (Ozawa et al., 1990). Yanagisawa et al. (Yanagisawa et al., 2008) reported that 1.0 g/cm^2 compressive stress was the optimal condition for osteoblast differentiation, and the study by Tripuwabhrut et al. (Tripuwabhrut et al., 2013) showed that osteoblast differentiation was enhanced when compressive stress increased from 2.0 g/cm^2 to 4.0 g/cm^2. Xiaoqing Shen et al. (Shen et al., 2017) showed that compressive stress at the range of 5.0 g/cm^2 had no significantly different effects on the survival rate of MC3T3-E1 cells.

These results indicate that CCP has a positive effect on the differentiation of MC3T3-E1 cells and osteoblasts, but the exact dose of CCP for MC3T3-E1 cells and specific effects are currently unclear. Recently, Shu et al. (Somemura et al., 2021) reported that treating osteoblasts in a three-dimensional (3D) cell-collagen sponge construct with 25.5 gf/cm^2 (2.5 kPa) for 24 h upregulated glucose transporter1 (Glut1), RUNX2 and ALP, whereas silent mating type information regulation 2 homolog 1 (sirtuin 1, SIRT1) was downregulated in osteoblasts induced by compressive mechanical loading. They hypothesized that the Glut1/SIRT1/RUNX2 pathway in osteoblasts may play a role in mechanical stress-induced bone formation and osteoblast differentiation. *In vitro* studies have repeatedly confirmed that osteocytes (not only osteoblasts, but also osteoblasts, osteoclasts and their progenitors) do indeed exhibit altered activity at hydrostatic pressures of up to 1 Hz, with amplitudes of tens (to hundreds) of kilopascals. Since *in-situ* tests are somewhat difficult to achieve, Whether hydrostatic pressure, identified *in vitro* as mechanical stimulation, actually occurs *in vivo* is controversial (Duncan and Turner, 1995). With this problem in mind, the multi-scale mechanical biology method and multi-scale mechanical model proposed by Scheiner et al. that connect porous micromechanics and mathematical systems biology provide valuable insights for this problem (Scheiner et al., 2014; Scheiner et al., 2016; Estermann and Scheiner, 2018). In addition, reports of CCP on osteoblast differentiation and osteoclast differentiation regulated by osteoblasts are still being explored (Tripuwabhrut et al., 2013). The effects of CCP strength and duration on osteoblasts will be precisely defined in future studies.

3.1.4 Tensile Strain

Various types of stress can produce relative strain when applied to an object. The ratio of the length, shape, and volume variation of the object before and after the action of tensile stress (single/bidirectional tensile stress) is called tensile strain. Ilizarov (Ilizarov, 1989) was the first to successfully apply traction stress to stimulate bone formation, and proposed the theory of "distraction osteogenesis". To date, the theory has been successfully applied in strategies for the repair and treatment of bone defects (Kani et al., 2020).

3.1.4.1 Tensile Strain and Osteoblasts

The tensile stress of osteoblasts cultured *in vitro* was mainly achieved by stretching the culture medium membrane that adhered to the osteoblasts. In applying stretch stress to the culture medium membrane, the strength and duration can be controlled to observe the different responses of osteoblasts to stretch tension under different conditions. Furthermore, this process passively pulls osteoblasts that have adhered to the culture medium membrane, which simulates osteoblast stress *in vivo*. Chen et al. (Chen et al., 2018) found that mechanical stretching of human jaw bone marrow MSCs using the Flexcell tension system *in vitro* significantly increased ALP activity and calcium deposition. Moreover, the expression levels of RUNX2 and osterix were significantly upregulated, whereas NF-κB was significantly downregulated. Davidson et al. (Davidson et al., 2013) performed a mandibular osteotomy and pull experiment on Sprague-Dawley rats using a pull osteogenesis technique. The results showed that BMP2, intranuclear SMAD family member 1 (SMAD1) phosphorylation and ALP activity were increased in the traction region, and the osteogenic effect was significantly increased. Wnt1 expression was found to be elevated in alveolar bone cells on the tension side of orthodontic tooth movement (OTM) mouse model for 5 days (Ei Hsu Hlaing et al., 2020).

In addition to mechanical tensile force acting directly on osteoblast precursors and osteoblasts, it can also induce osteogenesis indirectly by affecting other mechanosensitive cells. Dong et al. (Dong et al., 2021) reported that macrophages are exposed to cyclic stretching with a 5% strain at a frequency of 1.0 Hz for up to 12 h using the FX-4000 Flexcell, and the stretched macrophages were co-cultured with BMSCs. The expression of opsin (OPN) and RUNX2 was significantly increased and induced Yes-associated protein (YAP) activation and nuclear translocation, which subsequently regulated downstream BMP2 expression to promote BMSCs osteogenesis (Dong et al., 2021). Li et al.(2020b) induced distraction osteogenesis of osteoblasts, and found that their proliferation was enhanced and mRNA levels of ALP, RUNX2, osteocalcin (OCN), collagen type I, hypoxia-inducible factor (HIF)-1α and vascular endothelial growth factor (VEGF) were significantly increased.

However, *in vivo* studies showed that locally generated bacterial inflammation inhibited RUNX2 expression and up-regulated c-fos and interleukin (IL)-1β expression levels in osteoblasts induced by tensile strain, and reduced the osteogenesis of osteoblasts under continuous tensile stress (Lacey et al., 2009; Li et al., 2021). Obesity induced by high-fat diet decreases osteoblast activity in alveolar bone of the OTM stretching side (Luo et al., 2021). Therefore, it is necessary to consider several factors to maximize the function of osteoblasts using tensile stress.

3.1.5 Fluid Shear Stress

Fluid shear stress (FSS) is a type of mechanical stress caused by extracellular fluid, such as tissue fluid, flowing through the cell membrane surface, and the theory that FSS is induced by the flow of tissue fluid in the lacunar-canalicular system is widely accepted (Kumar et al., 2021). Applying loads (including mechanical loads, muscle contractions, blood pressure, and lymphatic drainage) to the bones causes the interstitial fluid to flow, which compresses the lacunar-canalicular system, thereby inducing various mechanical stimuli including FSS (Duncan and Turner, 1995; Tanaka et al., 2005; Price et al., 2011). FSS can further induce changes in the biomechanical properties of osteoblasts.

3.1.6 Fluid Shear Stress and Osteoblasts

Previous studies have shown that FSS inhibits tumor necrosis factor (TNF)-α-induced osteoblast apoptosis (Pavalko et al., 2003). More recent studies have shown that FSS can activate the ERK5-serine-threonine protein kinase B (AKT)-forkhead box O3a (FoxO3a)-Bim/FasL signaling pathway, inhibit the activation of caspase 3, and protect osteoblasts from apoptosis induced by TNF-α (Bin et al., 2016). Wang X. et al. (Wang et al., 2021e) found that the expression level of long-coding (RNA) lncRNA taurine up-regulated 1 (TUG1) increased in a time-dependent manner when MC3T3-E1 cells were exposed to 12 dyn/cm^2 FSS treatment for 30, 60, and 90 min. LncRNA TUG1 upregulated fibroblast growth factor receptor 1 (FGFR1) expression by sponging miR-34a, which promoted osteoblast proliferation and inhibited osteoblast apoptosis (Wang et al., 2021e).

This study also found that FSS downregulated miR-140-5p and promote osteoblast proliferation by activating the vascular endothelial growth factor-A (VEGFA)/ERK5 signaling pathway (Wang et al., 2021d). FSS increased the expression of Piezo1 in MC3T3-E1 cells, activated the AKT- serine-threonine protein kinase glycogen synthase kinase 3 (GSK3)/β-catenin pathway and upregulated the expression level of RUNX-2 (Song et al., 2020). FSS remodels the cytoskeleton of MC3T3-E1 cell; arranges F-actin proteins in one direction, making them more compact and uniform; and increases the expression level of phospho-paxillin and integrin-α5 (Jin et al., 2020).

Recently, the in-depth study of bone ingrowth between internal fixation materials and bone interface has encouraged the study of material-bone interface-mechanical stimulation as an emerging focus. Lei et al.(2021) reported the effect of FSS on human MG-63 osteoblast-like cells on titanium with different surface modifications, which was particularly evident on the implant-bone interface. This study found that FSS (12 dyn/cm^2) significantly induced cell proliferation and upregulated the expression level of focal adhesion kinase (FAK), which the authors speculated that FAK may play a key role in the mechanical transduction of the implant-bone interface (Lei et al., 2021).

FAK is a nonreceptor tyrosine kinase, which plays a key role in integrin-mediated signal transduction and downstream signaling pathways (Tapial Martinez et al., 2020). Wang J. et al. (Wang J. et al., 2021) found that the interface force or adsorption force of protein-material can regulate the organization of the actin cytoskeleton and promote the formation of focal adhesion, and that FSS promotes assembly of the actin cytoskeleton and decomposition of focal adhesions. These emerging studies will contribute to the designing of a harmonious bioreactor and mechanical load to facilitate the comprehensive study of bone tissue regeneration.

4 SIGNAL PATHWAYS MEDIATING EFFECTS OF MECHANICAL STRESS STIMULATION ON OSTEOBLASTS

Mechanical load induces stress stimulation of the bone and transmits the force to the bone cells. The receptors on the cell membrane are activated by binding of specific ligands, which triggers the signal cascade and enhances expression of downstream target genes, playing a role in bone metabolism. Mechanical transduction is a complex process regulated by multiple signal pathways.

4.1 Wnt/β-Catenin Signaling Pathway

The Wnt/β-catenin pathway is one of the most important pathways studied in bone metabolism research. Exposure of the transmembrane co-receptors low-density lipoprotein (LDL) receptor related protein 5 (Lrp5), Lrp6, and Frizzled (FZD) protein family to Wnt, activates the Lrp/FZD receptor complex on the cell surface, which inhibits the degradation activity of β-Catenin through the phosphorylation of downstream protein kinases. Subsequently, the stably accumulated β-catenin in the cytoplasm enters the nucleus and combines with the T-cell factor/lymphoid enhancer factor (TCF/LEF) transcription factor family to initiate the transcription of downstream target genes to promote the expression of osteogenic genes (such as *OPG*) and promote bone formation. Studies have found that mice with Lrp5 deletion mutations continue to show a state of low bone mass (Sawakami et al., 2006; Iwaniec et al., 2007).

More recent studies showed that human patients with Lrp5 missense mutation (A745V) had severe osteoporosis, which may be attributable to the weakening of the anabolic response of bones to mechanical stress (Kiel et al., 2007; Norwitz et al., 2019). Lrp5 and Lrp6 have been shown to be extremely important in bone cell mechanical transduction (Jing et al., 2016). In addition, under mechanical load, heterozygous deletion of β-catenin in a single osteocyte in mice eliminates the bone synthesis response to mechanical load and the ability to form new bone (Javaheri et al., 2014). Numerous studies using *in vitro* and *in vitro* models have also demonstrated the involvement of the Wnt pathway in mechanical stress (Bonewald and Johnson, 2008; Duan and Bonewald, 2016; Kang et al., 2016; Fu et al., 2020). However, SOST negatively regulates the Wnt/β -catenin pathway (Choi and Robling, 2021).

Dickkopf-related protein (DKK) 1 and DKK2 are expressed by osteocytes and negatively regulate Wnt/β-catenin. The mechanical load can inhibit the expression of DKK1 in osteocytes and promote the upregulation of Wnt signaling (Holguin et al., 2016). *In vivo* studies using hypergravity (3 × g) showed significantly reduced DKK2 levels in the serum and DKK2 mRNA levels in the soleus muscle of mice (Kawao et al., 2020). DKK2 was shown to inhibit mRNA levels of RUNX2, osterix, ALP, and osteocalcin and alkaline phosphatase activity and mineralization in osteoblasts, and enhance the phosphorylation of β-catenin in mouse osteoblasts (Kawao et al., 2020). Regulation of the Wnt pathway has a positive effect on compensatory mechanisms for coping with mechanical stress and changing bone mass, but the specific mechanism remains to be further studied.

4.2 Notch Signaling Pathway

The Notch signaling pathway, which is expressed in almost all organ systems, is highly conserved and plays an important role in the occurrence and development of diseases by regulating various cell processes (Andersson et al., 2011). Mammals have multiple Notch receptors, and the common types are Notch 1, Notch 2, Notch 3, and Notch-4. The Notch receptor is a one-way transmembrane protein that consists of the Notch extracellular domain (NECD), Notch transmembrane domain (NTM), and Notch intracellular domain (NICD). In mammalian cells, members of the delta-like ligand (DLL1, DLL3, and DLL4) and Jagged (JAG1 and JAG2) families act as ligands for Notch signaling receptors (Steinbuck and Winandy, 2018). Binding of the specific ligand to the receptor activates the Notch signaling pathway and its downstream target genes [including hes family bHLH transcription factor 1 (*Hes1*), hes related family bHLH transcription factor with YRPW motif 1 (*Hey1*), and *Hey2*] are transcribed. It is worth mentioning that Hes1 is a key factor in bone metabolism (Zanotti et al., 2011).

The role of Notch receptors in bone metabolism has always been controversial. Overexpression of NICD1 in osteocytes reduces bone resorption, leading to an increase in bone mass. Conversely, specific activation of Notch signaling in immature osteoblasts impaired their differentiation, leading to osteopenia (Canalis et al., 2013). Wang L. et al. (Wang et al., 2020a) found that mechanical stretch stress can activate the Notch1 signaling pathway and the expression of ALP, RUNX2, OCN, bone sialoprotein (BSP), and promote the osteogenic differentiation of human periodontal ligament stem cells. Ziouti et al. (Ziouti et al., 2019) found that applying tibial cyclic compression load (216 cycles at 4 Hz, peak strains at a tibial midshaft of +900 $\mu\varepsilon$) to wild-type mice induced specific Notch target genes (mRNA expression of Hes1, Hey1, and Hey2). Cyclic stretching of primary human BMSCs increased the gene expression of Notch receptors *Notch1* and *Notch2* by more than 60-fold and 30-fold, respectively. RUNX2 and mechanical response genes prostaglandin-endoperoxide synthase 2 (*PTGS2*) and *FOS* were upregulated. Studies have shown that the Notch pathway is activated and osteogenic gene expression is upregulated in osteoblasts under mechanical stress. However, the exact mechanism of the Notch pathway-related effects in osteoblasts under mechanical stress has not been fully elucidated.

4.3 ERK5 Signaling Pathway

ERK, which belongs to the mitogen-activated protein kinases (MAPKs) family, has strong catalytic activity and plays a key role in upstream signal transduction pathways including mechanical signals in cellular reactions (Fey et al., 2012; Yuan et al., 2020). Studies have shown that loading MC3T3-E1 cells with FSS increases cyclooxygenase (COX)-2 activity, which activates osteoblast-like cell proliferation and anabolic metabolism (Bo et al., 2016; Ding et al., 2019). Knockout of ERK5 using small interfering RNA (siRNA) prevented FSS from upregulating COX-2 and cyclic adenosine monophosphate (cAMP) (Jiang et al., 2015). Wang X. et al. found that FSS-induced downregulation of miR-140-5p regulates ERK5 signal activation through VEGFA and promotes osteoblast proliferation (Wang et al., 2021d). FSS inhibits caspase 3 activation to prevent osteoblast apoptosis by activating the ERK5-AKT-Foxo3a pathway in MC3T3-E1 cells (Bin et al., 2016). Other studies have shown that the effect of mechanical load on ERK5 is an important factor affecting the proliferation of osteoblasts (Li et al., 2012; Zhang et al., 2021).

4.4 RhoA Signaling Pathway

RhoA belongs to the Rho Family of small GTPases, and is a key regulator of actin cytoskeleton. The mammalian genome encodes about 20 kinds of Rho gtpase, and currently the most researched ones are RhoA, Rac1 and Cdc42 (Ridley and Hall, 1992). The activation and inactivation of RhoA is regulated by signals from intracellular and extracellular G protein coupled receptors, integrins and growth factor receptors (Kaneko-Kawano and Suzuki, 2015). Members of the Rho associated protein kinase (ROCK) family, including ROCK1 and ROCK2, are important effectors of RhoA (Arnsdorf et al., 2009). When exogenous forces or forces generated by the cell itself and the cytoskeleton act on the cell (Chen, 2008), cell surface adhesions, cytoskeleton and membrane tension work together to affect mechanosensors and stimulate mechanical responses (Vogel and Sheetz, 2006; Hoffman et al., 2011). Studies have shown that Rho/ROCK converts mechanical stimulation into gene expression changes through the actin-myocardin-related transcription factor (MRTF)-serum response factor (SRF) pathway (Zhao et al., 2007). Dupont et al. (Dupont et al., 2011) found that stretch stimulation can activate the RhoA/ROCK signaling pathway and YAP/transcriptional co-activator with PDZ-binding motif (TAZ), promote bone formation, inhibit adipogenesis, and form actin at the same time. Similarly, RhoA feels high ECM stiffness through focal adhesion, promotes actin polymerization and stress fiber formation, transmits stiffness signals to YAP/TAZ, and regulates the sensitivity of osteoblasts (Wagh et al., 2021). MRTF and YAP/TAZ have been confirmed as transcription factors activated by mechanical induction (Finch-Edmondson and Sudol, 2016; Cai et al., 2021). The activity of ROCK is positively correlated with ECM stiffness. Although stiffness sensing is related to the regulation of multiple signal transductions, RhoA/ROCK pathway is perhaps the most prominent (Selig et al., 2020). Studies have been found that RhoA and its effector protein ROCKII regulate the differentiation of C3H10T1/2 cells induced by oscillatory fluid flow to osteogenic differentiation. At the same time, activated RhoA and fluid flow have an additive effect on the expression of RUNX2 (Arnsdorf et al., 2009). Gardinier et al. (Gardinier et al., 2014) has shown that under the influence of FSS, the mechanical sensitivity of MC3T3-E1 cells is regulated by the activation of $P2Y_2$ receptors through the RhoA/ROCK signal cascade under the influence of FSS. The RhoA signalling pathway is central to mechanotransduction because it plays a key role in regulating the catin cytoskeleton and its response to mechanical force.

In addition, other signaling pathways such as the transforming growth factor-β (TGFβ)-Smad (Zou et al., 2021), NF-κB (Wang et al., 2015), and BMP(da Silva Madaleno et al., 2020; Wei et al., 2020), signaling pathways also have an important role in the responses of osteoblast-like cells under mechanical stimulation, and there is crosstalk between various signaling pathways (Kopf et al., 2014; Grafe et al., 2018; Shuai et al., 2018). Moreover, the effects of mechanical stimulation on the various signal pathways mediated the response of osteoblasts are interactive and related (**Table 1**). Once mechanical stimulus receptors are affected by mechanical loading and unloading, it is possible to activate multiple biological signaling pathways during the conversion of physical signals into chemical stimulation signals, thus generates positive or negative regulation of osteoblast cells. However, the current research is not thorough, and its mechanism needs to be further elucidated. Future research should continue to focus on clarifying the signal pathways mediating the mechanism underlying the actions of mechanical stimulation on osteoblast-like cells.

5 CONCLUSION

Loading and unloading mechanical stress affects the proliferation, differentiation, and function of osteoblast-like cells. Studies have shown that osteoblast-like cells, which are sensitive to mechanical stimulation, are the basic cell model for studying the processes of bone growth, development, and formation (Siddiqui and Partridge, 2016; Thomas and Jaganathan, 2021). The perception of mechanical stress by osteoblasts first involves actions on target genes through various pathways such as Ca^{2+}, Piezo1, ECM-integrin-cytoskeleton, and cell regulatory factors. Mechanoreceptor also regulates the expression of corresponding genes to convert mechanical stimulus signals to chemical stimuli, and then regulates various receptors on the cell membrane, cytoplasm, and nucleus through chemoreceptors to regulate the bone formation mechanism (Steward and Kelly, 2015; Augat et al., 2021). (**Figure 1**).

Mechanical stimulation is an important regulatory factor for bone growth, reconstruction, and metabolism. Number experimental studies have investigated osteogenic effects under mechanical stress (Chermside-Scabbo et al., 2020; Eichholz et al., 2020; Jeon et al., 2021; Lei et al., 2021). The influence of different mechanical forces on bone tissue produces various effects. Analyzing the mechanism mediating the effects of mechanical

TABLE 1 | Signal Pathways Mediating Effects of Mechanical Stress Stimulation on Osteoblast like cells. FSS, fluid shear stress; OPG: osteoprotegerin; DKK, Dickkopf-related protein; RUNX2, Runt-related transcription factor 2; ERK, Extracellular-regulated protein kinase; BMP, Bone Morphogenetic Protein; ALP, alkaline phosphatase; NF-κB, nuclear factor kappa-B; VEGFA, vascular endothelial growth factor-A; YAP, Yes-associated protein; OCN, osteocalcin; ECM, extracellular matrix; COX-2, cyclooxygenase; (MC3T3-E1) cells, mouse embryo osteoblast precursor; TAZ, transcriptional co-activator with PDZ-binding motif; ROCK, Rho associated protein kinase.

Stimulus type	Pathways	Mechanism	Effect	Reference
Axial compression	Activating Wnt signaling	Inhibiting the expression of DKK1	Upregulating the expression of OPG	Holguin et al. (2016)
Hypergravity		Inhibiting the expression of DDK2/enhancing the phosphorylation of β-catenin	Upregulating RUNX2/osterix/ALP/osteocalcin/ALP	Kawao et al. (2020)
Stretch stress	Activating Notch Signaling Pathway	Activating the expression of Piezo1	Upregulating ALP/RUNX2/OCN/BSP/ promoting the osteogenic differentiation	Wang et al. (2020a)
Cyclic stretch		Upregulating the expression of Notch1/Notch2	Upregulating the expression of RUNX2/PTGS2/FOS	Ziouti et al. (2019)
FSS	Activating ERK signaling pathway	Upregulating the expression of COX-2/cyclin E1, inhibiting caspase-3	Promoting the proliferation of MC3T3-E1 cells	
FSS		Downregulating the expression of miR-140-5p/KLF4, upregulating the expression of VEGFA	Promoting the proliferation of MC3T3-E1 cells	Wang et al. (2021d), Bin et al. (2016)
Stretch stimulation	Activating RhoA signaling pathway	Upregulating the expression of YAP/TAZ	Promoting the osteogenic differentiation	Dupont et al. (2011)
High ECM stiffness		Upregulating the expression of YAP/TAZ	Triggering F-actin polymerization	Wagh et al. (2021)
oscillatory fluid flow		Activating ROCKII	Upregulating the expression of RUNX2	Arnsdorf et al. (2009)
FSS		Activating ROCK	Opening up of mechano- and voltage-sensitive calcium channels	Gardinier et al. (2014)
Mechanical tensile strain	Activating NF-κB signaling pathway	Upregulating the expression of BMP-2/BMP-4	Upregulating the expression of ALP/OCN	Wang et al. (2015)

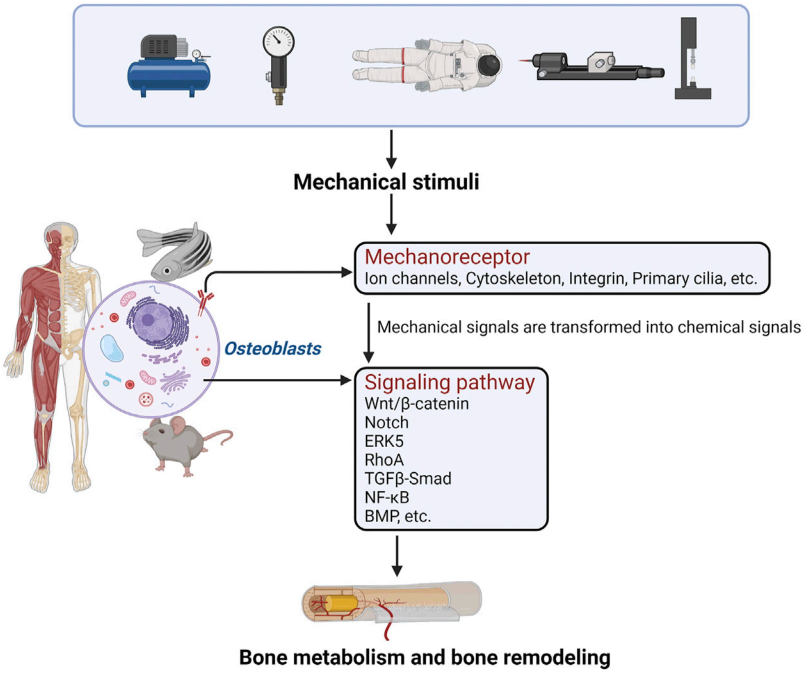

FIGURE 1 | The perception of mechanical stress by osteoblasts first involves actions on mechanoreceptors through various pathways. Mechanoreceptors also regulate the expression of corresponding genes to convert mechanical stimulus signals into chemical stimuli, and regulate the relevant signal transduction pathways. Finally, bone metabolism and bone formation are regulated.

stimulation on the regulation and metabolism of cell signaling pathways such as those of BMSCs, osteoblasts, osteoclasts, and osteocytes is currently a challenging research hotspot. Most previous studies used a single mechanical stimulus on a single mechanosensitive cell, and the mechanical loading methods and mechanical devices used did not have a relatively unified standard.

The results obtained from studies using randomly selected or combinations of different mechanical stimuli were no systematic and lacked standardization and accuracy. Consequently, designs of bone metabolism studies need to include a more suitable mechanical experimental environment to accurately control the mechanical parameters of mechanical stress stimulation, such as the type, duration, intensity, and cycle of mechanical stimulation). Furthermore, such studies should explore the influence of the body on mechanical stimulation. It is gratifying that mechanism-driven biology and biochemistry have been put into mathematical systems biology formats, this will certainly lead the research field to a more precise direction (Pastrama et al., 2018; Lavaill et al., 2020; Larcher and Scheiner, 2021).

This would provide an important theoretical basis for clinical treatment of bone diseases with a focus on issues such as bone health, fracture healing, and bone ingrowth at the bone-material interface. Further *in vivo* experiments need to study the changes in macroscopic bone tissue metabolic activity under stress stimulation, whereas future *in vitro* experiments should explore the specific mechanisms and signal transduction pathways mediating the effects of different mechanical stimuli on various mechanosensitive cells of bone tissue. These results could be used as a foundation for future orthopedics, stomatology, and tissue engineering research studies to advance the development of this discipline.

AUTHOR CONTRIBUTIONS

All authors listed have made a substantial, direct and intellectual contribution to the work, and approved it for publication.

FUNDING

This work was funded by the National Natural Science Foundation of China (82073539 and 81773432), the Foundation of The First Affiliated Hospital of Chengdu Medical College (CYFY-GQ35), the Project of Sichuan Provincial Department of Science and Technology (22MZGC0226) and the Foundation of Chengdu Medical College (CYZYB21-12).

ACKNOWLEDGMENTS

Figure created with Biorender.com.

REFERENCES

Aisha, M. D., Nor-Ashikin, M. N. K., Sharaniza, A. B. R., Nawawi, H., and Froemming, G. R. A. (2015). Orbital Fluid Shear Stress Promotes Osteoblast Metabolism, Proliferation and Alkaline Phosphates Activity *In Vitro*. *Exp. Cel Res.* 337 (1), 87–93. doi:10.1016/j.yexcr.2015.07.002

Andersson, E. R., Sandberg, R., and Lendahl, U. (2011). Notch Signaling: Simplicity in Design, Versatility in Function. *Development* 138 (17), 3593–3612. doi:10.1242/dev.063610

Arnsdorf, E. J., Tummala, P., Kwon, R. Y., and Jacobs, C. R. (2009). Mechanically Induced Osteogenic Differentiation - the Role of RhoA, ROCKII and Cytoskeletal Dynamics. *J. Cel Sci* 122 (Pt 4), 546–553. doi:10.1242/jcs.036293

Augat, P., Hollensteiner, M., and von Rüden, C. (2021). The Role of Mechanical Stimulation in the Enhancement of Bone Healing. *Injury* 52 (Suppl. 2), S78–S83. doi:10.1016/j.injury.2020.10.009

Berg, H. E., Eiken, O., Miklavcic, L., and Mekjavic, I. B. (2007). Hip, Thigh and Calf Muscle Atrophy and Bone Loss after 5-week Bedrest Inactivity. *Eur. J. Appl. Physiol.* 99 (3), 283–289. doi:10.1007/s00421-006-0346-y

Bin, G., Bo, Z., Jing, W., Jin, J., Xiaoyi, T., Cong, C., et al. (2016). Fluid Shear Stress Suppresses TNF-α-Induced Apoptosis in MC3T3-E1 Cells: Involvement of ERK5-AKT-FoxO3a-Bim/FasL Signaling Pathways. *Exp. Cel Res.* 343 (2), 208–217. doi:10.1016/j.yexcr.2016.03.014

Bo, Z., Bin, G., Jing, W., Cuifang, W., Liping, A., Jinglin, M., et al. (2016). Fluid Shear Stress Promotes Osteoblast Proliferation via the Gαq-ERK5 Signaling Pathway. *Connect. Tissue Res.* 57 (4), 299–306. doi:10.1080/03008207.2016.1181063

Bonewald, L. F., and Johnson, M. L. (2008). Osteocytes, Mechanosensing and Wnt Signaling. *Bone* 42 (4), 606–615. doi:10.1016/j.bone.2007.12.224

Bonnefoy, J., Ghislin, S., Beyrend, J., Coste, F., Calcagno, G., Lartaud, I., et al. (2021). Gravitational Experimental Platform for Animal Models, a New Platform at ESA's Terrestrial Facilities to Study the Effects of Micro- and Hypergravity on Aquatic and Rodent Animal Models. *Int. J. Mol. Sci.* 22 (6), 2961. doi:10.3390/ijms22062961

Bonucci, E. (2009). The Osteocyte: The Underestimated Conductor of the Bone Orchestra. *Rend. Fis. Acc. Lincei* 20 (3), 237–254. doi:10.1007/s12210-009-0051-y

Brand, R. A. (2010). Biographical Sketch: Julius Wolff, 1836-1902. *Clin. Orthop. Relat. Res.* 468 (4), 1047–1049. doi:10.1007/s11999-010-1258-z

Cai, X., Wang, K.-C., and Meng, Z. (2021). Mechanoregulation of YAP and TAZ in Cellular Homeostasis and Disease Progression. *Front. Cel Dev. Biol.* 9, 673599. doi:10.3389/fcell.2021.673599

Canalis, E., Parker, K., Feng, J. Q., and Zanotti, S. (2013). Osteoblast Lineage-Specific Effects of Notch Activation in the Skeleton. *Endocrinology* 154 (2), 623–634. doi:10.1210/en.2012-1732

Cao, Z., Zhang, Y., Wei, S., Zhang, X., Guo, Y., and Han, B. (2021). Comprehensive circRNA Expression Profile and Function Network in Osteoblast-Like Cells under Simulated Microgravity. *Gene* 764, 145106. doi:10.1016/j.gene.2020.145106

Chatani, M., Morimoto, H., Takeyama, K., Mantoku, A., Tanigawa, N., Kubota, K., et al. (2016). Acute Transcriptional Up-Regulation Specific to Osteoblasts/Osteoclasts in Medaka Fish Immediately after Exposure to Microgravity. *Sci. Rep.* 6, 39545. doi:10.1038/srep39545

Chen, X., Liu, Y., Ding, W., Shi, J., Li, S., Liu, Y., et al. (2018). Mechanical Stretch-Induced Osteogenic Differentiation of Human Jaw Bone Marrow Mesenchymal Stem Cells (hJBMMSCs) via Inhibition of the NF-Kb Pathway. *Cell Death Dis* 9 (2), 207. doi:10.1038/s41419-018-0279-5

Chen, C. S. (2008). Mechanotransduction - a Field Pulling Together? *J. Cel Sci* 121 (Pt 20), 3285–3292. doi:10.1242/jcs.023507

Chermside-Scabbo, C. J., Harris, T. L., Brodt, M. D., Braenne, I., Zhang, B., Farber, C. R., et al. (2020). Old Mice Have Less Transcriptional Activation but Similar Periosteal Cell Proliferation Compared to Young-Adult Mice in Response to *In Vivo* Mechanical Loading. *J. Bone Miner Res.* 35 (9), 1751–1764. doi:10.1002/jbmr.4031

Choi, R. B., and Robling, A. G. (2021). The Wnt Pathway: An Important Control Mechanism in Bone's Response to Mechanical Loading. *Bone* 153, 116087. doi:10.1016/j.bone.2021.116087 da Silva Madaleno, C., Jatzlau, J., and Knaus, P. (2020). BMP Signalling in a Mechanical Context - Implications for Bone Biology. *Bone* 137, 115416. doi:10.1016/j.bone.2020.115416

Davidson, E. H., Sultan, S. M., Butala, P., Knobel, D., and Warren, S. M. (2013). Lacunocanalicular Fluid Flow Transduces Mechanical Tension Stress during Distraction Osteogenesis. *J. Craniofac. Surg.* 24 (5), 1558–1564. doi:10.1097/SCS.0b013e31828f2060

Ding, N., Geng, B., Li, Z., Yang, Q., Yan, L., Wan, L., et al. (2019). Fluid Shear Stress Promotes Osteoblast Proliferation through the NFATc1-ERK5 Pathway. *Connect. Tissue Res.* 60 (2), 107–116. doi:10.1080/03008207.2018.1459588

Dong, L., Song, Y., Zhang, Y., Zhao, W., Wang, C., Lin, H., et al. (2021). Mechanical Stretch Induces Osteogenesis through the Alternative Activation of Macrophages. *J. Cel Physiol* 236 (9), 6376–6390. doi:10.1002/jcp.30312

Du, J., Yang, J., He, Z., Cui, J., Yang, Y., Xu, M., et al. (2020). Osteoblast and Osteoclast Activity Affect Bone Remodeling upon Regulation by Mechanical Loading-Induced Leukemia Inhibitory Factor Expression in Osteocytes. *Front. Mol. Biosci.* 7, 585056. doi:10.3389/fmolb.2020.585056

Duan, P., and Bonewald, L. F. (2016). The Role of the Wnt/β-Catenin Signaling Pathway in Formation and Maintenance of Bone and Teeth. *Int. J. Biochem. Cel Biol.* 77 (Pt A), 23–29. doi:10.1016/j.biocel.2016.05.015

Duncan, R. L., and Turner, C. H. (1995). Mechanotransduction and the Functional Response of Bone to Mechanical Strain. *Calcif Tissue Int.* 57 (5), 344–358. doi:10.1007/BF00302070

Dupont, S., Morsut, L., Aragona, M., Enzo, E., Giulitti, S., Cordenonsi, M., et al. (2011). Role of YAP/TAZ in Mechanotransduction. *Nature* 474 (7350), 179–183. doi:10.1038/nature10137

Ei Hsu Hlaing, E., Ishihara, Y., Odagaki, N., Wang, Z., Ikegame, M., and Kamioka, H. (2020). The Expression and Regulation of Wnt1 in Tooth Movement-Initiated Mechanotransduction. *Am. J. Orthod. Dentofacial Orthopedics* 158 (6), e151–e160. doi:10.1016/j.ajodo.2020.08.006

Eichholz, K. F., Woods, I., Riffault, M., Johnson, G. P., Corrigan, M., Lowry, M. C., et al. (2020). Human Bone Marrow Stem/Stromal Cell Osteogenesis Is Regulated via Mechanically Activated Osteocyte-Derived Extracellular Vesicles. *Stem Cell Transl Med* 9 (11), 1431–1447. doi:10.1002/sctm.19-0405

Estermann, S.-J., and Scheiner, S. (2018). Multiscale Modeling Provides Differentiated Insights to Fluid Flow-Driven Stimulation of Bone Cellular Activities. *Front. Phys.* 6, 76. doi:10.3389/fphy.2018.00076

Fey, D., Croucher, D. R., Kolch, W., and Kholodenko, B. N. (2012). Crosstalk and Signaling Switches in Mitogen-Activated Protein Kinase Cascades. *Front. Physio.* 3, 355. doi:10.3389/fphys.2012.00355

Finch-Edmondson, M., and Sudol, M. (2016). Framework to Function: Mechanosensitive Regulators of Gene Transcription. *Cell Mol Biol Lett* 21, 28. doi:10.1186/s11658-016-0028-7

Fu, J., Liu, X., Tan, L., Cui, Z., Liang, Y., Li, Z., et al. (2020). Modulation of the Mechanosensing of Mesenchymal Stem Cells by Laser-Induced Patterning for the Acceleration of Tissue Reconstruction through the Wnt/β-Catenin Signaling Pathway Activation. *Acta Biomater.* 101, 152–167. doi:10.1016/j.actbio.2019.10.041

Gardinier, J., Yang, W., Madden, G. R., Kronbergs, A., Gangadharan, V., Adams, E., et al. (2014). P2Y2 Receptors Regulate Osteoblast Mechanosensitivity during Fluid Flow. *Am. J. Physiology-Cell Physiol.* 306 (11), C1058–C1067. doi:10.1152/ajpcell.00254.2013

Globus, R. K., and Morey-Holton, E. (20161985). Hindlimb Unloading: Rodent Analog for Microgravity. *J. Appl. Physiol.* 120 (10), 1196–1206. doi:10.1152/japplphysiol.00997.2015

Grafe, I., Alexander, S., Peterson, J. R., Snider, T. N., Levi, B., Lee, B., et al. (2018). TGF-β Family Signaling in Mesenchymal Differentiation. *Cold Spring Harb Perspect. Biol.* 10 (5), a022202. doi:10.1101/cshperspect.a022202

Gu, Y., and Gu, C. (2014). Physiological and Pathological Functions of Mechanosensitive Ion Channels. *Mol. Neurobiol.* 50 (2), 339–347. doi:10.1007/s12035-014-8654-4

Hardy, E., and Fernandez-Patron, C. (2020). Destroy to Rebuild: The Connection between Bone Tissue Remodeling and Matrix Metalloproteinases. *Front. Physiol.* 11, 47. doi:10.3389/fphys.2020.00047

Ho, M.-L., Tsai, T.-N., Chang, J.-K., Shao, T.-S., Jeng, Y.-R., and Hsu, C. (2005). Down-Regulation of N-Methyl D-Aspartate Receptor in Rat-Modeled Disuse Osteopenia. *Osteoporos. Int.* 16 (12), 1780–1788. doi:10.1007/s00198-005-1928-y

Hoey, D. A., Chen, J. C., and Jacobs, C. R. (2012). The Primary Cilium as a Novel Extracellular Sensor in Bone. *Front. Endocrin.* 3, 75. doi:10.3389/fendo.2012.00075

Hoffman, B. D., Grashoff, C., and Schwartz, M. A. (2011). Dynamic Molecular Processes Mediate Cellular Mechanotransduction. *Nature* 475 (7356), 316–323. doi:10.1038/nature10316

Holguin, N., Brodt, M. D., and Silva, M. J. (2016). Activation of Wnt Signaling by Mechanical Loading Is Impaired in the Bone of Old Mice. *J. Bone Miner Res.* 31 (12), 2215–2226. doi:10.1002/jbmr.2900

Ilizarov, G. A. (1989). The Tension-Stress Effect on the Genesis and Growth of Tissues. Part I. The Influence of Stability of Fixation and Soft-Tissue Preservation. *Clin. Orthopaedics Relat. Res.* 238, 249–281. doi:10.1097/00003086-198901000-00038

Imamura, K., Ozawa, H., Hiraide, T., Shibasaki, Y., Fukuhara, T., Takahashi, N., et al. (1990). Continuously Applied Compressive Pressure Induces Bone Resorption by a Mechanism Involving Prostaglandin E2 Synthesis. *J. Cel. Physiol.* 144 (2), 222–228. doi:10.1002/jcp.1041440207

Iordachescu, A., Hughes, E. A. B., Joseph, S., Hill, E. J., Grover, L. M., and Metcalfe, A. D. (2021). Trabecular Bone Organoids: A Micron-Scale 'Humanised' Prototype Designed to Study the Effects of Microgravity and Degeneration. *NPJ Microgravity* 7 (1), 17. doi:10.1038/s41526-021-00146-8

Iura, A., McNerny, E. G., Zhang, Y., Kamiya, N., Tantillo, M., Lynch, M., et al. (2015). Mechanical Loading Synergistically Increases Trabecular Bone Volume and Improves Mechanical Properties in the Mouse when BMP Signaling Is Specifically Ablated in Osteoblasts. *PLoS One* 10 (10), e0141345. doi:10.1371/journal.pone.0141345

Iwaniec, U. T., Wronski, T. J., Liu, J., Rivera, M. F., Arzaga, R. R., Hansen, G., et al. (2007). PTH Stimulates Bone Formation in Mice Deficient in Lrp5. *J. Bone Miner Res.* 22 (3), 394–402. doi:10.1359/jbmr.061118

Javaheri, B., Stern, A. R., Lara, N., Dallas, M., Zhao, H., Liu, Y., et al. (2014). Deletion of a Single β-Catenin Allele in Osteocytes Abolishes the Bone Anabolic Response to Loading. *J. Bone Miner Res.* 29 (3), 705–715. doi:10.1002/jbmr.2064

Jeon, H. H., Teixeira, H., and Tsai, A. (2021). Mechanistic Insight into Orthodontic Tooth Movement Based on Animal Studies: A Critical Review. *J. Clin. Med.* 10 (8), 1733. doi:10.3390/jcm10081733

Jiang, J., Zhao, L.-G., Teng, Y.-J., Chen, S.-L., An, L.-P., Ma, J.-L., et al. (2015). ERK5 Signalling Pathway Is Essential for Fluid Shear Stress-Induced COX-2 Gene Expression in MC3T3-E1 Osteoblast. *Mol. Cel Biochem* 406 (1-2), 237–243. doi:10.1007/s11010-015-2441-z

Jin, J., Jaspers, R. T., Wu, G., Korfage, J. A. M., Klein-Nulend, J., and Bakker, A. D. (2020). Shear Stress Modulates Osteoblast Cell and Nucleus Morphology and Volume. *Int. J. Mol. Sci.* 21 (21), 8361. doi:10.3390/ijms21218361

Jing, D., Luo, E., Cai, J., Tong, S., Zhai, M., Shen, G., et al. (2016). Mechanical Vibration Mitigates the Decrease of Bone Quantity and Bone Quality of Leptin Receptor-Deficient Db/Db Mice by Promoting Bone Formation and Inhibiting Bone Resorption. *J. Bone Miner Res.* 31 (9), 1713–1724. doi:10.1002/jbmr.2837

Johnson, D. L., McAllister, T. N., and Frangos, J. A. (1996). Fluid Flow Stimulates Rapid and Continuous Release of Nitric Oxide in Osteoblasts. *Am. J. Physiology-Endocrinology Metab.* 271 (1 Pt 1), E205–E208. doi:10.1152/ajpendo.1996.271.1.E205

Kameyama, S., Yoshimura, Y., Kameyama, T., Kikuiri, T., Matsuno, M., Deyama, Y., et al. (2013). Short-Term Mechanical Stress Inhibits Osteoclastogenesis via Suppression of DC-STAMP in RAW264.7 Cells. *Int. J. Mol. Med.* 31 (2), 292–298. doi:10.3892/ijmm.2012.1220

Kaneko-Kawano, T., and Suzuki, K. (2015). Mechanical Stress Regulates Gene Expression via Rho/Rho-Kinase Signaling Pathway. *J. Phys. Fitness Sports Med.* 4 (1), 53–61. doi:10.7600/jpfsm.4.53

Kang, K. S., Hong, J. M., and Robling, A. G. (2016). Postnatal β-Catenin Deletion from Dmp1-Expressing Osteocytes/osteoblasts Reduces Structural Adaptation to Loading, but Not Periosteal Load-Induced Bone Formation. *Bone* 88, 138–145. doi:10.1016/j.bone.2016.04.028

Kani, K. K., Porrino, J. A., and Chew, F. S. (2020). External Fixators: Looking Beyond the Hardware Maze. *Skeletal Radiol.* 49 (3), 359–374. doi:10.1007/s00256-019-03306-w

Kawao, N., Morita, H., Iemura, S., Ishida, M., and Kaji, H. (2020). Roles of Dkk2 in the Linkage from Muscle to Bone during Mechanical Unloading in Mice. *Int. J. Mol. Sci.* 21 (7), 2547. doi:10.3390/ijms21072547

Kefauver, J. M., Ward, A. B., and Patapoutian, A. (2020). Discoveries in Structure and Physiology of Mechanically Activated Ion Channels. *Nature* 587 (7835), 567–576. doi:10.1038/s41586-020-2933-1

Kiel, D. P., Ferrari, S. L., Cupples, L. A., Karasik, D., Manen, D., Imamovic, A., et al. (2007). Genetic Variation at the Low-Density Lipoprotein Receptor-Related Protein 5 (LRP5) Locus Modulates Wnt Signaling and the Relationship of Physical Activity with Bone mineral Density in Men. *Bone* 40 (3), 587–596. doi:10.1016/j.bone.2006.09.029

Klein-Nulend, J., Burger, E. H., Semeins, C. M., Raisz, L. G., and Pilbeam, C. C. (1997). Pulsating Fluid Flow Stimulates Prostaglandin Release and Inducible Prostaglandin G/H Synthase mRNA Expression in Primary Mouse Bone Cells. *J. Bone Miner Res.* 12 (1), 45–51. doi:10.1359/jbmr.1997.12.1.45

Kong, L., Wang, B., Yang, X., He, B., Hao, D., and Yan, L. (2020). Integrin-Associated Molecules and Signalling Cross Talking in Osteoclast Cytoskeleton Regulation. *J. Cel Mol Med* 24 (6), 3271–3281. doi:10.1111/jcmm.15052

Kopf, J., Paarmann, P., Hiepen, C., Horbelt, D., and Knaus, P. (2014). BMP Growth Factor Signaling in a Biomechanical Context. *Biofactors* 40 (2), 171–187. doi:10.1002/biof.1137

Kounakis, K., and Tavernarakis, N. (2019). The Cytoskeleton as a Modulator of Aging and Neurodegeneration. *Adv. Exp. Med. Biol.* 1178, 227–245. doi:10.1007/978-3-030-25650-0_12

Kumar, R., Tiwari, A. K., Tripathi, D., Main, R. P., Kumar, N., Sihota, P., et al. (2021). Anatomical Variations in Cortical Bone Surface Permeability: Tibia Versus Femur. *J. Mech. Behav. Biomed. Mater.* 113, 104122. doi:10.1016/j.jmbbm.2020.104122

Lacey, D. C., Simmons, P. J., Graves, S. E., and Hamilton, J. A. (2009). Proinflammatory Cytokines Inhibit Osteogenic Differentiation from Stem Cells: Implications for Bone Repair during Inflammation. *Osteoarthritis and Cartilage* 17 (6), 735–742. doi:10.1016/j.joca.2008.11.011

Larcher, I., and Scheiner, S. (2021). Parameter Reduction, Sensitivity Studies, and Correlation Analyses Applied to a Mechanobiologically Regulated Bone Cell Population Model of the Bone Metabolism. *Comput. Biol. Med.* 136, 104717. doi:10.1016/j.compbiomed.2021.104717

Lavaill, M., Trichilo, S., Scheiner, S., Forwood, M. R., Cooper, D. M. L., and Pivonka, P. (2020). Study of the Combined Effects of PTH Treatment and Mechanical Loading in Postmenopausal Osteoporosis Using a New Mechanistic PK-PD Model. *Biomech. Model. Mechanobiol* 19 (5), 1765–1780. doi:10.1007/s10237-020-01307-6

Lei, X., Liu, Q., Li, S., Zhang, Z., and Yang, X. (2021). Effects of Fluid Shear Stress on Expression of Focal Adhesion Kinase in MG-63 Human Osteoblast-like Cells on Different Surface Modification of Titanium. *Bioengineered* 12 (1), 4962–4971. doi:10.1080/21655979.2021.1962686

Li, P., Ma, Y. C., Shen, H. L., Han, H., Wang, J., Cheng, H. J., et al. (2012). Cytoskeletal Reorganization Mediates Fluid Shear Stress-Induced ERK5 Activation in Osteoblastic Cells. *Cell. Biol. Int.* 36 (3), 229–236. doi:10.1042/CBI20110113

Li, X., Han, L., Nookaew, I., Mannen, E., Silva, M. J., Almeida, M., et al. (2019). Stimulation of Piezo1 by Mechanical Signals Promotes Bone Anabolism. *Elife* 8, e49631. doi:10.7554/eLife.49631

Li, W., Zhao, J., Sun, W., Wang, H., Pan, Y., Wang, L., et al. (2020a). Osteocytes Promote Osteoclastogenesis via Autophagy-Mediated RANKL Secretion under Mechanical Compressive Force. *Arch. Biochem. Biophys.* 694, 108594. doi:10.1016/j.abb.2020.108594

Li, Z., Zheng, J., Wan, D., and Yang, X. (2020b). Uniaxial Static Strain Promotes Osteoblast Proliferation and Bone Matrix Formation in Distraction Osteogenesis *In Vitro*. *Biomed. Res. Int.* 2020, 3906426. doi:10.1155/2020/3906426

Li, Y., Ling, J., and Jiang, Q. (2021). Inflammasomes in Alveolar Bone Loss. *Front. Immunol.* 12, 691013. doi:10.3389/fimmu.2021.691013

Luo, H., Wu, H., Tan, X., Ye, Y., Huang, L., Dai, H., et al. (2021). Osteopenic Effects of High-Fat Diet-Induced Obesity on Mechanically Induced Alveolar Bone Remodeling. *Oral Dis.* 27 (5), 1243–1256. doi:10.1111/odi.13651

Malone, A. M. D., Anderson, C. T., Tummala, P., Kwon, R. Y., Johnston, T. R., Stearns, T., et al. (2007). Primary Cilia Mediate Mechanosensing in Bone Cells by a Calcium-Independent Mechanism. *Proc. Natl. Acad. Sci.* 104 (33), 13325–13330. doi:10.1073/pnas.0700636104

Manolagas, S. C. (2010). From Estrogen-Centric to Aging and Oxidative Stress: a Revised Perspective of the Pathogenesis of Osteoporosis. *Endocr. Rev.* 31 (3), 266–300. doi:10.1210/er.2009-0024

Michael, M., and Parsons, M. (2020). New Perspectives on Integrin-Dependent Adhesions. *Curr. Opin. Cel Biol.* 63, 31–37. doi:10.1016/j.ceb.2019.12.008

Miwa, M., Kozawa, O., Tokuda, H., Kawakubo, A., Yoneda, M., Oiso, Y., et al. (1991). Effects of Hypergravity on Proliferation and Differentiation of Osteoblast-Like Cells. *Bone Mineral.* 14 (1), 15–25. doi:10.1016/0169-6009(91)90099-l

Nakajima, T. (1991). Effects of Hypergravity on Migration, Proliferation and Function of Mouse Osteoblastic Cell Line MC3T3-E1. *J. Stomatol.Soc.,Jpn.* 58 (2), 529–544. doi:10.5357/koubyou.58.529

Nomura, S., and Takano-Yamamoto, T. (2000). Molecular Events Caused by Mechanical Stress in Bone. *Matrix Biol.* 19 (2), 91–96. doi:10.1016/s0945-053x(00)00050-0

Norwitz, N. G., Mota, A. S., Misra, M., and Ackerman, K. E. (2019). LRP5, Bone Density, and Mechanical Stress: A Case Report and Literature Review. *Front. Endocrinol.* 10, 184. doi:10.3389/fendo.2019.00184

Owen, R., and Reilly, G. C. (2018). *In Vitro* Models of Bone Remodelling and Associated Disorders. *Front. Bioeng. Biotechnol.* 6, 134. doi:10.3389/fbioe.2018.00134

Ozawa, H., Imamura, K., Abe, E., Takahashi, N., Hiraide, T., Shibasaki, Y., et al. (1990). Effect of a Continuously Applied Compressive Pressure on Mouse Osteoblast-Like Cells (MC3T3-E1) *In Vitro*. *J. Cel. Physiol.* 142 (1), 177–185. doi:10.1002/jcp.1041420122

Parandakh, A., Tafazzoli-Shadpour, M., and Khani, M.-M. (2017). Stepwise Morphological Changes and Cytoskeletal Reorganization of Human Mesenchymal Stem Cells Treated by Short-Time Cyclic Uniaxial Stretch. In Vitro *Cell.Dev.Biol.-Animal* 53 (6), 547–553. doi:10.1007/s11626-017-0131-8

Pastrama, M.-I., Scheiner, S., Pivonka, P., and Hellmich, C. (2018). A Mathematical Multiscale Model of Bone Remodeling, Accounting for Pore Space-Specific Mechanosensation. *Bone* 107, 208–221. doi:10.1016/j.bone.2017.11.009

Pavalko, F. M., Gerard, R. L., Ponik, S. M., Gallagher, P. J., Jin, Y., and Norvell, S. M. (2003). Fluid Shear Stress Inhibits TNF-α-Induced Apoptosis in Osteoblasts: A Role for Fluid Shear Stress-Induced Activation of PI3-Kinase and Inhibition of Caspase-3. *J. Cel. Physiol.* 194 (2), 194–205. doi:10.1002/jcp.10221

Plotkin, L. I., Mathov, I., Aguirre, J. I., Parfitt, A. M., Manolagas, S. C., and Bellido, T. (2005). Mechanical Stimulation Prevents Osteocyte Apoptosis: Requirement of Integrins, Src Kinases, and ERKs. *Am. J. Physiology-Cell Physiol.* 289 (3), C633–C643. doi:10.1152/ajpcell.00278.2004

Price, C., Zhou, X., Li, W., and Wang, L. (2011). Real-time Measurement of Solute Transport within the Lacunar-Canalicular System of Mechanically Loaded Bone: Direct Evidence for Load-Induced Fluid Flow. *J. Bone Miner Res.* 26 (2), 277–285. doi:10.1002/jbmr.211

Prideaux, M., Findlay, D. M., and Atkins, G. J. (2016). Osteocytes: The Master Cells in Bone Remodelling. *Curr. Opin. Pharmacol.* 28, 24–30. doi:10.1016/j.coph.2016.02.003

Qin, W., Liu, L., Wang, Y., Wang, Z., Yang, A., and Wang, T. (2019). Mir-494 Inhibits Osteoblast Differentiation by Regulating BMP Signaling in Simulated Microgravity. *Endocrine* 65 (2), 426–439. doi:10.1007/s12020-019-01952-7

Qin, L., Liu, W., Cao, H., and Xiao, G. (2020). Molecular Mechanosensors in Osteocytes. *Bone Res.* 8, 23. doi:10.1038/s41413-020-0099-y

Ragnarsson, K. T. (2015). Bone Loss and Fractures in Limbs Paralyzed by Spinal Cord Injury: Prevention, Diagnosis, and Treatment. *J. Spinal Cord Med.* 38 (1), 10–12. doi:10.1179/2045772314Y.0000000200

Ridley, A. J., and Hall, A. (1992). The Small GTP-Binding Protein Rho Regulates the Assembly of Focal Adhesions and Actin Stress Fibers in Response to Growth Factors. *Cell* 70 (3), 389–399. doi:10.1016/0092-8674(92)90163-7

Robling, A. G., and Turner, C. H. (2009). Mechanical Signaling for Bone Modeling and Remodeling. *Crit. Rev. Eukar Gene Expr.* 19 (4), 319–338. doi:10.1615/critreveukargeneexpr.v19.i4.50

Rucci, N., Rufo, A., Alamanou, M., and Teti, A. (2007). Modeled Microgravity Stimulates Osteoclastogenesis and Bone Resorption by Increasing Osteoblast RANKL/OPG Ratio. *J. Cel. Biochem.* 100 (2), 464–473. doi:10.1002/jcb.21059

Rutkovskiy, A., Stensløkken, K.-O., and Vaage, I. J. (2016). Osteoblast Differentiation at a Glance. *Med. Sci. Monit. Basic Res.* 22, 95–106. doi:10.12659/msmbr.901142

Sandbo, N., Smolyaninova, L. V., Orlov, S. N., and Dulin, N. O. (2016). Control of Myofibroblast Differentiation and Function by Cytoskeletal Signaling. *Biochem. Mosc.* 81 (13), 1698–1708. doi:10.1134/S0006297916130071

Sawakami, K., Robling, A. G., Ai, M., Pitner, N. D., Liu, D., Warden, S. J., et al. (2006). The Wnt Co-Receptor LRP5 Is Essential for Skeletal Mechanotransduction but Not for the Anabolic Bone Response to Parathyroid Hormone Treatment. *J. Biol. Chem.* 281 (33), 23698–23711. doi:10.1074/jbc.M601000200

Saxena, R., Pan, G., Dohm, E. D., and McDonald, J. M. (2011). Modeled Microgravity and Hindlimb Unloading Sensitize Osteoclast Precursors to RANKL-Mediated Osteoclastogenesis. *J. Bone Miner Metab.* 29 (1), 111–122. doi:10.1007/s00774-010-0201-4

Scheiner, S., Pivonka, P., Smith, D. W., Dunstan, C. R., and Hellmich, C. (2014). Mathematical Modeling of Postmenopausal Osteoporosis and its Treatment by the Anti-Catabolic Drug Denosumab. *Int. J. Numer. Meth. Biomed. Engng.* 30 (1), 1–27. doi:10.1002/cnm.2584

Scheiner, S., Pivonka, P., and Hellmich, C. (2016). Poromicromechanics Reveals that Physiological Bone Strains Induce Osteocyte-Stimulating Lacunar Pressure. *Biomech. Model. Mechanobiol* 15 (1), 9–28. doi:10.1007/s10237-015-0704-y

Selig, M., Lauer, J. C., Hart, M. L., and Rolauffs, B. (2020). Mechanotransduction and Stiffness-Sensing: Mechanisms and Opportunities to Control Multiple Molecular Aspects of Cell Phenotype as a Design Cornerstone of Cell-Instructive Biomaterials for Articular Cartilage Repair. *Int. J. Mol. Sci.* 21 (15), 5399. doi:10.3390/ijms21155399

Selvakumarasamy, K., Poornachandra, S., and Amutha, R. (2019). K - Shrinkage Function for ECG Signal Denoising. *J. Med. Syst.* 43 (8), 248. doi:10.1007/s10916-019-1375-5

Shen, X.-Q., Geng, Y.-M., Liu, P., Huang, X.-Y., Li, S.-Y., Liu, C.-D., et al. (2017). Magnitude-Dependent Response of Osteoblasts Regulated by Compressive Stress. *Sci. Rep.* 7, 44925. doi:10.1038/srep44925

Shi, W., Zhang, Y., Chen, K., He, J., Feng, X., Wei, W., et al. (2020). Primary Cilia Act as Microgravity Sensors by Depolymerizing Microtubules to Inhibit Osteoblastic Differentiation and Mineralization. *Bone* 136, 115346. doi:10.1016/j.bone.2020.115346

Shuai, C., Yang, W., Peng, S., Gao, C., Guo, W., Lai, Y., et al. (2018). Physical Stimulations and Their Osteogenesis-Inducing Mechanisms. *Int. J. Bioprint* 4 (2), 138. doi:10.18063/IJB.v4i2.138

Siddiqui, J. A., and Partridge, N. C. (2016). Physiological Bone Remodeling: Systemic Regulation and Growth Factor Involvement. *Physiology* 31 (3), 233–245. doi:10.1152/physiol.00061.2014

Somemura, S., Kumai, T., Yatabe, K., Sasaki, C., Fujiya, H., Niki, H., et al. (2021). Physiologic Mechanical Stress Directly Induces Bone Formation by Activating Glucose Transporter 1 (Glut 1) in Osteoblasts, Inducing Signaling via NAD+-Dependent Deacetylase (Sirtuin 1) and Runt-Related Transcription Factor 2 (Runx2). *Int. J. Mol. Sci.* 22 (16), 9070. doi:10.3390/ijms22169070

Sonam, S., Sathe, S. R., Yim, E. K. F., Sheetz, M. P., and Lim, C. T. (2016). Cell Contractility Arising from Topography and Shear Flow Determines Human Mesenchymal Stem Cell Fate. *Sci. Rep.* 6, 20415. doi:10.1038/srep20415

Song, J., Liu, L., Lv, L., Hu, S., Tariq, A., Wang, W., et al. (2020). Fluid Shear Stress Induces Runx-2 Expression via Upregulation of PIEZO1 in MC3T3-E1 Cells. *Cell Biol Int* 44 (7), 1491–1502. doi:10.1002/cbin.11344

Stein, T. P. (2013). Weight, Muscle and Bone Loss during Space Flight: Another Perspective. *Eur. J. Appl. Physiol.* 113 (9), 2171–2181. doi:10.1007/s00421-012-2548-9

Steinbuck, M. P., and Winandy, S. (2018). A Review of Notch Processing with New Insights into Ligand-independent Notch Signaling in T-Cells. *Front. Immunol.* 9, 1230. doi:10.3389/fimmu.2018.01230

Steller, J., Alberts, J., and Ronca, A. (2018). Oxidative Stress as Cause, Consequence, or Biomarker of Altered Female Reproduction and Development in the Space Environment. *Int. J. Mol. Sci.* 19 (12), 3729. doi:10.3390/ijms19123729

Steward, A. J., and Kelly, D. J. (2015). Mechanical Regulation of Mesenchymal Stem Cell Differentiation. *J. Anat.* 227 (6), 717–731. doi:10.1111/joa.12243

Sugisawa, E., Takayama, Y., Takemura, N., Kondo, T., Hatakeyama, S., Kumagai, Y., et al. (2020). RNA Sensing by Gut Piezo1 Is Essential for Systemic Serotonin Synthesis. *Cell* 182 (3), 609–624. e621. doi:10.1016/j.cell.2020.06.022

Suniaga, S., Rolvien, T., Vom Scheidt, A., Fiedler, I. A. K., Bale, H. A., Huysseune, A., et al. (2018). Increased Mechanical Loading through Controlled Swimming Exercise Induces Bone Formation and Mineralization in Adult Zebrafish. *Sci. Rep.* 8 (1), 3646. doi:10.1038/s41598-018-21776-1

Tanaka, S. M., Sun, H. B., Roeder, R. K., Burr, D. B., Turner, C. H., and Yokota, H. (2005). Osteoblast Responses One Hour after Load-Induced Fluid Flow in a Three-Dimensional Porous Matrix. *Calcif Tissue Int.* 76 (4), 261–271. doi:10.1007/s00223-004-0238-2

Tapial Martínez, P., López Navajas, P., and Lietha, D. (2020). FAK Structure and Regulation by Membrane Interactions and Force in Focal Adhesions. *Biomolecules* 10 (2), 179. doi:10.3390/biom10020179

Thomas, S., and Jaganathan, B. G. (2021). Signaling Network Regulating Osteogenesis in Mesenchymal Stem Cells. *J. Cel Commun. Signal.* 16, 47–61. doi:10.1007/s12079-021-00635-1

Tripuwabhrut, P., Mustafa, M., Gjerde, C. G., Brudvik, P., and Mustafa, K. (2013). Effect of Compressive Force on Human Osteoblast-Like Cells and Bone Remodelling: an *In Vitro* Study. *Arch. Oral Biol.* 58 (7), 826–836. doi:10.1016/j.archoralbio.2013.01.004

Uda, Y., Azab, E., Sun, N., Shi, C., and Pajevic, P. D. (2017). Osteocyte Mechanobiology. *Curr. Osteoporos. Rep.* 15 (4), 318–325. doi:10.1007/s11914-017-0373-0

Uzbekov, R. E., Maurel, D. B., Aveline, P. C., Pallu, S., Benhamou, C. L., and Rochefort, G. Y. (2012). Centrosome Fine Ultrastructure of the Osteocyte Mechanosensitive Primary Cilium. *Microsc. Microanal* 18 (6), 1430–1441. doi:10.1017/S1431927612013281

Vogel, V., and Sheetz, M. (2006). Local Force and Geometry Sensing Regulate Cell Functions. *Nat. Rev. Mol. Cel Biol* 7 (4), 265–275. doi:10.1038/nrm1890

Wagh, K., Ishikawa, M., Garcia, D. A., Stavreva, D. A., Upadhyaya, A., and Hager, G. L. (2021). Mechanical Regulation of Transcription: Recent Advances. *Trends Cel Biol.* 31 (6), 457–472. doi:10.1016/j.tcb.2021.02.008

Wang, Q.-S., Zhang, X.-C., Li, R.-X., Sun, J.-G., Su, W.-H., Guo, Y., et al. (2015). A Comparative Study of Mechanical Strain, Icariin and Combination Stimulations on Improving Osteoinductive Potential via NF-kappaB Activation in Osteoblast-Like Cells. *Biomed. Eng. Online* 14, 46. doi:10.1186/s12938-015-0039-z

Wang, Y., Wang, K., Hu, Z., Zhou, H., Zhang, L., Wang, H., et al. (2018). MicroRNA-139-3p Regulates Osteoblast Differentiation and Apoptosis by Targeting ELK1 and Interacting with Long Noncoding RNA ODSM. *Cel Death Dis* 9 (11), 1107. doi:10.1038/s41419-018-1153-1

Wang, L., Wang, X., Ji, N., Li, H. M., and Cai, S. X. (2020a). Mechanisms of the Mechanically Activated Ion Channel Piezo1 Protein in Mediating Osteogenic Differentiation of Periodontal Ligament Stem Cells via the Notch Signaling Pathway. *Hua Xi Kou Qiang Yi Xue Za Zhi* 38 (6), 628–636. doi:10.7518/hxkq.2020.06.004

Wang, L., You, X., Lotinun, S., Zhang, L., Wu, N., and Zou, W. (2020b). Mechanical Sensing Protein PIEZO1 Regulates Bone Homeostasis via Osteoblast-Osteoclast Crosstalk. *Nat. Commun.* 11 (1), 282. doi:10.1038/s41467-019-14146-6

Wang, Y., Wang, K., Zhang, L., Tan, Y., Hu, Z., Dang, L., et al. (2020c). Targeted Overexpression of the Long Noncoding RNA ODSM Can Regulate Osteoblast Function *In Vitro* and *In Vivo*. *Cel Death Dis* 11 (2), 133. doi:10.1038/s41419-020-2325-3

Wang, F.-S., Wu, R.-W., Chen, Y.-S., Ko, J.-Y., Jahr, H., and Lian, W.-S. (2021a). Biophysical Modulation of the Mitochondrial Metabolism and Redox in Bone Homeostasis and Osteoporosis: How Biophysics Converts into Bioenergetics. *Antioxidants* 10 (9), 1394. doi:10.3390/antiox10091394

Wang, H., Dong, J., Li, G., Tan, Y., Zhao, H., Zhang, L., et al. (2021b). The Small Protein MafG Plays a Critical Role in MC3T3-E1 Cell Apoptosis Induced by Simulated Microgravity and Radiation. *Biochem. Biophysical Res. Commun.* 555, 175–181. doi:10.1016/j.bbrc.2021.03.133

Wang, J., Li, J., Liu, J., Lin, M., Mao, S., Wang, Y., et al. (2021c). Adsorption Force of Fibronectin: A Balance Regulator to Transmission of Cell Traction Force and Fluid Shear Stress. *Biomacromolecules* 22 (8), 3264–3273. doi:10.1021/acs.biomac.1c00375

Wang, X., Geng, B., Wang, H., Wang, S., Zhao, D., He, J., et al. (2021d). Fluid Shear Stress-Induced Down-Regulation of microRNA-140-5p Promotes Osteoblast Proliferation by Targeting VEGFA via the ERK5 Pathway. *Connect. Tissue Res.*, 1–13. doi:10.1080/03008207.2021.1891228

Wang, X., He, J., Wang, H., Zhao, D., Geng, B., Wang, S., et al. (2021e). Fluid Shear Stress Regulates Osteoblast Proliferation and Apoptosis via the lncRNA TUG1/

miR-34a/FGFR1 Axis. *J. Cel Mol Med* 25 (18), 8734–8747. doi:10.1111/jcmm.16829

Wei, Q., Holle, A., Li, J., Posa, F., Biagioni, F., Croci, O., et al. (2020). BMP-2 Signaling and Mechanotransduction Synergize to Drive Osteogenic Differentiation via YAP/TAZ. *Adv. Sci.* 7 (15), 1902931. doi:10.1002/advs.201902931

Whitfield, J. F. (2003). Primary Cilium?is it an Osteocyte's Strain-Sensing Flowmeter? *J. Cel. Biochem.* 89 (2), 233–237. doi:10.1002/jcb.10509

Wittkowske, C., Reilly, G. C., Lacroix, D., and Perrault, C. M. (2016). *In Vitro* Bone Cell Models: Impact of Fluid Shear Stress on Bone Formation. *Front. Bioeng. Biotechnol.* 4, 87. doi:10.3389/fbioe.2016.00087

Woo, S.-H., Ranade, S., Weyer, A. D., Dubin, A. E., Baba, Y., Qiu, Z., et al. (2014). Piezo2 Is Required for Merkel-Cell Mechanotransduction. *Nature* 509 (7502), 622–626. doi:10.1038/nature13251

Woodcock, E. M., Girvan, P., Eckert, J., Lopez-Duarte, I., Kubánková, M., van Loon, J. J. W. A., et al. (2019). Measuring Intracellular Viscosity in Conditions of Hypergravity. *Biophysical J.* 116 (10), 1984–1993. doi:10.1016/j.bpj.2019.03.038

Xiang, L.-X., Ran, Q., Chen, L., Xiang, Y., Li, F.-J., Zhang, X.-M., et al. (2020). CR6-interacting Factor-1 Contributes to Osteoclastogenesis by Inducing Receptor Activator of Nuclear Factor κB Ligand after Radiation. *World J Stem Cells* 12 (3), 222–240. doi:10.4252/wjsc.v12.i3.222

Xiao, Z., Zhang, S., Mahlios, J., Zhou, G., Magenheimer, B. S., Guo, D., et al. (2006). Cilia-Like Structures and Polycystin-1 in Osteoblasts/Osteocytes and Associated Abnormalities in Skeletogenesis and Runx2 Expression. *J. Biol. Chem.* 281 (41), 30884–30895. doi:10.1074/jbc.M604772200

Xing, Y., He, Z., Warnock, J. N., Hilbert, S. L., and Yoganathan, A. P. (2004). Effects of Constant Static Pressure on the Biological Properties of Porcine Aortic Valve Leaflets. *Ann. Biomed. Eng.* 32 (4), 555–562. doi:10.1023/b:abme.0000019175.12013.8f

Yanagisawa, M., Suzuki, N., Mitsui, N., Koyama, Y., Otsuka, K., and Shimizu, N. (2008). Compressive Force Stimulates the Expression of Osteogenesis-Related Transcription Factors in ROS 17/2.8 Cells. *Arch. Oral Biol.* 53 (3), 214–219. doi:10.1016/j.archoralbio.2007.08.012

Yang, J., Li, J., Cui, X., Li, W., Xue, Y., Shang, P., et al. (2020). Blocking Glucocorticoid Signaling in Osteoblasts and Osteocytes Prevents Mechanical Unloading-Induced Cortical Bone Loss. *Bone* 130, 115108. doi:10.1016/j.bone.2019.115108

Yuan, X., Serra, R. A., and Yang, S. (2015). Function and Regulation of Primary Cilia and Intraflagellar Transport Proteins in the Skeleton. *Ann. N.Y. Acad. Sci.* 1335, 78–99. doi:10.1111/nyas.12463

Yuan, J., Dong, X., Yap, J., and Hu, J. (2020). The MAPK and AMPK Signalings: Interplay and Implication in Targeted Cancer Therapy. *J. Hematol. Oncol.* 13 (1), 113. doi:10.1186/s13045-020-00949-4

Zanotti, S., Smerdel-Ramoya, A., and Canalis, E. (2011). HES1 (Hairy and Enhancer of Split 1) Is a Determinant of Bone Mass. *J. Biol. Chem.* 286 (4), 2648–2657. doi:10.1074/jbc.M110.183038

Zhang, B., An, L., Geng, B., Ding, N., Coalson, E., Wan, L., et al. (2021). ERK5 Negatively Regulates Kruppel-Like Factor 4 and Promotes Osteogenic Lineage Cell Proliferation in Response to MEK5 Overexpression or Fluid Shear Stress. *Connect. Tissue Res.* 62 (2), 194–205. doi:10.1080/03008207.2019.1670650

Zhao, X.-H., Laschinger, C., Arora, P., Sza´szi, K., Kapus, A., and McCulloch, C. A. (2007). Force Activates Smooth Muscle α-Actin Promoter Activity through the Rho Signaling Pathway. *J. Cel Sci* 120 (Pt 10), 1801–1809. doi:10.1242/jcs.001586

Zhou, S., Zu, Y., Sun, Z., Zhuang, F., and Yang, C. (2015). Effects of Hypergravity on Osteopontin Expression in Osteoblasts. *PLoS One* 10 (6), e0128846. doi:10.1371/journal.pone.0128846

Zhou, S., Yang, X., Hu, J., Mo, C., Cao, Y., and Yang, C. (2018). Continuous Hypergravity Alters the Cytoplasmic Elasticity of MC3T3-E1 Osteoblasts via Actin Filaments. *J. Biomech.* 72, 222–227. doi:10.1016/j.jbiomech.2018.02.024

Zhou, T., Gao, B., Fan, Y., Liu, Y., Feng, S., Cong, Q., et al. (2020). Piezo1/2 Mediate Mechanotransduction Essential for Bone Formation through Concerted Activation of NFAT-YAP1-Ss-Catenin. *Elife* 9, e52779. doi:10.7554/eLife.52779

Ziouti, F., Ebert, R., Rummler, M., Krug, M., Müller-Deubert, S., Lüdemann, M., et al. (2019). NOTCH Signaling Is Activated through Mechanical Strain in Human Bone Marrow-Derived Mesenchymal Stromal Cells. *Stem Cell Int.* 2019, 5150634. doi:10.1155/2019/5150634

Zou, M.-L., Chen, Z.-H., Teng, Y.-Y., Liu, S.-Y., Jia, Y., Zhang, K.-W., et al. (2021). The Smad Dependent TGF-β and BMP Signaling Pathway in Bone Remodeling and Therapies. *Front. Mol. Biosci.* 8, 593310. doi:10.3389/fmolb.2021.593310

Conflict of Interest: The authors declare that the research was conducted in the absence of any commercial or financial relationships that could be construed as a potential conflict of interest.

frontiers in Bioengineering and Biotechnology

ORIGINAL RESEARCH
published: 24 February 2022
doi: 10.3389/fbioe.2022.833887

Conductive Adhesive and Antibacterial Zwitterionic Hydrogel Dressing for Therapy of Full-Thickness Skin Wounds

Feng Wang[1†], Shuguang Wang[2†], Liping Nan[3†], Jiawei Lu[1], Ziqi Zhu[1], Jintao Yang[4], Dong Zhang[5], Junjian Liu[3], Xiao Zhao[6]* and Desheng Wu[1]**

[1]Department of Spine Surgery, Shanghai East Hospital, School of Medicine, Tongji University, Shanghai, China, [2]Department of Orthopedic, Shanghai East Hospital, School of Medicine, Tongji University, Shanghai, China, [3]Department of Orthopedic, Shanghai Tenth People's Hospital, School of Medicine, Tongji University, Shanghai, China, [4]College of Materials Science and Engineering, Zhejiang University of Technology, Hangzhou, China, [5]Department of Chemical, Biomolecular, and Corrosion Engineering, College of Engineering and Polymer Science, The University of Akron, Akron, OH, United States, [6]Department of Anesthesiology, Shanghai General Hospital Affiliated to Shanghai Jiaotong University, Shanghai, China

Edited by:
Xuqing Liu,
The University of Manchester,
United Kingdom

Reviewed by:
Paula Coutinho,
Instituto Politécnico da Guarda,
Portugal
Amirhosein Kefayat,
Isfahan University of Medical
Sciences, Iran
Jiajia Xue,
Beijing University of Chemical
Technology, China

***Correspondence:**
Junjian Liu
liujunjian1968@126.com
Xiao Zhao
zhaoxiaoshiyimazui@163.com
Desheng Wu
eastspinesci@163.com

†These authors have contributed equally to this work

Specialty section:
This article was submitted to
Biomaterials,
a section of the journal
Frontiers in Bioengineering and
Biotechnology

Received: 12 December 2021
Accepted: 31 January 2022
Published: 24 February 2022

Citation:
Wang F, Wang S, Nan L, Lu J, Zhu Z, Yang J, Zhang D, Liu J, Zhao X and Wu D (2022) Conductive Adhesive and Antibacterial Zwitterionic Hydrogel Dressing for Therapy of Full-Thickness Skin Wounds.
Front. Bioeng. Biotechnol. 10:833887.
doi: 10.3389/fbioe.2022.833887

Any sort of wound injury leads to the destruction of skin integrity and wound formation, causing millions of deaths every year and accounting for 10% of death rate insight into various diseases. The ideal biological wound dressings are expected to possess extraordinary mechanical characterization, cytocompatibility, adhesive properties, antibacterial properties, and conductivity of endogenous electric current to enhance the wound healing process. Recent studies have demonstrated that biomedical hydrogels can be used as typical wound dressings to accelerate the whole healing process due to them having a similar composition structure to skin, but they are also limited by ideal biocompatibility and stable mechanical properties. To extend the number of practical candidates in the field of wound healing, we designed a new structural zwitterion poly[3-(dimethyl(4-vinylbenzyl) ammonium) propyl sulfonate] (SVBA) into a poly-acrylamide network, with remarkable mechanical properties, stable rheological property, effective antibacterial properties, strong adsorption, high penetrability, and good electroactive properties. Both *in vivo* and *in vitro* evidence indicates biocompatibility, and strong healing efficiency, indicating that poly (AAm-*co*-SVBA) (PAS) hydrogels as new wound healing candidates with biomedical applications.

Keywords: conductive hydrogel, adhesive hydrogel, antibacterial hydrogel, wound dressing, wound healing

INTRODUCTION

Although the skin is the softest, most flexible outer tissue covering the body of a vertebrate animal, the inevitable skin trauma caused by burns, contusions, or bruises is a significant yet intractable healthcare issue around the world (Hernández Martínez et al., 2019). A wound visible with the naked eye easily tends to turn into a perfect breeding ground for pathogenic bacteria (*S. aureus*, *E. coli*) and fungus, which further impairs vital functions that the skin performs and causes pain, weak immune responses, disability, or even death. More importantly, the presence of a number of complex driven factors such as 1) the increasing prevalence of chronic conditions resulting in acute, chronic, surgical, and traumatic wounds, 2) the growing costs on chronic wounds, and 3) climbing use of regenerative medicine in wound disposal, leading to the global wound care market projected to reach over USD 27 billion by 2026 from USD 19.3 billion in 2021. Based on this status, the high growth potential of emerging economies and rapidly increasing wound treatment requirements have also opened a myriad of opportunities for exploiting more fundamental wound healing mechanisms and novel materials.

From the perspective of epidermal healing mechanisms, practical healing efficiency tends to be distinctly promoted in wounds subjected to a moist environment under an occlusive dressing film as compared to uncovered wounds. The sustaining moist environment will decrease the inflammatory and proliferative cells, resulting in faster healing of wound defects. To date, the widely accepted characteristics for ideal biological wound dressings can be summarized as 1) a certain adsorption capacity for removing excess exudates and toxins, 2) good air permeability to allow gaseous exchange and thermal insulation, and 3) adjusted adhesion to promote the wound/dressing interface binding force and to be removed easily without trauma to the wound (Zhu et al., 2016; Ni et al., 2021; Wang et al., 2021; Yuan J et al., 2021). Recent progress has demonstrated that biomedical hydrogels can be used as typical wound dressings to accelerate the whole healing process due to the similarities, in terms of composition structure (soft matrix with high water contents), to human tissues. In addition, hydrogels are hydrophilic, fully crosslinked polymeric materials that have enabled us to dynamically alter adhesion ability, leading to stable adhesion to the active epidermis. For instance, most as-prepared soft natural (gelatin, hyaluronic acid, and agar) or synthetic (polyAAm, polyHEAA, and polyNIPAm) hydrogels possess strong adhesion on common biomedical substrates (e.g., steel, titanium, glass, and ceramic), while the bonding energy is dramatically reduced once the excess exudates and toxins are absorbed (Zhang et al., 2020a; Zhang et al., 2020b; Zhang et al., 2020c; Mao et al., 2020; Zhang et al., 2021).

Skin is electro-sensitive tissue in our body (Kim et al., 2013). Some researchers have been exploring electrical stimulation and its effect on wound healing (Li M et al., 2019; Chen et al., 2021; Yuan J et al., 2021; Zheng et al., 2021). In addition, it has been confirmed that endogenous electric stimulus has a positive impact on wound healing (Qu et al., 2019). This electrical stimulation can mainly promote the proliferation of fibroblasts, the synthesis of ECM, and the secretion of growth factors and revascularization (Goding et al., 2017) by the activation of transmembrane channels and enhancement of intracellular Ca2+concentration (Li et al., 2019c; Naskar et al., 2020). Therefore, electrical stimulation has the potential to treat full-thickness skin wounds with simplicity due to its relatively easy application.

Although natural polysaccharide- and protein-based hydrogels are biodegradable, the undesirable weak mechanical properties, especially and surprisingly, brittleness, still limit further practical applications. How to balance ideal biocompatibility and stable mechanical properties is still being explored by researchers in biophysical, material, or biomedical science. Some synthetic acrylamide polymers can address the challenge of matrix-strength, but non-specific protein adhesion and, subsequently, potential organ rejection make it difficult to peel the hydrogels from wounds in escharosis regions after healing. With the development of zwitterionic hydrogels, e.g., polyCBMA, polySBMA, and poly(trimethylamine N-oxide) (polyTMAO) (Huang et al., 2021), the macrophase cells upon non-fouling polyzwitterionic matrix tend to differentiate the pro-healing states. Thus, it is also possible to achieve a good combination of the above-mentioned properties to achieve ideal wound healing by using synthetic hydrogels.

In this work, we ingeniously introduce a new structural salt-responsive zwitterion poly[3-(dimethyl(4-vinylbenzyl) ammonium) propyl sulfonate] (SVBA) into the polyAAm network to extend the practical candidates for the field of wound healing. The nature of polySVBA chains previously already presented unique salt-responsive properties and was applied to bacterial release (Zhang et al., 2018; Wu et al., 2019), selective oil/water separation (Wang et al., 2020), and thermal-induced soft actuators (He et al., 2019), etc. Interestingly, rigid aromatic backbone and sequential ionic interactions synergistically promote surface bonding, potential conductivity, matrix stretchability, and self-healing properties. On the one hand, compared to commercial Tegaderm (3M), more wettability groups (hydroxy, sulfonate, and amide) from copolymerized poly (AAm-*co*-SVBA) assist in trapping more moisture and maintaining long-term hydration micro-environments. On the other hand, this structural adhesive design can make the zwitterionic hydrogel matrix fit the organ wounds smoothly and perfectly, leading to the overall adsorption of excess exudates and toxins during dynamic healing processes. In addition, the challenge of inevitable protein adhesion (e.g., cells and pathogenic bacteria) will finally lead to the failure of healing, as the formed scab grows against the surface of the hydrogel and the healed area tends to tear as the hydrogel is removed. However, polyzwitterionic hydrogels are widely reported to be antifouling materials (Yuan H et al., 2021) that promote protein repellent, and thus a higher healing efficacy can be achieved. Both *in vivo* and *in vitro* evidence monitors the cytotoxicity, biocompatibility, and healing efficiency of the resultant polyzwitterions with refined structures, indicating that poly (AAm-*co*-SVBA) (PAS) hydrogels have become new wound healing candidates for biomedical applications.

EXPERIMENTAL SECTION

Materials

Acrylamide (AAm, 99.0%) and N,N′-Methylenebisacrylamide (MBAA, 97%) were purchased from Aladdin reagent Inc. (Shanghai), The detailed synthesis route of dimethyl-(4-vinylphenyl) ammonium propane sulfonate (SVBA) can be found in our previous report (He et al., 2019; Yuan H et al., 2021). In this experiment, all purified water was obtained from a Millipore system with an electronic conductance of 18.2 MΩ cm.

Preparation of Hydrogel

To obtain the functional polyzwitterionic hydrogel, a predetermined amount of cross-linking agent (MBAA, 1.0 mg ml^{-1}), monomer (0.168 g/ml), and 2-hydroxy-4′-(2-

hydroxyethoxy)-2-methylpropiophenone (I2959, photoinitiator, 10 mg ml^{-1}) were prepped. The solution was purged with nitrogen gas for 10 min to completely remove the oxygen gas, after that, the solution was slowly injected into a prepared mold by separating two glass slides with a 1.0 mm Teflon spacer. The dimension of the mold was 50 × 50 × 1 mm^3 (length × width × depth). After the system was irradiated by a 365 nm UV light for 1 h, the resultant hydrogel was released from the mold and immersed in pure water to remove unreacted monomers and free polymers. The cylinder hydrogel was prepared by using an injection syringe (1 ml) as the mold for the mechanical test.

Characterization

A series of samples with different ratios of AAm and SVBA were prepared using the same method (PAS-1, AAm: SVBA = 1:1; PAS-2, AAm: SVBA = 2:1). The hydrogel samples were lyophilized under vacuum for 48 h to remove water for morphology measurements. Prior to imaging, the lyophilized hydrogels were brittle-fractured in liquid nitrogen, then, the hydrogels were coated with Au and observed by scanning electron microscope (SEM, HITACHI S-4800, Japan) at an accelerating voltage of 5kV. The Fourier transformed infrared (FTIR) spectra were detected on a BRUKER Vector 22 Spectrometer (Germany) from 4,000 to 400 cm^{-1} in an ATR model. The tensile tests and compression tests were recorded on a universal testing machine (SANS CMT2503) at 75% humidity and room temperature. For tensile testing, the hydrogels of the cylindrical samples with a diameter of 4.5 mm and a height of 50 mm were stretched at a rate of 100 mm min^{-1}. For compression testing, the cylindrical samples with a diameter of 8.5 mm and a height of 40 mm were compressed at a velocity of 10 mm min^{-1}.

A rotational rheometer (Thermo Hakke) with a steel parallel plate of 10 mm radius was used to determine the rheological properties of the hydrogel. Dynamic frequency sweep measurements were performed at 37°C by an oscillation mode using a fixed oscillatory strain of 1% and a fixed gap of 1 mm. The temperature sweep measurements of the hydrogel were measured with a temperature range of 10–60°C, a fixed oscillatory strain from 0.1% to 600%, and a fixed frequency of 1 Hz. The strain measurements of the hydrogel from at the frequency of 1 Hz (37°C) were performed.

Adhesive Strength Test

The *in vitro* adhesion of the PAS-2 hydrogel was further assessed through different rat tissues. Four organs (i.e., heart, liver, lung, kidney) were excised from SD rats for tissue adhesive tests. A square-shaped PAS-2 hydrogel (of 6 mm per side) was attached to stainless steel tweezers before being attached to the water-moist surface of these organs.

In vitro Cytotoxicity Assay

The biocompatibility of hydrogels was evaluated in the fibroblast cell line (L929). In brief, cells were seeded onto 24-well culture plates and cultured overnight. Then, after ultraviolet treatment, PAS-2 hydrogel was added into the 24-well plates and co-cultured. The standard medium was changed daily. After 1, 3, and 5 days, the media and hydrogels were discarded. At the specified time points, a CCK-8 working solution (DMEM containing 10% CCK-8 solution) was added and incubated in the incubator for 2 h. The supernatant was collected and measured for the absorption value at 450 nm using a microplate reader (Bio-Rad, USA). A live/dead assay was carried out to evaluate the cytotoxicity of prepared hydrogels. Briefly, the cells were stained with calcein-AM/Propidium dye at the same time points as described above and observed under a confocal microscope (Leica, Germany). Every test was repeated three times.

Hemolytic Activity

Rat blood cells were used to evaluate the blood compatibility of PAS-2 hydrogel. Briefly, the erythrocytes of SD rats were collected by centrifugation (1,000 rpm, 10 min) from the whole blood, and then diluted by normal saline (NS). The prepared erythrocytes solution was incubated with PAS-2 hydrogel. In addition, erythrocytes treated with PBS served as a negative control and those treated with Triton X-100 (0.1%) served as a positive control After incubating at 37°C for 2 h, the supernatant was taken out via centrifugation and transferred to a 96-well plate to detect the absorbance at 570 nm. Every test was repeated three times.

$$\text{Hemolysis ratio (\%)} = \frac{ODa - ODb}{ODc - ODb} * 100\%$$

Where ODa is the absorbance of samples, and ODb and ODc represent the absorbance of PBS and Triton X-100.

Antibacterial Performance

The *in-vitro* antibacterial performance of PAS-2 hydrogel was tested against *S. aureus* (ATCC 29213) and *E. coli* (ATCC 25922) in this experiment by standard plate counting assays. *E. coli* and *S. aureus* were cultured in Luria-Bertani (LB) and Tryptic Soy Broth (TSB) medium, respectively. Briefly, a total volume of 300 μL hydrogel solutions and equal volumes of PBS were loaded into a 24-well plate and then irradiated by UV for 30 min to kill any microorganisms. Then, the bacterial suspension (300 μl, 10^6 CFU/ml) was mixed with PAS-2 hydrogel and PBS, respectively, which was incubated in a 37°C incubator for 12 h. The group of bacteria incubated with PBS was set as a control. Thereafter, the bacterial solution of two groups was isolated, then 20 μl was taken and seeded on the LB and TSB solid plate and placed at 37°C overnight. Finally, the number of viable colony units were photographed and counted.

Wound Healing Study

All experiments were authorized by the Animal Ethics Committee of Shanghai East Hospital (Shanghai, China). A total number of 27 adult Sprague-Dawley (SD, male, weigh, 250–300 g, age, 6 weeks old) rats, were purchased by Shanghai Slac Laboratory Animal Co. Ltd. Animal care and use followed the guidelines of Laboratory Animals published by the US National Institutes of Health.

Animals were bred in a rat box in a controlled environment (temperature: 26 ± 3°C, relative humidity: 70–85%, 12: 12 h light/ dark). Experimental animals were not restricted in how much water they could have and had a standard diet. Briefly, after a standard anesthesia procedure (60 mg kg^{-1} pentobarbital), the fur was shaved from the backs. A local full-thickness wound with a diameter of approximately 1.5 cm was produced on the dorsum of each rat. The rats were randomly assigned to three groups: the control group (gauze), the Tegaderm group (commercial film), and the PAS-2 group (PAS-2 hydrogel). At least nine rats were selected for each group. The dressing was refreshed on the 4, 8, and 12th days and the healing of the wound was recorded with a digital camera on the 0, 4, 8, and 12th days and the corresponding wound closure rate was calculated.

$$\text{Wound closure } rate = \frac{Area\ 0 - Area\ T}{Area\ 0} * 100\%.$$

Here, the Area 0 is the original wound area, the Area T represents the wound area at each time point (Cheng et al., 2020).

Histological Analysis

To evaluate the wound healing performance of PAS-2 hydrogel, the tissue samples of the wound were collected on the 4, 8, and 12th day and fixed with 4% paraformaldehyde for 1 h. Subsequently, the samples were embedded in paraffin, sectioned (4 μm), H&E and Masson stained, followed by histologic examination with optical microscopy (Leica Microsystems, Germany). A H&E-staining-based scoring system was used to evaluate wound repair (Eikebrokk et al., 2019). Masson staining was performed to evaluate collagen deposition using ImageJ software. In addition, the collagen amount and neovascularization in the wound tissue at day 12 were visualized by immunofluorescence staining of collagen type I (Col I) and alpha-smooth muscle actin (α-SMA). In short, after routinely de-waxing and rehydration, antigens were repaired and blocked with goat serum. The slides were incubated, respectively, overnight with primary antibodies at 4°C: rabbit polyclonal anti-collagen type I and anti-α-SMA (1: 100, CST, USA). After undergoing PBS washes, tissues were incubated with Cy3-conjugated goat anti-rabbit IgG (1: 200, Abcam, USA). Nuclei were stained with DAPI (Abcam, USA) after the incubation of the secondary antibody. The immunostaining results were observed by a fluorescence microscope (Nikon, Japan) and quantitatively analyzed by ImageJ software. The results were evaluated independently by two pathologists who were blinded to the treatments.

Statistical Analysis

The analysis data are expressed as the mean ± standard deviation of at least triplicate samples. The student's t-test was used to analyze the differences between two groups, and one-way analysis of variance (ANOVA) was used to analyze multiple groups. $^*p < 0.05$ was considered to be statistically significant ($^*p < 0.05$, $^{**}p < 0.01$, $^{***}p < 0.001$ and $^{****}p < 0.0001$).

RESULTS AND DISCUSSION

Synthesis and Characterization of the PAS-2 Hydrogel

In this study, a new polyzwitterionic hydrogel was designed. The schematic representation of the hydrogel dressing is presented in **Figure 1**. A new structural salt-responsive polySVBA was induced into the polyAAm network to form a poly(AAm-*co*-SVBA) (PAS) hydrogel (**Figure 2A**). The chemical structures of the resultant hydrogels and polymer were tested using FT-IR spectroscopy. **Figure 2B** summarizes the FT-IR spectra of lyophilized AAm, PAAm, PSVBA, PAS-1, and PAS-2, respectively. For PAAm polymer, there were two characteristic peaks at 1,649 cm^{-1} and 1,599 cm^{-1} attributed to the asymmetrical stretching vibration of–C=O and the characteristic absorption peak of–N–H on amide groups. In addition, the characteristic absorption peaks at 1,174 cm^{-1} and 1,043 cm^{-1} for pure PSVBA hydrogel corresponded to the–CH stretching vibration on aromatic rings. However, once two networks were rationally combined, the ATR-FTIR spectra of polyzwitterionic PAS (including PAS-1 and PSA-2) possessed a certain shift—the obvious characteristic absorption peaks at 1,652 cm^{-1} and 1,601 cm^{-1} corresponding to the stretching vibration of–C=O and–N–H can be detected. In the meantime, the signal of the aromatic ring (-CH) shifted to 1,168 cm^{-1} and 1,038 cm^{-1}, indicating the successful combination of PAAm and PSVBA networks in polyzwitterionic PAS hydrogels.

As shown in **Figure 2C**, the morphology of the hydrogels was observed by SEM. The PAAm exhibited a smooth surface with few porous structures. However, the introduction of polySVBA into the PAAm networks caused a remarkable increase in porosity. With a decrease in the weight ratio of the polySVBA from 66.7% to 50%, the PAS-1 and PAS-2 hydrogels showed interconnected porous structures. In addition, compared with the PAS-1 hydrogel, PAS-2 hydrogel revealed a highly porous structure and had a reduction in pore diameter, thereby leading to a decrease in the ability of the hydrogel.

Rheological Properties of PAS-2 Hydrogel

For an eligible wound dressing, it must maintain the structural integrity under appropriate external force so that it can protect injured tissue. Therefore, favorable mechanical performances are very important for an ideal skin wound dressing. In this study, the viscoelasticity and stability of the dynamic crosslinked hydrogels were investigated by rheological tests. The strain amplitude sweep results were shown in **Figure 2D**. The loss modulus (G'') was lower than the storage modulus (G') under small, applied stress, indicating that the solid-like hydrogel was successfully formed (Xing et al., 2016). Moreover, the storage modulus G' of the hydrogels began to decrease gradually with the increasingly applied stress. For single-network hydrogels PAAm, when the strain increased to 90%, the G' curves overlapped, and the network was collapsed. In contrast, the curves overlapped only when the strain exceeded 100% for the double-network hydrogel PAS-1 and PAS-2, which demonstrated that the double-network hydrogel was more stable and could bear larger stress than the single-network hydrogel. Similar results were observed in frequency sweep and temperature sweep. The G' was always higher than G'' of the hydrogels, further indicating that the hydrogels had both a stable structure and elasticity (**Figures 2E,F**). Put simply, all the rheological test results demonstrated that the mechanical properties of the PAS-1 and PAS-2 hydrogels were more excellent than PAAm hydrogels. The increased cross-linking density of the hydrogels by the secondary photo-cross-

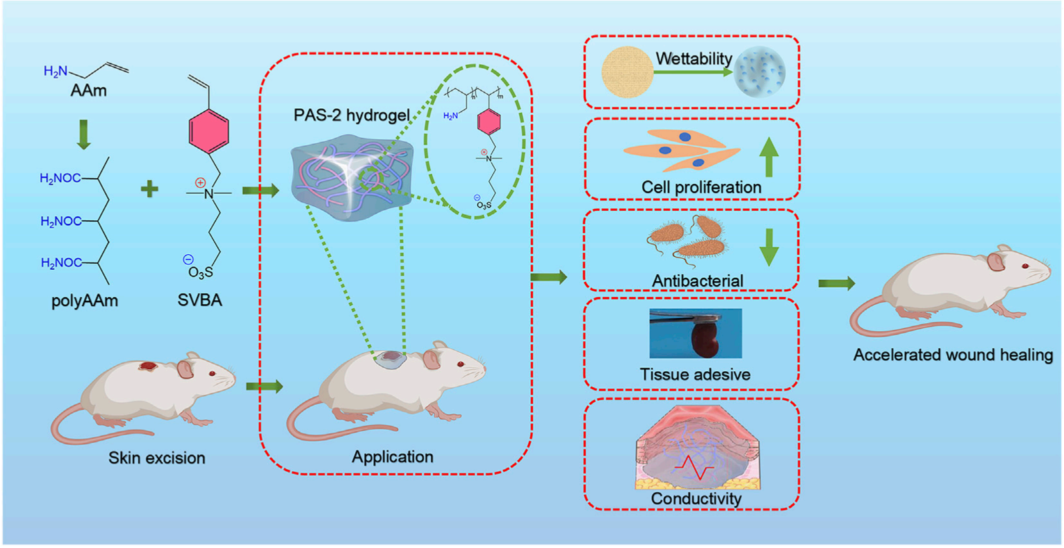

FIGURE 1 | Schematic representations of PAS-2 hydrogel for wound healing.

linking might contribute to the better mechanical properties of the co-network hydrogels (Wang et al., 2018; Cheng et al., 2019).

Compression and Tensile Properties

The compression and tensile properties of hydrogels are slightly influenced by the composition of the co-networks. The compression and tensile strength of the hydrogels were measured with a universal test machine. As shown in **Figure 3A**, the compression stress of PAAm was 0.062 MPa at a strain of 60%. After the salt-responsive SVBA was induced, the compression stress of PAS-1 and PAS-2 hydrogels decreased to 0.022 and 0.034 MPa with a strain of 60%. The tensile test was presented in **Figure 3B**. It was found that the tensile stress of PAAm hydrogel was 12 kPa at a strain of 100%, and the elongation at break was 250%. However, the tensile stress and elongation at the break point were both decreased as the SVBA was added. The tensile stress of both PAS-1 and PAS-2 hydrogels decreased from 8 to 4 kPa. Meanwhile, the elongation at break decreased from 240% to 180%. When compared with PAAm (0.04 MPa), the compression modulus of both PAS-1 and PAS-2 hydrogels decreased to 0.01 and 0.02 MPa (**Figure 3C**), which is comparable to the soft tissues of the human body (Feiner and Dvir, 2017). Typically, the ideal hydrogel dressing for wound healing is required to have low modulus, appropriate compressibility, and stretchability to avoid rupture during movement.

Conductivity of the Hydrogels

It has been confirmed that electrically conductive polymers have a positive effect on cell adhesion, proliferation, and migration (Guo et al., 2011; Xie et al., 2015; Wu et al., 2017). Skin is an electrical signal sensitive tissue and previous studies have revealed that conductive wound dressings could favor wound healing (Li M et al., 2019; Qu et al., 2019; He et al., 2020). The conductivity of the PAS-2 hydrogel was evaluated by using a four-point probe method. As shown in **Figures 3A,D** LED bulb was lighted by a 1.5 V power supplier in a PAS-2 hydrogel connected circuit. The LED light became dimmed when the hydrogel was cut into two halves. Then, the two furcated parts were concatenated, and the LED bulb was lit again. **Figure 3E** illustrates that the resistance could be stably recovered once the two fractured hydrogels were put together. All the results indicated that the PAS-2 hydrogel possessed a good electroactivity. The electroactivity of the hydrogel may be attributed to SVBA. Zwitterionic hydrogels have an anti-polyelectrolyte effect, maintaining high solvent content and low polymer chain density even in a high salt environment, which provides an ion migration pathway and maintains very high ionic conductivity (Lee et al., 2018). The PAS-2 hydrogel contained cation and anion pairs, which can transmit electrical signals through the relative motion of positive and negative ions (Roshanbinfar et al., 2018).

Adhesive Properties of the Hydrogels

Excellent adhesive property is important for a hydrogel wound dressing. Adhesive hydrogels can adhere to an irregular wound site and act as a physical barrier, protecting the wound from the adverse external environment (Le et al., 2018). We tested the adhesive properties of all hydrogels using the 90° peeling test. The force/width–displacement curves of different hydrogels and the interfacial toughness derived from force/width-displacement curves are illustrated in **Figures 4A,B**. It can be observed that the addition of SVBA changed the physical network structure and the network polymerization efficiency, the interfacial toughness of different hydrogels on aluminum increased from 400 ± 20 to 900 ± 150 J m^2. To further examine the PAS-2 hydrogel possess good surface adhesion properties on different solid substrates. We performed a peeling test on the surfaces of titanium, glass, and steel. As shown in **Figure 4C**, the adhesion of PAS-2 hydrogel to

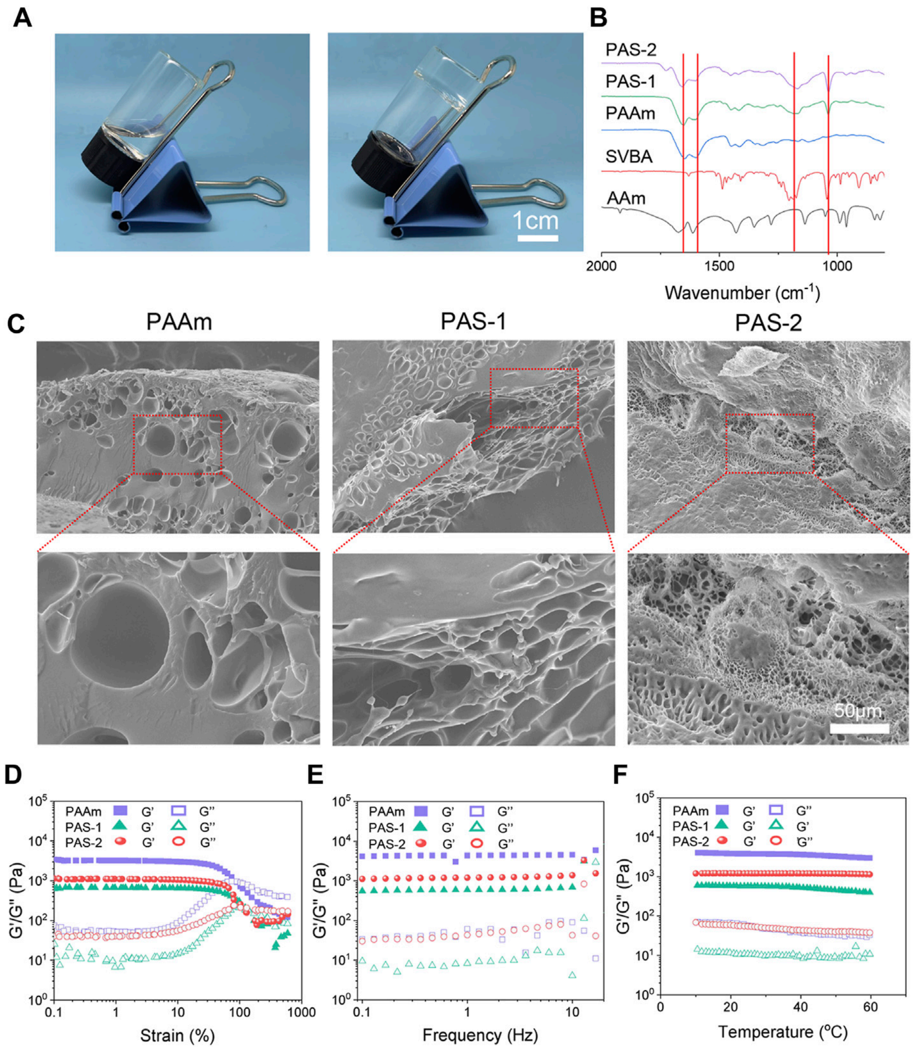

FIGURE 2 | Microscopic morphology and mechanical characterization of prepared hydrogels. **(A)** Photographs of PAS-2 hydrogel. **(B)** FT-IR spectra of the AAm, PSBVA, PAAm hydrogel, PAS-1 hydrogel, and PAS-2 hydrogel. **(C)** SEM images of PAAm, PAS-1, and PAS-2 hydrogels. **(D)** G′ and G″ of the PAAm, PAS-1, and PAS-2 hydrogels on the strain sweep test. **(E)** Rheological analysis of PAAm, PAS-1, and PAS-2 hydrogels at 1% strain. **(F)** Rheological analysis of PAAm, PAS-1, and PAS-2 hydrogels when the temperature altered.

titanium substrates was stronger than that on steel and glass. The interfacial toughness of PAS-2 hydrogel was ~1050 J m^2 on titanium, ~700 J m^2 on steel, and ~502 J m^2 on glass, respectively (**Figure 4D**). Visual inspection showed that the hydrogel can be easily peeled from the glass surface owing to the relatively smaller interfacial toughness (**Figure 4E**). In contrast, the PAS-2 hydrogel was sticky and adhered to the surface of the titanium. Different interfacial toughness of the same PAS-2 hydrogel on different substrate results from the hydrogel-substrate interaction. By incorporating SVBA into PAAm networks, the adhesive properties of hydrogels were improved. Besides mechanical properties, the ability for bio-adhesion to wound dressings is also important for potential clinical applications. the PAS-2 hydrogel also had high bio-adhesion properties to biological tissues (**Figure 4F**), such as the heart, liver, spleen, and kidney, which are crucial for clinical applications.

Cytocompatibility and Hemocompatibility of PAS-2 Hydrogel

Biomaterials possessing favorable biocompatibility are the prerequisite for new wound dressings (Zhao et al., 2018; Li S et al., 2019). Thus, the viability of L929 cells was employed to estimate the cytocompatibility of PAS-2 hydrogel with living/dead staining and CCK-8. As shown in **Figure 5A**, after co-incubation for 1, 3, and 5 days, dead cells (red) were scarcely detected in two groups and there was no difference in living cell number between the PAS-2 hydrogel and control groups ($p > 0.05$) (**Figure 5B**). The image of the CCK8 assay was also

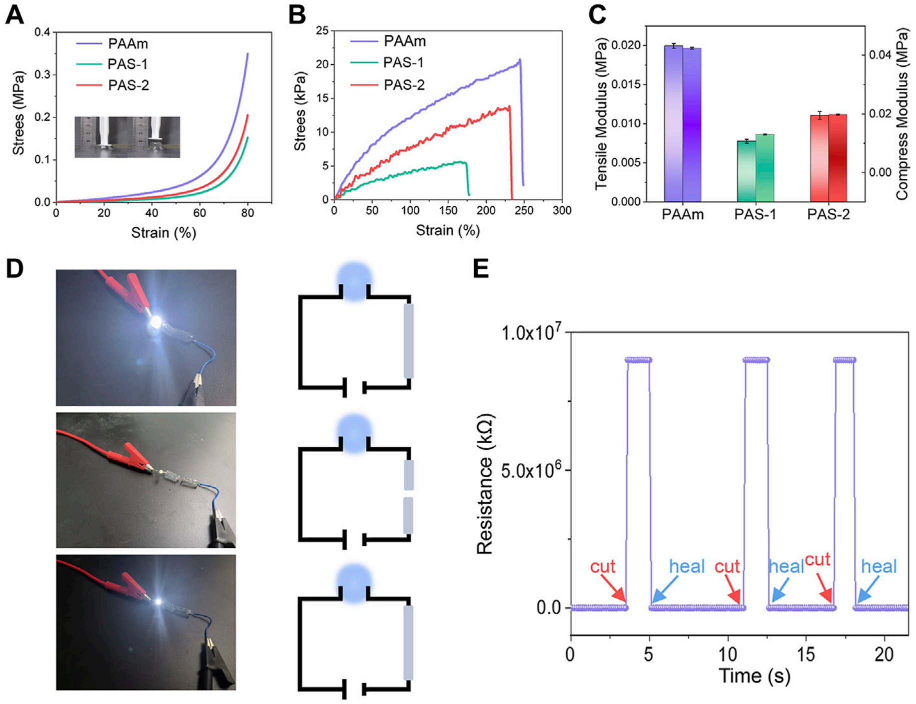

FIGURE 3 | Mechanical properties and electrochemical sensitivity of prepared hydrogels. **(A)** Compress stress-strain curves of PAAm, PAS-1, and PAS-2 hydrogels. **(B)** Tensile stress-strain curves of PAAm, PAS-1, and PAS-2 hydrogels. **(C)** Tensile modulus and compress modulus of PAAm, PAS-1, and PAS-2 hydrogels. **(D)** Experiment of PAS-2 hydrogel in a DIODE circuit under different situations. **(E)** Relative resistance changes of PAS-2 hydrogel in response to different situations.

consistent with the results of the living/dead staining (**Figure 5C**).

To further explore the safety of PAS-2 hydrogel, the hemocompatibility of the hydrogel was evaluated 2 h after treatment by employing an *in vitro* hemolysis assay. The macroscopic color of PAS-2, PBS (negative control group), and Triton X-100 (positive control group) groups are shown in **Figure 5D**. The supernatant of the PAS-2 group was colorless and transparent, which was similar to the PBS group, while the Triton X-100 group was bright red. Furthermore, the hemolysis ratio was 1.14 and 1.21 for PBS and triton X-100 groups ($p >$ 0.05), respectively, indicating that PAS-2 hydrogel had no significant effect on the hemolysis ratio. Overall, all these data confirmed that PAS-2 hydrogel had better cytocompatibility and they are taken as promising novel materials in wound dressing.

Antibacterial Performance of PAS-2 Hydrogel

A promising wound dressing should have effective antibacterial activity to protect the wound from bacterial infection and inhibit the propagation of microorganisms to reduce inflammation in the site of the wound (Ak and Gülçin, 2008). In this work, we used *E. coli* and *S. aureus* to evaluate the antibacterial activity of PAS-2 hydrogel. polySVBA is an important component in the PAS-2 hydrogel, the nature of polySVBA chains already presented unique salt-responsive properties and were applied to bacterial release. As shown in **Figures 5F,G**, we found significantly fewer bacteria adhered to the interface of the PAS-2 hydrogel ($p <$ 0.05) (**Figure 5E**), indicating that the PAS-2 hydrogel displayed an obvious inhibitory effect on *E. coli* and *S. aureus*. This antibacterial action is one of the most important properties of this wound dressing. The antibacterial rate of PAS-2 hydrogel was 78% (*S. aureus*) and 72% (*E. coli*), which was lower than that of previous studies (Khodabakhshi et al., 2019; Eskandarinia et al., 2020). This inconsistency is probably related to the addition of antimicrobial substances in previous works. The PAS-2 exhibited weaker antibacterial activity against *S. aureus* in comparison with *E. coli*. This may be derived from the structural difference of the two bacterial. The *S. aureus* is only covered by a single peptidoglycan layer, while *E. coli* has a thick membrane of lipopolysaccharide (Eskandarinia et al., 2019; Kefayat et al., 2021). Based on the above results, PAS-2 hydrogel can reduce bacterial growth to inhibit infection and shorten the wound healing time.

In vivo Wound Healing

PAS-2 hydrogel dressing could provide the wound with a long-term hydration micro-environment, antibacterial properties, and conduct bioelectro-stimulation. The wound healing behavior of the PAS-2 hydrogel was further evaluated in a rat full-thickness circular skin defect model. After 15 mm skin defects were created, the wounds were treated by the gauze (control), Tegaderm™ (commercial film dressing), and PAS-2 hydrogel and photographed on day 0, day 4, day 8, and day 12. As shown in **Figures 6A–C**, on the fourth day, although re-epithelialization

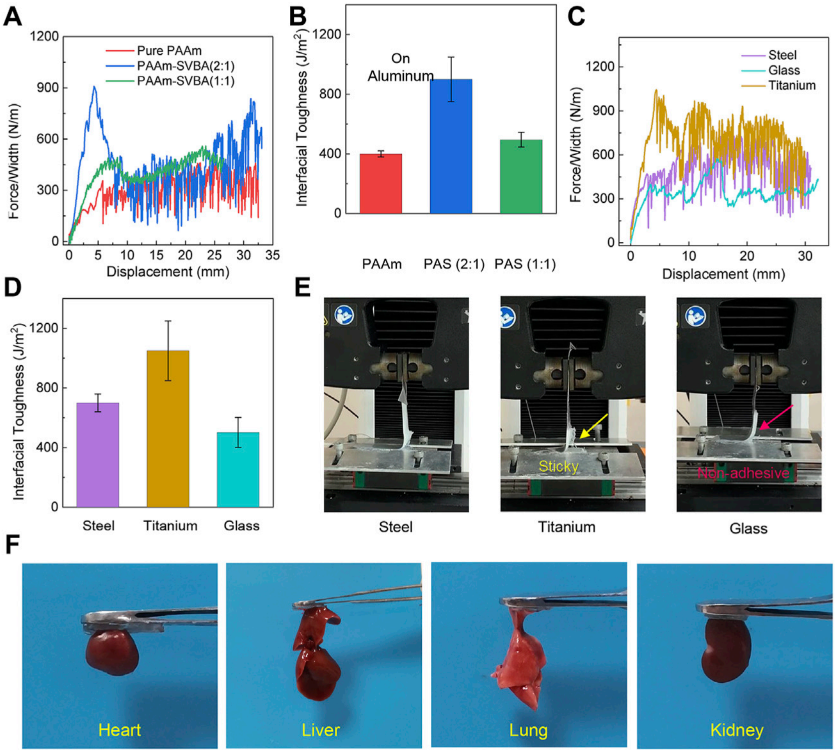

FIGURE 4 | Interfacial toughness and adhesive properties of prepared hydrogels. **(A)** Peeling force/width curves of PAAm, PAS-1, and PAS-2 hydrogels on nonporous glass at a peeling rate of 100 mm/min. **(B)** Peeling Interfacial toughness of PAAm, PAS-1, and PAS-2 hydrogels on nonporous Aluminum at a peeling rate of 100 mm/min. **(C)** Peeling force/width curves of PAS-2 hydrogel on three nonporous solid surfaces at a peeling rate of 100 mm/min. **(D)** Interfacial toughness of PAS-2 hydrogel on different nonporous solid surfaces (steel, glass, titanium) at a peeling rate of 100 mm/min. **(E)** Visualization of peeling off of PAS-2 hydrogel from steel, glass, and titanium. **(F)** Photographs of tissue adhesion situations of PAS-2 hydrogel on four different organs of SD rat (heart, liver, lung, kidney).

of the wounds occurred in all groups, the hydrogel group (43.33%) showed a higher wound close rate than the Tegaderm group (37%) and control group (31.33%) ($p < 0.05$). On the eighth day, importantly, the wound closure rate of the PAS-2 hydrogel group exceeded nearly 11% ($p < 0.05$) than the control group. In addition, statistically significant differences were observed in the wound closure rate between the groups (control vs. Tegaderm group; control vs. PAS-2 group; Tegaderm group vs. PAS-2 group). Furthermore, when the wounds were treated for 12 days, the wound closure rate in all groups increased obviously. It was clear that there was almost completely healed in the PAS-2 group (wound close rate = 95.33%), while in the control group 11% ($p < 0.05$) of wounds were not completely healed. All the results showed that the PAS-2 group had better treatment efficacy than the Tegaderm group. This is because, compared to the Tegaderm™ film, a larger number of wettability groups (hydroxy, sulfonate, and amide) from copolymerized poly (AAm-co-SVBA) assist to trap more moisture and maintain long-term hydration micro-environments. This structural adhesive design can make the zwitterionic hydrogel matrix fit the organ wounds smoothly and perfectly, leading to the overall adsorption of excess exudates and toxins during the dynamic healing processes. Besides the features listed above, the electroactivity of PAS-2 hydrogel also contributed to promoting the wound healing process (Gharibi et al., 2015). Overall, the PAS-2 group displayed a better therapeutic effect on wound healing than commercial film dressing.

Histological Examination

Classical cutaneous wound healing is a complex biological process that consists of hemostasis, inflammation, re-epithelialization, innate and adaptive immune response, and tissue repair (Fang et al., 2009). To further explore the wound repair efficiency of PAS-2 hydrogel, HE and Masson's staining was performed on the wound tissue to further observe the quality of the regenerated tissue and pathological changes in different groups. As shown in **Figure 7A**, the images of the PAS-2 group showed fewer inflammatory cells on the site of the wounds, which was mainly due to the scavenging effect of the polySVBA, which killed the bacteria on the wounds, but there were more inflammatory cells in the control and Tegaderm groups, which could inhibit the formation of granulation tissue and the epithelial layer. On the fourth day, there was no obvious sign of healing in the control group. In the Tegaderm group, the wound showed thickened basal membrane and sporadic keratinocytes, but the wound can be seen as the confluence of keratinocytes in the PAS-2 group. On the eighth day, the keratinocytes approaching confluence and thickened basal membrane were seen in the control and Tegaderm groups, meanwhile, we can see confluent epithelium, but nuclei not

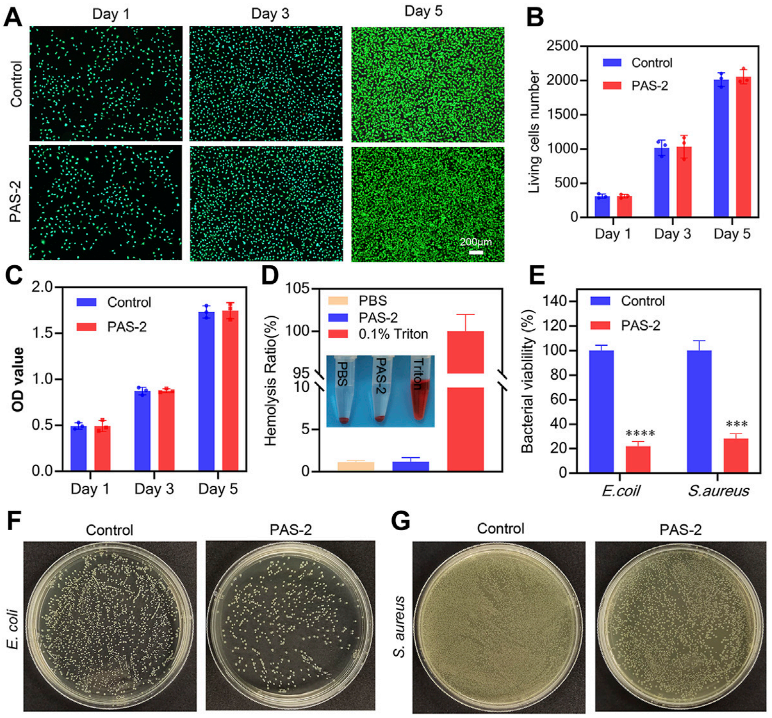

FIGURE 5 | Cytocompatibility, hemocompatibility, and antibacterial properties of PAS-2 hydrogel. **(A)** Cytocompatibility of PAS-2 hydrogel indicated by live/dead staining after co-cultured with PAS-2 hydrogel on day 1, day 3, and day 5 and corresponding data analysis **(B)**, a normal culture medium without hydrogel was used as the control. **(C)** Quantitative analysis of L929 cell viability after co-cultured with PAS-2 hydrogel on day 1, day 3, and day 5, a normal culture medium without hydrogel was used as the control. **(D)** Image and the quantitative analysis of the hemolytic activity of the PAS-2 hydrogel. **(E)** The corresponding quantitative bacterial survival rate of *E. coli* and *S. aureus*. **(F, G)** Macroscopical image of the survival *E. coli* and *S. aureus* clones on agar plates after treated with PAS-2 hydrogel. *$p < 0.05$, **$p < 0.01$, ***$p < 0.001$, ****$p < 0.0001$.

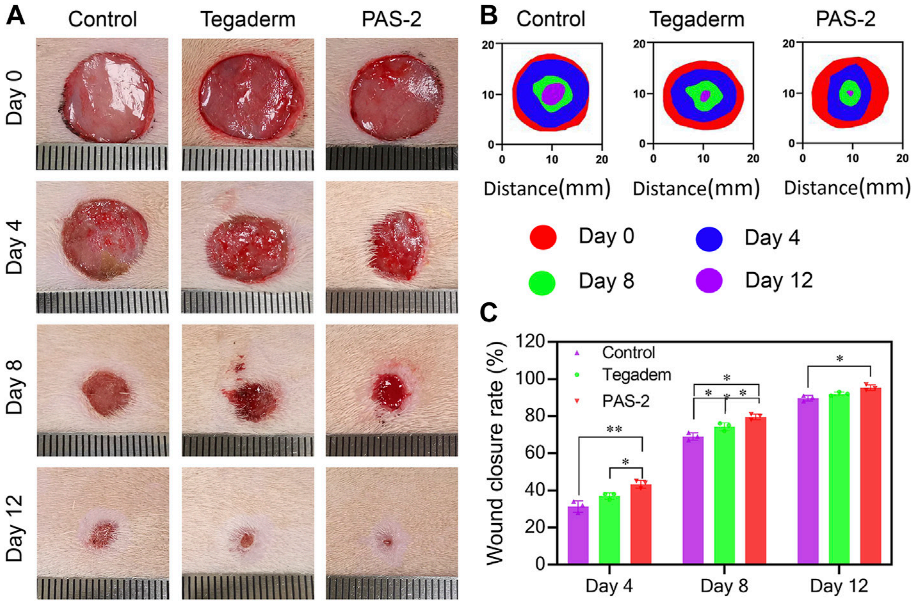

FIGURE 6 | *In vivo* assessment of PAS-2 hydrogel for skin full-thickness wound healing. **(A)** Photographs of the wound on day 0, day 4, day 8, and day 12 for gauze (control), Tegaderm™ film, and PAS-2 hydrogel. **(B)** Corresponding traces of wound healing on day 0, day 4, day 8, and day 12. **(C)** The statistical analysis of wound closure for gauze (control), Tegaderm™ film, and PAS-2 hydrogel. *$p < 0.05$, **$p < 0.01$, ***$p < 0.001$, ****$p < 0.0001$.

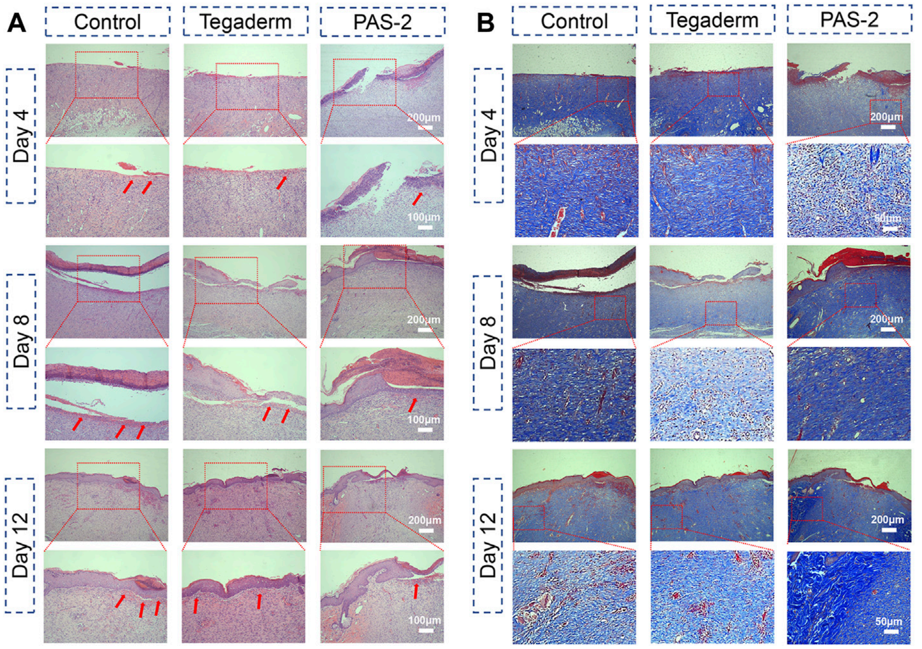

FIGURE 7 | Histomorphological evaluation of the regenerated skin tissue after healing for 4, 8, and 12 days. **(A)** Images of H&E staining of the regenerated tissues in the control (gauze), Tegaderm, and PAS-2 groups after healing for 4, 8, and 12 days (red arrows: inflammatory cell). **(B)** Images of Masson's staining of the regenerated tissues in the control (gauze), Tegaderm, and PAS-2 groups after healing for 4, 8, and 12 days.

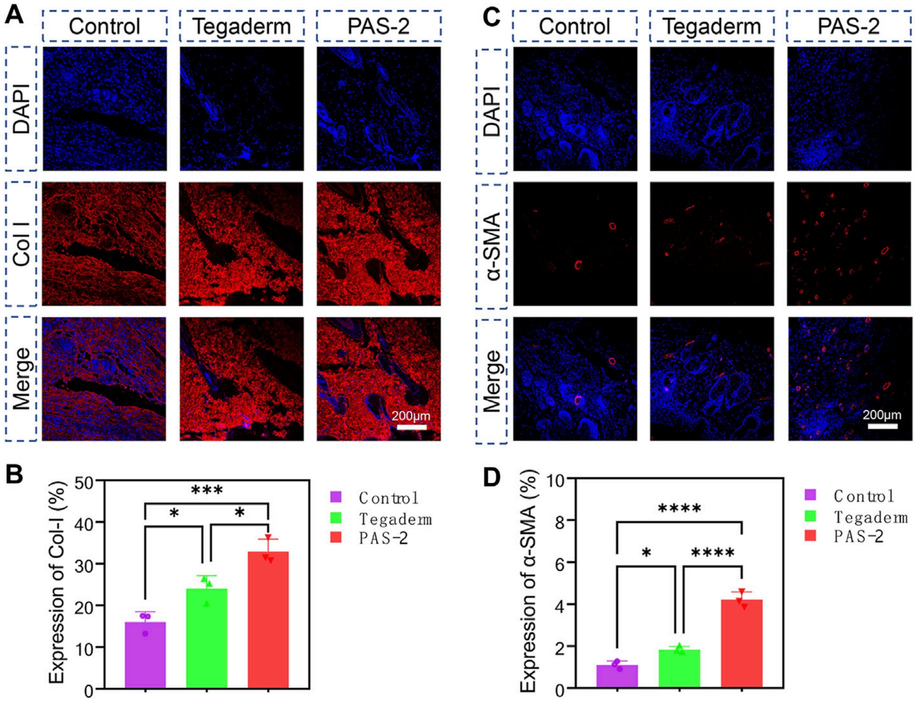

FIGURE 8 | Immunofluorescence staining of Collagen I (Col I) and alpha-smooth muscle actin (α-SMA) in control, Tegaderm, and PAS-2 groups. Representative images of the regenerated wound tissue on the 12th day by immunofluorescence staining labeling with Collagen I (Col I) **(A)** and α-SMA **(C)**. Quantitative statistical analysis of the expression of Col I **(B)** and α-SMA **(D)**. $^{*}p < 0.05$, $^{**}p < 0.01$, $^{***}p < 0.001$, $^{****}p < 0.0001$.

distinctly basal in the PAS-2 group. On the 12th day, the keratin and partly clear palisades can be seen in the PAS-2 group, this is a distinguishing trait of wound healing that is rarely seen in other groups. According to the scoring system of the skin wound model (Eikebrokk et al., 2019), the scores of the PAS-2 group were significantly higher than the control group (**Supplementary Figure S1A**). The difference was statistically significant ($p < 0.05$).

The collagen deposition in the wound was assessed by Masson staining. As can be seen from **Figure 7B**, the collagen in the wounds treated with hydrogel or commercial film were stained blue. Compared with the control and Tegaderm groups with less collagen, the wounds treated by the PAS-2 group could see a large amount of collagen density on day 8 and day 12. Moreover, the collagen dense of the PAS-2 group was higher than the control and Tegaderm groups (**Supplementary Figure S1B**) on day 12 ($p < 0.05$), indicating that the deposition of collagen could be promoted in the granulation tissue by the application of polyAAm and polySVBA.

The essential component for the function and structure of the skin is collagen, which includes the fibrillar collagen I and III. Collagen I is an important biomarker for the remodeling of damaged skin tissue (Cheng et al., 2020). In addition, after skin injuries, the expression of α-smooth muscle actin (α-SMA) during wound healing is important for cell migration, fibroblasts transdifferentiation, vascularization, and wound contraction (Yan et al., 2021). The expression of collagen I and α-SMA were evaluated by immunohistochemical staining of the wound tissue on day 12 to further investigate the mechanism of PAS-2 hydrogel promoting wound healing. The expression of collagen I (**Figure 8A**) and α-SMA (**Figure 8C**) in the PAS-2 group was significantly superior to the other groups, furthermore, statistical analysis confirmed that the expression of collagen I (**Figure 8B**) and α-SMA (**Figure 8D**) in the PAS-2 group was significantly higher than that in wounds treated with gauze or Tegaderm™ film ($p < 0.05$). These results showed that PAS-2 hydrogel can upregulate the expression of collagen I and α-SMA to accelerate vascular angiogenesis and promote the formation of granulation tissue. To summarize, the PAS-2 hydrogel remarkably enhanced wound healing, which was reflected as the attenuated inflammation infiltration, enhanced vascularization, collagen deposition, and remodeling.

CONCLUSION

In this work, we designed and introduced a new structural zwitterion poly[3-(dimethyl(4-vinylbenzyl) ammonium) propyl sulfonate] (SVBA) into the polyAAm network to obtain a novel salt-responsive conductive hydrogel. Because of the SVBA addition, the PAS-2 hydrogel was endowed with good electroactive properties and remarkable mechanical properties. In addition, The PAS-2 hydrogel displayed excellent cytocompatibility, stable rheological property, effective antibacterial property, strong adsorption, and high penetrability. For the *in vivo* wound healing test, the PAS-2 hydrogel exhibited faster wound healing, a higher healing score, higher collagen deposition, fewer inflammatory infiltration, and more angiogenesis than the commercial film and gauze. Finally, all these results demonstrated that the salt-responsive conductive PAS-2 hydrogel film could promote the wound healing process effectively and can be a promising candidate as film wound dressing for cutaneous skin wound healing.

DATA AVAILABILITY STATEMENT

The raw data supporting the conclusion of this article will be made available by the authors, without undue reservation.

ETHICS STATEMENT

The animal study was reviewed and approved by the Animal Ethics Committee of Shanghai East Hospital.

AUTHOR CONTRIBUTIONS

DW, JY, and DZ contributed to the conception and design of the study. JL organized the database. ZZ performed the statistical analysis. FW, SW, and LN wrote the first draft of the manuscript. JL, XZ, and DW wrote sections of the manuscript. All authors contributed to manuscript revision, read, and approved the submitted version.

FUNDING

This work was supported by the National Natural Science Foundation of China (81972106). The authors acknowledge financial support from the Science and Technology Commission of Shanghai Municipality (19441901900, 19ZR1439700).

SUPPLEMENTARY MATERIAL

The Supplementary Material for this article can be found online at: https://www.frontiersin.org/articles/10.3389/fbioe.2022.833887/full#supplementary-material

REFERENCES

Ak, T., and Gülçin, İ. (2008). Antioxidant and Radical Scavenging Properties of Curcumin. *Chemico-Biological Interactions* 174 (1), 27–37. doi:10.1016/j.cbi.2008.05.003

Chen, Y., Liang, Y., Liu, J., Yang, J., Jia, N., Zhu, C., et al. (2021). Optimizing Microenvironment by Integrating Negative Pressure and Exogenous Electric fields via a Flexible Porous Conductive Dressing to Accelerate Wound Healing. *Biomater. Sci.* 9 (1), 238–251. doi:10.1039/d0bm01172j

Cheng, L., Cai, Z., Ye, T., Yu, X., Chen, Z., Yan, Y., et al. (2020). Injectable Polypeptide-Protein Hydrogels for Promoting Infected Wound Healing. *Adv. Funct. Mater.* 30 (25), 2001196. doi:10.1002/adfm.202001196

Cheng, Y., Hu, Z., Zhao, Y., Zou, Z., Lu, S., Zhang, B., et al. (2019). Sponges of Carboxymethyl Chitosan Grafted with Collagen Peptides for Wound Healing. *Ijms* 20 (16), 3890. doi:10.3390/ijms20163890

Eikebrokk, T. A., Vassmyr, B. S., Ausen, K., Gravastrand, C., Spigset, O., and Pukstad, B. (2019). Cytotoxicity and Effect on Wound Re-epithelialization after Topical Administration of Tranexamic Acid. *BJS Open* 3 (6), 840–851. doi:10.1002/bjs5.50192

Eskandarinia, A., Kefayat, A., Gharakhloo, M., Agheb, M., Khodabakhshi, D., Khorshidi, M., et al. (2020). A Propolis Enriched Polyurethane-Hyaluronic Acid Nanofibrous Wound Dressing with Remarkable Antibacterial and Wound Healing Activities. *Int. J. Biol. Macromolecules* 149, 467–476. doi:10.1016/j.ijbiomac.2020.01.255

Eskandarinia, A., Kefayat, A., Rafienia, M., Agheb, M., Navid, S., and Ebrahimpour, K. (2019). Cornstarch-based Wound Dressing Incorporated with Hyaluronic Acid and Propolis: *In Vitro* and *In Vivo* Studies. *Carbohydrate Polymers* 216, 25–35. doi:10.1016/j.carbpol.2019.03.091

Fang, J., Seki, T., and Maeda, H. (2009). Therapeutic Strategies by Modulating Oxygen Stress in Cancer and Inflammation. *Adv. Drug Deliv. Rev.* 61 (4), 290–302. doi:10.1016/j.addr.2009.02.005

Feiner, R., and Dvir, T. (2017). Tissue-electronics Interfaces: from Implantable Devices to Engineered Tissues. *Nat. Rev. Mater.* 3 (1), 17076. doi:10.1038/natrevmats.2017.76

Gharibi, R., Yeganeh, H., Rezapour-Lactoee, A., and Hassan, Z. M. (2015). Stimulation of Wound Healing by Electroactive, Antibacterial, and Antioxidant Polyurethane/Siloxane Dressing Membranes: *In Vitro* and *In Vivo* Evaluations. *ACS Appl. Mater. Inter.* 7 (43), 24296–24311. doi:10.1021/acsami.5b08376

Goding, J., Gilmour, A., Martens, P., Poole-Warren, L., and Green, R. (2017). Interpenetrating Conducting Hydrogel Materials for Neural Interfacing Electrodes. *Adv. Healthc. Mater.* 6 (9), 1601177. doi:10.1002/adhm.201601177

Guo, B., Finne-Wistrand, A., and Albertsson, A.-C. (2011). Facile Synthesis of Degradable and Electrically Conductive Polysaccharide Hydrogels. *Biomacromolecules* 12 (7), 2601–2609. doi:10.1021/bm200389t

He, J., Shi, M., Liang, Y., and Guo, B. (2020). Conductive Adhesive Self-Healing Nanocomposite Hydrogel Wound Dressing for Photothermal Therapy of Infected Full-Thickness Skin Wounds. *Chem. Eng. J.* 394, 124888. doi:10.1016/j.cej.2020.124888

He, X., Zhang, D., Wu, J., Wang, Y., Chen, F., Fan, P., et al. (2019). One-Pot and One-step Fabrication of Salt-Responsive Bilayer Hydrogels with 2D and 3D Shape Transformations. *ACS Appl. Mater. Inter.* 11 (28), 25417–25426. doi:10.1021/acsami.9b06691

Hernández Martínez, S. P., Rivera González, T. I., Franco Molina, M. A., Bollain y Goytia, J. J., Martínez Sanmiguel, J. J., Zárate Triviño, D. G., et al. (2019). A Novel Gold Calreticulin Nanocomposite Based on Chitosan for Wound Healing in a Diabetic Mice Model. *Nanomaterials* 9 (1), 75. doi:10.3390/nano9010075

Huang, H., Zhang, C., Crisci, R., Lu, T., Hung, H.-C., Sajib, M. S. J., et al. (2021). Strong Surface Hydration and Salt Resistant Mechanism of a New Nonfouling Zwitterionic Polymer Based on Protein Stabilizer TMAO. *J. Am. Chem. Soc.* 143 (40), 16786–16795. doi:10.1021/jacs.1c08280

Kefayat, A., Hamidi Farahani, R., Rafienia, M., Hazrati, E., and Hosseini Yekta, N. (2021). Synthesis and Characterization of Cellulose Nanofibers/chitosan/cinnamon Extract Wound Dressing with Significant Antibacterial and Wound Healing Properties. *J. Iran Chem. Soc.* doi:10.1007/s13738-021-02374-x

Khodabakhshi, D., Eskandarinia, A., Kefayat, A., Rafienia, M., Navid, S., Karbasi, S., et al. (2019). *In Vitro* and *In Vivo* Performance of a Propolis-Coated Polyurethane Wound Dressing with High Porosity and Antibacterial Efficacy. *Colloids Surf. B: Biointerfaces* 178, 177–184. doi:10.1016/j.colsurfb.2019.03.010

Kim, H. N., Jiao, A., Hwang, N. S., Kim, M. S., Kang, D. H., Kim, D.-H., et al. (2013). Nanotopography-guided Tissue Engineering and Regenerative Medicine. *Adv. Drug Deliv. Rev.* 65 (4), 536–558. doi:10.1016/j.addr.2012.07.014

Le, T. M. D., Duong, H. T. T., Thambi, T., Giang Phan, V. H., Jeong, J. H., and Lee, D. S. (2018). Bioinspired pH- and Temperature-Responsive Injectable Adhesive Hydrogels with Polyplexes Promotes Skin Wound Healing. *Biomacromolecules* 19 (8), 3536–3548. doi:10.1021/acs.biomac.8b00819

Lee, C.-J., Wu, H., Hu, Y., Young, M., Wang, H., Lynch, D., et al. (2018). Ionic Conductivity of Polyelectrolyte Hydrogels. *ACS Appl. Mater. Inter.* 10 (6), 5845–5852. doi:10.1021/acsami.7b15934

Li, M., Chen, J., Shi, M., Zhang, H., Ma, P. X., and Guo, B. (2019). Electroactive Anti-oxidant Polyurethane Elastomers with Shape Memory Property as Non-adherent Wound Dressing to Enhance Wound Healing. *Chem. Eng. J.* 375, 121999. doi:10.1016/j.cej.2019.121999

Li, S., Lu, D., Tang, J., Min, J., Hu, M., Li, Y., et al. (2019c). Electrical Stimulation Activates Fibroblasts through the Elevation of Intracellular Free Ca2+: Potential Mechanism of Pelvic Electrical Stimulation Therapy. *Biomed. Res. Int.* 2019c, 1–10. doi:10.1155/2019/7387803

Mao, S., Zhang, D., Zhang, Y., Yang, J., and Zheng, J. (2020). A Universal Coating Strategy for Controllable Functionalized Polymer Surfaces. *Adv. Funct. Mater.* 30 (40), 2004633. doi:10.1002/adfm.202004633

Naskar, S., Kumaran, V., Markandeya, Y. S., Mehta, B., and Basu, B. (2020). Neurogenesis-on-Chip: Electric Field Modulated Transdifferentiation of Human Mesenchymal Stem Cell and Mouse Muscle Precursor Cell Coculture. *Biomaterials* 226, 119522. doi:10.1016/j.biomaterials.2019.119522

Ni, Y., Zhang, D., Wang, Y., He, X., He, J., Wu, H., et al. (2021). Host-Guest Interaction-Mediated Photo/Temperature Dual-Controlled Antibacterial Surfaces. *ACS Appl. Mater. Inter.* 13 (12), 14543–14551. doi:10.1021/acsami.0c21626

Qu, J., Zhao, X., Liang, Y., Xu, Y., Ma, P. X., and Guo, B. (2019). Degradable Conductive Injectable Hydrogels as Novel Antibacterial, Anti-oxidant Wound Dressings for Wound Healing. *Chem. Eng. J.* 362, 548–560. doi:10.1016/j.cej.2019.01.028

Roshanbinfar, K., Vogt, L., Greber, B., Diecke, S., Boccaccini, A. R., Scheibel, T., et al. (2018). Electroconductive Biohybrid Hydrogel for Enhanced Maturation and Beating Properties of Engineered Cardiac Tissues. *Adv. Funct. Mater.* 28 (42), 1803951. doi:10.1002/adfm.201803951

Wang, S., Guan, S., Li, W., Ge, D., Xu, J., Sun, C., et al. (2018). 3D Culture of Neural Stem Cells within Conductive PEDOT Layer-Assembled Chitosan/gelatin Scaffolds for Neural Tissue Engineering. *Mater. Sci. Eng. C* 93, 890–901. doi:10.1016/j.msec.2018.08.054

Wang, S., Shi, K., Lu, J., Sun, W., Han, Q., Che, L., et al. (2021). Microsphere-Embedded Hydrogel Sustained-Release System to Inhibit Postoperative Epidural Fibrosis. *ACS Appl. Bio Mater.* 4 (6), 5122–5131. doi:10.1021/acsabm.1c00347

Wang, X., Zhang, D., Wu, J., Protsak, I., Mao, S., Ma, C., et al. (2020). Novel Salt-Responsive SiO2@Cellulose Membranes Promote Continuous Gradient and Adjustable Transport Efficiency. *ACS Appl. Mater. Inter.* 12 (37), 42169–42178. doi:10.1021/acsami.0c12399

Wu, J., Zhang, D., Wang, Y., Mao, S., Xiao, S., Chen, F., et al. (2019). Electric Assisted Salt-Responsive Bacterial Killing and Release of Polyzwitterionic Brushes in Low-Concentration Salt Solution. *Langmuir* 35 (25), 8285–8293. doi:10.1021/acs.langmuir.9b01151

Wu, Y., Wang, L., Guo, B., and Ma, P. X. (2017). Interwoven Aligned Conductive Nanofiber Yarn/Hydrogel Composite Scaffolds for Engineered 3D Cardiac Anisotropy. *ACS Nano* 11 (6), 5646–5659. doi:10.1021/acsnano.7b01062

Xie, M., Wang, L., Guo, B., Wang, Z., Chen, Y. E., and Ma, P. X. (2015). Ductile Electroactive Biodegradable Hyperbranched Polylactide Copolymers Enhancing Myoblast Differentiation. *Biomaterials* 71, 158–167. doi:10.1016/j.biomaterials.2015.08.042

Xing, R., Liu, K., Jiao, T., Zhang, N., Ma, K., Zhang, R., et al. (2016). An Injectable Self-Assembling Collagen-Gold Hybrid Hydrogel for Combinatorial Antitumor

Photothermal/Photodynamic Therapy. *Adv. Mater.* 28 (19), 3669–3676. doi:10.1002/adma.201600284

Yan, L., Han, K., Pang, B., Jin, H., Zhao, X., Xu, X., et al. (2021). Surfactin-reinforced Gelatin Methacrylate Hydrogel Accelerates Diabetic Wound Healing by Regulating the Macrophage Polarization and Promoting Angiogenesis. *Chem. Eng. J.* 414, 128836. doi:10.1016/j.cej.2021.128836

Yuan, H., Chen, L., and Hong, F. F. (2021). Homogeneous and Efficient Production of a Bacterial Nanocellulose-Lactoferrin-Collagen Composite under an Electric Field as a Matrix to Promote Wound Healing. *Biomater. Sci.* 9 (3), 930–941. doi:10.1039/d0bm01553a

Yuan, J., Zhang, D., He, X., Ni, Y., Che, L., Wu, J., et al. (2021). Cationic Peptide-Based Salt-Responsive Antibacterial Hydrogel Dressings for Wound Healing. *Int. J. Biol. Macromolecules* 190, 754–762. doi:10.1016/j.ijbiomac.2021.09.019

Zhang, D., Fu, Y., Huang, L., Zhang, Y., Ren, B., Zhong, M., et al. (2018). Integration of Antifouling and Antibacterial Properties in Salt-Responsive Hydrogels with Surface Regeneration Capacity. *J. Mater. Chem. B* 6 (6), 950–960. doi:10.1039/c7tb03018e

Zhang, D., Liu, Y., Liu, Y., Peng, Y., Tang, Y., Xiong, L., et al. (2021). A General Crosslinker Strategy to Realize Intrinsic Frozen Resistance of Hydrogels. *Adv. Mater.* 33 (42), 2104006. doi:10.1002/adma.202104006

Zhang, D., Ren, B., Zhang, Y., Xu, L., Huang, Q., He, Y., et al. (2020a). From Design to Applications of Stimuli-Responsive Hydrogel Strain Sensors. *J. Mater. Chem. B* 8 (16), 3171–3191. doi:10.1039/c9tb02692d

Zhang, D., Tang, Y., Zhang, Y., Yang, F., Liu, Y., Wang, X., et al. (2020b). Highly Stretchable, Self-Adhesive, Biocompatible, Conductive Hydrogels as Fully Polymeric Strain Sensors. *J. Mater. Chem. A.* 8 (39), 20474–20485. doi:10.1039/d0ta07390c

Zhang, D., Yang, F., He, J., Xu, L., Wang, T., Feng, Z.-Q., et al. (2020c). Multiple Physical Bonds to Realize Highly Tough and Self-Adhesive Double-Network Hydrogels. *ACS Appl. Polym. Mater.* 2 (3), 1031–1042. doi:10.1021/acsapm.9b00889

Zhao, X., Guo, B., Wu, H., Liang, Y., and Ma, P. X. (2018). Injectable Antibacterial Conductive Nanocomposite Cryogels with Rapid Shape Recovery for Noncompressible Hemorrhage and Wound Healing. *Nat. Commun.* 9 (1), 2784. doi:10.1038/s41467-018-04998-9

Zheng, M., Wang, X., Yue, O., Hou, M., Zhang, H., Beyer, S., et al. (2021). Skin-inspired Gelatin-Based Flexible Bio-Electronic Hydrogel for Wound Healing Promotion and Motion Sensing. *Biomaterials* 276, 121026. doi:10.1016/j.biomaterials.2021.121026

Zhu, Y., Zhang, J., Yang, J., Pan, C., Xu, T., and Zhang, L. (2016). Zwitterionic Hydrogels Promote Skin Wound Healing. *J. Mater. Chem. B* 4 (30), 5105–5111. doi:10.1039/c6tb00540c

Conflict of Interest: The authors declare that the research was conducted in the absence of any commercial or financial relationships that could be construed as a potential conflict of interest.

frontiers
in Bioengineering and Biotechnology

ORIGINAL RESEARCH
published: 16 March 2022
doi: 10.3389/fbioe.2022.850650

$Ti_3C_2T_x$ MXene-Coated Electrospun PCL Conduits for Enhancing Neurite Regeneration and Angiogenesis

Li-Ping Nan[1†], Zeng Lin[1†], Feng Wang[2†], Xue-Han Jin[1], Jia-Qi Fang[1], Bo Xu[1], Shu-Hao Liu[1], Fan Zhang[1], Zhong Wu[1], Zi-Fei Zhou[1], Feng Chen[1], Wen-Tao Cao[1*], Jian-Guang Wang[1*] and Jun-Jian Liu[1*]

[1]Department of Orthopedic, Shanghai Tenth People's Hospital, School of Medicine, Tongji University, Shanghai, China,
[2]Department of Spine Surgery, Shanghai East Hospital, School of Medicine, Tongji University, Shanghai, China

***Correspondence:**
Wen-Tao Cao
wt_cao@tongji.edu.cn
Jian-Guang Wang
jianguangwang@163.com
Jun-Jian Liu
liujunjian1968@126.com

†These authors have contributed equally to this work

Specialty section:
This article was submitted to Biomaterials, a section of the journal Frontiers in Bioengineering and Biotechnology

Received: 08 January 2022
Accepted: 10 February 2022
Published: 16 March 2022

Citation:
Nan L-P, Lin Z, Wang F, Jin X-H, Fang J-Q, Xu B, Liu S-H, Zhang F, Wu Z, Zhou Z-F, Chen F, Cao W-T, Wang J-G and Liu J-J (2022) $Ti_3C_2T_x$ MXene-Coated Electrospun PCL Conduits for Enhancing Neurite Regeneration and Angiogenesis. Front. Bioeng. Biotechnol. 10:850650. doi: 10.3389/fbioe.2022.850650

An electrical signal is the key basis of normal physiological function of the nerve, and the stimulation of the electric signal also plays a very special role in the repair process of nerve injury. Electric stimulation is shown to be effective in promoting axonal regeneration and myelination, thereby promoting nerve injury repair. At present, it is considered that electric conduction recovery is a key aspect of regeneration and repair of long nerve defects. Conductive neural scaffolds have attracted more and more attention due to their similar electrical properties and good biocompatibility with normal nerves. Herein, PCL and MXene-PCL nerve guidance conduits (NGCs) were prepared; their effect on nerve regeneration was evaluated *in vitro* and *in vivo*. The results show that the NGCs have good biocompatibility *in vitro*. Furthermore, a sciatic nerve defect model (15 mm) of SD rats was made, and then the fabricated NGCs were implanted. MXene-PCL NGCs show similar results with the autograft in the sciatic function index, electrophysiological examination, angiogenesis, and morphological nerve regeneration. It is possible that the conductive MXene-PCL NGC could transmit physiological neural electric signals, induce angiogenesis, and stimulate nerve regeneration. This paper presents a novel design of MXene-PCL NGC that could transmit self-originated electric stimulation. In the future, it can be combined with other features to promote nerve regeneration.

Keywords: MXene, electrical stimulation, electrospinning, peripheral nerve injuries, vascular endothelial growth factor, nerve guide conduits

INTRODUCTION

Peripheral nerve injury (PNI) can lead to persistent neurological damage in children and adults due to motor vehicle accidents, combat trauma, neoplasms, and vascular and compression disorders (Foster et al., 2018; Karsy et al., 2019; Dervan et al., 2021). Inadequate functional outcomes as nerves slowly regenerate is deemed a fundamental challenge of successful PNI recovery (Black and Lasek, 1979). At present, although autologous nerve transplantation is still the gold standard for the treatment of PNI, a lack of donor nerve sources and dysfunction of the donor site are the main limitations in clinical use (Liu et al., 2022; Wang et al., 2022). Nerve guidance conduits (NGCs) can provide a specific microenvironment for nerve repair and regeneration, promote peripheral nerve regeneration through various approaches, and become a potential substitute for autologous nerve, which has important research value and clinical application prospects (Qian et al., 2018b; Fregnan et al., 2020; Yoo et al., 2020; Zhang et al., 2020; Qian et al., 2021a; Qian et al., 2021b).

Biodegradable materials, such as polycaprolactone, chitosan, and polylactic acid, are used to fabricate NGCs in many studies (Barroca et al., 2018; Qian et al., 2020; Sun et al., 2021; Zeng et al., 2021). Electrical signals play an important role in normal nerve function and nerve regeneration (Qian et al., 2019; Qian et al., 2020; Wang et al., 2020; Kasper et al., 2021). The conductive NGC is a promising substitute for autograft in repairing PNI (Zhang et al., 2020; Zhao et al., 2020; Jin et al., 2021; Song et al., 2021). Generally, a perfect NGC usually needs to afford the appropriate mechanical properties to provide a cavity for nerve regeneration and good electrical conductivity to transmit nerve signals, promote nerve regeneration and myelination, and prevent scar tissue infiltration (Sun et al., 2019; Yan et al., 2020; Senger et al., 2021). The latest studies indicate that the electrophysiological properties of the biomaterial could be improved after being blended in the conductive particles or polymers, such as graphene, carbon nanotubes (CNTs), and $Ti_3C_2T_x$ MXene (Qian et al., 2018a; Mao et al., 2020; Rastin et al., 2020; Zhang et al., 2021). The cytotoxicity of CNTs limits their usage in the clinic (Andón and Fadeel, 2013; Zhang et al., 2022). Similarly, graphene could also lead to cytotoxicity due to its dosage (Shin et al., 2016). On the contrary, $Ti_3C_2T_x$ MXene has gradually become a research hot spot in the field of electronic biosensing and tissue engineering due to its excellent characteristics, such as decent biocompatibility, large specific surface area, and good electrical conductivity and hydrophilicity (Xu et al., 2016; Cao W. T. et al., 2019; Basara et al., 2020; Wang et al., 2021; Wei et al., 2021; Zhou et al., 2021). $Ti_3C_2T_x$ MXene can promote proliferation and differentiation in BMSCs, transmit electric signals, and accelerate tissue regeneration (Huang et al., 2020; Mao et al., 2020). We believe that the MXene composite nanofibers could be an ideal choice to provide a good microenvironment for nerve regeneration considering its excellent biocompatibility and unique nanofibrous structure. This study is aimed to explore the effects of MXene on nerve regeneration in PNI. Here, we engineer a MXene-PCL NGC by using electrospinning and spray-coated technology. The obtained MXene-PCL conduit could afford a good environment for RSC adhesion and proliferation on the PCL side. The MXene-PCL shows excellent performance in promoting nerve regeneration in a long-range sciatic nerve defect model in Sprague Dawley (SD) rats. We found that the MXene-PCL NGCs showed similar results with the autograft in restoring the nerve structure and function. These data suggest that MXene plays an important role in neural regeneration.

MATERIALS AND METHODS

Materials

The PCL pellets (CAPA6800, Perstorp Ltd, Sweden, Mw = 80,000 kDa) used in this experiment are medical grade (approved by the United States Food and Drug Administration), and melt at 60°C. Lithium fluoride (LiF ≥99%) and 2,2,2-trifluoroethanol (TFE) were purchased from Sigma (St. Louis, MO). Hydrochloric acid (HCl), absolute ethyl alcohol, and absolute methyl alcohol were purchased from Aladdin Reagents (Shanghai) Co., Ltd., China. The Ti_3AlC_2 powder was purchased from Jilin 11 technology Co., Ltd. All reagents were analytical grade.

Fabrication of Delaminated $Ti_3C_2T_x$ (D-$Ti_3C_2T_x$) MXene

The d-$Ti_3C_2T_x$ was synthesized by a typical chemical exfoliation process as we described previously with some modifications (Cao W.-T. et al., 2019). Typically, 1 g of Ti_3AlC_2 powder was dissolved in a mixture of 9 M HCl (20 ml) and 1 g LiF. Then, the obtained suspension was allowed to process for 48 h at 35°C in a water bath for etching the aluminum (Al) layer. The resultant suspension was washed repeatedly using deionized water until its pH reached about 5. Finally, the obtained sediment was further delaminated by ultrasonication in an ice bath and centrifuged to obtain uniform d-Ti_3C_2 MXene nanosheets suspension. The obtained MXene nanosheets suspension was further stored in a refrigerator at 4°C to prevent oxidation.

Fabrication of PCL and MXene–PCL NGCs

For the preparation of pure PCL NGCs, 2 g of PCL pellets was added into 12 ml of trifluoroethanol to form 17% (w/v) transparent adhesive solution with stirring for 24 h at room temperature. The NGCs were prepared by using electrospinning equipment (Changsha Nayi Instrument Technology Co., Ltd, China). Briefly, the obtained solutions were transferred into a 5-ml syringe and electrospun at 0.8 ml/h under 12-kV high DC voltage. The distance from the rotational collector (200 rpm, a tungsten steel rod with a diameter of 2 mm) to the metal needle is 25 cm. Then, the obtained PCL NGCs were gently detached. To prepare MXene-PCL NGCs, MXene solution (an aqueous solution containing 40 mg $ml-^{1}$ MXene) was uniformly coated on the outer surface of PCL NGC by spraying technology, and the thin conductive sheath was formed by spontaneous adhesion. In addition, we tried to coat the MXene on a variety of other materials (bacterial cellulose membrane, textiles, paper, Latex, and melt-blown fabric).

Characterization of the NGCs

The morphology and surface structure of MXene-PCL and PCL NGCs were characterized by a digital camera and scanning electron microscope separately, and the size and morphology of MXene nanosheets were examined using a transmission electron microscope (TEM, JEOL JEM-2010 (HT)). Fourier-transform infrared (FTIR) spectroscopy spectra was obtained using a FTIR spectrometer (Nicolet iS 10). The conductivity capability of the nano scaffolds was measured using four-point probes (ST2258C, China). The tensile stress–strain mechanical property was evaluated using an electronic tensile test machine (HY-940FS, Shanghai, China). To measure the porosity (%) of PCL scaffolds, we obtained a certain volume of PCL scaffolds and weighed the mass to calculate the density ρ_1. Furthermore, the density of PCL particles is measured as ρ_2. Then the porosity (%) of the PCL scaffolds = $(1 - (\rho_1/\rho_2)) \times 100\%$. Similarly, the density of MXene-PCL NGC was measured as ρ_3, the bulk density of

MXene and PCL was calculated as ρ_4, and the porosity (%) of the MXene-PCL scaffolds = $(1 - (\rho_3/\rho_4)) \times 100\%$.

Cell Viability Assays

Rat Schwann cells (RSCs) were provided by the Chinese Academy of Sciences (Shanghai, China). The MXene-PCL and PCL film were soaked in 75% alcohol and rinsed repeatedly with PBS at least three times. Then, they were placed in a sterile Petri dish, dried in a fume hood, and irradiated on the front and back sides for 2 h separately to achieve sterilization by an ultraviolet lamp. We seeded the cells on the PCL side of MXene-PCL scaffolds, PCL scaffolds, and TCP at a density of $2 \times 10^4\ \mathrm{cm}^{-2}$. After incubation for 24 h, a LIVE/DEAD kit (Beyotime, China) was used for cell viability analysis according to the standard protocols. Finally, cells in each group were photographed under a fluorescence microscope.

Cytotoxicity Assay

The Cell Counting Kit 8 (CCK-8, Beyotime, China) was used to assess cytotoxicity. The cells were cultured on the PCL side of MXene-PCL scaffolds and PCL scaffolds in 24-well plates for 6, 12, 24, 72, and 168 h. Subsequently, a CCK-8 detection solution was added to each well to ensure that the concentration of CCK-8 in the medium solution was 10%. After incubation at 37°C for 3 h, the absorbance of the supernatant was detected by a microplate reader (Thermo 3,001, Thermo Fischer Scientific, United States) at a wavelength of 450 nm. TCP was used as a control. This was repeated at least three times for each group.

Cell Morphology

RSCs were seeded onto the PCL side of MXene-PCL nanofiber membrane, and PCL nano scaffolds separately. After 4 days, the morphology of the cells on the different scaffolds were observed by scanning electron microscopy (ZEISS Gemini 300). First, the medium was discarded, washed with PBS, and fixed with 2.5% glutaraldehyde at room temperature for 2 h. We added 1% osmium acid and incubated at 4°C for 2 h after discarding the fixation solution, followed by alcohol gradient (10, 30, 50, 70, 80, 90, 95, 100%) dehydration for 15 min each. After drying at room temperature, SEM pictures were taken to evaluate the adhesion and morphology of cells on the different scaffolds.

In addition, phalloidin staining was also used to observe the adhesion ability and morphology of RSCs on the different scaffolds. After the cells were cultured on MXene-PCL and PCL nanoscaffolds for 4 days, the cell culture medium was discarded and washed with PBS twice. Then, the cells were fixed in 3.7% formaldehyde solution prepared by PBS at room temperature for about 20 min and washed with PBS containing 0.1% Triton X-100 three times, 5 min each. Actin-tracker Red (Beyotime, China) was diluted with PBS containing 5% BSA (Beyotime, China) and 0.1% Triton X-100 (Beyotime, China) at a ratio of 1:200. The solution was added to each slide in a ratio of 200 μl and incubated in a slide dyeing box at room temperature away from light for 60 min. Then, we washed the cells with PBS containing 0.1% Triton X-100 three times, 5 min each. Finally, a fluorescence microscope was used for observation.

In Vitro Degradation

The NGCs were dried to a constant weight, and the sample mass W_0 was recorded. Then, we placed the samples in a quantitative PBS solution at 37°C. At fixed time points, each sample was dried and weighed W_1. The formula of mass loss rate W% is as follows: $W\% = (W_0 - W_1)/W_0 \times 100\%$.

Animal Surgery

SD rats (male, weighing 150–200 g) were used to evaluate the nerve regeneration capacity. The modal rats were assigned into three groups randomly: PCL, autograft, and MXene-PCL groups. Animals were deeply anesthetized with 2% pentobarbital sodium. The sciatic nerve and its main branches were exposed, and a 15-mm long nerve defect was created under aseptic conditions. In the autograft group, the nerve was sutured end to end after rotating the nerve stump around 180°. In the PCL or MXene-PCL groups, the nerve defect was sutured with a nerve conduit. After that, the soft tissue and skin were sequentially sutured. To prevent infection, antibiotic (ceftriaxone sodium, 0.1 g/kg) was injected for three consecutive days. Postoperative assessments took place at weeks 4, 8, and 12. Ethical approval for animal studies was obtained from the Institutional Animal Care and Use Committee of Shanghai Tenth People's Hospital (SHDSYY-2021–2,305).

Sciatic Nerve Electrophysiological and Function Analysis

The rats' footprints were acquired to calculate the sciatic functional index (SFI) at weeks 4, 8, and 12 postoperative. The formula used to measure nerve function was as follows: $SFI = (13.3 \times (EIT - NIT)/NIT) + (-38.3 \times (EPL - NPL)/NPL) + (109.5 \times (ETS - NTS)/NTS) - 8.8$. In this formula, the IT stands for the distance from the second to the fourth toes; the PL represents the length from the distal of the third toe to the heel; TS is the length from the first to the fifth toe, N means the normal side, and E means the experimental side. The SFI is scored from 0 (normal function) to 100 (the function is completely impaired). Electrical signals such as compound motor action potential (CMAP) and nerve conduction velocity (NCV) were recorded by electrophysiology analysis at 12 weeks postoperative.

Gastrocnemius Muscle Weight Analysis

The wet weight of the gastrocnemius muscle was measured at week 12 after implantation. The gastrocnemius muscles from both legs were dissected, and the fat tissues attached were carefully removed with ophthalmic micro-scissors. The normalized wet weight of gastrocnemius muscle (%) = Wo/Wn, where Wo is the gastrocnemius muscle weight of the operated leg and Wn is the gastrocnemius muscle weight of the nonoperated leg.

Histological Analysis

Regenerated nerves were collected on completion of the electrophysiological experiments at week 12 postoperatively.

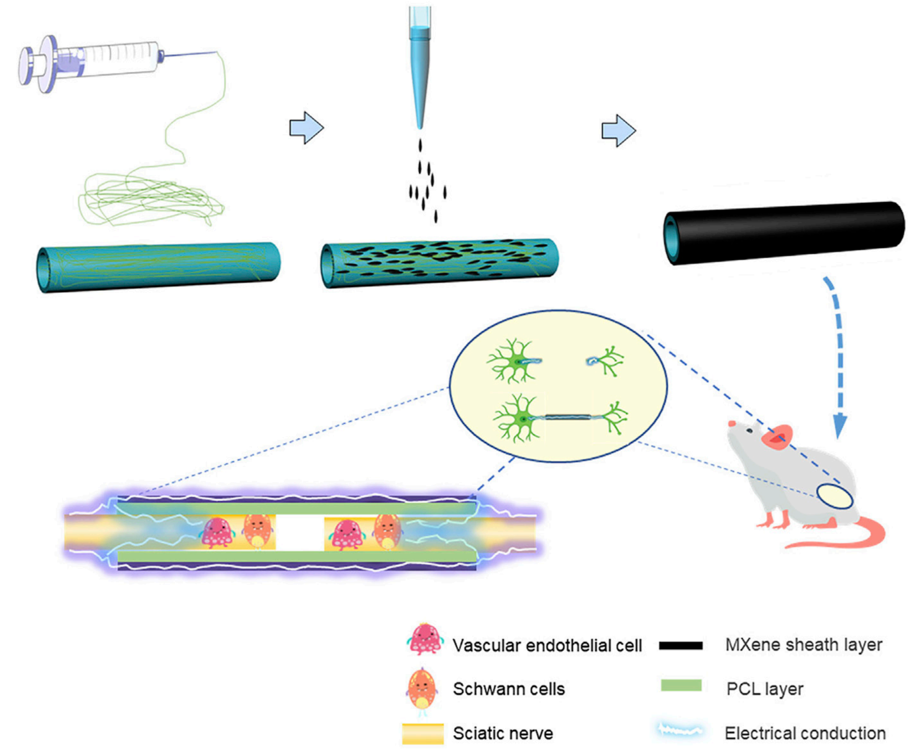

FIGURE 1 | Schematic summary illustration of the work conducted in this article. The PCL NGCs were prepared by electrospinning, to prepare MXene-PCL NGCs, MXene solution was uniformly coated on the outer surface of PCL NGC by spraying technology. The obtained MXene-PCL NGCs that could transmit self-originated electrical stimulation were implanted in the rat model and finally repaired the peripheral nerve defects.

The cross-sectional morphologies of the nerves (in the middle of the specimens) were visualized by TB staining, hematoxylin-eosin (HE) staining, and TEM. For HE staining, the samples were fixed with 4% paraformaldehyde and then embedded in paraffin, cut into sections by using a microtome. For TEM and TB staining, the tissues were fixed at 4°C in 2.5% glutaraldehyde, followed by embedding in Epon812, cut into ultrathin sections. The sections were observed using an immunofluorescence microscope (Leica, United States). The superfine microstructure of the regenerated myelin sheath was observed via a TEM (China Titan) at a voltage of 80 kV. The diameter and density of the axon and the thickness of the myelin sheath were quantitatively analyzed by ImageJ software. The S100/MBP and NF200/Tuj1 triple immunofluorescence staining were used to assess nerve myelin protein and nerve axon protein of the regenerated nerve, respectively. Tissues were fixed with 1% tetraoxide solution, dehydrated, and embedded in Epon812 resin. The cross-section was cut to a thickness of 4 μm and mounted on 2% gelatin-coated slides. The primary antibodies (Abcam, United States) included anti-Tuj1 (1:200), anti-MBP (1:200), anti-NF 200 (1:200), and anti-S100 (1:200). All slides were evaluated using an immunofluorescence microscope (Leica, United States). At week 12 after surgery, the paraffin sections of regenerated sciatic nerve sections were prepared, respectively, for immunofluorescence staining with CD34 antibody and immunohistochemistry (ICH) staining with CD31 antibody as described above. The primary antibodies included rabbit anti-CD34 antibody (1:200, ABclonal, A7429) and rabbit anti-CD31 antibody (1:200, Bioss, bs-0195R). The microvessel density (MVD) and CD 31 areas were measured by ImageJ software. The morphology of muscle fibers (from the gastrocnemius muscle of the operated leg) and major organs (heart, liver, spleen, lung, and kidney) were evaluated by HE staining.

Statistical Analysis

Images from immunofluorescence staining, TEM, HE, and immunohistochemistry staining were analyzed using Prism 8 (GraphPad, United States) and ImageJ software. All measurements were performed five times, and the results are presented as the mean ± s.d. Differences between the values were analyzed with one-way analysis with Tukey's *post hoc* with GraphPad Prism. For all figures, NS: $p > .05$; $*p < .05$.

RESULTS

Fabrication and Characterization of PCL and MXene-PCL NGCs

Long gap nerve defect still is a common clinical disease with poor prognosis, and the conductive NGCs may have clinical

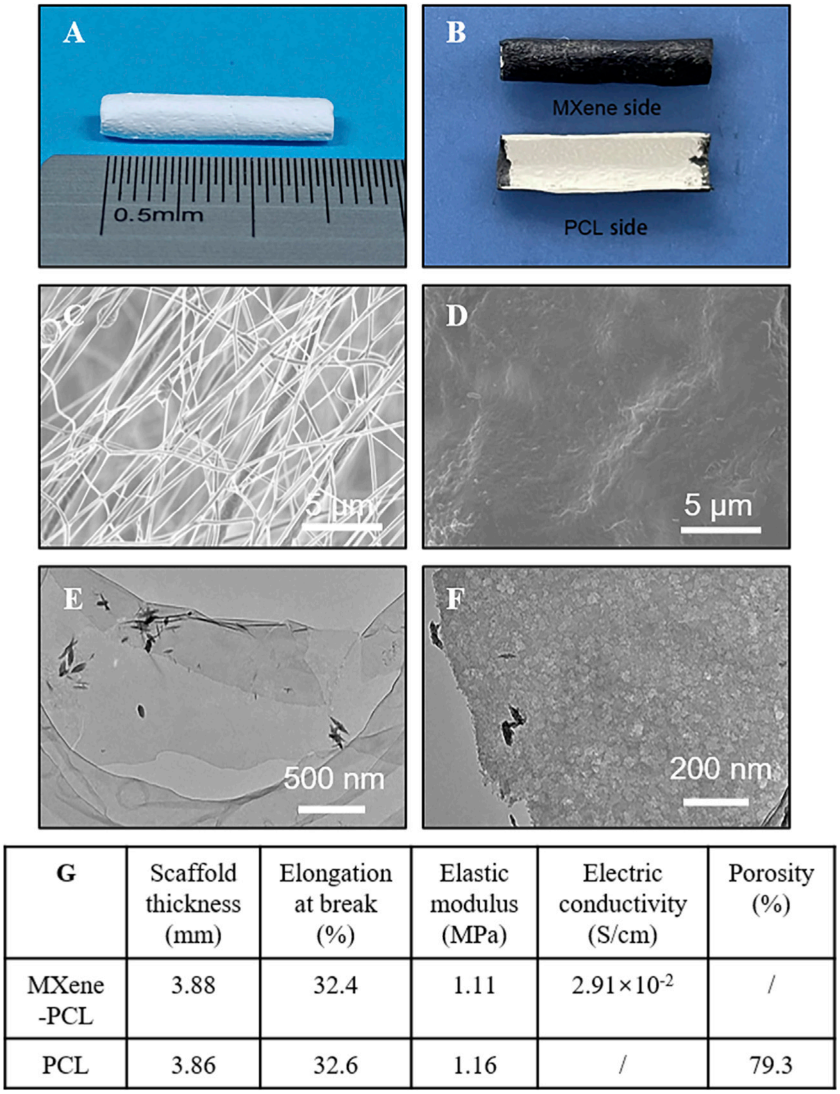

G	Scaffold thickness (mm)	Elongation at break (%)	Elastic modulus (MPa)	Electric conductivity (S/cm)	Porosity (%)
MXene -PCL	3.88	32.4	1.11	2.91×10^{-2}	/
PCL	3.86	32.6	1.16	/	79.3

FIGURE 2 | Materials characterization. Representative optical microscope pictures of the PCL NGC **(A)**, and MXene-PCL NGC **(B)**. SEM images photographed from PCL side (inner surface) **(C)** and the Mxene side (outer surface) of the MXene-PCL NGC. Low- **(E)** and high-magnification TEM image **(F)** of d-Ti_3C_2 MXene nanosheets. Summarizing table of the MXene-PCL and PCL scaffolds' mechanical and electrical characteristics **(G)**.

utility in curing this disease. MXene shows good electrical conductivity, could promote tissue regeneration, and has potential application in neural tissue engineering. There is extensive literature supporting that the optimal porosity of the NGC is a critical feature for achieving neovascularization, modulating the immune response, and nerve growth patency (Shen et al., 2021; Yu et al., 2021). In this study, we fabricated PCL NGCs by electrospinning (**Figure 1**), which had a porous structure and appropriate mechanical properties, and size (**Figure 2**). To prepare MXene-PCL NGCs, MXene solution was uniformly coated on the outer surface of PCL NGC by spraying technology, and the thin conductive sheath was formed by spontaneous adhesion. Thus, the MXene-PCL NGC with PCL inner cavity and MXene outside sheath was obtained finally. The morphologies of MXene-PCL and PCL NGCs were first characterized using an optical microscope (OM) and SEM (**Figure 2**). The obtained PCL NGC has a milky white color, and the MXene-PCL NGC showed a white inner cavity and a black shell. The infrared absorption peak of MXene-PCL composite film (MXene side as the front side) was completely consistent with those of pure MXene film, indicating that MXene formed dense films on the surface of PCL through self-adhesion (**Supplementary Figure S1**, Supporting Information). Further tests indicated that the MXene is also easy to coat on other materials (including bacterial cellulose membrane, textiles, paper, latex, and melt-blown fabric) (**Supplementary Figure S2**, Supporting Information). SEM images obtained from the PCL side of MXene-PCL film showed a loose porous appearance formed by PCL fibers interlaced. Meanwhile, the MXene sheath is

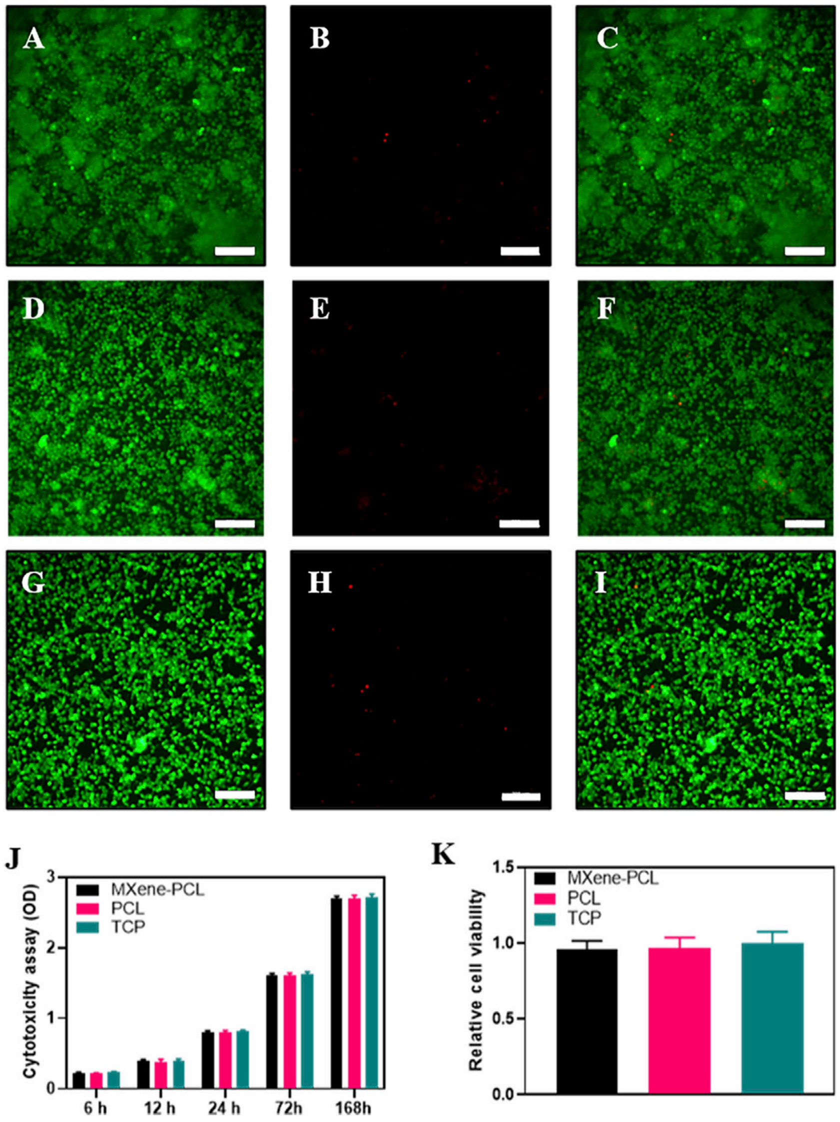

FIGURE 3 | Biocompatibility assessments. LIVE/DEAD cell staining on MXene-PCL scaffolds **(A–C)**, PCL scaffolds **(D–F)** and TCP **(G–I)**. Live cells (green fluorescence, **(A,D,G)**. Dead cells (red fluorescence, **(B,E,H)**. Merged images **(C,F,I)**. Cytotoxicity was monitored by CCK-8 assay for RSCs cultured on MXene-PCL scaffolds, PCL scaffolds, and TCP at 6, 12, 24, 72, and 168 h J). Relative cell viability was evaluated by the LIVE/DEAD cell staining for MXene-PCL scaffolds, PCL scaffolds and TCP **(H)**. Experiments were repeated three times. The scale bar is 200 μm.

relatively smooth. TEM analysis further revealed the MXene had a lamellar nanostructure. We further estimated the mechanical and electrical properties of the MXene-PCL and PCL NGCs. The scaffold thickness, average elastic modulus, and the elongation at break, and porosity results were similar for both materials (**Figure 2** and **Supplementary Figure S3**, Supporting Information). Therefore, the addition of the MXene sheath is too thin to influence these properties. The electrical conductivity changed from 0 S/cm (PCL NGC) to 2.91×10^{-2} S/cm (MXene-PCL NGC) after coating of MXene sheath. According to the results presented above, the MXene-PCL NGC exhibited excellent mechanical and topological properties, ideal rigidity and flexibility, microporosity for cell adhesion and proliferation in the PCL side, and relatively high electrical conductivity on the outer surface.

Biocompatibility of the NGCs

Biosafety is always a considerable concern for potential clinical applications of electroactive nanoparticles, such as MXene. Previous research claims that MXene-contained materials were noncytotoxic, healable, and degradable (Xu et al., 2016; Wang et al., 2019; Basara et al., 2020; Wang et al., 2021; Wei et al., 2021; Zhou et al., 2021). The design in which the MXene was coated outside the conduit rather than inside could avoid the potential toxicity caused by direct contact between the MXene particles and newly regenerated nerves to some extent. For this study, we used

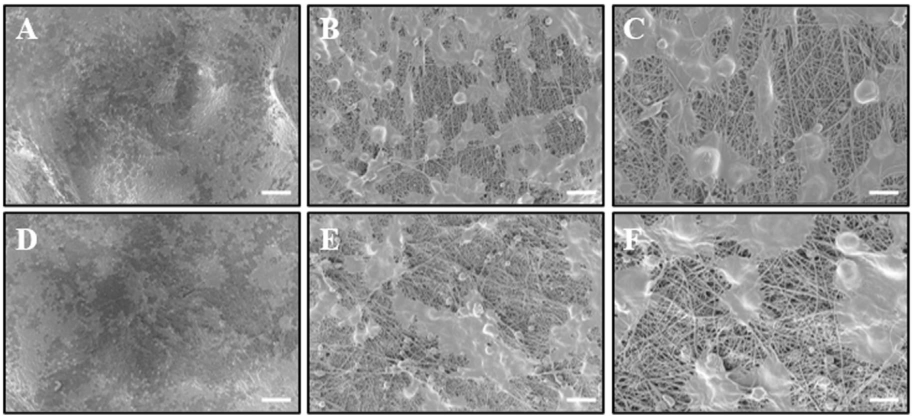

FIGURE 4 | Observation of RSC morphology on the PCL side of MXene-PCL and PCL NGC scaffolds through SEM. RSCs were seeded on the MXene side of MXene-PCL scaffold **(A–C)** and PCL scaffold **(D–F)** for 72 h before being examined by SEM. The scale bars are 100 μm **(A,D)**, 20 μm **(B,E)**, and 10 μm **(C,F)**, respectively.

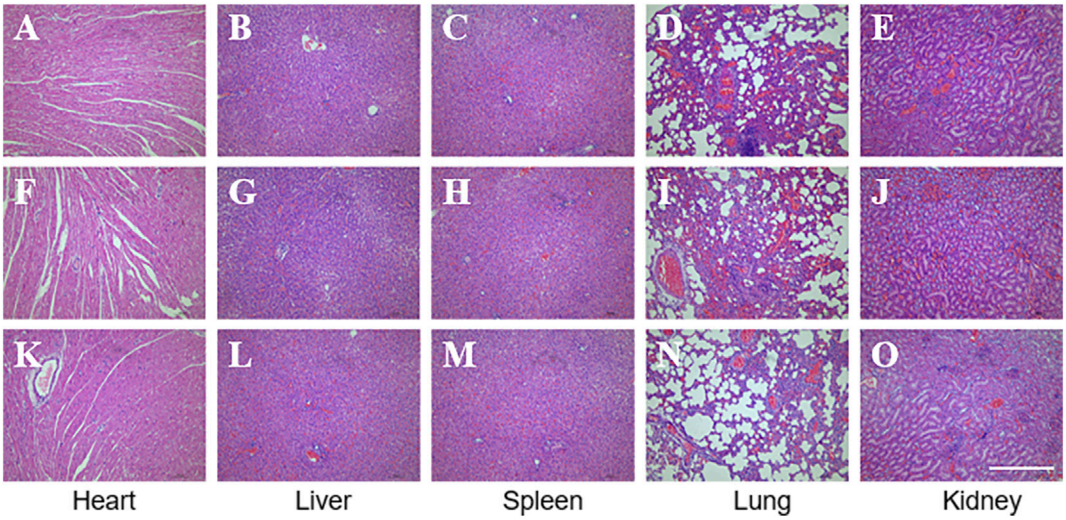

FIGURE 5 | Biosafety evaluation of MXene-based nano scaffolds *in vivo*. HE staining of the major functioning organs of Mxene-PCL group **(A–E)**, PCL group **(F–J)**, and autologous nerve graft group **(K–O)**. The scale bar is 400 μm.

Schwann cells to evaluate the potential toxicity of PCL or MXene-PCL scaffold at different time points. According to CCK-8 results, Schwann cells on both scaffolds were active and showed no statistically significant differences in cell proliferation after culturing for 6, 12, 24, 72, and 168 h compared with the TCP controls (**Figure 3**). The LIVE/DEAD test results revealed negligible differences among the TCP, MXene-PCL, and TCP groups (**Figure 3**). Cell attachment on the scaffolds is a crucial factor for cell viability. The morphology and attachment of RSCs after seeding on the scaffolds for 72 h are examined by SEM. The results show that the RSCs adhered to the surface of PCL fiber and extended many pseudopodia (**Figure 4**). Similar results could be obtained by staining actin cytoskeleton with phalloidin (**Supplementary Figure S4**, Supporting Information). Furthermore, the heart, liver, spleen, lung, and kidney were harvested from the rats at week 12 postoperatively. There were no abnormalities observed from the major organs' histological assessment (**Figure 5**). Taken as a whole, these results indicate that the MXene-PCL NGCs are biocompatible and could afford a beneficial microenvironment for cell growth and support nerve regeneration.

The modal rats were assigned into three groups randomly: PCL, autograft, and MXene-PCL groups. Postoperative assessments took place at weeks 4, 8, and 12. All rats were raised in an SPF-level environment; none was infected postoperatively. No animals showed any signs of operative complications, and the wounds healed well. At week 12, all the structures of the NGCs in animals remained intact, but the surface was degraded to a certain extent, and this can be confirmed to some extent by comparing **Figure 2** and

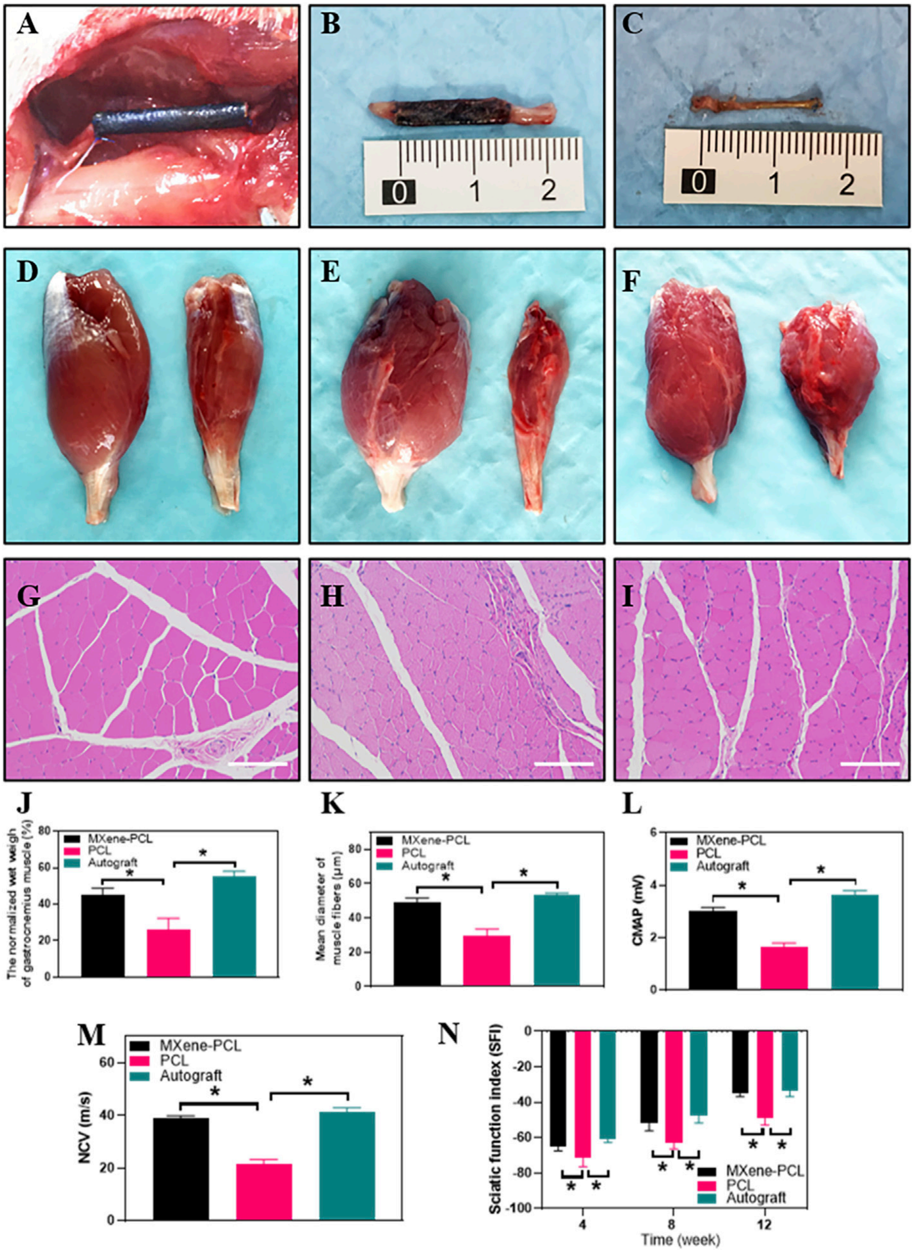

FIGURE 6 | Morphology of the MXene-PCL NGC and regenerated nerve, muscle reinnervation, SFI, and electrophysiological assessment. Morphology of MXene-PCL NGC at the time of implantation **(A)**, at 12 weeks after implantation **(B)** and the regenerated nerves obtained from Mxene-PCL NGC group **(C)**. Representative optical **(D–F)** and HE staining pictures of gastrocnemius muscle at 12 weeks postoperatively **(G–I)**. The normalized wet weight of gastrocnemius muscle **(J)**, Mean diameter of muscle fibers **(K)**, compound motor action potential **(L)**, and nerve conduction velocity at 12 weeks after implantation. The sciatic functional index assessment at 4, 8 and 12 weeks after implantation. MXene-PCL group **(A–D)**, and **(G)**; PCL group **(E,H)**; Autograft group **(F,I)**. Experiments were repeated three times. $^*p < .05$. The scale bars are 200 μm.

Supplementary Figure S5, Supporting Information. Although the degradation rate of PCL is very slow (**Supplementary Figure S5**, Supporting Information) (Lam et al., 2009), it does not affect the biocompatibility or nerve regeneration in this experiment. The pictures present the morphology of MXene-PCL NGC before and at implantation and the macroscopic view of NGCs and the regenerated nerves from different groups at 12 weeks after implantation (**Figure 6**, and **Supplementary Figure S5**, Supporting Information).

Reinnervation of Gastrocnemius Muscle

The reinnervation of the gastrocnemius muscle was evaluated 12 weeks after implantation. The gastrocnemius muscle is an

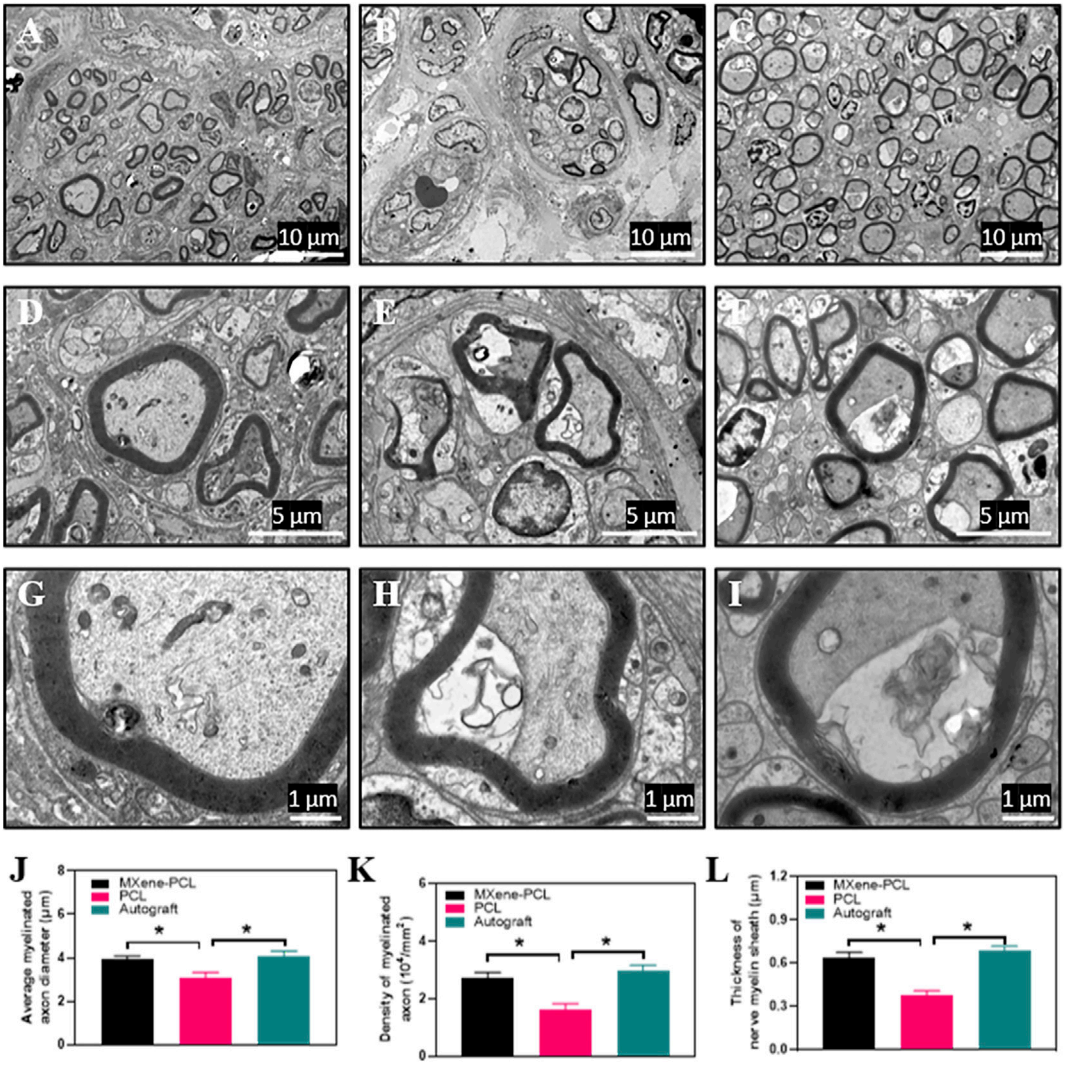

FIGURE 7 | TEM images for cross-sections of regenerated nerves from the MXene-PCL conduit **(A,D,G)**, the PCL conduit **(B,E,H)**, and the autograft **(C,F,I)**, at 12 weeks postoperatively. The statistical analysis of average myelinated axon diameter **(J)**, the density of myelinated axon **(K)** and thickness of nerve myelin sheath **(L)**. All specimens were observed by TEM. Experiments were repeated three times. $^*p < .05$. The scale bars are 10 μm **(A–C)**, 5 μm **(D–F)** and 1 μm **(G–I)**, respectively.

important target organ innervated by the sciatic nerve. Once the nerve damage occurs, the innervated muscles atrophy. To some extent, muscle recovery is positively correlated with nerve injury. The results show that the MXene-PCL group restored the muscle weight compared with the PCL group and showed no notable difference to that in the autograft groups. The diameters of muscle fibers in the MXene-PCL group were notably longer than that of the PCL group and showed no significant difference from that in the autograft group (**Figure 6**).

Functional Recovery Evaluation of Sciatic Nerve

The SFI and electrophysiological assessment methods were conducted to evaluate the functional recovery of the sciatic nerve. The step length of each paw and the length and width of the paw prints were measured according to the footprints (**Supplementary Figure S6**, Supporting Information). We found that the SFI of the MXene-PCL group (−34.9) was obviously better than the PCL group (−48.8, $p < .05$) and showed no obvious difference to that of the autograft group (−33.8, $p > .05$) at postoperative 12 weeks. Electrophysiological analysis shows that the regenerated nerve CMAP and NCV of the MXene-PCL group (38.9 m s^{-1} and 3.0 mV) were notably higher than that of the PCL group (21.4 m s^{-1} and 1.6 mV, $p < .05$) and showed no notable difference from that in the autograft groups (41.28 m s^{-1} and 3.6 mV, $p > .05$) (**Figure 6**) at 12 weeks after implantation.

Histological Analysis

For validating the morphological improvement, TEM, HE, and toluidine blue staining were performed. The results reveal that the

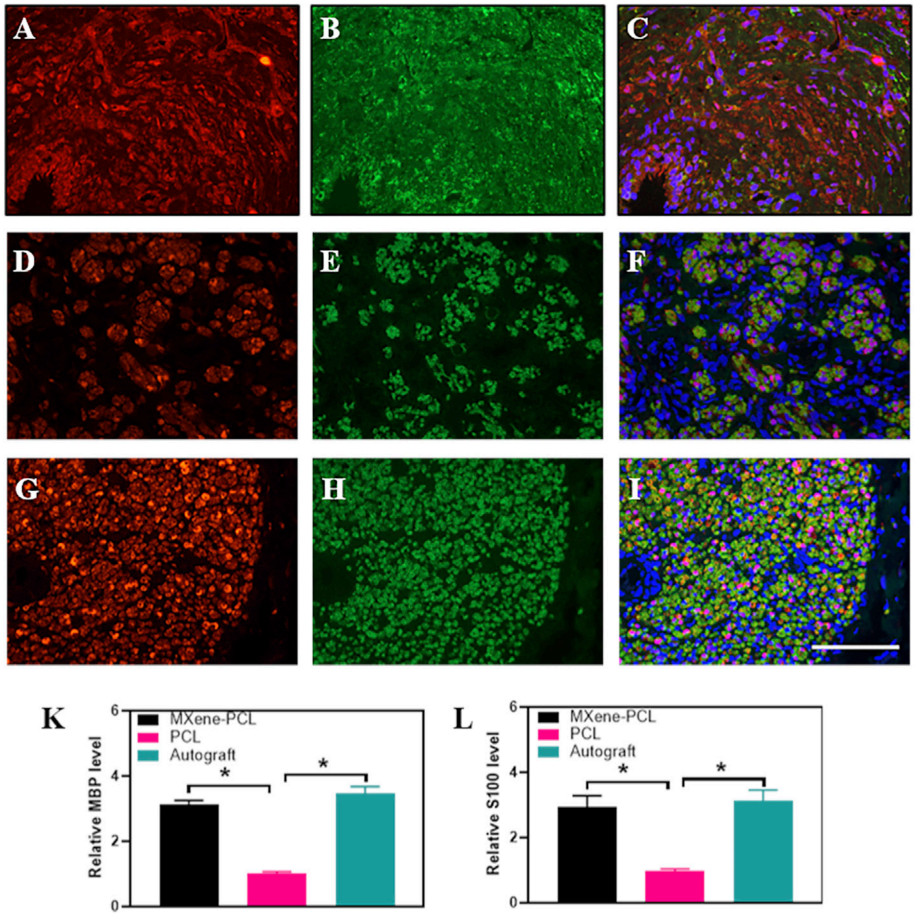

FIGURE 8 | Immunofluorescence staining of S100 (red) and MBP (green) from MXene-PCL group **(A–C)**, PCL group **(D–F)**, and autograft group **(G–I)** at 12 weeks postoperatively. The Relative expression level of MBP **(K)** and S100 **(L)**. Experiments were repeated three times. $^*p < .05$. The scale bar is 200 μm.

MXene-PCL contributed to the regeneration of nerve fibers and myelination compared with the PCL group. The myelin wrapped around the axon in a compact, multilayered spiral in the MXene-PCL and autograft groups (**Figure** 7, and **Supplementary Figure S7**, Supporting Information).

We found that the diameter and density of the myelinated axon, the thickness of the myelin sheaths of MXene-PCL group (3.91 μm, 2.71×10^4 and 0.64 μm) showed no notable difference to that in the autograft groups (4.09 μm, 2.98×10^4 and 0.685 μm), respectively (**Figure 7**). In contrast, only a few nerve fibers and many vacuoles appeared in the PCL group, and the diameter and density of myelinated axon myelin thickness were significantly less than that in the MXene-PCL and autograft groups.

To evaluate the effect of the electroconductive MXene-PCL NGC on nerve regeneration, the Schwann cell marker protein 100 (S100) and neuron-specific protein (MBP) and the typical axon protein of neurofilament protein 200 (NF200) and β-III-tubulin (Tuj 1) were evaluated by immunofluorescence staining. The results reveal that the expression level of MBP and S100 in the MXene-PCL group was 3.12 and 2.93 times higher than that in the PCL group, respectively ($p < .05$) while 3.48 and 2.93 times higher in the autograft group than that in the PCL group. The expression level of NF200 in the MXene-PCL and autograft groups was 2.16 and 2.90 times higher than that in PCL group. The expression level of Tuj 1 in the MXene-PCL and autograft groups was 3.40 and 4.22 times of the PCL group ($p < .05$). The above results confirmed that the MXene-PCL NGC effectively improved the myelination and regeneration of the nerve fibers with a similar effect to the autograft nerve (**Figure 8**, and **Supplementary Figure S8**, Supporting Information). Taking a step further, we evaluated the neovascularization by immunohistochemistry of specific protein markers of endothelial cells (CD31) and immunofluorescence of hematopoietic progenitor cell markers (CD34). It was found that the MXene-PCL and autograft groups showed more vascular-like structures than that of the PCL group by nerve cross-section staining. The average microvessel density calculated from CD34 and CD31 areas of the MXene-PCL group (43.67 mm^{-2} and 2.44 mm^2) were notably higher than that of the PCL group (26.00 mm^{-2} and 1.64 mm^2, $p < .05$) and showed no notable difference from that in the autograft groups (45.67 mm^{-2} and 2.71 mm^2, $p > .05$) at 12 weeks postoperative (**Figure 9**).

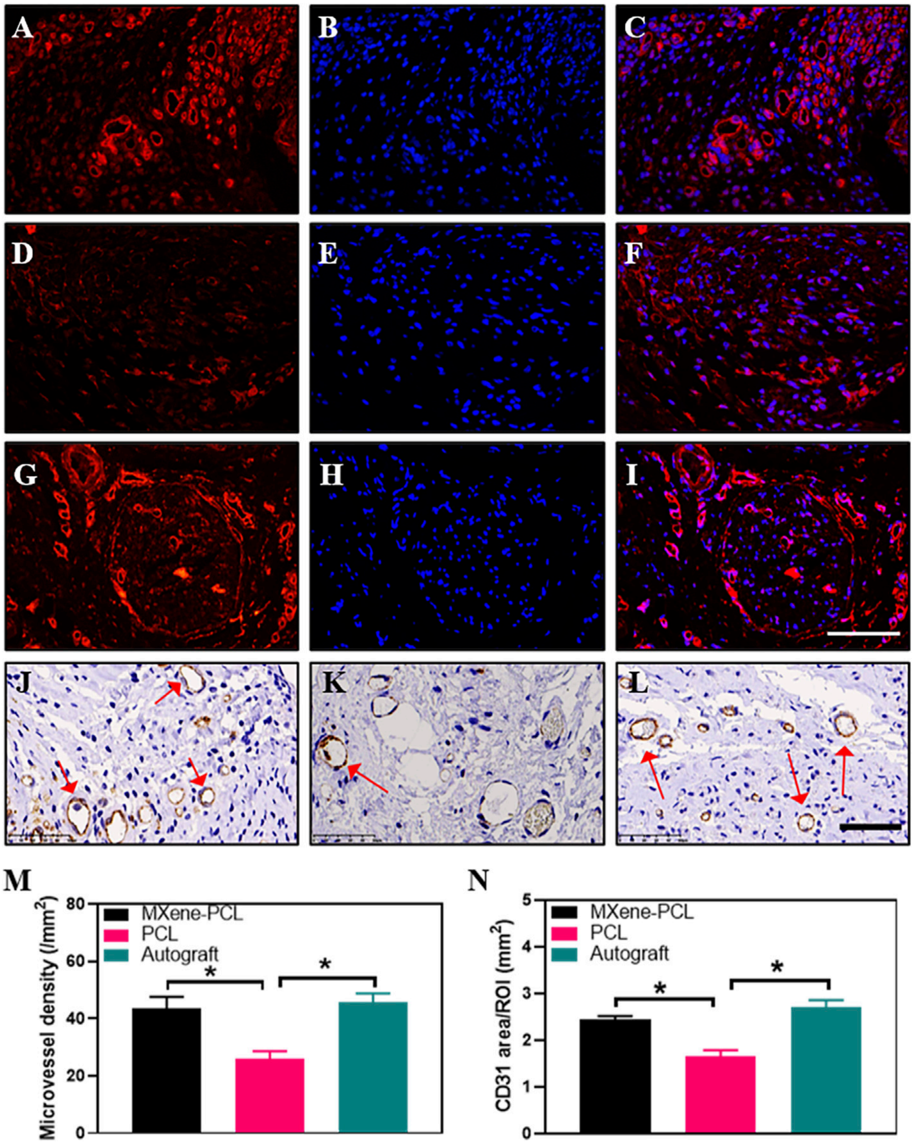

FIGURE 9 | Immunofluorescence staining for CD34 (red), DAPI (blue), and Immunohistochemistry staining for CD31 from MXene-PCL group **(A–C,J)**, PCL group **(D–F,K)**, and autograft group **(G–I,L)** at 12 weeks postoperatively. Microvessel density was calculated from CD34 staining **(M)**. CD31 area was calculated from CD31 staining **(N)**. Experiments were repeated three times. $^*p < .05$. The scale bars are 100 μm **(A–I)**, and 50 μm **(J–L)**.

DISCUSSION

Promoting nerve regeneration and transmitting electrophysiological signals are two important aspects for the repair of peripheral nerve defects (Zhao et al., 2020; Kasper et al., 2021; Kunisaki et al., 2021). The fabricated MXene-PCL NGC by electrospinning could provide suitable mechanical support, affording a necessary lumen for nerve regeneration. In addition, the nerve signal is a kind of electrical signal, the transmission of the electrical signal from upstream to downstream, and forming complete feedback is indispensable to exert its function (Silverå Ejneby et al., 2021). $Ti_3C_2T_x$ MXene is hailed as a new two-dimensional material to rival graphene. It has gradually become a research hot spot in the field of electronic biosensing and tissue engineering due to its excellent characteristics, such as decent biocompatibility, large specific surface area, good electrical conductivity, and hydrophilicity (Mao et al., 2020; Rui Li et al., 2021; Zhou et al., 2021). The facile fabrication process of the MXene-PCL NGC manufacturing process (just using the spraying method) made it easy to transformed for further applications. There are many reports on its application of probing neural activity and artificial synapse (Xu et al., 2016; Wang et al., 2021; Wei et al., 2021). $Ti_3C_2T_x$ MXene could not only promote proliferation and differentiation in BMSCs, but also transmit electric signals and accelerate tissue regeneration (Basara et al., 2020; Huang et al., 2020; Mao et al., 2020; Rastin et al., 2020). It has never been applied as an electroactive polymer for nerve regeneration *in vivo*. Here, we engineered a MXene-PCL NGC by using electrospinning and spray-coated technology; the prepared MXene-PCL membrane showed high conductivity (0.03 S/cm). Prior to *in vivo* experiments, the cell viability and affinity of the prepared materials were evaluated using RSCs cells. As anticipated, the obtained MXene-PCL conduct could afford a beneficial environment for RSC adhesion and proliferation with good cell affinity.

In addition, a 15-mm long sciatic nerve defect SD rat model was used to investigate its repair effect on nerve regeneration *in vivo*. The nerve defect was sutured with NGC or autologous nerve. The MXene-PCL NGC showed similar results with the autograft in sciatic function index, electrophysiological examination, and morphological nerve regeneration at 12 weeks postoperative. The conductive MXene-PCL NGC could transmit physiological neural electrical signals, facilitate angiogenesis, and feed to stimulate nerve regeneration. Taken together, the MXene-PCL NGC revealed better effects in promoting nerve regeneration due to the cooperation of multiple other factors: a suitable mechanical support, affording a necessary lumen (Gryshkov et al., 2021; Qian et al., 2021b), conducting of nerve signals from upstream to downstream, and forming complete feedback. As shown in **Figure 1**, the MXene-NGC could restore physiological nerve signal transduction from upstream to downstream and form complete biofeedback to the proximal and distal nerve stumps. The bioelectrical properties of cell membranes could create a vulnerable local electric field, the free electrons from the environment could create certain current through conductive material, and in our study, the additional application of conductive MXene would enhance the electric field, which, in turn, could promote cell proliferation under the interactive stimuli from surrounding cells (Heo et al., 2011; Park et al., 2011; Guo et al., 2016; Jin et al., 2021).

The conductive MXene-PCL NGC matched well with the electrophysiological properties of the sciatic nerve; meanwhile, a higher signal of CD34 and CD31 indicated the electrical signals could stimulate neovascularization. In turn, the vascular would strengthen the nutritional supply for neural functional reconstruction (Saio et al., 2021; Thibodeau et al., 2021; Wu et al., 2021; Xiaobin Li et al., 2021). The conductive MXene NGC showed a better effect in nerve regeneration than nonconductive NGC. Said another way, the conductive MXene-PCL NGC could transmit physiological neural electrical signals, creating a good microenvironment for nerve regeneration, and feeding to stimulate nerve regeneration (Zhou et al., 2016; Jin et al., 2021).

This paper presents a novel design of a MXene-PCL NGC that could transmit self-originated electrical stimulation. In the future, it can be combined with other features to promote nerve regeneration.

CONCLUSION

In summary, we prepared a conductive MXene-PCL NGC for the repair of PNI. Our data confirms that NGC supports well the attachment and proliferation of RSCs. In addition, the NGC could transmit physiological neural electrical signals and increase angiogenesis. The MXene-PCL NGC could transmit physiologic nervous electric signals, creating a good microenvironment for nerve regeneration and feeding to stimulate nerve regeneration. The design that the conductive layer was coated outside the conduit rather than inside could avoid the potential toxicity caused by direct contact between the MXene particles and newly regenerated nerves, and it is easy to prepare the MXene-PCL NGC just using the spraying method. In the near-term future, we desired to further reveal the network between electrical signals and nerve regeneration.

DATA AVAILABILITY STATEMENT

The original contributions presented in the study are included in the article/**Supplementary Material**, further inquiries can be directed to the corresponding authors.

ETHICS STATEMENT

The animal study was reviewed and approved by Experimental Animal Ethics Committee of Shanghai Tenth People's Hospital.

AUTHOR CONTRIBUTIONS

All authors helped to perform the research; L-PN, ZL, and FW wrote the paper and contributed equally to this work; W-TC, BX, and L-PN Prepared materials and carried out *in vitro* experiments; X-HJ, S-HL, and J-QF did the *in vivo* tests. FZ, ZW, Z-FZ, and FC helped analyze the data of both *in vivo* tests and simulation results. J-JL, J-GW, and W-TC are the funders for this publication, and they both revised it critically for important intellectual content, J-JL, J-GW, and W-TC are co-corresponding authors. All authors have read and approved the final manuscript.

FUNDING

The authors acknowledge financial support from the financial support from the Science and Technology Commission of Shanghai Municipality (19441901900,19ZR1439700), the Fundamental Research Funds for the Central Universities (22120210582), and China Postdoctoral Science Foundation (2021TQ0247).

SUPPLEMENTARY MATERIAL

The Supplementary Material for this article can be found online at: https://www.frontiersin.org/articles/10.3389/fbioe.2022.850650/full#supplementary-material

REFERENCES

Andón, F. T., and Fadeel, B. (2013). Programmed Cell Death: Molecular Mechanisms and Implications for Safety Assessment of Nanomaterials. *Acc. Chem. Res.* 46, 733–742. doi:10.1021/ar300020b

Barroca, N., Marote, A., Vieira, S. I., Almeida, A., Fernandes, M. H. V., Vilarinho, P. M., et al. (2018). Electrically Polarized PLLA Nanofibers as Neural Tissue Engineering Scaffolds with Improved Neuritogenesis. *Colloids Surf. B: Biointerfaces* 167, 93–103. doi:10.1016/j.colsurfb.2018.03.050

Basara, G., Saeidi-Javash, M., Ren, X., Bahcecioglu, G., Wyatt, B. C., Anasori, B., et al. (2022). Electrically Conductive 3D Printed Ti3C2T MXene-PEG Composite Constructs for Cardiac Tissue Engineering. *Acta Biomater.* 139, 179–189. doi:10.1016/j.actbio.2020.12.033

Black, M. M., and Lasek, R. J. (1979). Slowing of the Rate of Axonal Regeneration during Growth and Maturation. *Exp. Neurol.* 63, 108–119. doi:10.1016/0014-4886(79)90188-2

Cao, W.-T., Feng, W., Jiang, Y.-Y., Ma, C., Zhou, Z.-F., Ma, M.-G., et al. (2019a). Two-dimensional MXene-Reinforced Robust Surface Superhydrophobicity with Self-Cleaning and Photothermal-Actuating Binary Effects. *Mater. Horiz.* 6, 1057–1065. doi:10.1039/C8MH01566J

Cao, W. T., Ma, C., Mao, D. S., Zhang, J., Ma, M. G., and Chen, F. (2019b). MXene-Reinforced Cellulose Nanofibril Inks for 3D-Printed Smart Fibres and Textiles. *Adv. Funct. Mater.* 29, 1905898. doi:10.1002/adfm.201905898

Dervan, A., Franchi, A., Almeida-Gonzalez, F. R., Dowling, J. K., Kwakyi, O. B., Mccoy, C. E., et al. (2021). Biomaterial and Therapeutic Approaches for the Manipulation of Macrophage Phenotype in Peripheral and Central Nerve Repair. *Pharmaceutics* 13, 2161. doi:10.3390/pharmaceutics13122161

Foster, C. H., Karsy, M., Jensen, M. R., Guan, J., Eli, I., and Mahan, M. A. (2019). Trends and Cost-Analysis of Lower Extremity Nerve Injury Using the National Inpatient Sample. *Neurosurg.* 85, 250–256. doi:10.1093/neuros/nyy265

Fregnan, F., Muratori, L., Bassani, G. A., Crosio, A., Biagiotti, M., Vincoli, V., et al. (2020). Preclinical Validation of SilkBridgeTM for Peripheral Nerve Regeneration. *Front. Bioeng. Biotechnol.* 8, 835. doi:10.3389/fbioe.2020.00835

Gryshkov, O., Al Halabi, F., Kuhn, A. I., Leal-Marin, S., Freund, L. J., Förthmann, M., et al. (2021). PVDF and P(VDF-TrFE) Electrospun Scaffolds for Nerve Graft Engineering: A Comparative Study on Piezoelectric and Structural Properties, and *In Vitro* Biocompatibility. *Int. J. Mol. Sci.* 22, 11373. doi:10.3390/ijms222111373

Guo, R., Zhang, S., Xiao, M., Qian, F., He, Z., Li, D., et al. (2016). Accelerating Bioelectric Functional Development of Neural Stem Cells by Graphene Coupling: Implications for Neural Interfacing with Conductive Materials. *Biomaterials* 106, 193–204. doi:10.1016/j.biomaterials.2016.08.019

Hao, P., Yang, Z.-Y., Li, X.-G., Liu, F.-D., Duan, H.-M., Hao, F., et al. (2022). Biomimetic Chitosan Scaffolds with Long-Term Controlled Release of Nerve Growth Factor Repairs 20-Mm-Long Sciatic Nerve Defects in Rats. *Neural Regen. Res.* 17, 1146–1155. doi:10.4103/1673-5374.324860

Heo, C., Yoo, J., Lee, S., Jo, A., Jung, S., Yoo, H., et al. (2011). The Control of Neural Cell-To-Cell Interactions through Non-contact Electrical Field Stimulation Using Graphene Electrodes. *Biomaterials* 32, 19–27. doi:10.1016/j.biomaterials.2010.08.095

Huang, R., Chen, X., Dong, Y., Zhang, X., Wei, Y., Yang, Z., et al. (2020). MXene Composite Nanofibers for Cell Culture and Tissue Engineering. *ACS Appl. Bio Mater.* 3, 2125–2131. doi:10.1021/acsabm.0c00007

Jin, F., Li, T., Yuan, T., Du, L., Lai, C., Wu, Q., et al. (2021). Physiologically Self-Regulated, Fully Implantable, Battery-free System for Peripheral Nerve Restoration. *Adv. Mater.* 33, 2104175. doi:10.1002/adma.202104175

Karsy, M., Watkins, R., Jensen, M. R., Guan, J., Brock, A. A., and Mahan, M. A. (2019). Trends and Cost Analysis of Upper Extremity Nerve Injury Using the National (Nationwide) Inpatient Sample. *World Neurosurg.* 123, e488–e500. doi:10.1016/j.wneu.2018.11.192

Kasper, M., Ellenbogen, B., Hardy, R., Cydis, M., Mojica-Santiago, J., Afridi, A., et al. (2021). Development of a Magnetically Aligned Regenerative Tissue-Engineered Electronic Nerve Interface for Peripheral Nerve Applications. *Biomaterials* 279, 121212. doi:10.1016/j.biomaterials.2021.121212

Kunisaki, A., Kodama, A., Ishikawa, M., Ueda, T., Lima, M. D., Kondo, T., et al. (2021). Carbon-nanotube Yarns Induce Axonal Regeneration in Peripheral Nerve Defect. *Sci. Rep.* 11, 19562. doi:10.1038/s41598-021-98603-7

Lam, C. X. F., Hutmacher, D. W., Schantz, J.-T., Woodruff, M. A., and Teoh, S. H. (2009). Evaluation of Polycaprolactone Scaffold Degradation for 6 Monthsin Vitroandin Vivo. *J. Biomed. Mater. Res.* 90A, 906–919. doi:10.1002/jbm.a.32052

Mao, L., Hu, S., Gao, Y., Wang, L., Zhao, W., Fu, L., et al. (2020). Biodegradable and Electroactive Regenerated Bacterial Cellulose/MXene (Ti 3 C 2 T X) Composite Hydrogel as Wound Dressing for Accelerating Skin Wound Healing under Electrical Stimulation. *Adv. Healthc. Mater.* 9, 2000872. doi:10.1002/adhm.202000872

Park, S. Y., Park, J., Sim, S. H., Sung, M. G., Kim, K. S., Hong, B. H., et al. (2011). Enhanced Differentiation of Human Neural Stem Cells into Neurons on Graphene. *Adv. Mater.* 23, H263–H267. doi:10.1002/adma.201101503

Qian, Y., Cheng, Y., Cai, J., Zhao, X., Ouyang, Y., Yuan, W.-E., et al. (2019). Advances in Electrical and Magnetic Stimulation on Nerve Regeneration. *Regenerative Med.* 14, 969–979. doi:10.2217/rme-2018-0079

Qian, Y., Cheng, Y., Song, J., Xu, Y., Yuan, W. E., Fan, C., et al. (2020). Mechano-Informed Biomimetic Polymer Scaffolds by Incorporating Self-Powered Zinc Oxide Nanogenerators Enhance Motor Recovery and Neural Function. *Small* 16, 2000796. doi:10.1002/smll.202000796

Qian, Y., Song, J., Zhao, X., Chen, W., Ouyang, Y., Yuan, W., et al. (2018a). 3D Fabrication with Integration Molding of a Graphene Oxide/Polycaprolactone Nanoscaffold for Neurite Regeneration and Angiogenesis. *Adv. Sci.* 5, 1700499. doi:10.1002/advs.201700499

Qian, Y., Zhao, X., Han, Q., Chen, W., Li, H., and Yuan, W. (2018b). An Integrated Multi-Layer 3D-Fabrication of PDA/RGD Coated Graphene Loaded PCL Nanoscaffold for Peripheral Nerve Restoration. *Nat. Commun.* 9, 323. doi:10.1038/s41467-017-02598-7

Qian, Y., Lin, H., Yan, Z., Shi, J., and Fan, C. (2021a). Functional Nanomaterials in Peripheral Nerve Regeneration: Scaffold Design, Chemical Principles and Microenvironmental Remodeling. *Mater. Today* 51, 165–187. doi:10.1016/j.mattod.2021.09.014

Qian, Y., Wang, X., Song, J., Chen, W., Chen, S., Jin, Y., et al. (2021b). Preclinical Assessment on Neuronal Regeneration in the Injury-Related Microenvironment of Graphene-Based Scaffolds. *NPJ Regen. Med.* 6, 31. doi:10.1038/s41536-021-00142-2

Rastin, H., Zhang, B., Mazinani, A., Hassan, K., Bi, J., Tung, T. T., et al. (2020). 3D Bioprinting of Cell-Laden Electroconductive MXene Nanocomposite Bioinks. *Nanoscale* 12, 16069–16080. doi:10.1039/d0nr02581j

Rui Li, R., Xu, J., Rao, Z., Deng, R., Xu, Y., Qiu, S., et al. (2021). Facilitate Angiogenesis and Neurogenesis by Growth Factors Integrated Decellularized Matrix Hydrogel. *Tissue Eng. A* 27, 771–787. doi:10.1089/ten.TEA.2020.0227

Saio, S., Konishi, K., Hohjoh, H., Tamura, Y., Masutani, T., Iddamalgoda, A., et al. (2021). Extracellular Environment-Controlled Angiogenesis, and Potential Application for Peripheral Nerve Regeneration. *Int. J. Mol. Sci.* 22, 11169. doi:10.3390/ijms222011169

Senger, J.-L. B., Rabey, K. N., Acton, L., Lin, Y.-H. S., Lingrell, S., Chan, K. M., et al. (2021). Recovering the Regenerative Potential in Chronically Injured Nerves by Using Conditioning Electrical Stimulation. *J. Neurosurg.*, 1–13. doi:10.3171/2021.4.jns21398

Shen, J., Wang, J., Liu, X., Sun, Y., Yin, A., Chai, Y., et al. (2021). *In Situ* Prevascularization Strategy with Three-Dimensional Porous Conduits for Neural Tissue Engineering. *ACS Appl. Mater. Inter.* 13, 50785–50801. doi:10.1021/acsami.1c16138

Shin, S. R., Li, Y.-C., Jang, H. L., Khoshakhlagh, P., Akbari, M., Nasajpour, A., et al. (2016). Graphene-based Materials for Tissue Engineering. *Adv. Drug Deliv. Rev.* 105, 255–274. doi:10.1016/j.addr.2016.03.007

Silverå Ejneby, M., Jakešová, M., Ferrero, J. J., Migliaccio, L., Sahalianov, I., Zhao, Z., et al. (2021). Chronic Electrical Stimulation of Peripheral Nerves via Deep-Red Light Transduced by an Implanted Organic Photocapacitor. *Nat. Biomed. Eng.* doi:10.1038/s41551-021-00817-7

Song, S., Mcconnell, K. W., Amores, D., Levinson, A., Vogel, H., Quarta, M., et al. (2021). Electrical Stimulation of Human Neural Stem Cells via Conductive Polymer Nerve Guides Enhances Peripheral Nerve Recovery. *Biomaterials* 275, 120982. doi:10.1016/j.biomaterials.2021.120982

Sun, X., Bai, Y., Zhai, H., Liu, S., Zhang, C., Xu, Y., et al. (2019). Devising Micro/nano-Architectures in Multi-Channel Nerve Conduits towards a Pro-regenerative Matrix for the Repair of Spinal Cord Injury. *Acta Biomater.* 86, 194–206. doi:10.1016/j.actbio.2018.12.032

Sun, Y., Chi, X., Meng, H., Ma, M., Wang, J., Feng, Z., et al. (2021). Polylysine-decorated Macroporous Microcarriers Laden with Adipose-Derived Stem Cells Promote Nerve Regeneration *In Vivo*. *Bioactive Mater.* 6, 3987–3998. doi:10.1016/j.bioactmat.2021.03.029

Thibodeau, A., Galbraith, T., Fauvel, C. M., Khuong, H. T., and Berthod, F. (2022). Repair of Peripheral Nerve Injuries Using a Prevascularized Cell-Based Tissue-Engineered Nerve Conduit. *Biomaterials* 280, 121269. doi:10.1016/j.biomaterials.2021.121269

Wang, Y., Wang, X., Li, X., Bai, Y., Xiao, H., Liu, Y., et al. (2019). Engineering 3D Ion Transport Channels for Flexible MXene Films with superior Capacitive Performance. *Adv. Funct. Mater.* 29, 1900326. doi:10.1002/adfm.201900326

Wang, Y., Zhang, Y., Zhang, Z., Su, Y., Wang, Z., Dong, M., et al. (2020). An Injectable High-Conductive Bimaterial Scaffold for Neural Stimulation. *Colloids Surf. B: Biointerfaces* 195, 111210. doi:10.1016/j.colsurfb.2020.111210

Wang, K., Jia, Y., and Yan, X. (2021). Neuro-Receptor Mediated Synapse Device Based on Crumpled MXene Ti 3 C 2 T X Nanosheets. *Adv. Funct. Mater.* 31, 2104304. doi:10.1002/adfm.202104304

Wang, B., Kou, Y.-H., Jiang, B.-G., Lu, C.-F., Liu, Z.-Y., Han, S., et al. (2022). Chitin Scaffold Combined with Autologous Small Nerve Repairs Sciatic Nerve Defects. *Neural Regen. Res.* 17, 1106–1114. doi:10.4103/1673-5374.324859

Wei, H., Yu, H., Gong, J., Ma, M., Han, H., Ni, Y., et al. (2021). Redox MXene Artificial Synapse with Bidirectional Plasticity and Hypersensitive Responsibility. *Adv. Funct. Mater.* 31, 2007232. doi:10.1002/adfm.202007232

Wu, P., Tong, Z., Luo, L., Zhao, Y., Chen, F., Li, Y., et al. (2021). Comprehensive Strategy of Conduit Guidance Combined with VEGF Producing Schwann Cells Accelerates Peripheral Nerve Repair. *Bioactive Mater.* 6, 3515–3527. doi:10.1016/j.bioactmat.2021.03.020

Xiaobin Li, X., He, L., Li, Y., Chao, M., Li, M., Wan, P., et al. (2021). Healable, Degradable, and Conductive MXene Nanocomposite Hydrogel for Multifunctional Epidermal Sensors. *ACS Nano* 15, 7765–7773. doi:10.1021/acsnano.1c01751

Xu, B., Zhu, M., Zhang, W., Zhen, X., Pei, Z., Xue, Q., et al. (2016). Ultrathin MXene-Micropattern-Based Field-Effect Transistor for Probing Neural Activity. *Adv. Mater.* 28, 3333–3339. doi:10.1002/adma.201504657

Yan, J., Wu, R., Liao, S., Jiang, M., and Qian, Y. (2020). Applications of Polydopamine-Modified Scaffolds in the Peripheral Nerve Tissue Engineering. *Front. Bioeng. Biotechnol.* 8, 590998. doi:10.3389/fbioe.2020.590998

Yoo, J., Park, J. H., Kwon, Y. W., Chung, J. J., Choi, I. C., Nam, J. J., et al. (2020). Augmented Peripheral Nerve Regeneration through Elastic Nerve Guidance Conduits Prepared Using a Porous PLCL Membrane with a 3D Printed Collagen Hydrogel. *Biomater. Sci.* 8, 6261–6271. doi:10.1039/d0bm00847h

Yu, J., Lin, Y., Wang, G., Song, J., Hayat, U., Liu, C., et al. (2022). Zein-induced Immune Response and Modulation by Size, Pore Structure and Drug-Loading: Application for Sciatic Nerve Regeneration. *Acta Biomater.* 140, 289–301. doi:10.1016/j.actbio.2021.11.035

Zeng, W., Hui, H., Liu, Z., Chang, Z., Wang, M., He, B., et al. (2021). TPP Ionically Cross-Linked Chitosan/PLGA Microspheres for the Delivery of NGF for Peripheral Nerve System Repair. *Carbohydr. Polym.* 258, 117684. doi:10.1016/j.carbpol.2021.117684

Zhang, D., Yao, Y., Duan, Y., Yu, X., Shi, H., Nakkala, J. R., et al. (2020). Surface-Anchored Graphene Oxide Nanosheets on Cell-Scale Micropatterned Poly(d,l-Lactide-Co-Caprolactone) Conduits Promote Peripheral Nerve Regeneration. *ACS Appl. Mater. Inter.* 12, 7915–7930. doi:10.1021/acsami.9b20321

Zhang, J., Zhang, X., Wang, C., Li, F., Qiao, Z., Zeng, L., et al. (2021). Conductive Composite Fiber with Optimized Alignment Guides Neural Regeneration under Electrical Stimulation. *Adv. Healthc. Mater.* 10, 2000604. doi:10.1002/adhm.202000604

Zhang, Y., Li, X., Liang, J., Luo, Y., Tang, N., Ye, S., et al. (2022). Microcystis Aeruginosa's Exposure to an Antagonism of Nanoplastics and MWCNTs: The Disorders in Cellular and Metabolic Processes. *Chemosphere* 288, 132516. doi:10.1016/j.chemosphere.2021.132516

Zhao, Y., Liang, Y., Ding, S., Zhang, K., Mao, H.-q., and Yang, Y. (2020). Application of Conductive PPy/SF Composite Scaffold and Electrical Stimulation for Neural Tissue Engineering. *Biomaterials* 255, 120164. doi:10.1016/j.biomaterials.2020.120164

Zhou, Z.-F., Zhang, F., Wang, J.-G., Chen, Q.-C., Yang, W.-Z., He, N., et al. (2016). Electrospinning of PELA/PPY Fibrous Conduits: Promoting Peripheral Nerve Regeneration in Rats by Self-Originated Electrical Stimulation. *ACS Biomater. Sci. Eng.* 2, 1572–1581. doi:10.1021/acsbiomaterials.6b00335

Zhou, L., Zheng, H., Liu, Z., Wang, S., Liu, Z., Chen, F., et al. (2021). Conductive Antibacterial Hemostatic Multifunctional Scaffolds Based on Ti3C2Tx MXene Nanosheets for Promoting Multidrug-Resistant Bacteria-Infected Wound Healing. *ACS Nano* 15, 2468–2480. doi:10.1021/acsnano.0c06287

Conflict of Interest: The authors declare that the research was conducted in the absence of any commercial or financial relationships that could be construed as a potential conflict of interest.

frontiers | Frontiers in Bioengineering and Biotechnology

ORIGINAL RESEARCH
published: 16 May 2022
doi: 10.3389/fbioe.2022.850184

Parametric Design of Hip Implant With Gradient Porous Structure

Xiangsheng Gao[1,2], Yuhang Zhao[1], Min Wang[1], Ziyu Liu[2,3] and Chaozong Liu[2]**

[1]Beijing Key Laboratory of Advanced Manufacturing Technology, Faculty of Materials and Manufacturing, Beijing University of Technology, Beijing, China, [2]Division of Surgery and Interventional Science, University College London, Royal National Orthopaedic Hospital, London, United Kingdom, [3]School of Engineering Medicine, Beihang University, Beijing, China

Edited by:
Yun Qian,
Shanghai Jiao Tong University, China

Reviewed by:
Yuting Lv,
Shandong University of Science and Technology, China
Ningxia Yin,
Guangdong Ocean University, China
Ying Ba,
North China University of Science and Technology, China
Qiang Chen,
Southeast University, China
Fang Han,
Dalian University of Technology, China

Correspondence:
Ziyu Liu
liu_ziyu@buaa.edu.cn
Chaozong Liu
chaozong.liu@ucl.ac.uk

Specialty section:
This article was submitted to Biomaterials, a section of the journal Frontiers in Bioengineering and Biotechnology

Received: *07 January 2022*
Accepted: *11 April 2022*
Published: *16 May 2022*

Citation:
Gao X, Zhao Y, Wang M, Liu Z and Liu C (2022) Parametric Design of Hip Implant With Gradient Porous Structure. Front. Bioeng. Biotechnol. 10:850184. doi: 10.3389/fbioe.2022.850184

Patients who has been implanted with hip implant usually undergo revision surgery. The reason is that high stiff implants would cause non-physiological distribution loadings, which is also known as stress shielding, and finally lead to bone loss and aseptic loosening. Titanium implants are widely used in human bone tissues; however, the subsequent elastic modulus mismatch problem has become increasingly serious, and can lead to stress-shielding effects. This study aimed to develop a parametric design methodology of porous titanium alloy hip implant with gradient elastic modulus, and mitigate the stress-shielding effect. Four independent adjustable dimensions of the porous structure were parametrically designed, and the Kriging algorithm was used to establish the mapping relationship between the four adjustable dimensions and the porosity, surface-to-volume ratio, and elastic modulus. Moreover, the equivalent stress on the surface of the femur was optimized by response surface methodology, and the optimal gradient elastic modulus of the implant was obtained. Finally, through the Kriging approximation model and optimization results of the finite element method, the dimensions of each segment of the porous structure that could effectively mitigate the stress-shielding effect were determined. Experimental results demonstrated that the parameterized design method of the porous implant with gradient elastic modulus proposed in this study increased the strain value on the femoral surface by 17.1% on average. Consequently, the stress-shielding effect of the femoral tissue induced by the titanium alloy implant was effectively mitigated.

Keywords: hip implant, stress-shielding, kriging algorithm, gradient porous structure, parametric design

Highlights

- ➢ Propose a Kriging-based parametric design method for gradient porous structure.
- ➢ Optimize the elastic modulus based on the response surface methodology to adjust the stress distribution of femur.
- ➢ Develop an implant with gradient porous structure to mitigate the stress-shielding effect and verified by experiments.

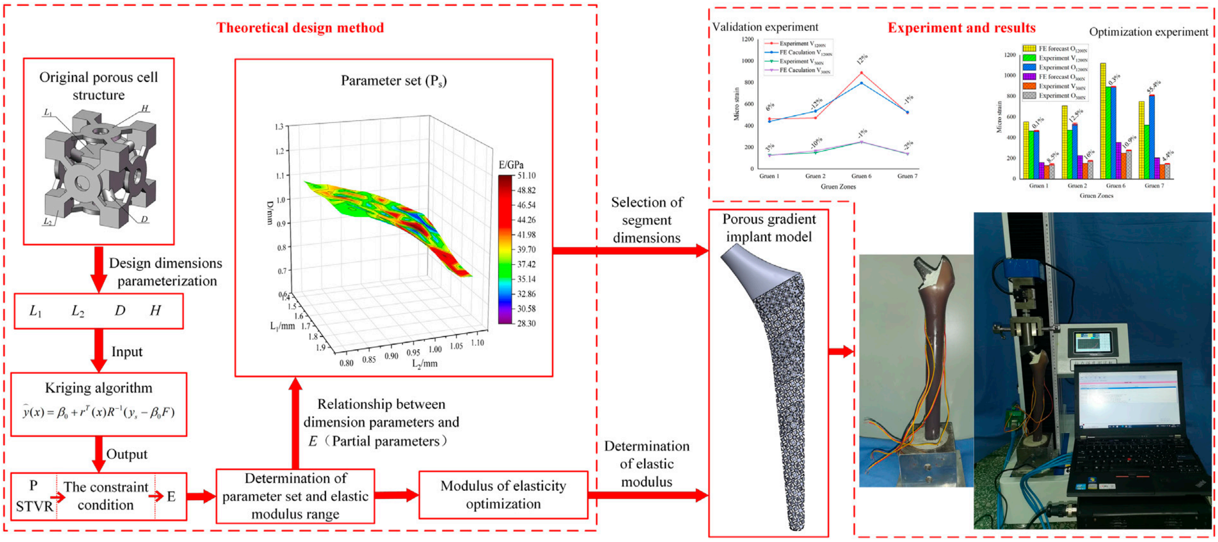

GRAPHICAL ABSTRACT |

INTRODUCTION

Patients who has been implanted with hip implant may suffer secondary injuries after periprosthetic fracture or feeling severe painfulness. One of the reasons is that high stiff implants would cause non-physiological distribution loadings, which is also known as stress shielding, and finally lead to bone loss and aseptic loosening (Naghavi et al., 2019).

However, inserting a stiff implant into human body would result in non-physiological distribution loadings (Ahmed et al., 2020). In that case, it would cause a decrease of the periprosthetic bone strain (Huiskes et al., 1992) and then lead to bone loss and aseptic loosening (Xu and Robinson, 2008; Jeyapalina et al., 2014). Managing stress distribution would one of the main issue for implants, and the design should provide suitable strain-related stimulus for altering bone mass by bone remodeling (bone resorption or bone apposition) (Prendergast and Taylor, 1994).

In recent years, cellular metallic structures are of particular interest in orthopedic implant applications, since they can be effectively used for the replacement of broken or damaged bones (Abate et al., 2021). In all metal implant materials that can be designed for cell structure, titanium alloys are promising materials used as bone implants due to their unique properties such as high specific strength, excellent biocompatibility, and corrosion resistance (Geetha et al., 2009; Niinomi et al., 2012). Nevertheless, the elastic modulus of human bone (<30 GPa) is much lower than that of solid titanium (~110 GPa) (Abdel-Hady Gepreel and Niinomi, 2013). The mismatch of the elastic modulus between bone tissues and solid implants causes stress shielding that can weaken the bone and stop bone growth. Previous studies have reported that this stress can be reduced by implants with porous structure, mainly by adjusting their pore size and porosity (Gibson, 2005), (Honda et al., 2013). For example, trabecular metal with a porous structure has been found in several studies to show good results in revision arthroplasty for severe acetabular bone loss (Christie, 2002; Flecher, Sporer, and Paprosky, 2008; Davies et al., 2011). Such porous structures have been proven to provide a firm fixation of the implant (Nazir et al., 2019), since they can not only reduce the elastic modulus of the titanium alloy, but also facilitate bone osseointegration (Takemoto et al., 2005; Wiria et al., 2010; Torres-Sanchez et al., 2017) and in-growth (Babaie and Bhaduri, 2018).

More specifically, the elastic modulus of a titanium alloy can be adjusted by the design of the porous structure, thereby mitigating the stress shielding effect. The elastic modulus of an implant can be custom-defined, and by controlling the porosity, the implant can obtain mechanical properties and structure similar to those of bone (Yan et al., 2015). For example, Lee et al. (2014) investigated the effect of space scaffolding on the structure and mechanical properties of porous titanium, and they concluded that porosity determines the modulus of elasticity. Mullen (Mullen et al., 2009) constructed a honeycomb titanium structure based on octahedral cells and Arabnejad (Arabnejad et al., 2016) developed two high-strength tensile dominant topologies; both exhibited the potential of such structures for orthopaedic implants. Based on newly-designed honeycomb structures and five different existing honeycomb structures, Abate et al. (2020) discussed the optimization effects of cell size, lattice topology, porosity, and honeycomb structure on mechanical properties. Their results demonstrated that the optimized honeycomb structures had much lower stress and deformation. Xu et al. (2021) investigated six composite lattice structures with different support radii consisting of simple cubic, body-centered cubic (BCC), and edge-centered cubic cells. Luxner et al. (2007) and Han et al. (2017) also suggested that BCC structures can have relatively higher porosity controllability and better mechanical properties than other structures. Among these structures, the BCC structure was found more suitable for parametric design. The excellent properties of the BCC structure had also been demonstrated experimentally by Cuadrado (Cuadrado et al., 2017).

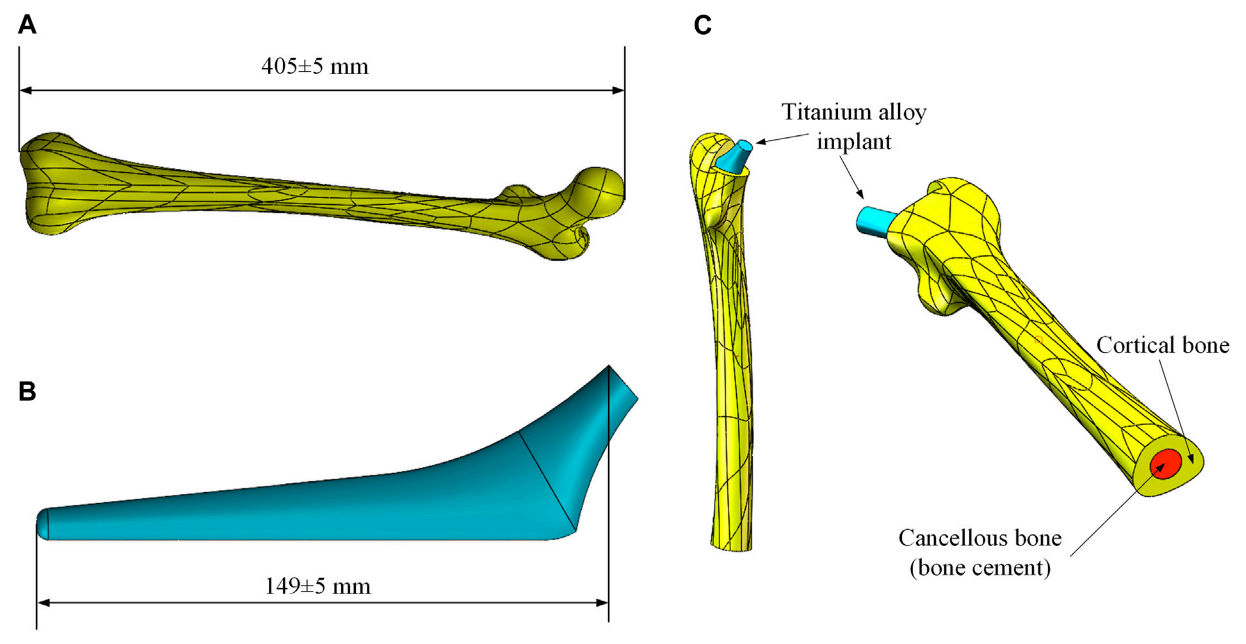

FIGURE 1 | Femur and implant models. **(A)** Femoral model; **(B)** Titanium alloy implant model; **(C)** Combined models.

Previous studies have assessed the actual performance of implants using porous structures within the femur. For instance, in order to reduce the stiffness and allow the inward growth of bone tissue, Jetté et al. (2018) proposed a hip implant design characterized by a porous structure based on a diamond cubic lattice. Alkhatib et al. (2019) developed finite element (FE) models of titanium alloy porous implants and effective porous implants, and verified that porosity affects the stress-shielding effect. Functional gradient materials (FGM) have gradually become the focus of the implant structure research, providing a new method for implant structure design (Moussa et al., 2020). To minimize the stress shielding effect and extend the life of implants, Sun et al. (2018) developed a FE model for bone implants and provided a general approach for designing patient-specific implants with a gradient modulus distribution. Oshkour et al. (2013) developed a functional gradient hip implant to reduce the stress shielding effect and improve the total hip replacement performance. Limmahakhun et al. (2017) assessed the possibility of using graded porous Co-Cr alloys in implants. A comparison of four shapes of femoral stems demonstrated that round implants undergo less deformation and have lower von Mises stresses (Chethan et al., 2019). In general, implants with a functional gradient structure similar to that of bone tissue are ideal for achieving the required mechanical and biological properties (Leong et al., 2008; Han et al., 2019; Chen H. et al., 2020).

In the design of hip implants with porous structure, the design methods are divided into parametric and non-parametric methods based on whether the porous structure is generated by an algorithm. In non-parametric design, most of the structures were similar, and only minor changes could be made (Chen H. et al., 2020). In parametric design, different methods were mainly used to calculate and predict certain characteristic quantities after parameterization. For instance, Ahmadi et al. (2014) proposed an analytical solution to predict the elastic modulus, Poisson's ratio, elastic buckling limit, and yield stress of a diamond cell structure based on some specific parameters. Shi et al. (2019) parametrically designed the porous structures based on three-dimensional periodic miniaturized surface (TPMS), which have a good osseointegration effect. However, no parametric optimization of porous structures was conducted in these researches. In terms of the hip implant design, the stress distribution is uneven, the elastic modulus of implant should be adjusted with the stress distribution, so the gradient porous structures should be used in the implant design. Recently, there is a lack of effective methods and corresponding experimental analysis for the femur implant design with gradient modulus.

TABLE 1 | Material properties of each part (Liu et al., 2019).

Material	Elastic modulus (GPa)	Poisson's ratio
Ti-6AL-4V	114	0.36
Bone cement (PMMA)	1.6	0.3
Cortical bone	13.7	0.3

At present, the Kriging approximation model is widely used in the engineering field. For example, Gao et al. (2013) proposed a Kriging approximation model that can quickly and effectively estimate the dynamic characteristics of the machine tool in order to study the changes of the dynamic characteristics of the machine tool in the manufacturing space. However, it has not been fully developed and applied in the field of biomedical engineering. Therefore, a

TABLE 2 | Mesh properties for convergence analysis.

Element size (mm)	No. of elements	Average mesh quality
1	230,515	0.75797
2	98,395	0.78819
3	55,036	0.78044
4	34,418	0.75964
5	29,244	0.75425

new parametric design method was proposed to mitigate the stress-shielding effect by optimizing the porous structure of gradient implants using the Kriging algorithm and FE method based on the target elastic modulus on the femoral surface in this study. The contents of this paper are arranged as follows. In **Section 2**, the development of the FE model of the hip implant was discussed and validation experiments were carried out; in **Section 3**, a Kriging model was developed to express the relationship between adjustable dimensions and STVR, porosity and elastic modulus, and from these relationships the adjustable dimensions set and the range of elastic modulus for subsequent optimization were derived. Through the FE method, optimization of the elastic modulus was carried out based on the constraint range of elastic modulus, and the optimal porous structure dimensions were determined based on the optimized elastic modulus and the adjustable dimension parameter set; in **Section 4**, the effects of the optimized design were analyzed and experimentally verified, and finally, in **Section 5**, the content of this research was summarized.

MODELING OF FEMUR BONE/IMPLANT INTERACTION

FE Modeling

In clinical practice, the most widely used material for artificial substitute bone is titanium alloy. The aim of this research is to reduce the elastic modulus of the titanium alloy implant by properly designing its gradient porous structure, so that it can adjust the stress distribution of the femur. This way, the stress-shielding effect caused by the modulus inequality will be mitigated. Therefore, it is necessary to develop a three-dimensional solid model for the subsequent parametric design, which comprises the femoral body and the titanium alloy implant. The models used in this study were taken from the GRABCAD (Popular models, 2020), and the selected femoral model and internal implant model were displayed in **Figures 1A,B**, respectively.

Before the development of the FE model, the excess part of the bone was excised for placing the implant and the cancellous bone. Since the elastic modulus of cancellous bone is similar to that of bone cement, the cancellous bone was replaced with bone cement in this study. Based on the shape of the femur, a solid model of bone cement was designed in the middle of its interior (The red part in **Figure 1C**). The final femoral model was illustrated in **Figure 1C**. This model was then imported into FE analysis software for static analysis. The material properties of each part of the model were listed in **Table 1**.

In this research, a binding contact was adopted. Convergence analysis was performed on the stress under different elements sizes in order to determine which element size was stable and accurate. Five different global element sizes were selected for comparison (**Table 2**), and the equivalent stress distribution under these sizes when the other conditions were the same was shown in **Figure 2A**.

Figure 2A shows the equivalent stress distribution results, where it could be observed that, when the global element size was greater than 2 mm, the equivalent stress magnitude at each position exhibited a large change. When the global element size was less than 2 mm, the change of the equivalent stress at each position became smaller and more stable. Consequently, in this study, a global element size of 2 mm was used to develop the mesh.

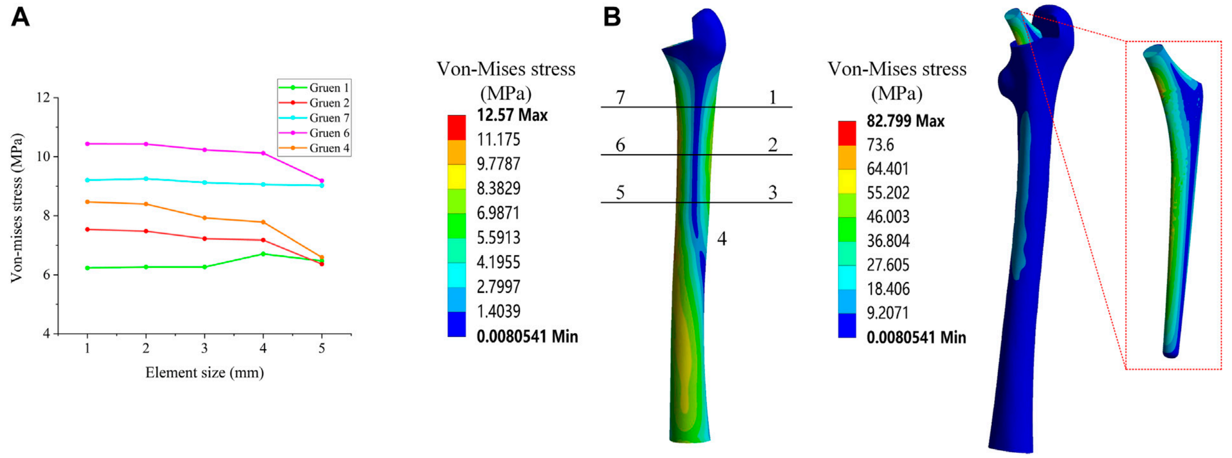

FIGURE 2 | (A) Mesh convergence analysis; **(B)** Von Mises stress distribution and Gruen zones partition method.

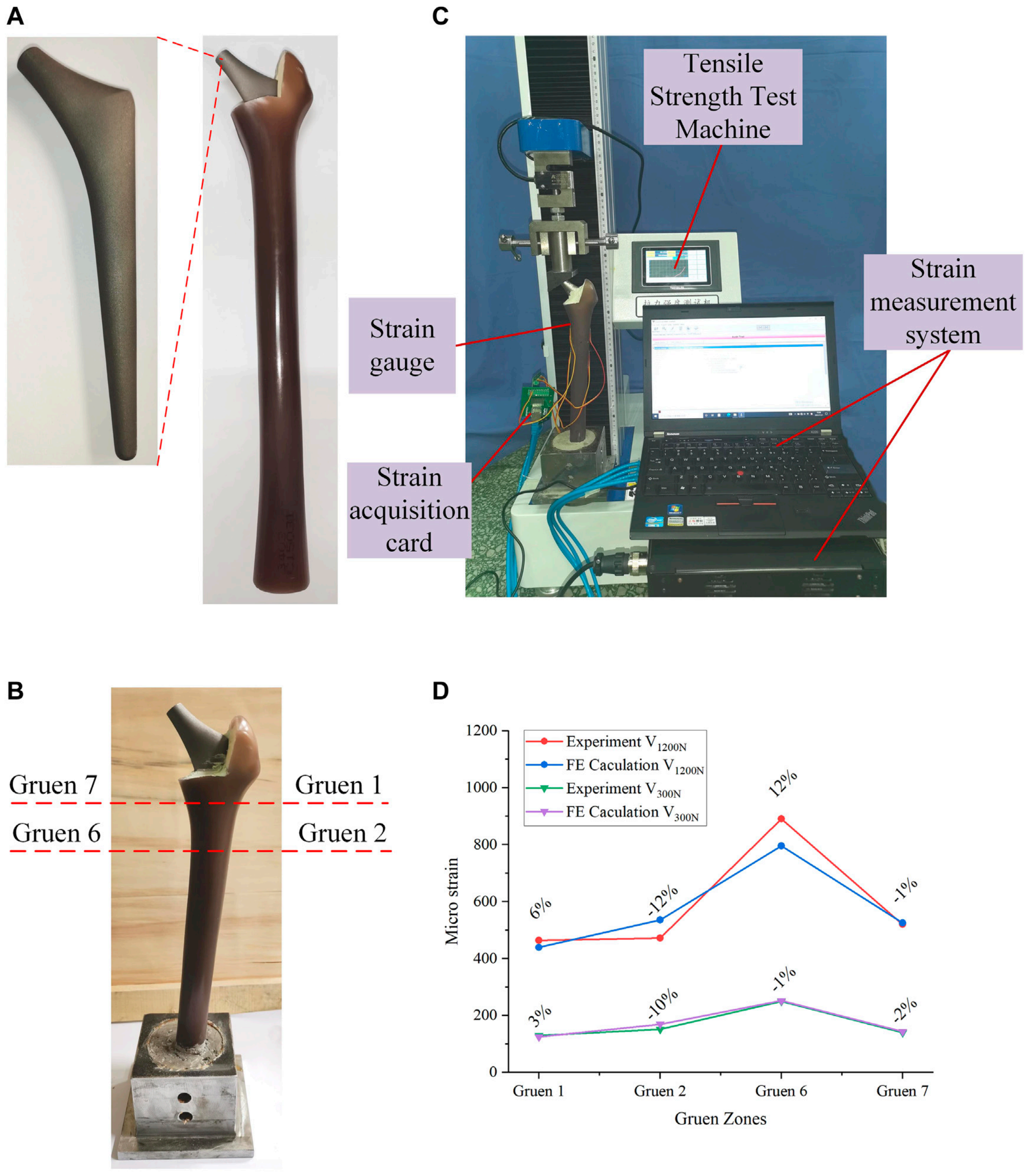

FIGURE 3 | (A) Experimental processing of the bionic femur; **(B)** Combination and fixation of the femur and implant; **(C)** The process of validation experiment; **(D)** Comparison of validation experimental results and simulation results.

The load of an Asian adult male standing on one leg was considered, as referenced in previous studies (Alkhatib et al., 2019)' (Farmakis et al., 2019). More specifically, a positive pressure of 1200 N was used as the main load acting on the upper end of the implant. As the most commonly used evaluation index in the field of hip implant research, and referring to previous studies (Nam et al., 2019), the equivalent stress of the seven Gruen zones on the surface of the femur were also used as the main evaluation index in this study. The contours of the average equivalent stress distribution calculated by the FE model are presented in **Figure 2B**.

FE Model Validation

The content of this section focuses mainly on the experimental validation of the FE model developed in **Section 2.1**. The materials required for the experiments include: femur, titanium alloy implant, bone cement, strain gauge, and tensile strength test machine. The femur was a composite femur purchased from the Sawbones website (Best Anatomical Medical Training Models Company, 2020) for mechanical experiments, and its mechanical properties were similar to those of human bones. The bone cement was

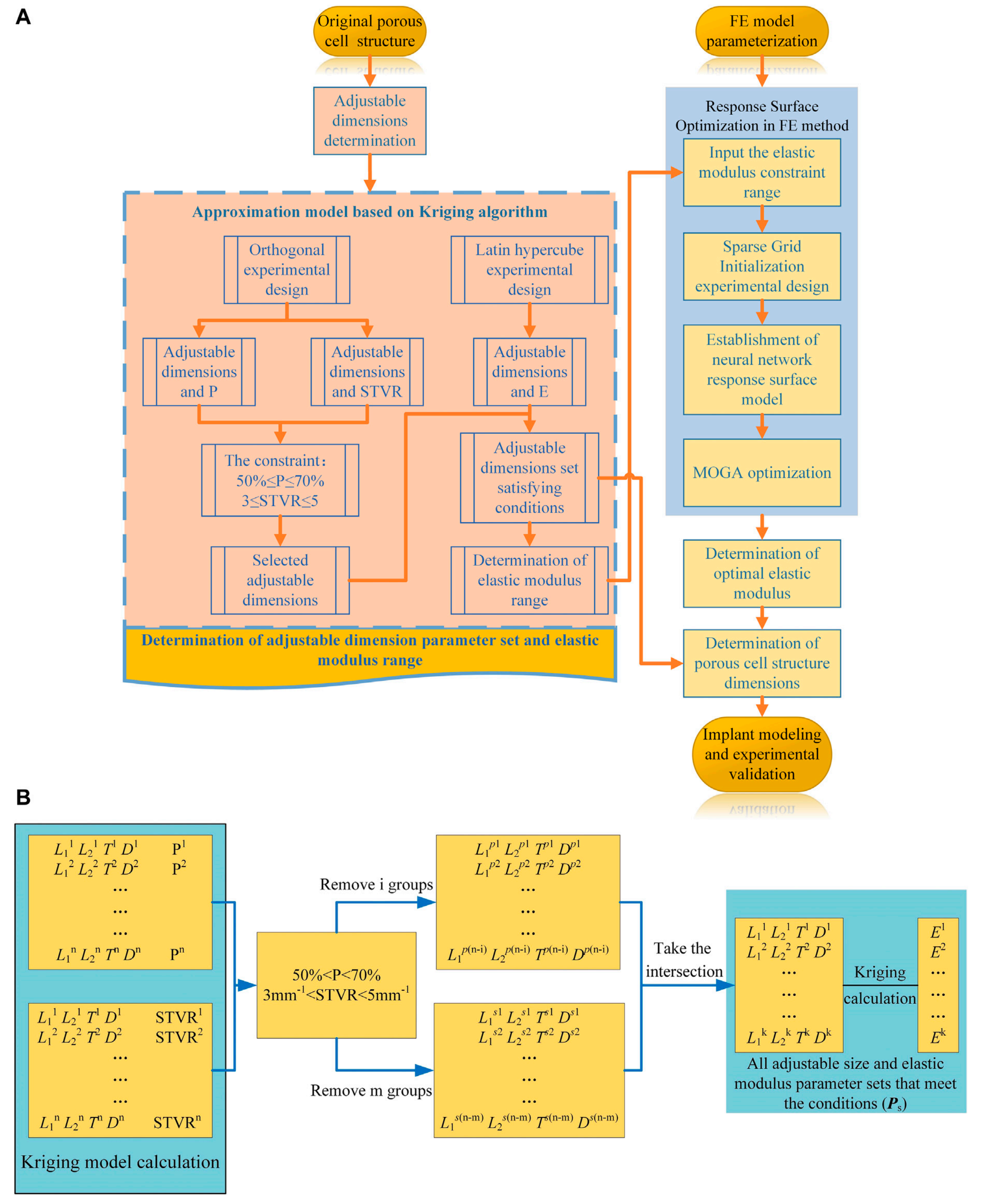

FIGURE 4 | Optimization process. **(A)** Flowchart of the implant design and optimization process; **(B)** Process of parametric optimization based on Kriging model.

purchased from Heraeus Medical GmbH in Germany, and the titanium alloy implants were made of Ti-6Al-4V through 3D printing.

The processed titanium alloy implant was inserted into the cavity reserved at the upper end of the femur and fixed with bone cement (**Figure 3A**). After the bone cement solidified, the femur was fixed in the designed base with cement, and was allowed to solidify for 48 h (**Figure 3B**). In the experiment, a load of 1200 N was applied by the tensile strength test machine, and the strain gauges were used to measure the micro-strain of the four Gruen zones on the outer femur surface. It should be noted that, due to the experimental conditions, the experimental values of all seven Gruen zones could not be measured in this study, so the strain was measured at four Gruen zones and the subsequent optimization process was based on the four Gruen zones used in this experiment. The positions of the four measurement Gruen zones used for simulation and experimentation were calibrated on the basis of a reference point, i.e., a reference point at the same position was selected on the model and the experimental entity, and the subsequent measurement points were calibrated on the basis of this reference point. In addition, another experiment under a load of 300 N was performed in order to compare the experimental results. The experimental loading situation was demonstrated in **Figure 3C**. The micro-strain of each zone under these two load conditions could be observed in the **Supplementary Material**. The micro-strain values measured experimentally at the four Gruen zones on the femoral surface were compared with the those calculated by the FE model; thus, the correctness of the FE model was verified based on the magnitude of the error.

The comparison between the experimental and FE analysis results was shown in **Figure 3D**. Among them, V_{1200N} and V_{300N} represent the micro-strain values when the load was 1200 and 300 N, respectively. As it could be observed in **Figure 3D**, when the load was 1200 N, the maximum error was 12% and the smallest difference between the micro-strain values was in the Gruen seven zone, where the error was only -1%. In the 300 N load test, the maximum error appeared also in the Gruen 2 zone (10%), while the minimum error was found in the Gruen 6 zone. After experimental measurement and analysis, it was found that the micro-strain value in Gruen 2 was far from the FE result. This may have been caused by a number of reasons, including the lack of a reference coordinate system in the experiment, i.e., the experimental and simulation points may have not been corresponding exactly. Moreover, the relative difference between the numerical and experimental values may have also been caused by the difference between the numerical simulation and the actual boundary conditions at the femur and implant interface (Jetté et al., 2018). At the same time, the use of bone cement may have also affected the results. But in general, the error between the micro-strain values calculated by the FE model and the experimental results was small; thus, the FE model developed in this study could be considered correct and valid.

IMPLANT STRUCTURE DESIGN AND OPTIMIZATION

The FE model was experimentally verified in **Section 2**, and the parametric design of the porous structure of the implant was based on this model. In this section, the parametric design of the titanium alloy implant was mainly divided into two parts: the determination of the dimension parameter set (P_s) of the porous structure based on the Kriging model and the optimization of the gradient elastic modulus based on the response surface methodology.

In the process of parametric optimization in this section, the mapping relationship between the internal dimensions of the cellular structure and the equivalent stress on the femoral surface cannot be directly established by the FE method. Moreover, compared with the FE method, the Kriging method can also perform personalized optimization according to the constraints of the cell. Therefore, in order to improve the efficiency of optimization and realize the parametric design of porowus structures, the respective advantages of the two methods were combined for the design of implants with gradient moduli in this study. In order to express the mapping relationship between various parameters, the Kriging approximation model was developed based on the original porous cell structure, and the dimension parameter set for subsequent optimization design was determined. Specifically, the Kriging model was developed to express the relationship between adjustable dimensions and STVR, porosity and elastic modulus, and the adjustable dimensions set and the set of elastic modulus for subsequent optimization were derived from these relationships. The upper and lower limits of the adjustable dimension parameter set satisfying the conditions (**Eqs 3** and **4**) was used to determine the upper and lower limits of the elastic modulus to be input into the response surface optimization range settings, and then the elastic modulus was optimized by the response surface optimization provided by the FE method (**Figure 4A**). The optimal equivalent elastic modulus of each segment could be determined when the conditions of **Eq. 2** were satisfied. The dimension parameters of each cell were determined in the adjustable dimension parameter set (P_s) based on this optimal elastic modulus and finally the optimal dimensions were modelled and experimentally tested. The specific implementation process was illustrated in **Figure 4A**. The formulation used for optimization, which is based on linear static FE analysis, and the specific parametric optimization process based on this optimization formula was shown in **Figure 4B**.

The general optimization algorithm is defined as follows:

$$\text{Find}\, E = [E_1, E_2, E_3, E_4, E_5, E_6, E_7] \tag{1}$$

$$\text{Max}\, \sigma = [\sigma_1, \sigma_2, \sigma_3, \sigma_4] \tag{2}$$

The constraints are as follows:

I Porosity

$$50\% \leq P \leq 70\% \tag{3}$$

II Surface-to-volume ratio

$$3\text{mm}^{-1} \leq STVR \leq 5\text{mm}^{-1} \tag{4}$$

III Equivalent elastic modulus

$$E_i \in \{P_s\} \tag{5}$$

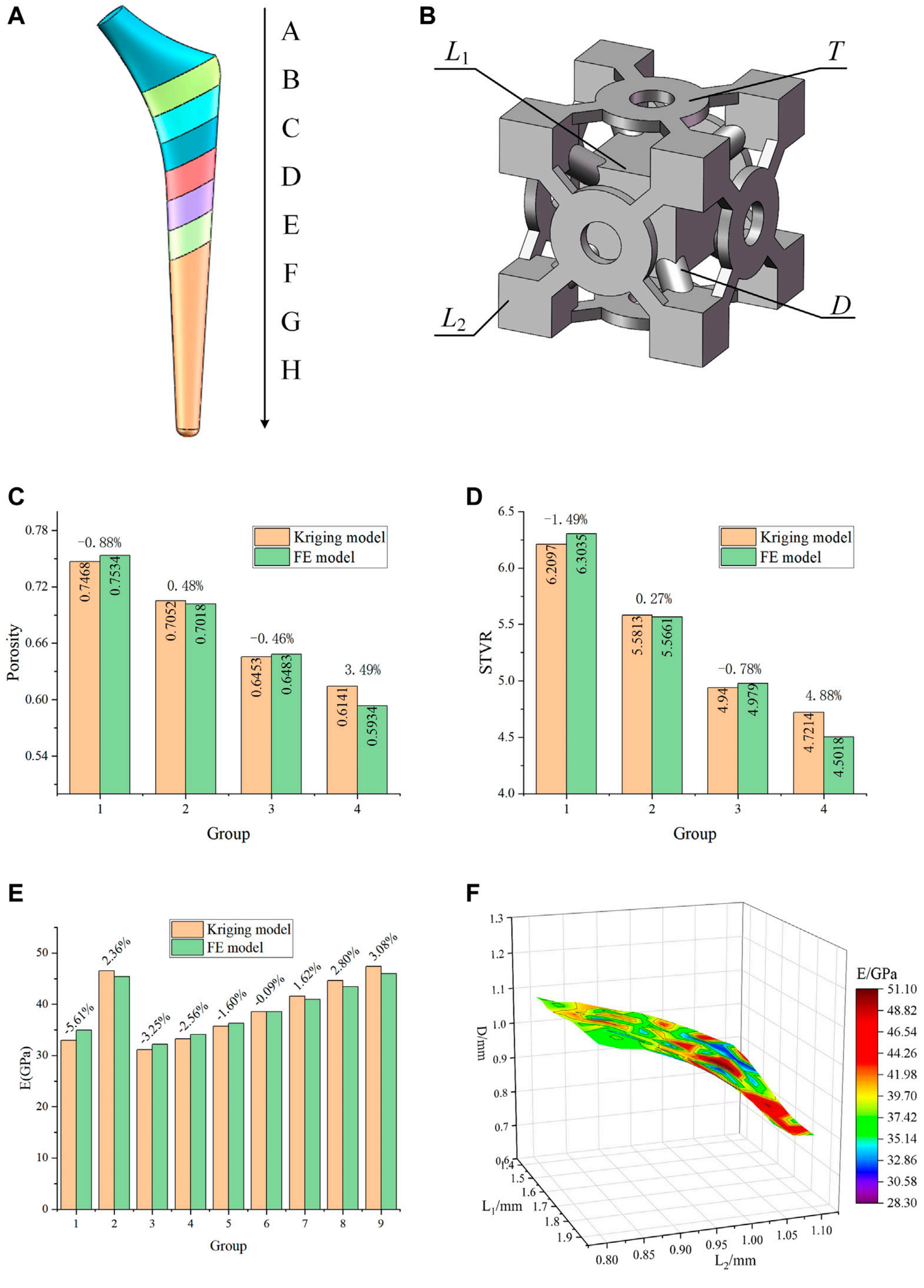

FIGURE 5 | Designed porous structure and error analysis of the Kriging model. **(A)** Segmented implant; **(B)** Initial cell structure and adjustable dimensions; **(C)** Error of porosity calculated by the Kriging model and the FE model; **(D)** Error of STVR calculated by the Kriging model and the FE model; **(E)** Error of elastic modulus calculated by the Kriging model and the FE model; **(F)** Relationship between *E* and the three groups of dimensions in the dimension parameter set.

where $\boldsymbol{E}$, $\boldsymbol{\sigma}$, and P_s are the equivalent elastic modulus of each implant segment (Implant was divided into eight segments, which will be explained in detail later), the equivalent stress on the outer surface of the femur (The zone where the equivalent stress is located was consistent with the zone used for the experimental measurement), and an adjustable dimension parameter set, respectively. The stress-shielding effect is mainly due to the high elastic modulus materials that bear most of the stress, resulting in the stress acting on the femur less than required for normal growth. Therefore, the stress-shielding effect can be mitigated by increasing the stress stimulation on the femur. However, due to experimental conditions, increasing the stress on the outer surface of the femur will be the goal of optimization (**Eq. 2**).

Determination of the Dimension Parameter Set Based on the Kriging Model

In order to satisfy the optimization goals for the different femur positions, the solid model of the titanium alloy implant was divided into eight segments from A to H (**Figure 5A**). In the A segment, which was the main force-bearing part, titanium alloy entities were used. The elastic modulus of the other seven segments varied according to the optimization results. In order to simplify the optimization process and guarantee the adjustability of the structure, a BCC cell able to individually change the local dimensions was designed (**Figure 5B**). This type of structure is universal, and the subsequent optimization was based on this structure. By changing its internal dimensions, each segment could obtain a suitable elastic modulus.

Considering the requirements for bone in-growth and manufacturability, Chen et al. (2020) reported that a scaffold with a porosity of 60% has the best cell proliferation and osteogenic differentiation (*in vitro* experiment) and bone in-growth (*in vivo* experiment). Jetté et al. (2018) suggested that, when designing porous structures, the porosity should be between 40 and 70%. Abate et al. (2021) showed that the cellular implants with porosity of 56 and 58% have the potential to be used in orthopedic and prosthetic applications to improve osseointegration. When using BCC structures, the porosity in the range of 50–70% can be used to design gradient porous implants so that the mechanical properties of cortical bone can be simulated (Chowdhury et al., 2021). At the same time, bone growth, migration, and cell adhesion are also affected by the surface-to-volume ratio (STVR) of the porous structure. Studies by Beaupré (Beaupre et al., 1990) and Coelho (Coelho et al., 2009) had indicated that a tight bone fixation could be provided by the implant if the STVR of their porous structure was in a range of 3–5 mm^{-1}. Therefore, in this study, a porosity ranging within 50–70% and an STVR ranging within 3-5 mm^{-1} were used as constraints for the optimization of the porous cell structure dimensions. The porosity and STVR should satisfy the above constraints by changing the adjustable dimensions of the porous structure. According to the original structure in **Figure 5B**, the freely and independent adjustable dimensions were the side length L_1 of the center cube, the side length L_2 of the outer cube, the pillar diameter D, and the thickness T of the connecting plate. Therefore, only the mapping relationships between the four dimensions and P, STVR were needed in order to determine all the structural dimensions that satisfy the above constraints.

In order to determine these mapping relationship, two Kriging approximation model were developed, where the four adjustment dimensions were used as the input parameters, P and STVR were used as the output response parameters, and the genetic algorithm was used to optimize the Kriging model parameters and increase its precision. In order to develop a Kriging model, it is necessary to design orthogonal experiments for the input and output parameters. This method can make the role of each factor clear, and can pick out representative test points for experiments to find the best level matching, and can greatly reduce the number of experiments, and there is no strict limit on the number of factors. The optimization process of the Kriging model and the results of the orthogonal experiment were provided in the **Supplementary Material**. In this study, a total of 16 sets of experiments with four factors and four levels were used and the model was determined based on the results of the orthogonal experiments. Four groups of adjustment dimensions that were not trained by the Kriging model and completely different from those listed in the **Supplementary Material** were selected to compare the actual value calculated by the FE model with that predicted by this model and evaluate the accuracy of the model. The results were presented in **Figures 5C,D**.

As it can be observed in **Figures 5C,D**, the error between the results predicted by the developed Kriging model and those obtained by the FE simulation was small. Regardless of whether it was the predicted porosity or STVR, after inputting the same dimensions parameters, the maximum error between the results obtained by the Kriging model and the FE model appeared in Group 4. The reason is that when one or more of the four adjustable dimensions are too large or too small, the design deviation will increase significantly. Nevertheless, the maximum error within the dimension design range was only 4.88%, and this model could be considered accurate. All manufacturable adjustable dimensions were input into the model, and the porosity and STVR values corresponding to all manufacturable adjustable dimensions could be determined through the Kriging model. After removing the values that do not satisfy the constraints (**Figure 4B**), the adjustable dimensions set that satisfy the conditions could be obtained.

Similarly, the mapping relationship between the adjustable dimensions and the elastic modulus of this structure also needs to be expressed through a Kriging model. Different from the previous experimental design method, since the relationship between adjustable dimensions and elastic modulus is more complicated, the design of experiment needs to be completed with the help of FE method. After its parameterized modeling, the original porous structure was imported into the ANSYS, which was used to calculate the deformation values. The adjustment dimensions were used as the input parameters and the deformation values were used as the output parameters. Subsequently, the Latin hypercube experimental design method was used to obtain 25 groups of experiments (**Supplementary Material**). In order to establish the mapping relationship between the adjustment dimensions and the elastic modulus, it is necessary to convert the deformation values into the elastic modulus, as described by **Eq. 6**. The Kriging model between the adjustable dimensions and the elastic modulus was determined through these 25 groups of experimental data.

$$E = \frac{F/S}{\Delta L/L} \tag{6}$$

TABLE 3 | Optimization results.

Implant segment	Elastic modulus (GPa)	Gruen zones	Von mises stress (MPa)
B	50.669	Gruen 1	7.793
C	29.814	Gruen 2	9.679
D	51.047	Gruen 6	14.810
E	39.613	Gruen 7	10.733
F	28.465	—	—
G	31.316	—	—
H	28.717	—	—

where E is the elastic modulus of the porous structure, F is the force acting on the porous structure, S is its cross-sectional area, ΔL is the amount of deformation, and L is its total length in the direction of deformation.

In order to verify the accuracy of this model, nine groups of untrained adjustable dimensions were selected, and the actual value calculated by the FE model was compared with that predicted by the model. The error of this model was evaluated as shown in **Figure 5E**, where it can be observed that the maximum error between the elastic modulus predicted by the Kriging model and that calculated by the FE model was only 5.61%; thus, this model could be considered as accurate. The previously obtained values of all the eligible adjustable dimensions were substituted into this Kriging model to calculate the elastic modulus. Therefore, the elastic modulus range used for subsequent optimization and its corresponding adjustable parameter set (P_s) were determined by the constraint conditions of P and STVR. Among them, all the dimension parameter sets were discrete. Three sets of $\boldsymbol{L_1}$, $\boldsymbol{L_2}$, and $\boldsymbol{D}$ among the four sets of dimension parameters and the calculated elastic modulus $\boldsymbol{E}$ were selected to express this dimension parameter set (P_s), as shown in **Figure 5F**.

Elastic Modulus Optimization Based on the Response Surface Method

In **Section 3.1**, the elastic modulus range that satisfies the constraints was determined through the Kriging model. In this section, the response surface optimization of FE method was used to select from that range appropriate elastic modulus values for the implant.

After the FE model had been parameterized, the elastic modulus was set as the input value, and the equivalent stress as the output value. The response surface optimization was used to perform the final optimization design. Response surface optimization comprises mainly three parts: experimental design, approximation model development, and genetic algorithm optimization. In this study, the extremes of the elastic modulus range obtained in **Section 3.1** were set as the upper and lower limits of the input values that need to be defined during the experimental design of the parameterized model. The sparse grid initialization method was used to determine the experimental samples in the experimental design, one advantage of sparse grid initialization is that it refines only in the directions necessary, so that fewer design points are needed for the same quality response surface and another is that it is effective at handling discontinuities. A neural network approximation model was developed using these samples in the response surface type selection. Multilayer perceptron neural networks is used in the neural network model inside workbench, this model works well for highly nonlinear responses and is suitable for use when the number of input parameters is high. Finally, the multi-objective genetic algorithm (MOGA) was used to optimize the elastic modulus based on the approximation model, and the maximum value of the equivalent stress on the femoral surface was taken as the target for optimization. Through the above optimization design method, the elastic modulus of the reference point used for the design of the implant and the corresponding equivalent stress value of the femoral surface were obtained.

As it can be seen in **Table 3**, the elastic modulus of each segment of the optimized implant was different, and the elastic modulus of Segments B and D were larger. In order to verify the effectiveness of this optimization method, the elastic modulus values listed in **Table 3** were added to the FE model to perform simulations. The simulation results were compared with the equivalent stress in **Table 3**, and the comparison results were shown in **Figure 6B**. It could be observed that the difference between the equivalent stress obtained after optimization and that calculated by the actual elastic modulus was not large, and the maximum error was 4.26%, which was in line with the expectations.

The dimensions of each part corresponding to the optimized elastic modulus in **Table 3** could be found from the adjustable dimension parameter set (P_s) in **Section 3.1** and the solid model of the porous structure determined by these dimensions was designed. The porous structure of the B-H segments could be obtained according to the optimized adjustable dimensions, as shown in **Figure 6A**. Based on the porous structure model, the actual elastic modulus of the structure designed according to the optimization results can be calculated, and then, the corresponding equivalent stress on the femoral surface could be obtained from the FE model. The prediction results generated by the Kriging approximation model will produce errors, and errors may also occur during modeling. Consequently, it is necessary to consider the cumulative error of the equivalent stress predicted by the Kriging model; that is, the error between the optimized equivalent stress and the equivalent stress of solid modeling based on the Kriging model predictions. This error was presented in **Figure 6C**. At the same time, in order to comprehend the actual effect of the optimization method involved in this research, the equivalent stress obtained by this method was compared with that of the

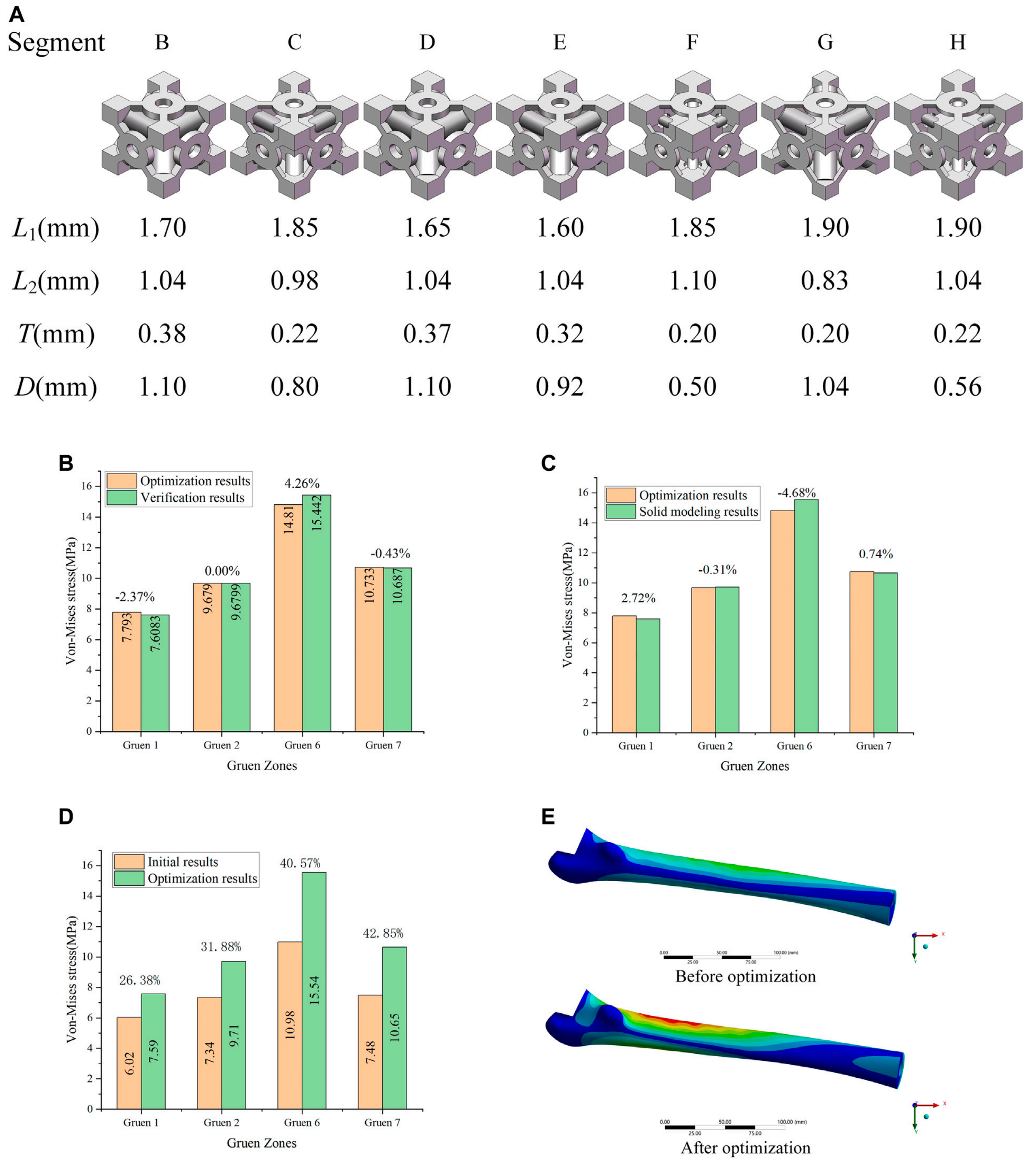

FIGURE 6 | (A) Porous structure of the B-H segment; **(B)** Validation of optimization results; **(C)** Error between the optimization of the elastic modulus and the solid modeling after optimization; **(D)** Optimization effect analysis; **(E)** Equivalent stress distribution of the femur before and after optimization.

initial femoral surface without optimization, and the results were shown in **Figure 6D**.

It can be observed that the equivalent stress on the femoral surface calculated by the FE model was not much different from the optimized result, and the maximum error was within 5%. Consequently, the method proposed in this study to optimize the porous structure of the implant was effective, and the error produced was small. According to the comparison between optimized and

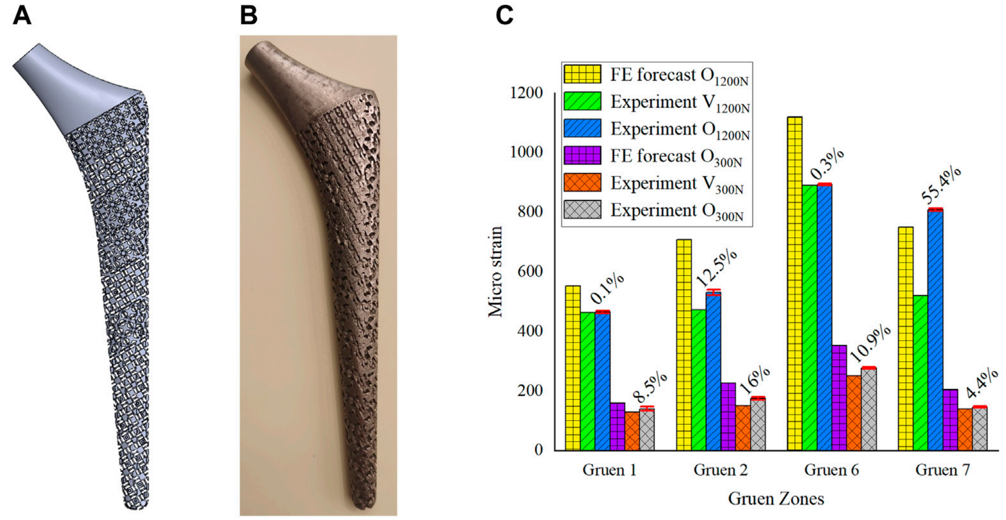

FIGURE 7 | (A) 3D model of gradient porous implant; **(B)** The hip implant manufactured by 3D printing; **(C)** Analysis of the optimization effect.

initial results (**Figure 6D**), the equivalent stress on the femoral surface was increased by at least 26% after optimization compared to the unoptimized results. The best optimization effect was in Gruen 7, where the equivalent stress was increased by 42.8%. In addition, it could be seen from **Figure 6E** that compared with the equivalent stress of the femur before optimization, the equivalent stress of the femur after optimization increases significantly, and the area where the stress increases was also larger.

Through the mutual validation of the FE model, the implant with porous structure optimized by the proposed method also exhibited good results in the calculation, and the equivalent stress on the surface of the femur was improved.

EXPERIMENTAL RESULTS

In **Section 3**, the porous cell structures were parametrically designed and the Kriging model and FE method were used to obtain a set of dimensions parameters that satisfy the constraints (**Figure 6A**). After optimizing the elastic modulus, the optimal porous structure model of each segment of the titanium alloy implant was developed (**Figure 7A**). In order to verify the actual effect of this optimization method, the experimental analysis was performed again with full reference to the model validation experiment performed in **Section 2.2**. In order to ensure the validity of this optimization effect analysis experiment, 10 measurements were taken for this optimization experiment and performed statistical analysis on these 10 experiments as shown in **Figure 7C**. The 3D printed implant used in the experiments was presented in **Figure 7B** and the experimental data were provided in the **Supplementary Material**. The effect of the optimization results obtained by the experiment was depicted in **Figure 7C**.

In **Figure 7C**, V_{1200N} is the validation experimental result before optimization (**Section 2.2**), O_{1200N} is the experimental result after optimization, and there are also optimization results predicted by the FE model. The same is true for the experiment under a load of 300 N. From the statistical analysis obtained from 10 experiments in **Figure 7C**, it could be seen that the results of multiple experiments performed in this optimization experiment were relatively stable, and it could be observed that the experimental measurement results after optimization were better than those before optimization. The micro-strain on the femoral surface was increased by 17.1% on average under 1200 N load and by 10% on average under 300 N load. The most obvious improvement in both cases was still at Gruen 7, which was the same as the FE prediction. Under the load of 300N, the implant was firmly attached to the femur by the bone cement, and the stress stimulation on the femur was relatively uniform, so it could be seen that the micro strain on the femoral surface increased more evenly. However, at a load of 1200 N, due to the high load applied to the implant, the force state between the implant and the femur is similar to that of a lever, i.e. Gruen 2, the support point, and Gruen 7, the stress point, are the main load-bearing areas, while Zones 1 and 6 are unstressed or less stressed, which results in a non-uniform growth of micro strain on the femoral surface as shown in **Figure 7**. In addition, due to some of the reasons mentioned in **Section 2.2** and the manufacturing errors of 3D printed porous implants, the experimental results were generally inferior to the FE simulation ones.

CONCLUSION

In this paper, a new parametric design method was proposed to mitigate the stress-shielding effect by optimizing the gradient porous structure of implants. A FE model of a hip implant for elastic modulus optimization was developed and validated experimentally. The porous structure was parametrically designed, the mapping relationship between the adjustable dimensions and porosity, STVR, and elastic modulus was established, and the adjustable dimensions set and the set of elastic modulus for subsequent optimization were derived from these relationships. These parameter sets calculated by the Kriging model were used as the constraints for the subsequent optimization of input and output parameters. By combining the results calculated by the kriging model, an optimal implant with porous structure and gradient elastic modulus was designed by the FE method. The experimental results demonstrated that the femoral surface micro-strain was increased by 17.1% and 10% on average compared with the unoptimized results. Consequently, it can be concluded that the parametric optimization design method proposed in this paper was effective and could substantially mitigate the stress-shielding effect by reducing the elastic modulus of the implant. The parametric design method proposed in this research is based on a general structure, the local dimensions of which can change individually; thus, this method is suitable for various situations where the elastic modulus needs to be adjusted through porous structure parametric design. In the future, the method of parametric design in this paper will be used to study the differentiation of the porous structure of implants in femurs of different ages.

DATA AVAILABILITY STATEMENT

The original contributions presented in the study are included in the article/**Supplementary Material**, further inquiries can be directed to the corresponding authors.

AUTHOR CONTRIBUTIONS

All authors listed have made a substantial, direct, and intellectual contribution to the work and approved it for publication. XG conceived the modeling and analysis, and wrote the manuscript as well. YZ and XG conducted the experiment and modeling. MW conducted the data analysis. CL and ZL supervised this work and revised the manuscript.

FUNDING

The author(s) disclosed receipt of the following financial support for the research, authorship, and/or publication of this article: This study was supported by the National Natural Science Foundation of China (grant numbers: 51875008, 51505012, and 51575014), Royal Society *via* an International Exchange Programme (Grant No: IEC\NSFC\191253), International Research Cooperation Seed Fund of Beijing University of Technology (grant number: 2021A10), European Commission *via* a H2020-MSCA-RISE programme (BAMOS, Grant No: 734156), Innovative UK *via* Newton Fund (Grant No:102872) and Engineering and Physical Science Research Council (EPSRC) *via* DTP CASE programme (Grant No:EP/T517793/1).

ACKNOWLEDGMENTS

This is a short text to acknowledge the contributions of specific colleagues, institutions, or agencies that aided the efforts of the authors.

SUPPLEMENTARY MATERIAL

The Supplementary Material for this article can be found online at: https://www.frontiersin.org/articles/10.3389/fbioe.2022.850184/full#supplementary-material

REFERENCES

Abate, K. M., Nazir, A., and Jeng, J.-Y. (2021). Design, Optimization, and Selective Laser Melting of Vin Tiles Cellular Structure-Based Hip Implant. *Int. J. Adv. Manuf Technol.* 112, 2037–2050. doi:10.1007/s00170-020-06323-5

Abate, K. M., Nazir, A., Yeh, Y.-P., Chen, J.-E., and Jeng, J.-Y. (2020). Design, Optimization, and Validation of Mechanical Properties of Different Cellular Structures for Biomedical Application. *Int. J. Adv. Manuf Technol.* 106, 1253–1265. doi:10.1007/s00170-019-04671-5

Abdel-Hady Gepreel, M., and Niinomi, M. (2013). Biocompatibility of Ti-Alloys for Long-Term Implantation. *J. Mech. Behav. Biomed. Mater.* 20, 407–415. doi:10.1016/j.jmbbm.2012.11.014

Ahmadi, S. M., Campoli, G., Amin Yavari, S., Sajadi, B., Wauthle, R., Schrooten, J., et al. (2014). Mechanical Behavior of Regular Open-Cell Porous Biomaterials Made of Diamond Lattice Unit Cells. *J. Mech. Behav. Biomed. Mater.* 34, 106–115. doi:10.1016/j.jmbbm.2014.02.003

Ahmed, K., Greene, R. J., Aston, W., Briggs, T., Pendegrass, C., Moazen, M., et al. (2020). Experimental Validation of an ITAP Numerical Model and the Effect of Implant Stem Stiffness on Bone Strain Energy. *Ann. Biomed. Eng.* 48, 1382–1395. doi:10.1007/s10439-020-02456-6

Alkhatib, S. E., Mehboob, H., and Tarlochan, F. (2019). Finite Element Analysis of Porous Titanium Alloy Hip Stem to Evaluate the Biomechanical Performance During Walking and Stair Climbing. *J. Bionic Eng.* 16, 1103–1115. doi:10.1007/s42235-019-0122-4

Arabnejad, S., Burnett Johnston, R., Pura, J. A., Singh, B., Tanzer, M., and Pasini, D. (2016). High-Strength Porous Biomaterials for Bone Replacement: A Strategy to Assess the Interplay Between Cell Morphology, Mechanical Properties, Bone Ingrowth and Manufacturing Constraints. *Acta Biomater.* 30, 345–356. doi:10.1016/j.actbio.2015.10.048

Babaie, E., and Bhaduri, S. B. (2018). Fabrication Aspects of Porous Biomaterials in Orthopedic Applications: A Review. *ACS Biomater. Sci. Eng.* 4, 1–39. doi:10.1021/acsbiomaterials.7b00615

Beaupré, G. S., Orr, T. E., and Carter, D. R. (1990). An Approach for Time-Dependent Bone Modeling and Remodeling-Theoretical Development. *J. Orthop. Res.* 8 (5), 651–661. doi:10.1002/jor.1100080506

Best Anatomical Medical Training Models Company (2020). Sawbones Is the Leader in Medical Training Models for Orthopedic and Medical Education. Sawbones Available at: https://www.sawbones.com/.

Chen, H., Han, Q., Wang, C., Liu, Y., Chen, B., and Wang, J. (2020a). Porous Scaffold Design for Additive Manufacturing in Orthopedics: A Review. *Front. Bioeng. Biotechnol.* 8, 609. doi:10.3389/fbioe.2020.00609

Chen, Z., Yan, X., Yin, S., Liu, L., Liu, X., Zhao, G., et al. (2020b). Influence of the Pore Size and Porosity of Selective Laser Melted Ti6Al4V ELI Porous Scaffold on Cell Proliferation, Osteogenesis and Bone Ingrowth. *Mater. Sci. Eng. C* 106, 110289. doi:10.1016/j.msec.2019.110289

Chethan, K. N., Shyamasunder Bhat, N., Zuber, M., and Satish Shenoy, B. (2019). Finite Element Analysis of Different Hip Implant Designs Along with Femur Under Static Loading Conditions. *J. Biomed. Phys. Eng.* 9, 507–516. doi:10.31661/jbpe.v0i0.1210

Chowdhury, S., Anand, A., Singh, A., and Pal, B. (2021). Evaluation of Mechanical Properties of Ti-25Nb BCC Porous Cell Structure and Their Association with Structure Porosity: A Combined Finite Element Analysis and Analytical Approach for Orthopedic Application. *Proc. Inst. Mech. Eng. H* 235, 827–837. doi:10.1177/09544119211011309

Christie, M. J. (2002). Clinical Applications of Trabecular Metal. *Am. J. Orthop. (Belle Mead. Nj)* 31, 219–220. Available at: http://europepmc.org/abstract/MED/12008854.

Coelho, P. G., Fernandes, P. R., Rodrigues, H. C., Cardoso, J. B., and Guedes, J. M. (2009). Numerical Modeling of Bone Tissue Adaptation-A Hierarchical Approach for Bone Apparent Density and Trabecular Structure. *J. Biomech.* 42, 830–837. doi:10.1016/j.jbiomech.2009.01.020

Cuadrado, A., Yánez, A., Martel, O., Deviaene, S., and Monopoli, D. (2017). Influence of Load Orientation and of Types of Loads on the Mechanical Properties of Porous Ti6Al4V Biomaterials. *Mater. Des.* 135, 309–318. doi:10.1016/j.matdes.2017.09.045

Davies, J. H., Laflamme, G. Y., Delisle, J., and Fernandes, J. (2011). Trabecular Metal Used for Major Bone Loss in Acetabular Hip Revision. *The J. Arthroplasty* 26, 1245–1250. doi:10.1016/j.arth.2011.02.022

Farmakis, I.-I. K., Potsika, V. T., Smyris, A.-F., Gelalis, I. D., Fotiadis, D. I., and Pakos, E. E. (2019). A Biomechanical Study of the Effect of Weight Loading Conditions on the Mechanical Environment of the Hip Joint Endoprosthesis. *Clin. Biomech.* 70, 197–202. doi:10.1016/j.clinbiomech.2019.10.002

Flecher, X., Sporer, S., and Paprosky, W. (2008). Management of Severe Bone Loss in Acetabular Revision Using a Trabecular Metal Shell. *J. Arthroplasty* 23, 949–955. doi:10.1016/j.arth.2007.08.019

Gao, X.-s., Zhang, Y.-d., Gao, H.-d., and Gao, H.-w. (2013). Dynamic Characteristic Analysis of Whole Machine Tools Based on Kriging Model. *J. Cent. South. Univ.* 20, 3094–3102. doi:10.1007/s11771-013-1833-z

Geetha, M., Singh, A. K., Asokamani, R., and Gogia, A. K. (2009). Ti Based Biomaterials, the Ultimate Choice for Orthopaedic Implants - A Review. *Prog. Mater. Sci.* 54, 397–425. doi:10.1016/j.pmatsci.2008.06.004

Gibson, L. J. (2005). Biomechanics of Cellular Solids. *J. Biomech.* 38, 377–399. doi:10.1016/j.jbiomech.2004.09.027

Han, C., Yan, C., Wen, S., Xu, T., Li, S., Liu, J., et al. (2017). Effects of the Unit Cell Topology on the Compression Properties of Porous Co-Cr Scaffolds Fabricated via Selective Laser Melting. *Rpj* 23, 16–27. doi:10.1108/RPJ-08-2015-0114

Han, Q., Wang, C., Chen, H., Zhao, X., and Wang, J. (2019). Porous Tantalum and Titanium in Orthopedics: A Review. *ACS Biomater. Sci. Eng.* 5, 5798–5824. doi:10.1021/acsbiomaterials.9b00493

Honda, T., Katano, Y., Kuzuya, T., Hayashi, K., Ishigami, M., Itoh, A., et al. (2013). Comparison of the Efficacy of Ribavirin Plus Peginterferon Alfa-2b for Chronic Hepatitis C Infection in Patients with and without Coagulation Disorders. *J. Med. Virol.* 85, 228–234. doi:10.1002/jmv.23444

Huiskes, R., Weinans, H., and Rietbergen, B. V. (1992). The Relationship Between Stress Shielding and Bone Resorption Around Total Hip Stems and the Effects of Flexible Materials. *Clin. Orthopaedics Relat. Res.* 274, 124–134. doi:10.1097/00003086-199201000-00014

Jetté, B., Brailovski, V., Dumas, M., Simoneau, C., and Terriault, P. (2018). Femoral Stem Incorporating a Diamond Cubic Lattice Structure: Design, Manufacture and Testing. *J. Mech. Behav. Biomed. Mater.* 77, 58–72. doi:10.1016/j.jmbbm.2017.08.034

Jeyapalina, S., Beck, P. J., Bloebaum, R. D., and Bachus, K. N. (2014). Progression of Bone Ingrowth and Attachment Strength for Stability of Percutaneous Osseointegrated Prostheses. *Clin. Orthopaedics Relat. Research®* 472, 2957–2965. doi:10.1007/s11999-013-3381-0

Lee, B., Lee, T., Lee, Y., Lee, D. J., Jeong, J., Yuh, J., et al. (2014). Space-Holder Effect on Designing Pore Structure and Determining Mechanical Properties in Porous Titanium. *Mater. Des.* 57, 712–718. doi:10.1016/j.matdes.2013.12.078

Leong, K., Chua, C., Sudarmadji, N., and Yeong, W. (2008). Engineering Functionally Graded Tissue Engineering Scaffolds. *J. Mech. Behav. Biomed. Mater.* 1, 140–152. doi:10.1016/j.jmbbm.2007.11.002

Limmahakhun, S., Oloyede, A., Chantarapanich, N., Jiamwatthanachai, P., Sitthiseripratip, K., Xiao, Y., et al. (2017). Alternative Designs of Load–Sharing Cobalt Chromium Graded Femoral Stems. *Mater. Today Commun.* 12, 1–10. doi:10.1016/j.mtcomm.2017.05.002

Liu, T. S., Gao, R., Wei, T., and Sun, H. Q. (2019). Three-Dimensional Finite Element Analysis of the Stress Distribution of Bone Tissue Around Porous Titanium Implant. *Zhonghua Kou Qiang Yi Xue Za Zhi* 54, 35–40. doi:10.3760/cma.j.issn.1002-0098.2019.01.007

Luxner, M. H., Stampfl, J., and Pettermann, H. E. (2007). Numerical Simulations of 3D Open Cell Structures - Influence of Structural Irregularities on Elasto-Plasticity and Deformation Localization. *Int. J. Sol. Structures* 44, 2990–3003. doi:10.1016/j.ijsolstr.2006.08.039

Moussa, A., Rahman, S., Xu, M., Tanzer, M., and Pasini, D. (2020). Topology Optimization of 3D-Printed Structurally Porous Cage for Acetabular Reinforcement in Total Hip Arthroplasty. *J. Mech. Behav. Biomed. Mater.* 105, 103705. doi:10.1016/j.jmbbm.2020.103705

Mullen, L., Stamp, R. C., Brooks, W. K., Jones, E., and Sutcliffe, C. J. (2009). Selective Laser Melting: A Regular Unit Cell Approach for the Manufacture of Porous, Titanium, Bone In-Growth Constructs, Suitable for Orthopedic Applications. *J. Biomed. Mater. Res.* 89B, 325–334. doi:10.1002/jbm.b.31219

Naghavi, S. A., Hua, J., Moazen, M., Taylor, S., and Liu, C. (2019). *On the FE Modelling of Short-Stem Porous Hip Implant Design for Preventing Stress Shielding & Promoting Osseointegration 2nd International Conference on Biomaterials, Bio-Design and Manufacturing.*

Nam, D., Salih, R., Barrack, R. L., and Nunley, R. M. (2019). An Evaluation of Proximal Femur Bone Density in Young, Active Patients Undergoing Total Hip Arthroplasty at One Year Postoperatively. *HIP Int.* 29, 51–57. doi:10.1177/1120700018761152

Nazir, A., Abate, K. M., Kumar, A., and Jeng, J.-Y. (2019). A State-Of-The-Art Review on Types, Design, Optimization, and Additive Manufacturing of Cellular Structures. *Int. J. Adv. Manuf. Technol.* 104, 3489–3510. doi:10.1007/s00170-019-04085-3

Niinomi, M., Nakai, M., and Hieda, J. (2012). Development of New Metallic Alloys for Biomedical Applications. *Acta Biomater.* 8, 3888–3903. doi:10.1016/j.actbio.2012.06.037

Oshkour, A. A., A Abu Osman, N., Davoodi, M. M., Yau, Y. H., Tarlochan, F., B Wan Abas, W. A., et al. (2013). Finite Element Analysis on Longitudinal and Radial Functionally Graded Femoral Prosthesis. *Int. J. Numer. Meth. Biomed. Engng.* 29 (12), 1412–1427. doi:10.1002/cnm.2583

Popular models (2020). *3D CAD Model Collection*. GrabCAD Community Library. Available at: https://grabcad.com/dashboard.

Prendergast, P. J., and Taylor, D. (1994). Prediction of Bone Adaptation Using Damage Accumulation. *J. Biomech.* 27, 1067–1076. doi:10.1016/0021-9290(94)90223-2

Shi, J., Liang, H., Jiang, J., Tang, W., and Yang, J. (20192019). Design and Performance Evaluation of Porous Titanium alloy Structures for Bone Implantation. *Math. Probl. Eng.* 2019, 1–9. doi:10.1155/2019/5268280

Sun, C., Wang, L., Kang, J., Li, D., and Jin, Z. (2018). Biomechanical Optimization of Elastic Modulus Distribution in Porous Femoral Stem for Artificial Hip Joints. *J. Bionic Eng.* 15, 693–702. doi:10.1007/s42235-018-0057-1

Takemoto, M., Fujibayashi, S., Neo, M., Suzuki, J., Kokubo, T., and Nakamura, T. (2005). Mechanical Properties and Osteoconductivity of Porous Bioactive Titanium. *Biomaterials* 26, 6014–6023. doi:10.1016/j.biomaterials.2005.03.019

Torres-Sanchez, C., Al Mushref, F. R. A., Norrito, M., Yendall, K., Liu, Y., and Conway, P. P. (2017). The Effect of Pore Size and Porosity on Mechanical Properties and Biological Response of Porous Titanium Scaffolds. *Mater. Sci. Eng. C* 77, 219–228. doi:10.1016/j.msec.2017.03.249

Wiria, F. E., Shyan, J. Y. M., Lim, P. N., Wen, F. G. C., Yeo, J. F., and Cao, T. (2010). Printing of Titanium Implant Prototype. *Mater. Des.* 31, S101–S105. doi:10.1016/j.matdes.2009.12.050

Xu, W., and Robinson, K. (2008). X-Ray Image Review of the Bone Remodeling Around an Osseointegrated Trans-Femoral Implant and a Finite Element Simulation Case Study. *Ann. Biomed. Eng.* 36, 435–443. doi:10.1007/s10439-007-9430-7

Xu, W., Yu, A., Lu, X., Tamaddon, M., Wang, M., Zhang, J., et al. (2021). Design and Performance Evaluation of Additively Manufactured Composite Lattice Structures of Commercially Pure Ti (CP-Ti). *Bioactive Mater.* 6, 1215–1222. doi:10.1016/j.bioactmat.2020.10.005

Yan, C., Hao, L., Hussein, A., and Young, P. (2015). Ti-6Al-4V Triply Periodic Minimal Surface Structures for Bone Implants Fabricated via Selective Laser Melting. *J. Mech. Behav. Biomed. Mater.* 51, 61–73. doi:10.1016/j.jmbbm.2015.06.024

Conflict of Interest: The authors declare that the research was conducted in the absence of any commercial or financial relationships that could be construed as a potential conflict of interest.

frontiers | Frontiers in Bioengineering and Biotechnology

ORIGINAL RESEARCH
published: 23 May 2022
doi: 10.3389/fbioe.2022.904629

Knowledge Domain and Hotspots Predict Concerning Electroactive Biomaterials Applied in Tissue Engineering: A Bibliometric and Visualized Analysis From 2011 to 2021

Wentao Xiong[1†], Sheng Wang[2†], Ziheng Wei[3†], Yibo Cai[1], Bo Li[4], Feng Lin[1*] and Demeng Xia[5*]*

[1]Department of Orthopedic, Hainan Hospital of Chinese PLA General Hospital, Sanya, China, [2]Department of Emergency, Changhai Hospital, Naval Medical University, Shanghai, China, [3]Department of Orthopedics, Shanghai General Hospital Affiliated to Shanghai Jiaotong University, Shanghai, China, [4]Department of Orthopedics, Changhai Hospital, Naval Medical University, Shanghai, China, [5]Luodian Clinical Drug Research Center, Shanghai Baoshan Luodian Hospital, Shanghai University, Shanghai, China

Edited by:
Yun Qian,
Shanghai Jiao Tong University, China

Reviewed by:
Ouyang Chen,
Duke University, United States
Andy Wai Kan Yeung,
University of Hong Kong, China
Qi Gan,
East China University of Science and Technology, China

***Correspondence:**
Bo Li
smmulibo@163.com
Feng Lin
lyf1011@aliyun.com
Demeng Xia
demengxia@163.com

†These authors have contributed equally to this work

Specialty section:
This article was submitted to Biomaterials, a section of the journal Frontiers in Bioengineering and Biotechnology

***Received:** 25 March 2022*
***Accepted:** 09 May 2022*
***Published:** 23 May 2022*

Citation:
Xiong W, Wang S, Wei Z, Cai Y, Li B, Lin F and Xia D (2022) Knowledge Domain and Hotspots Predict Concerning Electroactive Biomaterials Applied in Tissue Engineering: A Bibliometric and Visualized Analysis From 2011 to 2021. Front. Bioeng. Biotechnol. 10:904629. doi: 10.3389/fbioe.2022.904629

Objective: Electroactive biomaterials used in tissue engineering have been extensively studied. Electroactive biomaterials have unique potential advantages in cell culture and tissue regeneration, which have attracted the attention of medical researchers worldwide. Therefore, it is important to understand the global scientific output regarding this topic. An analysis of publications on electroactive biomaterials used in tissue engineering over the past decade was performed, and the results were summarised to track the current hotspots and highlight future directions.

Methods: Globally relevant publications on electroactive biomaterials used in tissue engineering between 2011 and 2021 were extracted from the Web of Science database. The VOSviewer software and CiteSpace were employed to visualise and predict trends in research on the topic.

Results: A total of 3,374 publications were screened. China contributed the largest number of publications (995) and citations (1581.95, actual value ×0.05). The United States achieved the highest H-index (440 actual values ×0.05). The journal Materials Science & Engineering C-materials for Biological Applications (IF = 7.328) published the most studies on this topic (150). The Chinese Academy of Science had the largest number of publications (107) among all institutions. The publication titled Nanotechnological strategies for engineering complex tissues by Dir, T of the United States had the highest citation frequency (985 times). Regarding the function of electroactive materials, the keyword “sensors” emerged in recent years. Regarding the characterisation of electroactive materials, the keyword “water contact angle” appeared lately. Regarding electroactive materials in nerve and cardiac tissue engineering, the keywords “silk fibroin and conductive hydrogel” appeared recently. Regarding the application of electroactive materials in bone tissue engineering, the keyword “angiogenesis” emerged in recent years. The current research trend indicates that although new functional materials are constantly being developed, attention should also be paid to their application and transformation in tissue engineering.

Conclusion: The number of publications on electroactive biomaterials used in tissue engineering is expected to increase in the future. Topics like sensors, water contact angle, angiogenesis, silk fibroin, and conductive hydrogels are expected to be the focuses of research in the future; attention should also be paid to the application and transformation of electroactive materials, particularly bone tissue engineering. Moreover, further development of the field requires joint efforts from all disciplines.

Keywords: electroactive biomaterials, tissue engineering, bibliometrics, hotspot, web of science

INTRODUCTION

The loss or failure of an organ or tissue is one of the most frequent, devastating, and costly problems in human health (Langer and Vacanti, 1993). Current treatments include organ transplantation, surgical reconstruction, mechanical devices, or metabolite supplementation (Lalan et al., 2001). While these strategies represent significant advances in the field of medicine, some inherent limitations are unavoidable, such as tissue transplantation being limited by the nature of the material, which often brings new trauma or secondary injury to patients. In addition, tissue transplantation is often limited by a lack of donors and has risks like disease transmission and immune rejection.

Artificial bioengineered tissue repair materials, with excellent biocompatibility and bioactivity, created *via* tissue engineering (TE) have gradually become a promising strategy in the clinical treatment of tissue defect repair in recent years. In addition, they have the advantages of ubiquitous sources, easy preparation, and safety. In TE the principles and methods of engineering and the life sciences are applied for developing biological substitutes for restoring, maintaining, or improving functions (Nerem, 1992). It is one of the most relevant topics within the field of advanced therapies (Santisteban-Espejo et al., 2018), and has a wide range of potential applications in tissue repair and regeneration.(Naveau et al., 2017). TE has been widely used in the regeneration of skin (Debels et al., 2015), bone (Pati et al., 2015), cartilage (Ren et al., 2015), nerve tissue (Georgiou et al., 2015), and blood vessels (Jaspan and Hines, 2015). Undoubtedly, TE is becoming a novel approach to future therapeutic applications in the clinical treatment of tissue defect repair.

The rapid development of bioscaffolds in tissue engineering over the past few decades has been fuelled by rising standards for effective bioscaffolds, which play an important role in the tissue repair process. A new generation of smart bioscaffolds not only serves as a medium or matrix for cell adhesion but also modulates cells, supports the process of cell proliferation, and promotes new tissue specialisation (Sukmana, 2012; Guo and Ma, 2018). Inspired by studies on the electrophysiological behaviour of cells and tissues, electroactive biomaterials have been proposed for and applied in tissue engineering and regenerative medicine research.

Electroactive biomaterials originated from the first measurements of the piezoelectric effect of bone tissue in 1957 by (Brown, 1980). Subsequently, research on the role of the piezoelectric effect in regulating cell behaviour and controlling the growth and remodelling of bone tissue has become more and more extensive, which has led to a series of piezoelectric materials being proposed and applied in the field of biomedical research. In addition to piezoelectric materials, researchers developed conductive polymers and carbon-based nanomaterials. Conductive polymers can concentrate externally applied electrical stimuli in their surrounding areas by regulating the loaded stimuli spatially (Guarino et al., 2013), promoting intracellular DNA synthesis, and accelerating cell division and proliferation (Stewart et al., 2015). Carbon-based nanomaterials, such as graphene sheets and carbon nanotubes, possess unique mechanical, electrical, and optical properties, have good biocompatibility at a certain concentration, and can support cell adhesion, proliferation, and differentiation. They present new opportunities for tissue engineering and are potential candidates for the development of artificial scaffolds (Ku et al., 2013). In conclusion, electroactive biomaterials can be combined with a human bioelectric system to directly transmit electrical, electrochemical, and electromechanical signals to cells and induce cell differentiation and tissue regeneration. Therefore, these materials have unique potential advantages in cell culture and tissue regeneration (Guimard et al., 2007) (**Figure 1**), which has attracted the attention of medical researchers worldwide.

Recently, many reviews have highlighted the current strategies and future prospects of electroactive biomaterials in TE; however, researchers may merely explore the literature in a single direction, which may lead to narrow-minded exploration. Moreover, each article summarises different keywords, and a large number of keywords make it difficult to accurately locate information in the PubMed, Web of Science (WOS), and Scopus databases. Hence, comprehensively analysing the status of this topic and revealing the current or future hotspots from multiple perspectives are urgent requirements.

Bibliometrics is a statistical and quantitative method used to analyse the academic influence and characteristics of scientific output. Combined with creative design and information visualisation, bibliometric mapping can visually represent bibliometric data (Zou et al., 2018). We performed a bibliometric analysis using international databases to identify

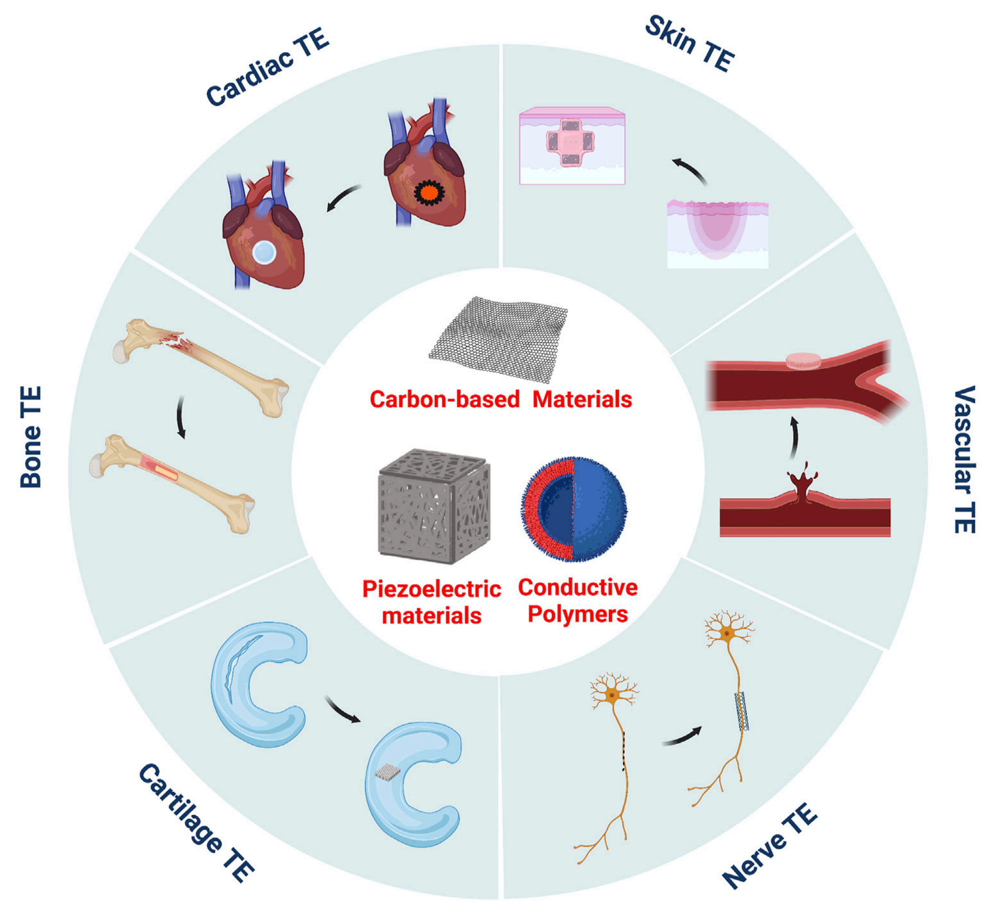

FIGURE 1 | Electroactive biomaterials have been widely used in the TE of skin, bone, cartilage, nerve tissue, cardiac or blood vessels.

hotspots in previous reports, such as research progress on heat stroke (Xia D. M et al., 2021) and hotspots concerning the use of stem cells for cartilage regeneration (Xia D et al., 2021). In bibliometrics, co-occurrence analysis is used to define research hotspots. We consider that if two terms appear in the same article concurrently, they may have a potential relationship. Furthermore, if these two terms appear frequently at the same time in the same article, they are considered to be closely related. After some analysis of these co-occurrence relations, such as cluster analysis or factor analysis, keywords that reach a threshold are considered to represent hot topics in the research area (Li et al., 2015). In addition, bibliometrics have been widely used in the fields of information science, chemistry, and physics, and show potential in the field of medicine (van Eck and Waltman, 2010). Using bibliometrics, researchers can determine more specific research themes, thereby achieving a more comprehensive understanding of the relationships between specific research areas.

We applied a bibliometric analysis to uncover global research trends, evaluate achievements related to electroactive biomaterials used in TE and predict possible future hotspots. As expected, the data extracted from this analysis could indicate the most productive areas in the evolution of electroactive biomaterials with the goal of facilitating the clinical translation of electroactive biomaterials into tissue engineering and providing references for future developments.

MATERIALS AND METHODS

Data Sources and Search Strategies

Web of Science (WOS), a database containing a large amount of physical, biological, and medical information, has often been used in bibliometric research. In our research, we performed a search for studies relevant to electroactive biomaterials used in tissue engineering (TE) between January 2011 and December 2021. All searches were conducted on 17 February 2022 to avoid bias according to database renewal. The search strategy was as follows: TS = [(electroactive, conductive, piezoelectric, or carbon-based) and (material or biomaterial, hydrogel, scaffolds, polymers, or ceramics) or polypyrrole or PPy, polyaniline, PANi, aniline oligomer, polyvinylidene fluoride, PVDF, Kynoar, L-polylactic acid, polylactic-L acid, PLLA, graphene, carbon nanotubes, or CNT] and (tissue engineer* or regenerat* medicine). The types of studies we included were strictly screened; only original articles or reviews were included in

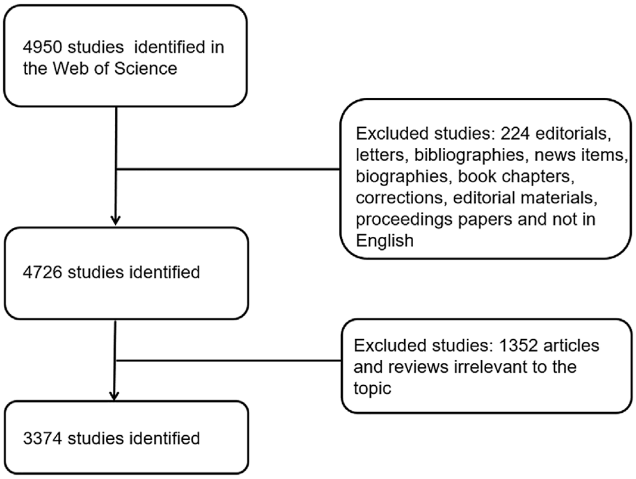

FIGURE 2 | Flow diagram of the inclusion process. The detailed process of screening and enrolment (irrelevant articles were manually screened by two authors through abstracts and full texts), and articles irrelevant to the topic were excluded.

our analysis, and all other types of studies were excluded. Finally, articles irrelevant to the topic were filtered manually. The process associated with research screening was undertaken by two authors (WTX and SW); if there was disagreement during the screening process, it was up to an experienced corresponding author to decide whether to include that paper in our study. Detailed information on enrolment and selection is shown in **(Figure 2).**

Data Collection and Processing

Basic information on the research in terms of titles, keywords, authors, publication dates, countries and regions of origin, institutions, journals, and overall information about the article in terms of number of citations, H-index, etc. were extracted from the identified publications by three authors (WTX, SW, and DMX). Several data analysis tools were used for data analysis and processing. Microsoft Excel 2016, GraphPad Prism 8, VOSviewer version 1.6.12, and CiteSpace version 5.6. R5 64 and an online analysis platform (http://bibliometric.com/) were applied to present, analyse, and describe the data.

Bibliometric Analysis

WOS, as a database covering a large amount research on medical, physical, and materials sciences, has a wide-ranging and comprehensive content; therefore, WOS was chosen as our preferred database for bibliometric research. The three most important indicators of article quality evaluation include the impact factor (IF), H-index, and relative research interest (RRI), and these were the objects of our research. The impact factor (IF) was taken from the Journal Citation Reports (JCRs), which is recognised as a key indicator in evaluating articles (Kavic and Satava, 2021). In general, the impact factor can directly reflect the quality and influence of an article. The H-index of an article, as a measure of academic productivity, indicates that a researcher or country has published at least H papers on a particular topic, that each paper has been cited at least H times. The indicator is objective in assessing the quality of the article (Favre et al., 2020). The relative research interest (RRI) is related to the number of publications in the field and the total number of publications included in the WOS database, which is meaningful for evaluating the popularity of research in the field (Wang et al., 2019). VOSviewer, a practical statistical software, can use text downloaded by WOS to perform a visual analysis of the references, institutions, authors, and terms. This software was used to display the time distribution and dynamic variability of keywords, and accurately reveals the evolution trend of hotspots in the research field (Chen et al., 2021). CiteSpace, which uses the Java programming language, is a useful tool for data analysis and processing. In addition to conventional analysis, an analysis of the cooperative relationships between related fields is unique in this research field (Yao et al., 2020).

RESULTS

Field Activity Analysis

According to the inclusion criteria, 3,374 articles related to electroactive biomaterials used in TE were included in the final analysis. By analysing and summarising the data, six aspects of the contributions, i.e., countries, contributions of different journals, top 10 articles, contributions of different institutions, keywords, and related fields were presented in the results. The specific process is shown in **Figure 3**.

Global Contribution to the Field

According to the national distribution of publications, China (995 publications) was the most productive country, followed by the United States (626 publications), Iran (417 publications), India (236 publications), and South Korea (228 publications) (**Figure 4A**). The top 10 countries with the most publications are shown in **Figure 4**.

In terms of total citations, the top five countries/regions are China with 31,639, the United States with 30,806, Iran with 9146, India with 6,995, and South Korea with 9862, respectively. The countries/regions with the highest H-index are as follows: the United States 88, China 83, India 45, Iran 44, and South Korea 40 (**Figure 4A**). According to the annual distribution of publications, although there was a slight decline during 2011–2012, the overall trend in publication output increased from 2011 to 2021 (100–500 publications per year). The trend of RRI was similar, suggesting that the field of electroactive biomaterials used in TE is receiving more attention in general (**Figure 4B**). It can be predicted that the growth trend in the number of publications in this field will accelerate in the future.

Collaborations between countries/regions are shown in **Figure 5**. The size of the circles indicates the number of publications and the width of the connecting line between the two circles indicates the degree of collaboration (**Figure 5A**). Many countries/regions have some years with a concentrated article output. The United States and South Korea had the most publications before 2017. China, Italy, and England intensively

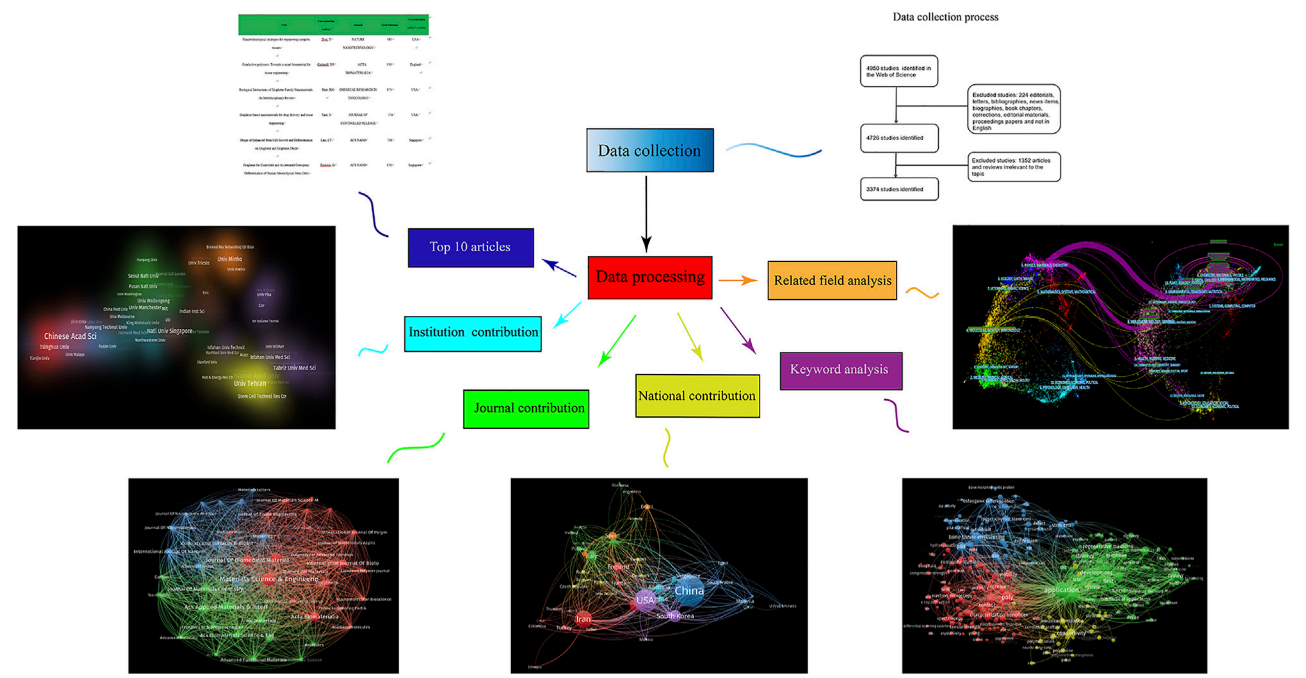

FIGURE 3 | Flow diagram of six aspects of electroactive biomaterials used in tissue engineering. Contributions of countries, contributions of different journals and top 10 articles, contributions of different institutions, keywords, and related fields are listed.

published articles in 2018. Articles from Iran were published mainly after 2018 (**Figure 5B**). As the top two countries with the most publications, the United States and China cooperated the most in this field, and the United States had the strongest total link strength, which means that the United States had the predominant influence in this field (**Figure 4C**).

Analysis of Journal Distribution

Different journals are active in different fields of publication. Therefore, we performed a journal distribution analysis of publications on the use of electroactive biomaterials in TE. The journal Materials Science & Engineering C-materials for Biological Applications (IF = 7.328) published the most studies, with 150 publications. There were 107 articles on electroactive biomaterials used in TE in ACS Applied Materials & Interfaces (IF = 9.229), 91 articles in the Journal of Biomedical Materials Research Part A (IF = 4.396, 2019), and 81 articles in RSC Advances (IF = 3.361). The top 10 journals with the highest number of publications are listed in **Table 1**. The journals did not just represent themselves; the fields behind them are more worthy of exploration and research. Materials Science and Engineering C-materials for Biological Applications and the Journal of Biomedical Materials Research Part A have the closest relationship. As far as this field is concerned, journals with high volumes of publications also have a high centrality and a focus on tissue engineering and materials science (**Figure 6B**).

Analysis of Institution Distribution

Five of the top 10 institutions in this field are in Iran, the other three institutions are in China, and one is in the United States (**Table 2**). In terms of publication ranking, the first was the Chinese Academy of Sciences (107 publications), followed by the University of Tehran (78 publications), the Shanghai Jiao Tong University (77 publications), Islamic Azad University, and Sichuan University (73 publications). The top 10 institutions with the most publications are shown in **Table 2**.

Figures 6B,C highlight the close and complex collaborative relationships between different institutions. VOS viewer was employed to analyse the centrality of these institutions; the circle indicates centrality, and the area of the circle is proportional to its centrality. Asterisks of the same colour indicate that such organisations belong to the same organisation. The Chinese Academy of Sciences and the University of Tehran are the most prominent institutions, which suggests that they are regarded as pivotal points (**Figure 6B**). The shade of the colour indicates the time of publication. Although Tarbiat Modares University ranks sixth in terms of the number of articles published, its articles are relatively new, and we predict that this institution will be a centre of research in this area in the future. In **Figure 6C**, the Chinese institution clusters in the lower left corner and the Iranian institution clusters in the lower right corner are lighter in colour, indicating that these two countries have recently exhibited significant research interest in this field.

Overview of Landmark Articles and Authors

The top 10 authors with the highest total citations of papers published between 2011 and 2021 are shown in **Table 3**. As presented in **Table 3**, there are three from the United States, two from Singapore and China each, and one each from England,

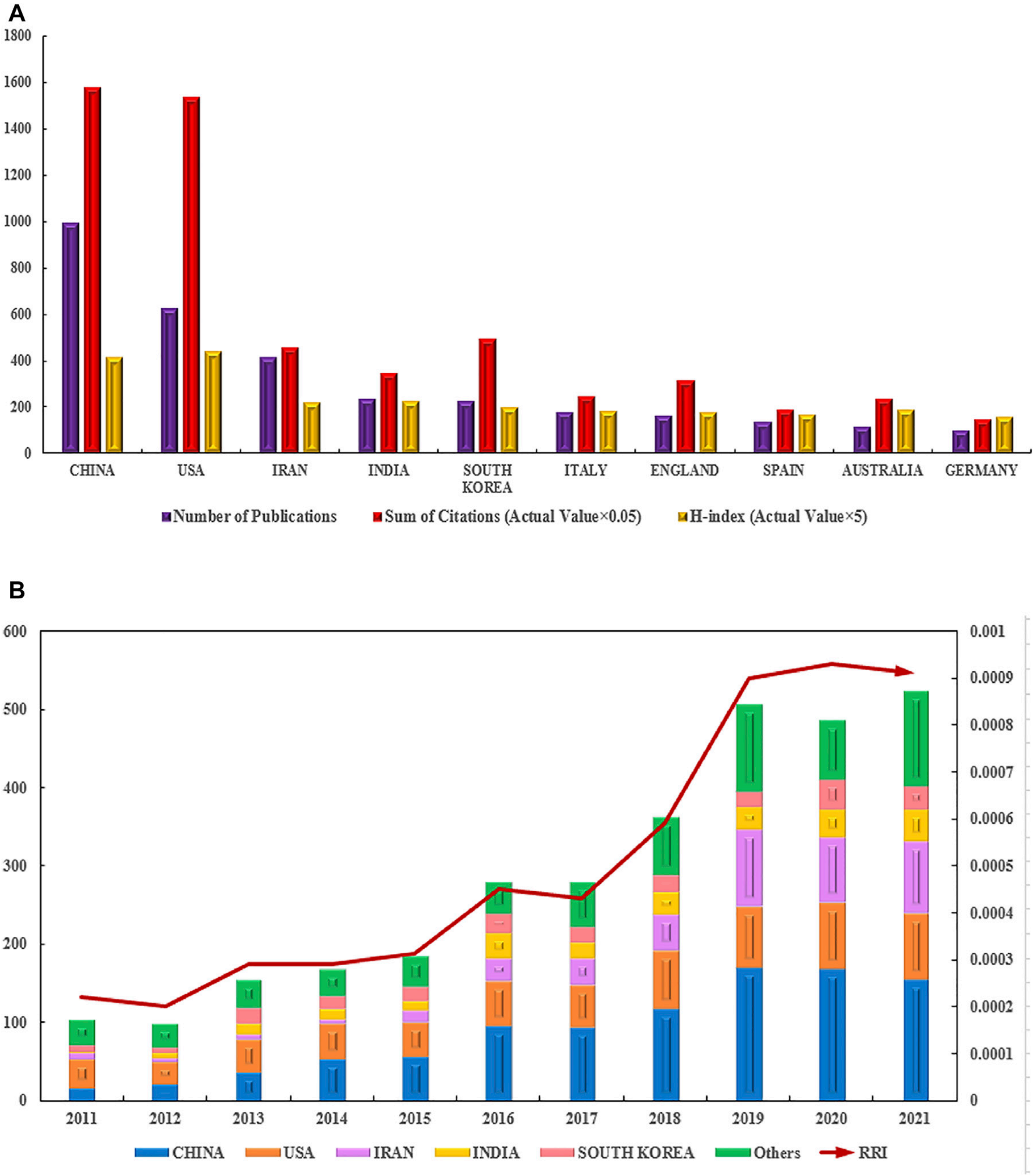

FIGURE 4 | Contributions of different countries/regions to the research field regarding electroactive biomaterials used in TE. **(A)** The number of publications, citation frequency (× 0.05) and H-index (× 5) in the top 10 countries or regions; **(B)** The number of publications worldwide and the timings of the relative research interests of electroactive biomaterials used in TE. (RRI = Relative research interest).

Canada, and Iran. Notably, the publication titled Nanotechnological strategies for engineering complex tissues by Dir, T of the United States had the highest citation frequency (985 times). The second-ranked journal and third-ranked journal are Conductive polymers: Towards a smart biomaterial for tissue engineering and Biological interactions of graphene-family nanomaterials: an interdisciplinary review. The content of this article is also the embodiment of the research direction, and nanomaterials have gradually become the focus of our research.

Co-Occurrence Analysis of Key Words

We analysed keywords extracted from 3,374 publications using VOSviewer. As shown in **Figure 7A**, from a total of 288 keywords, defined as terms that occurred more than 35 times within the titles and abstracts in all papers during the analysis process, the

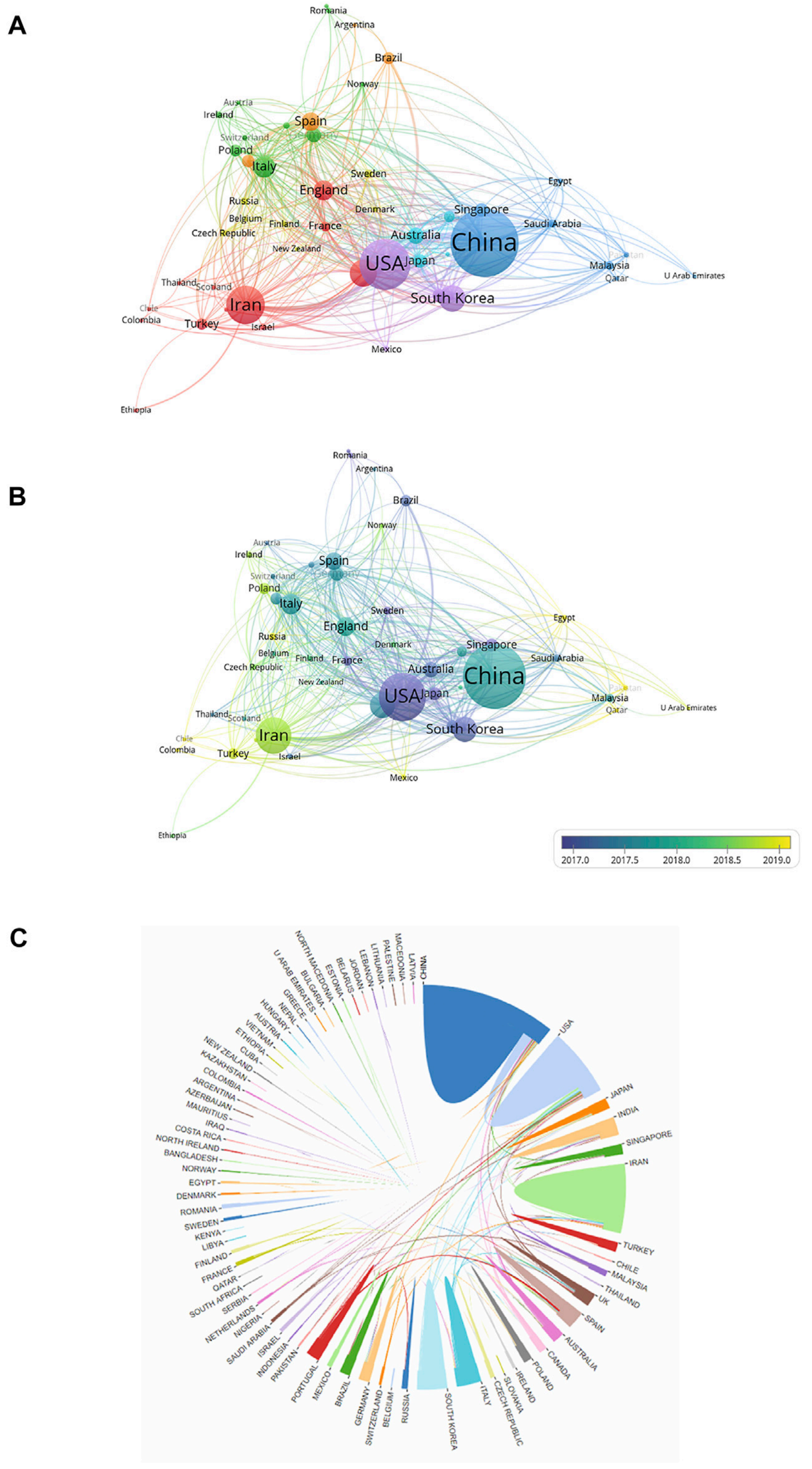

FIGURE 5 | Cooperation network of countries/regions with regard to research on electroactive biomaterials used in TE. **(A)** The network of cooperative relations between countries/regions was established with VOSviewer; **(B)** Concentrated years of publications for different countries; **(C)** The cooperative relations between countries/regions were visualized.

TABLE 1 | The top 10 journals publishing articles on the electroactive biomaterials used in TE.

SCR[a]	Journal	Contribution (%)	IF[b]
1st	Materials science & engineering C-materials for biological applications	4.707	7.328
2nd	ACS applied materials & interfaces	3.357	9.229
3rd	Journal of biomedical materials research Part a	2.855	4.396
4th	Rsc advances	2.542	3.361
5th	Acta biomaterialia	2.447	8.947
6th	International journal of biological macromolecules	2.196	6.953
7th	Polymers	2.102	4.329
8th	Journal of materials chemistry B	2.04	6.331
9th	Biomaterials	1.945	12.48
10th	ACS biomaterials science & engineering	1.883	4.749

SCR, standard competition ranking; IF, impact factor; OA open access.

[a] *Equal journals have the same rank, and then a gap is left in the ranks.*

[b] *The impact factor was reported according to journal citation reports (JCR) 2021.*

top four keywords that were frequently mentioned are: application (1,513 times), engineering (1,366 times), poly (810 times) and development (539 times). Detailed data on the co-occurrence of all included keywords are presented in **Figure 7A**.

The keywords were divided into four clusters: characterisation of electroactive materials, function of electroactive materials, applications of electroactive materials in bone tissue engineering, and applications of electroactive materials in nerve and cardiac tissue engineering (**Figure 7B**). Keywords represent the main topics of publications. Co-occurrence analysis of keywords is conducive to systematically understanding the relationship between keywords, and consequently, grasping the relationship between various topics in this field. Further cluster analysis helps us to systematically understand current progress in this field. VOSviewer was employed to analyse keywords (defined as words that were used more than 35 times in titles and abstracts across all publications) in all included publications. For the characterisation of electroactive materials, the keyword with the highest frequency was poly (810 times). For the function of electroactive materials, this word was application (1,513 times). For the applications of electroactive materials in bone tissue engineering, the word was bone tissue engineering (513 times). For the applications of electroactive materials in nerve and cardiac tissue engineering, the word was conductivity (473 times). (**Figures 7A,B**).

As shown in **Figure 7C**, VOSviewer coloured all keywords according to the average number of times the word appeared. Specifically, blue indicates that the word appeared relatively early, while yellow indicates a more recent appearance. Compared with the keywords that appear most frequently, recent keywords can represent current research hotspots, which is of greater interest to us. VOSviewer colours all keywords according to the average number of times the word has appeared. In the cluster of characterisations of electroactive materials, the most recent keyword was water contact angle [42 times, average appearing year (AAY) 2018.3]. In the cluster of functions of electroactive materials, the newest keyword was sensor (82 times, AAY 2018.9). In the cluster of applications of electroactive materials in bone tissue engineering, the newest keyword was angiogenesis (50 times, AAY 2019.14). In the cluster of applications of electroactive materials in nerve and cardiac tissue engineering, the newest keywords were silk fibroin (71 times, AAY 2018.6) and conductive hydrogel (71 times, AAY 2018.3).

Related Field Analysis

In **Figure 8**, the 3,374 publications included in our research are mainly divided into two fields, one of which includes physics, materials, and chemistry, and the second field, which includes molecular, biological sciences, and immunology. In addition, the references of these 3,374 articles were mainly distributed across the following fields: physics, materials, and chemistry, and molecular, biological, and immunological studies. We found that the use of electroactive biomaterials in TE mainly involved subdisciplines in the fields of physics, materials, chemistry, molecular biology, and immunology. The development of this field is related to a combination of medical and engineering-related disciplines.

DISCUSSION

Trends in Research on the Electroactive Biomaterials Used in TE

China contributed the most to the publication volume of all countries (**Figure 3A**). The proportion of global output is increasing year by year, which shows that China attaches great importance to scientific research in this area (**Figure 4B**). This is followed by the United States, but publication in the United States has the highest H-index, which shows that United States publication has a greater impact around the world. The country contact map based on WOS data shows that China has connections with many countries which are active in this field, especially with the United States (**Figure 4A**), and that these two countries have the most publications, which indicates that mutual cooperation plays an important role in advancing the development of this field. Although Iran ranks third in the number of publications, Iran's publications are mostly after 2018, and their research results are the latest (**Figure 4B**). With regard to research institutions, the results were also significantly influenced by country; five of the top 10 institutions were from Iran (**Table 2**), and the latest

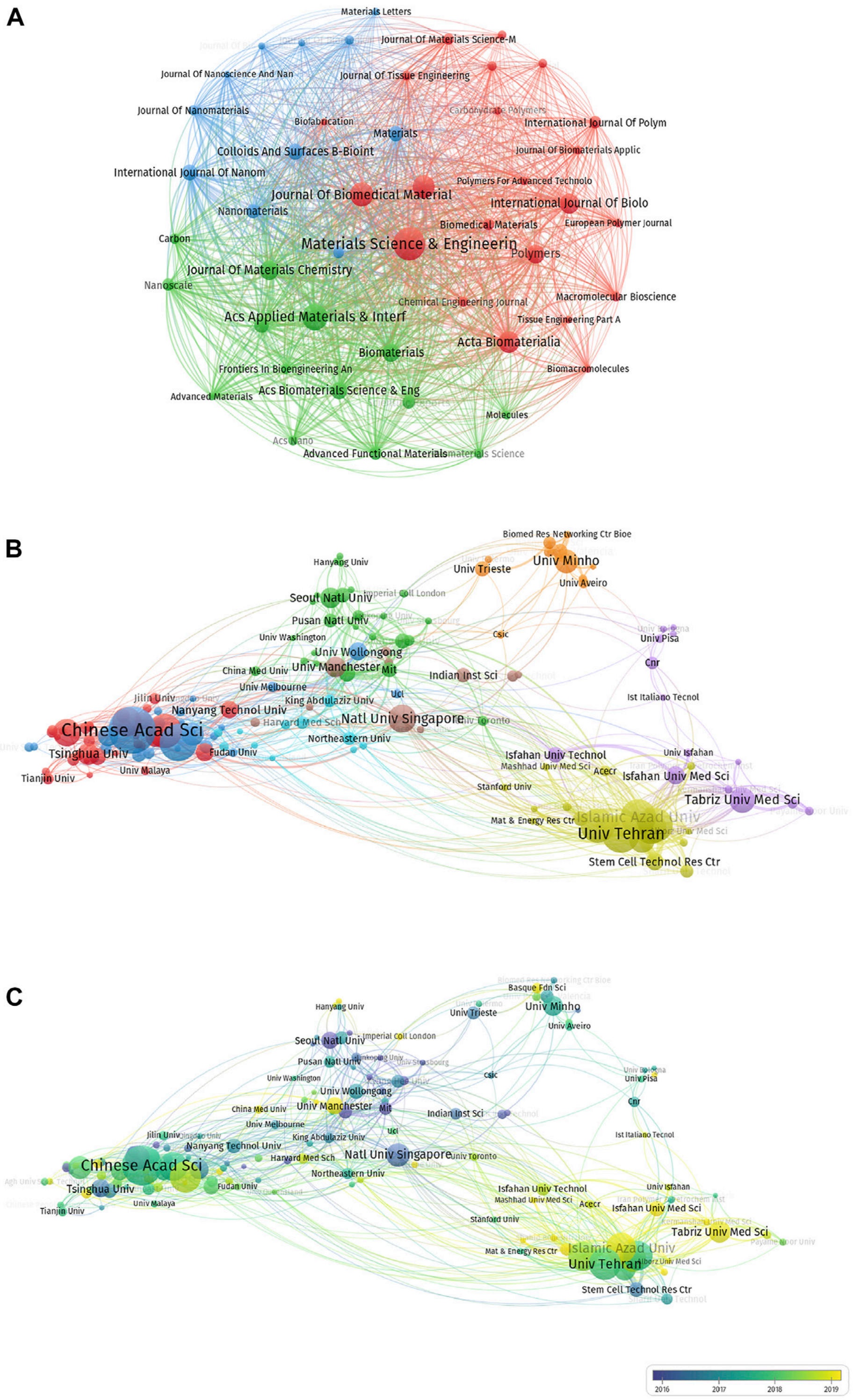

FIGURE 6 | The distribution of journals and institutions engaged in research on electroactive biomaterials used in TE. **(A)** Top 10 journals by number of publications, blue bar representing the proportion and red bar representing IF; **(A)**. The network of relationships between with different journals in VOSviewer. **(B)** The network of institutions produced in VOSviewer. The size of the circles reveals the number of publications; **(C)** Concentrated years of publications for different countries.

TABLE 2 | Top 10 institutes with the most publications on the electroactive biomaterials used in TE.

Rank	Institution	Contribution (%)	Country
1st	Chinese acad sci	3.36	China
2nd	Univ tehran	2.45	Iran
3rd	Shanghai jiao tong univ	2.42	China
4th	Islamic azad univ	2.29	Iran
4th	Sichuan univ	2.29	China
6th	Amirkabir univ Technol	2.23	Iran
6th	TarbiaT. modares univ	2.23	Iran
8th	Univ tehran med sci	2.04	Iran
9th	Univ michigan	1.85	United states
10th	Xi an jiao tong univ	1.79	China

publications were also concentrated in Iranian institutions (**Figure 6C**). This shows that Iran's research in this field is playing an increasingly important role, and that it has emerged as a new research centre.

The top 10 most-cited publications reflect the research hotspots and priorities in the field of electroactive biomaterials used in TE (**Table 3**). Two of the top three publications are related to nanomaterials, Nanotechnological strategies for engineering complex tissues mainly discusses the impact of nanostructures (Dvir et al., 2011) on the properties of scaffolds and their uses in monitoring the behaviour of engineered tissues. Biological interactions of graphene-family nanomaterials: An interdisciplinary review also proposed a systematic nomenclature for this set of graphene-family nanomaterials (GFNs) and discussed specific material properties relevant in biomolecular and cellular interactions (Sanchez et al., 2012), which indicates that nanomaterials are receiving increasing attention in this field. We also found that seven of the top 10 articles were related to graphene, with papers on the topics of neural stem cells, bone marrow mesenchymal stem cells, platelets, drug transport vectors, and other hot topics. Graphene and its derivatives have many applications in the field of TE owing to their superior properties, such as electrical conductivity, biocompatibility, transparency, high surface area, and superior mechanical strength (Tahriri et al., 2019). In particular, research on genotoxicity and biocompatibility of stem cell regeneration has attracted much attention (Akhavan et al., 2012; Li et al., 2013). We also found that seven were related to bone tissue engineering and four were related to nerve tissue engineering. This shows that the application of electroactive materials in bone and nerve tissue engineering is a research hotspot, and it also reflects the clinical transformation trend of electroactive materials in the future.

In terms of journals, the impact factors were generally high, including in biomedicine and materials (**Table 1**), which mainly includes a combination of physics, materials, chemistry, molecular biology, and immunology (**Figure 8**). This suggests that progress in the field requires collaboration across disciplines. Moreover, there has been a steady increase in scholarly interest, as reflected by the rapid increase in the RRI (**Figure 4B**) in recent years. We believe that there are two main reasons why this has received much attention. On the one hand, with increasing cases of organ shortages and donor scarcity within the last three decades, the research focus in the field of TE continues to advance toward a potential therapy for various types of tissue damage (Sharma et al., 2019; Matai et al., 2020). However, after years of development, an increasing number of electroactive biomaterials are expected to become a new generation of tissue defect repair materials because of their biocompatibility and easily modified surface characteristics, which can convert different types of signals such as mechanical, thermal, and magnetic signals into electrical signals to ultimately regulate

TABLE 3 | The top 10 authors with the highest total citations of papers published between 2011 and 2021.

Title	Corresponding authors	Journal	Total citations	Corresponding author's country	Research field
Nanotechnological strategies for engineering complex tissues	Dvir, T	Nature nanotechnology	985	United states	Bone TE. Nerve TE. Cardiac TE
Conductive polymers: Towards a smart biomaterial for tissue engineering	Cartmell, SH	Acta biomaterialia	930	England	Nerve TE
Biological interactions of graphene-family nanomaterials: An interdisciplinary review	Hurt, RH	Chemical research in toxicology	873	United states	Bone TE. Cartilage TE
Graphene-based nanomaterials for drug delivery and tissue engineering	Sant, S	Journal of controlled release	774	United states	Bone TE. Nerve TE
Origin of enhanced stem cell growth and differentiation on graphene and graphene oxide	Lim, CT	ACS nano	736	Singapore	Bone TE
Graphene for controlled and accelerated osteogenic differentiation of human mesenchymal stem cells	Pastorin, G	ACS nano	676	Singapore	Bone TE. Cartilage TE. Skin TE
Carbon-nanotube-embedded hydrogel sheets for engineering cardiac constructs and bioactuators	Tang, XW	ACS nano	567	Canada	Cardiac TE
Size-dependent genotoxicity of graphene nanoplatelets in human stem cells	Akhavan	Biomaterials	516	Iran	Bone TE
Three-dimensional graphene foam as a biocompatible and conductive scaffold for neural stem cells	Dai, JW	Scientific reports	481	China	Nerve TE
Lightweight conductive graphene/thermoplastic polyurethane foams with ultrahigh compressibility for piezoresistive sensing	Liu, CT	Trends in cell biology	470	China	Material preparation

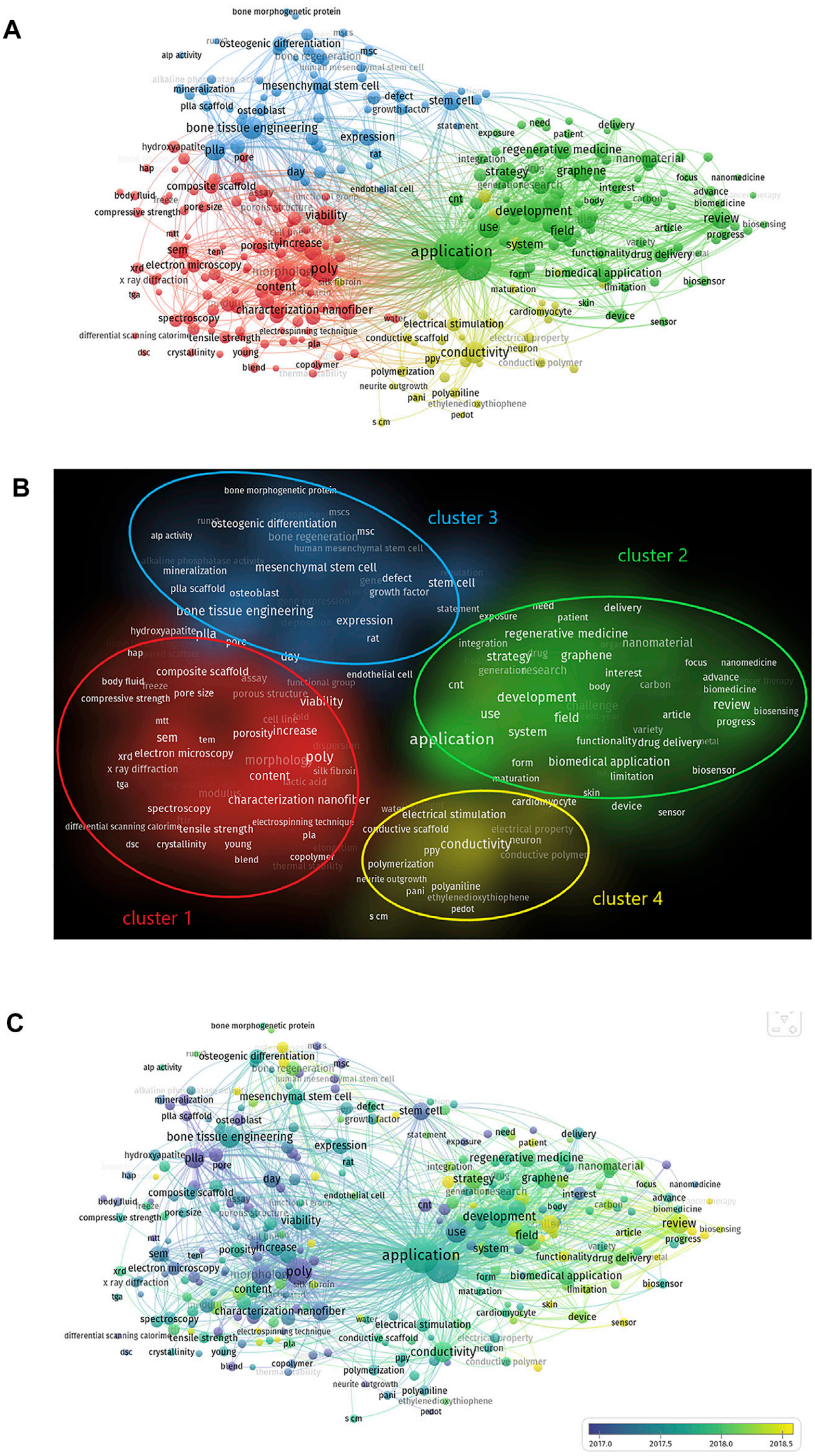

FIGURE 7 | The analysis of keywords in publications on electroactive biomaterials used in TE. **(A)** Mapping of keywords in the field of the use of ultrasound in emergency medicine. The size of the circle represents the frequency with which keywords appear. **(B)** Mapping of the keywords in the area of electroactive biomaterials used in TE. The words were divided into four clusters in accordance with different colours that were generated by default, specifically, characterization of electroactive materials (lower left in red), function of electroactive materials (upper right in green), application of electroactive materials in bone tissue engineering (upper left in blue) and application of electroactive materials in nerve and cardiac tissue engineering (lower right in yellow); **(C)** The distribution of keywords is presented according to the average time of appearance. The blue colour represents an early appearance, and the yellow colour represents a late appearance.

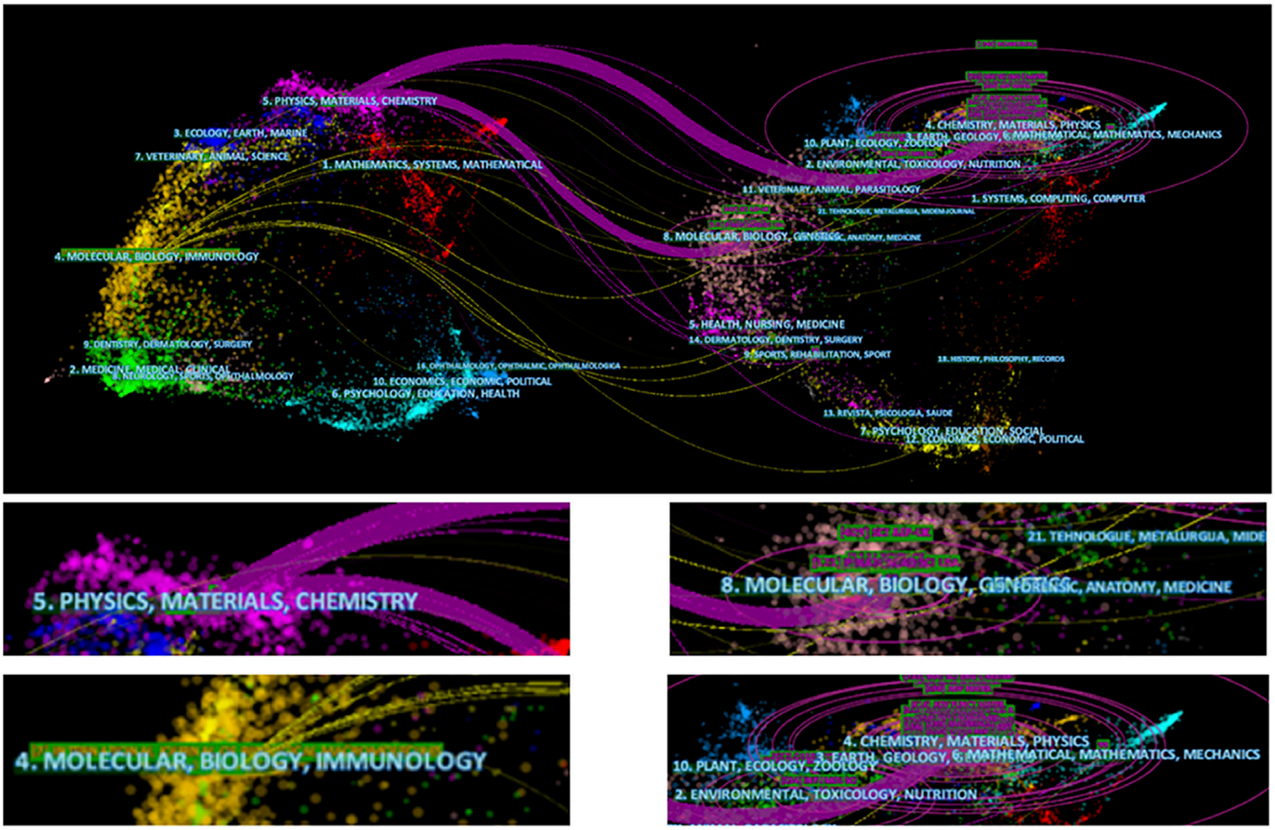

FIGURE 8 | Fields related to electroactive biomaterials used in TE. The lefthand side represents the fields of the articles included in the study, and the righthand side represents the fields of the references of the articles.

tissue regeneration (Finkenstadt and Willett, 2006; Balint et al., 2014).

Research Focused on Electroactive Biomaterials Used in TE

According to the map based on bibliographic data from the co-occurrence analysis of all keywords (**Figures 7A,C**), the keywords were divided into four clusters (**Figure 7B**). The latest keywords of the four clusters will describe future research hotspots in this field comprehensively and profoundly.

With respect to the latest research hotspots, in the cluster of functions of electroactive materials, the newest keyword of this cluster is a sensor with an AAY of 2018.9878. The potential reasons for this are as follows: First, electroactive materials are most commonly applied in sensors and actuators because of their ability to deliver electrical signals to cells and tissue (Bar-Cohen et al., 2017). Furthermore, because of the characteristics of sensors, electroactive materials are emerging as new disease-modifying therapies that offer the possibility of improving tissue repair and regeneration and re-establishing functionality at both the cellular and organ levels (Pinho et al., 2021). With developments in materials, manufacturing, biotechnology, and microelectromechanical systems (MEMS), many exciting biosensors and bioactuators have been developed based on biocompatible piezoelectric materials. These biodevices can be safely integrated into biological systems for applications such as sensing biological forces, stimulating tissue growth and healing, and diagnosing medical problems (Chorsi et al., 2019). This suggests that advances in sensors are laying the foundation for an entire field of development, and they are also becoming a hotspot in future research.

Regarding the topic of the characterisation of electroactive material clusters, the water contact angle was the most recent keyword, with an AAY of 2018.381. Biological interactions take place at the surface of biomaterials, where they are in direct contact with the host tissue. Some current studies confirm that one of the disadvantages of some biomaterials is their hydrophobicity, which limits their applications in TE. Moreover surfaces with a moderate wettability (water contact angle of 30–60°) have been shown to be favourable for cell adhesion and proliferation (Andrade et al., 1979; Hsu and Chen, 2000). Another study showed that electroactive barium titanate-coated titanium scaffolds improve osteogenesis and osseointegration for large segmental bone defects, and this success is closely related to the water contact angle (Fan et al., 2020). In view of this, Guo (Guo et al., 2012; Guo et al., 2019) [42,4342,43] made electroactive porous tubular scaffolds with a hydrophilic surface with a water contact angle of approximately 30° by doping the films with (±)-10-camphorsulfonic acid. These degradable electroactive tubular scaffolds are good candidates for neural tissue engineering applications, and studies in this field are becoming more detailed (Guo et al., 2012). We predict that the hydrophilicity of electroactive materials in TE will be one of the evaluation standards for electroactive materials in the future. Therefore, determination of the water contact angle is an indispensable step in future electroactive material research. This also suggests that more attention should be paid to research on the water contact angles of similar materials.

Regarding the electroactive materials used in nerve and cardiac tissue engineering, the latest terms were silk fibroin (AAY 2018.3099) and conductive hydrogel (AAY 2018.662), occurring 71 times (**Figure 7C**). Nerve restoration and repair in the central nervous system are complicated and require several factors to be considered in the design of scaffolds, such as bioactivity and neuroinductive, neuroconductive, and antioxidant properties. According to publication numbers, the term silk fibroin (SF) has attracted more attention among researchers. SF has unique mechanical properties and biocompatibility (Altman et al., 2003), and nerve guidance channels made up of electrospun and woven silk fibroin/poly (lactic-co-glycolic acid) are biocompatible and have a favourable mechanical strength (Wang et al., 2015). In conservative therapy for myocardial infarction (MI), electroactive silk fibroin/PLA nanofibrous bioactive scaffolds have been proven to inspire the rejuvenation of injured myocardium (Yan et al., 2020). Similarly, cerium oxide nanoparticles encapsulated in fabricated hybrid silk fibroin nanofibres have been reported as an artificial neural guidance conduit applicable in peripheral nerve regeneration (Saremi et al., 2021). Although research on silk fibroin used in TE is still in its infancy, it provides new perspectives for therapeutic strategies in nerve tissue and cardiac tissue regeneration.

(Dvir et al., 2011) and (Shin et al., 2012; Khorshidi and Karkhaneh, 2018) reported a successful demonstration of a myocardial tissue engineering scaffold based on conductive hydrogel that can promote the bridging of electrical signal pathways of adjacent cells, thus achieving myocardial tissue regeneration and functional reconstruction. This success encouraged the development of a wide range of conductive hydrogel-based myocardial tissue engineering scaffolds. For example, Liu et al. (2022) and Wei et al. (2022) developed paintable and rapidly bondable conductive hydrogels as therapeutic cardiac patches, which can improve the reconstruction of cardiac function and revascularization of infarct myocardium (Wei et al., 2022). Works by Qian et al. (2018a), Qian et al. (2018b), and Xu et al. (2018) successfully demonstrated that nerve tissue engineering scaffold-coated graphene-loaded polycaprolactone based on a conductive hydrogel can transmit electrical signals, thus realising nerve tissue regeneration and functional reconstruction. This success has promoted the development of a wide range of nerve tissue-engineering scaffolds based on conductive hydrogels (Xu et al., 2018). Although conductive hydrogels have shown potential in tissue engineering applications, research on them is still in the early stages, because they currently have constraints, such as the inability to balance high mechanical properties and high electrical conductivity, and difficulties with adjusting mechanical properties (Liu et al., 2020). In practice, there is still abundant room for further progress in conductive hydrogel research on TE.

Regarding the cluster of applications of electroactive materials in bone tissue engineering, angiogenesis is the most recent keyword (cluster3), with an AAY of 2019.14. This word is also the latest keyword in all clusters. Recent research has shown that electroactive materials can induce vascular endothelial cell luminal formation *in vitro* and neovascularization *in vivo* (Augustine et al., 2017). Research indicated that polarised nanocomposite membranes and DBB granules have a synergistic effect in promoting bone defect repair by means of active early neovascularization (Bai et al., 2019). Meanwhile, in treatments for the regeneration of infectious bone defects, vancomycin—and strontium-loaded microspheres, which are made of a block copolymer consisting of poly (L-lactide) (PLLA) and poly (ethyl glycol) (PEG) blocks, have broad applications in the field of bone tissue engineering, one of which is its capacity for enhancing angiogenesis (Wei et al., 2019). Early neovascularization has a profound effect on subsequent bone remodelling and maturation; therefore, it has received increasing attention in recent years.

To summarise the general trends of the four groups in this study, the most fundamental one is the characterisation of electroactive materials. Recently, more attention has been paid to the application of electroactive materials in bone tissue engineering (**Figure 7C**), which suggests that although new functional materials are constantly being developed, attention should also be paid to their applications and subsequent transformations in tissue engineering. In addition, electroactive materials have some defects in application. First of all, some electroactive biomaterials may have immune rejection after implantation because of their poor biocompatibility. Secondly, some electroactive biomaterials have limited degradability, which limits their application as tissue regeneration and repair materials. Improving the above shortcomings will be the future direction of researchers.

In addition, in terms of research fields, subjects related to materials, such as physics, chemistry, and biology (**Figure 8**), are worthy of attention. In terms of research, research is not limited to material applications. Basial research, including molecular, mechanical, and immunological research (**Figure 8**), cannot be ignored. It is believed that the development of any field requires multidisciplinary communication and assistance, similar to what is currently seen for the electroactive biomaterials in the TE field.

Limitation

Publications in the WOS database were investigated in this study to obtain objective and reliable results. It has been confirmed that document type labels in web of science are more accurate than Scopus in previous report, So we perform WOS-based retrieval preferentially (Yeung, 2019). However, owing to the limitation of searching for studies in English and constant updates of the database, our results may differ slightly from the reality. In addition, for more comprehensive results, databases such as Scopus, and Google Scholar could be included and compared in future studies. Due to the characteristics of database retrieval, we can't analyse the hot spots and future trends of the application of electroactive materials in each type of tissue engineering in detail, and we hope to be able to more detailed analysis in the future research.

CONCLUSION

China has contributed the most to the field of electroactive biomaterials used in TE, and Iran has shown the highest research interest in this area in recent years, and cooperation between countries is crucial. The number of future publications in this field is expected to increase. Sensors, the water contact angle, angiogenesis, silk fibroin, and conductive hydrogels are the focus of our attention in the future, and attention should also be paid to the applications and transformations of electroactive materials, and bone tissue engineering in particular. An overall analysis of the field from the perspective of physics, chemistry, biology, molecular mechanics, and immunology is the latest research direction. Similarly, the development of the field requires joint efforts from all disciplines.

DATA AVAILABILITY STATEMENT

The original contributions presented in the study are included in the article/**Supplementary Material**, further inquiries can be directed to the corresponding authors.

AUTHOR CONTRIBUTIONS

DX, FL, and BL contributed to conception and design of the study. DX organized the database. SW, WX performed the statistical analysis. WX wrote the first draft of the manuscript. WX, SW, ZW, and YC wrote sections of the manuscript. All authors contributed to manuscript revision, read, and approved the submitted version.

FUNDING

We acknowledge support from Hainan Province Clinical Medical Center.

SUPPLEMENTARY MATERIAL

The Supplementary Material for this article can be found online at: https://www.frontiersin.org/articles/10.3389/fbioe.2022.904629/full#supplementary-material

REFERENCES

Akhavan, O., Ghaderi, E., and Akhavan, A. (2012). Size-dependent Genotoxicity of Graphene Nanoplatelets in Human Stem Cells. *Biomaterials* 33 (32), 8017–8025. doi:10.1016/j.biomaterials.2012.07.040

Altman, G. H., Diaz, F., Jakuba, C., Calabro, T., Horan, R. L., Chen, J., et al. (2003). Silk-based Biomaterials. *Biomaterials* 24 (3), 401–416. doi:10.1016/S0142-9612(02)00353-8

Andrade, J. D., King, R. N., Gregonis, D. E., and Coleman, D. L. (1979). Surface Characterization of Poly(hydroxyethyl Methacrylate) and Related Polymers. I. Contact Angle Methods in Water. *J. Polym. Sci. C Polym. Symp.* 66 (1), 313–336. doi:10.1002/polc.5070660130

Augustine, R., Dan, P., Sosnik, A., Kalarikkal, N., Tran, N., Vincent, B., et al. (2017). Electrospun Poly(vinylidene Fluoride-Trifluoroethylene)/zinc Oxide Nanocomposite Tissue Engineering Scaffolds with Enhanced Cell Adhesion and Blood Vessel Formation. *Nano Res.* 10 (10), 3358–3376. doi:10.1007/s12274-017-1549-8

Bai, Y., Dai, X., Yin, Y., Wang, J., Sun, X., Liang, W., et al. (2019). Biomimetic Piezoelectric Nanocomposite Membranes Synergistically Enhance Osteogenesis of Deproteinized Bovine Bone Grafts. *Ijn* 14, 3015–3026. doi:10.2147/ijn.S197824

Balint, R., Cassidy, N. J., and Cartmell, S. H. (2014). Conductive Polymers: towards a Smart Biomaterial for Tissue Engineering. *Acta Biomater.* 10 (6), 2341–2353. doi:10.1016/j.actbio.2014.02.015

Bar-Cohen, Y., Cardoso, V. F., Ribeiro, C., and Lanceros-Méndez, S. (2017). Electroactive Polymers as Actuators. *Advanced Piezoelectric Materials. Second Ed.*, 319–352. doi:10.1016/b978-0-08-102135-4.00008-4

Brown, R. T. (1980). Topics in Applied Physics. *Proc. IEEE* 68 (3), 429. doi:10.1109/proc.1980.11665

Chen, Y., Cheng, L., Lian, R., Song, Z., and Tian, J. (2021). COVID-19 Vaccine Research Focusses on Safety, Efficacy, Immunoinformatics, and Vaccine Production and Delivery: a Bibliometric Analysis Based on VOSviewer. *Bst* 15 (2), 64–73. doi:10.5582/bst.2021.01061

Chorsi, M. T., Curry, E. J., Chorsi, H. T., Das, R., Baroody, J., Purohit, P. K., et al. (2019). Piezoelectric Biomaterials for Sensors and Actuators. *Adv. Mat.* 31 (1), 1802084. doi:10.1002/adma.201802084

Debels, H., Hamdi, M., Abberton, K., and Morrison, W. (2015). Dermal Matrices and Bioengineered Skin Substitutes: Critical Review of Current Options. *Plastic Reconstr. Surg. Glob. Open* 3 (1), e284. doi:10.1097/gox.0000000000000219

Dvir, T., Timko, B. P., Kohane, D. S., and Langer, R. (2011). Nanotechnological Strategies for Engineering Complex Tissues. *Nat. Nanotech* 6 (1), 13–22. doi:10.1038/nnano.2010.246

Fan, B., Guo, Z., Li, X., Li, S., Gao, P., Xiao, X., et al. (2020). Electroactive Barium Titanate Coated Titanium Scaffold Improves Osteogenesis and Osseointegration with Low-Intensity Pulsed Ultrasound for Large Segmental Bone Defects. *Bioact. Mater.* 5 (4), 1087–1101. doi:10.1016/j.bioactmat.2020.07.001

Favre, J., Germond, T., Clavert, P., Collin, P., Michelet, A., and Lädermann, A. (2020). Want a Better H-Index? - All You Need to Know about Copyright and Open Access. *Orthop. Traumatology Surg. Res.* 106 (8), 1475–1480. doi:10.1016/j.otsr.2020.05.015

Finkenstadt, V. L., and Willett, J. L. (2006). Characterization of Functionalized Electroactive Biopolymers. *ACS Symp. Ser.* 935, 256–261.

Georgiou, M., Golding, J. P., Loughlin, A. J., Kingham, P. J., and Phillips, J. B. (2015). Engineered Neural Tissue with Aligned, Differentiated Adipose-Derived Stem Cells Promotes Peripheral Nerve Regeneration across a Critical Sized Defect in Rat Sciatic Nerve. *Biomaterials* 37, 242–251. doi:10.1016/j.biomaterials.2014.10.009

Guarino, V., Alvarez-Perez, M. A., Borriello, A., Napolitano, T., and Ambrosio, L. (2013). Conductive PANi/PEGDA Macroporous Hydrogels for Nerve Regeneration. *Adv. Healthc. Mater.* 2 (1), 218–227. doi:10.1002/adhm.201200152

Guimard, N. K., Gomez, N., and Schmidt, C. E. (2007). Conducting Polymers in Biomedical Engineering. *Prog. Polym. Sci.* 32 (8), 876–921. doi:10.1016/j.progpolymsci.2007.05.012

Guo, B., and Ma, P. X. (2018). Conducting Polymers for Tissue Engineering. *Biomacromolecules* 19 (6), 1764–1782. doi:10.1021/acs.biomac.8b00276

Guo, B., Qu, J., Zhao, X., and Zhang, M. (2019). Degradable Conductive Self-Healing Hydrogels Based on Dextran-Graft-Tetraaniline and N-Carboxyethyl Chitosan as Injectable Carriers for Myoblast Cell Therapy and Muscle Regeneration. *Acta Biomater.* 84, 180–193. doi:10.1016/j.actbio.2018.12.008

Guo, B., Sun, Y., Finne-Wistrand, A., Mustafa, K., and Albertsson, A.-C. (2012). Electroactive Porous Tubular Scaffolds with Degradability and Non-cytotoxicity for Neural Tissue Regeneration. *Acta Biomater.* 8 (1), 144–153. doi:10.1016/j.actbio.2011.09.027

Hsu, S.-H. S. -h., and Chen, W.-C. (2000). Improved Cell Adhesion by Plasma-Induced Grafting of L-Lactide onto Polyurethane Surface. *Biomaterials* 21 (4), 359–367. doi:10.1016/s0142-9612(99)00191-x

Jaspan, V. N., and Hines, G. L. (2015). The Current Status of Tissue-Engineered Vascular Grafts. *Cardiol. Rev.* 23 (5), 236–239. doi:10.1097/crd.0000000000000060

Kavic, M. S., and Satava, R. M. (2021). Scientific Literature and Evaluation Metrics: Impact Factor, Usage Metrics, and Altmetrics. *Jsls* 25 (3), e2021.00010. doi:10.4293/jsls.2021.00010

Khorshidi, S., and Karkhaneh, A. (2018). Hydrogel/fiber Conductive Scaffold for Bone Tissue Engineering. *J. Biomed. Mat. Res.* 106 (3), 718–724. doi:10.1002/jbm.a.36282

Ku, S. H., Lee, M., and Park, C. B. (2013). Carbon-based Nanomaterials for Tissue Engineering. *Adv. Healthc. Mater.* 2 (2), 244–260. doi:10.1002/adhm.201200307

Lalan, B.A., S., Pomerantseva, M.D., I., and Vacanti, M.D., J. P. (2001). Tissue Engineering and its Potential Impact on Surgery. *World J. Surg.* 25 (11), 1458–1466. doi:10.1007/s00268-001-0131-3

Langer, R., and Vacanti, J. P. (1993). Tissue Engineering. *Science* 260 (5110), 920–926. doi:10.1126/science.8493529

Li, F., Li, M., Guan, P., Ma, S., and Cui, L. (2015). Mapping Publication Trends and Identifying Hot Spots of Research on Internet Health Information Seeking Behavior: a Quantitative and Co-word Biclustering Analysis. *J. Med. Internet Res.* 17 (3), e81. doi:10.2196/jmir.3326

Li, N., Zhang, Q., Gao, S., Song, Q., Huang, R., Wang, L., et al. (2013). Three-dimensional Graphene Foam as a Biocompatible and Conductive Scaffold for Neural Stem Cells. *Sci. Rep.* 3, 1604. doi:10.1038/srep01604

Liu, K., Wei, S., Song, L., Liu, H., and Wang, T. (2020). Conductive Hydrogels-A Novel Material: Recent Advances and Future Perspectives. *J. Agric. Food Chem.* 68 (28), 7269–7280. doi:10.1021/acs.jafc.0c00642

Matai, I., Kaur, G., Seyedsalehi, A., McClinton, A., and Laurencin, C. T. (2020). Progress in 3D Bioprinting Technology for Tissue/organ Regenerative Engineering. *Biomaterials* 226, 119536. doi:10.1016/j.biomaterials.2019.119536

Naveau, A., Smirani, R., Catros, S., De Oliveira, H., Fricain, J.-C., and Devillard, R. (2017). A Bibliometric Study to Assess Bioprinting Evolution. *Appl. Sci.* 7 (12), 1331. doi:10.3390/app7121331

Nerem, R. M. (1992). Tissue Engineering in the USA. *Med. Biol. Eng. Comput.* 30 (4), Ce8–CE12. doi:10.1007/bf02446171

Pati, F., Song, T.-H., Rijal, G., Jang, J., Kim, S. W., and Cho, D.-W. (2015). Ornamenting 3D Printed Scaffolds with Cell-Laid Extracellular Matrix for Bone Tissue Regeneration. *Biomaterials* 37, 230–241. doi:10.1016/j.biomaterials.2014.10.012

Pinho, T. S., Cunha, C. B., Lanceros-Méndez, S., and Salgado, A. J. (2021). Electroactive Smart Materials for Neural Tissue Regeneration. *ACS Appl. Bio Mat.* 4 (9), 6604–6618. doi:10.1021/acsabm.1c00567

Qian, Y., Song, J., Zhao, X., Chen, W., Ouyang, Y., Yuan, W., et al. (2018a). 3D Fabrication with Integration Molding of a Graphene Oxide/Polycaprolactone Nanoscaffold for Neurite Regeneration and Angiogenesis. *Adv. Sci.* 5 (4), 1700499. doi:10.1002/advs.201700499

Qian, Y., Zhao, X., Han, Q., Chen, W., Li, H., and Yuan, W. (2018b). An Integrated Multi-Layer 3D-Fabrication of PDA/RGD Coated Graphene Loaded PCL Nanoscaffold for Peripheral Nerve Restoration. *Nat. Commun.* 9 (1), 323. doi:10.1038/s41467-017-02598-7

Ren, K., He, C., Xiao, C., Li, G., and Chen, X. (2015). Injectable Glycopolypeptide Hydrogels as Biomimetic Scaffolds for Cartilage Tissue Engineering. *Biomaterials* 51, 238–249. doi:10.1016/j.biomaterials.2015.02.026

Sanchez, V. C., Jachak, A., Hurt, R. H., and Kane, A. B. (2012). Biological Interactions of Graphene-Family Nanomaterials: an Interdisciplinary Review. *Chem. Res. Toxicol.* 25 (1), 15–34. doi:10.1021/tx200339h

Santisteban-Espejo, A., Campos, F., Martin-Piedra, L., Durand-Herrera, D., Moral-Munoz, J. A., Campos, A., et al. (2018). Global Tissue Engineering Trends: A Scientometric and Evolutive Study. *Tissue Eng. Part A* 24 (19-20), 1504–1517. doi:10.1089/ten.TEA.2018.0007

Saremi, J., Khanmohammadi, M., Azami, M., Ai, J., Yousefi-Ahmadipour, A., and Ebrahimi-Barough, S. (2021). Tissue-engineered Nerve Graft Using Silk-fibroin/polycaprolactone Fibrous Mats Decorated with Bioactive Cerium Oxide Nanoparticles. *J. Biomed. Mater Res.* 109 (9), 1588–1599. doi:10.1002/jbm.a.37153

Sharma, P., Kumar, P., Sharma, R., Kumar, P., Sharma, R., Dhar Bhatt, V., et al. (2019). Tissue Engineering; Current Status & Futuristic Scope. *JMedLife* 12 (3), 225–229. doi:10.25122/jml-2019-0032

Shin, S. R., Bae, H., Cha, J. M., Mun, J. Y., Chen, Y.-C., Tekin, H., et al. (2012). Carbon Nanotube Reinforced Hybrid Microgels as Scaffold Materials for Cell Encapsulation. *ACS Nano* 6 (1), 362–372. doi:10.1021/nn203711s

Stewart, E., Kobayashi, N. R., Higgins, M. J., Quigley, A. F., Jamali, S., Moulton, S. E., et al. (2015). Electrical Stimulation Using Conductive Polymer Polypyrrole Promotes Differentiation of Human Neural Stem Cells: a Biocompatible Platform for Translational Neural Tissue Engineering. *Tissue Eng. Part C. Methods* 21 (4), 385–393. doi:10.1089/ten.TEC.2014.0338

Sukmana, I. (2012). Bioactive Polymer Scaffold for Fabrication of Vascularized Engineering Tissue. *J. Artif. Organs* 15 (3), 215–224. doi:10.1007/s10047-012-0644-6

Tahriri, M., Del Monico, M., Moghanian, A., Tavakkoli Yaraki, M., Torres, R., Yadegari, A., et al. (2019). Graphene and its Derivatives: Opportunities and Challenges in Dentistry. *Mater. Sci. Eng. C* 102, 171–185. doi:10.1016/j.msec.2019.04.051

van Eck, N. J., and Waltman, L. (2010). Software Survey: VOSviewer, a Computer Program for Bibliometric Mapping. *Scientometrics* 84 (2), 523–538. doi:10.1007/s11192-009-0146-3

Wang, M., Liu, P., Gu, Z., Cheng, H., and Li, X. (2019). A Scientometric Review of Resource Recycling Industry. *Ijerph* 16 (23), 4654. doi:10.3390/ijerph16234654

Wei, P., Jing, W., Yuan, Z., Huang, Y., Guan, B., Zhang, W., et al. (2019). Vancomycin- and Strontium-Loaded Microspheres with Multifunctional Activities against Bacteria, in Angiogenesis, and in Osteogenesis for Enhancing Infected Bone Regeneration. *ACS Appl. Mat. Interfaces* 11 (34), 30596–30609. doi:10.1021/acsami.9b10219

Wei, X., Chen, S., Xie, T., Chen, H., Jin, X., Yang, J., et al. (2022). An MMP-Degradable and Conductive Hydrogel to Stabilize HIF-1α for Recovering Cardiac Functions. *Theranostics* 12 (1), 127–142. doi:10.7150/thno.63481

Xia, D.-M., Wang, X.-R., Zhou, P.-Y., Ou, T.-L., Su, L., and Xu, S.-G. (2021). Research Progress of Heat Stroke during 1989-2019: a Bibliometric Analysis. *Mil. Med. Res.* 8 (1), 5. doi:10.1186/s40779-021-00300-z

Xia, D., Wu, J., Zhou, F., Wang, S., Zhang, Z., Zhou, P., et al. (2021). Mapping Thematic Trends and Analysing Hotspots Concerning the Use of Stem Cells for Cartilage Regeneration: A Bibliometric Analysis from 2010 to 2020. *Front. Pharmacol.* 12, 737939. doi:10.3389/fphar.2021.737939

Xu, C., Guan, S., Wang, S., Gong, W., Liu, T., Ma, X., et al. (2018). Biodegradable and Electroconductive Poly(3,4-Ethylenedioxythiophene)/carboxymethyl Chitosan Hydrogels for Neural Tissue Engineering. *Mater. Sci. Eng. C* 84, 32–43. doi:10.1016/j.msec.2017.11.032

Yan, C., Ren, Y., Sun, X., Jin, L., Liu, X., Chen, H., et al. (2020). Photoluminescent Functionalized Carbon Quantum Dots Loaded Electroactive Silk Fibroin/PLA Nanofibrous Bioactive Scaffolds for Cardiac Tissue Engineering. *J. Photochem. Photobiol. B Biol.* 202, 111680. doi:10.1016/j.jphotobiol.2019.111680

Yang, Y.-m., Wang, Y.-l., Gu, X.-m., Kong, Y., and Feng, Q.-l. (2015). Electrospun and Woven Silk Fibroin/poly(lactic-Co- Glycolic Acid) Nerve Guidance Conduits for Repairing Peripheral Nerve Injury. *Neural Regen. Res.* 10 (10), 1635–1642. doi:10.4103/1673-5374.167763

Yao, L., Hui, L., Yang, Z., Chen, X., and Xiao, A. (2020). Freshwater Microplastics Pollution: Detecting and Visualizing Emerging Trends Based on Citespace II. *Chemosphere* 245, 125627. doi:10.1016/j.chemosphere.2019.125627

Yeung, A. (2019). Comparison between Scopus, Web of Science, PubMed and Publishers for Mislabelled Review Papers. *Curr. Sci.* 16 (11), 1909–1914. doi:10.18520/cs/v116/i11/1909-1914

Zou, X., Yue, W. L., and Vu, H. L. (2018). Visualization and Analysis of Mapping Knowledge Domain of Road Safety Studies. *Accid. Analysis Prev.* 118, 131–145. doi:10.1016/j.aap.2018.06.010

Conflict of Interest: The authors declare that the research was conducted in the absence of any commercial or financial relationships that could be construed as a potential conflict of interest.

Frontiers in Bioengineering and Biotechnology

TYPE Original Research
PUBLISHED 22 July 2022
DOI 10.3389/fbioe.2022.944435

Adhesive hydrogel wrap loaded with Netrin-1-modified adipose-derived stem cells: An effective approach against periarterial inflammation after endovascular intervention

Yihong Jiang[1†], Yuting Cai[2,3†], Jiateng Hu[1†], Xing Zhang[1*], Jiahao Lei[1], Zhaoxi Peng[1], Qun Huang[1], Zhijue Xu[1], Bo Li[1], Jinbao Qin[1], Weimin Li[1], Dazhi Sun[3*], Kaichuang Ye[1*] and Xinwu Lu[1*]

[1]Department of Vascular Surgery, Shanghai Ninth People's Hospital, Shanghai Jiao Tong University School of Medicine, Shanghai, China, [2]Department of Chemical and Biological Engineering, William Mong Institute of Nano Science and Technology, The Hong Kong University of Science and Technology, Kowloon, Hong Kong SAR, China, [3]Guangdong Provincial Key Laboratory of Functional Oxide Materials and Devices, Southern University of Science and Technology, Shenzhen, Guangdong, China

Endovascular interventions, such as balloon dilation and stent implantation, are currently recommended as the primary treatment for patients with peripheral artery disease (PAD), greatly improving patient prognosis. However, the consequent lumen restenosis that occurs after endovascular interventions has become an important clinical problem. Inflammation has been proven to be crucial to postoperative restenosis. In previous studies we have identified that Netrin-1-modified adipose-derived stem cells (N-ADSCs) transplantation is an effective anti-inflammatory strategy to repair vascular damage. Nevertheless, it remained to be explored how one could constantly deliver N-ADSCs onto damaged arteries. Therefore, we developed an adhesive double network (DN) hydrogel wrap loaded with N-ADSCs for sustained perivascular delivery. Inspired by the adhesion mechanism of mussels, we developed an adhesive and tough polyacrylamide/calcium-alginate/reduced graphene oxide/polydopamine (PAM/CA/rGO/PDA) hydrogel. Dopamine was attached to graphene sheets and limitedly oxidized to generate free catechol groups. The hydrogel could wrap damaged arteries and induce anti-inflammatory effects through N-ADSCs. *In vitro* experiments demonstrated that N-ADSCs significantly promoted the M2 polarization of macrophages to anti-inflammatory phenotypes and reduced the expression of inflammatory factors. *In vivo* experiments in a rat carotid artery guidewire injury model showed that the adhesive hydrogel wrap loaded with N-ADSCs could significantly reduce arterial inflammation, inhibit intimal hyperplasia and improve re-endothelialization. Altogether, this newly developed N-ADSCs-loaded hydrogel wrap provides an effective slow-releasing system, which

OPEN ACCESS

EDITED BY
Yun Qian,
Shanghai Jiao Tong University, China

REVIEWED BY
Jing Chen,
Ningbo Institute of Materials Technology and Engineering (CAS), China
Jin Wang,
Southwest Jiaotong University, China

*CORRESPONDENCE
Xing Zhang,
zhangxing@shsmu.edu.cn
Dazhi Sun,
sundz@sustc.edu.cn
Kaichuang Ye,
ykaichuang@163.com
Xinwu Lu,
luxinwu@shsmu.edu.cn

[†]These authors have contributed equally to this work

SPECIALTY SECTION
This article was submitted to Biomaterials, a section of the journal Frontiers in Bioengineering and Biotechnology

RECEIVED 15 May 2022
ACCEPTED 27 June 2022
PUBLISHED 22 July 2022

CITATION
Jiang Y, Cai Y, Hu J, Zhang X, Lei J, Peng Z, Huang Q, Xu Z, Li B, Qin J, Li W, Sun D, Ye K and Lu X (2022), Adhesive hydrogel wrap loaded with Netrin-1-modified adipose-derived stem cells: An effective approach against periarterial inflammation after endovascular intervention.
Front. Bioeng. Biotechnol. 10:944435.
doi: 10.3389/fbioe.2022.944435

may be a promising way to prevent and treat restenosis after endovascular interventions.

KEYWORDS

endovascular interventions, Netrin-1, adipose-derived stem cells, macrophages, intimal hyperplasia, re-endothelialization, adhesive hydrogel, dopamine

Introduction

Peripheral artery disease (PAD) is an ischemic disease caused by peripheral atherosclerotic stenosis and occlusion, which affects 230 million individuals worldwide. Up to 11% of PAD patients develop chronic limb-threatening ischemia (CLTI) with high rates of amputation and death. Endovascular interventions have gradually replaced open surgeries in the treatment of PAD. Indeed, the 2020 Global Vascular Guidelines recommended endovascular interventions (e.g., balloon dilation, stent implantation) as the first line of treatment for CLTI patients (Conte et al., 2019). However, endovascular interventions lead to a risk of up to 55% of postoperative vascular lumen restenosis. Although new drug-coated balloons and stents are currently being developed and implemented, the long-term restenosis rate is still 10%–20% (Razavi et al., 2018).

The pathophysiological mechanism that concurs lumen restenosis involves endothelial cell injury and intimal hyperplasia caused by chronic inflammation. Endovascular interventions inevitably result in mechanical injury of endothelial cells, impaired endothelial integrity, and endothelial cell dysfunction. These alterations lead to macrophage infiltration and migration of medial smooth muscle cells to the intima, culminating in lumen restenosis (Yahagi et al., 2014). Devices coated with paclitaxel or sirolimus were shown to inhibit smooth muscle cell proliferation as well as endothelial cell regeneration (Krankenberg et al., 2015). Therefore, the inhibition of inflammatory macrophage responses and intimal hyperplasia, coupled with the promotion of re-endothelialization are key to reduce postoperative lumen restenosis.

As innate immune cells, macrophages are the main inflammatory cells responsible for luminal restenosis (Sinha et al., 2021). Macrophages have remarkable plasticity and are mainly activated into two polarization phenotypes upon environmental stimuli. M1 macrophages are pro-inflammatory, thus aggravating inflammatory responses, while M2 macrophages are anti-inflammatory, thus inhibiting M1 macrophages, clearing apoptotic cells, and promoting tissue repair (Tabas and Lichtman, 2017). Previous studies have shown that after endovascular interventions, M1 macrophage infiltration and the consequent inflammatory response are directly related to vascular intimal hyperplasia (Kamann et al., 2019). Meanwhile, M2 macrophages can inhibit the phenotypic transformation of smooth muscle cells and reduce intimal hyperplasia (Yan et al., 2020). Our previous study has shown that depletion of macrophages can partially reduce luminal restenosis (Zhang et al., 2019), however this also eliminates beneficial M2 macrophages. Therefore, novel strategies are needed to inhibit M1 and promote M2 macrophages.

Given the rapid development of regenerative medicine and stem cell transplantation, various stem cells have been used in bioengineering protocols. Adipose-derived stem cells (ADSCs) have a high proliferation rate and multi-directional differentiation potential. Previous studies have found that transplanted ADSCs induce paracrine effects rather than differentiating into a specific cell type (Gnecchi et al., 2016). ADSCs secrete large amounts of exosomes, beneficial growth factors and cytokines to accelerate tissue repair (Adamiak et al., 2018). Indeed, ADSC exosomes and their conditional medium can induce macrophage polarization to the M2 phenotype to protect nerves and blood vessels from inflammation and help tissue regeneration and repair (He et al., 2019).

Netrin-1 was the first identified axon guidance factor. Netrin-1 and G-netrin share homology to the laminin gamma chain since they have a repeating 3 laminar epidermal growth factor (V-1, V-2, V-3) and a carboxy-terminal region. Studies have demonstrated that Netrin-1 promotes neuronal migration and secretion, and regulates endothelial and stem cell survival, adhesion, migration, proliferation and differentiation (Ding et al., 2014). Recent studies have found that Netrin-1 can inhibit the migration and chemokine production of inflammatory cells (Xia et al., 2022). Netrin-1 was reported to induce M2-type polarization of macrophages, thereby reducing inflammation and reducing atherosclerosis (Ranganathan et al., 2013). Our previous study showed that ADSCs overexpressing Netrin-1 (N-ADSCs) secreted abundant Netrin-1 protein and various beneficial cytokines after *in vivo* transplantation, which significantly promoted angiogenesis and muscle regeneration in diabetic denervated mice (Zhang et al., 2018). However, novel strategies are needed to continuously release Netrin-1 and cytokines *in vivo*. Recently, hydrogels have become a promising tissue engineering material that can mimic the natural cellular environment (Zhu and Marchant, 2011). With 3D networks and high porosity, hydrogels can achieve high loading of drugs and cells for sustained delivery, which in turn leads to promising therapeutic results (Vo et al., 2012). Compared with the delivery of single network (SN) hydrogels, double network (DN) hydrogels can protect cells from mechanical damage and promote cell retention *in vivo* (Gu et al., 2018). Meanwhile, adhesiveness is a vital characteristic of hydrogels that improve tissue repair, since this material can tightly stick to damaged tissues (Ghandforoushan et al., 2022). Based on the adhesive mechanism of mussels, highly adhesive hydrogels were fabricated by introducing catechol groups of polydopamine (PDA) (Han et al., 2017). In addition, graphene oxide showed potential for accelerating stem cell adhesion, proliferation, and differentiation (Lee et al., 2011).

Therefore, in the present study we designed a polyacrylamide/calcium-alginate/reduced graphene oxide/polydopamine (PAM/CA/rGO/PDA) hydrogel to treat PAD rats subjected to endovascular interventions. These hydrogels were wrapped around the artery and injected with N-ADSCs, so that the retained N-ADSCs could sustainably and effectively release Netrin-1 and beneficial cytokines. Such sustained release would induce the M2 polarization of perivascular macrophages, thereby reducing inflammation, inhibiting intimal hyperplasia and promoting re-endothelization. These newly developed hydrogels are a promising strategy to improve the clinical treatment of lumen restenosis after endovascular interventions.

Materials and methods

Synthesis of graphene oxide

The GO solution was synthesized as described previously (Zhuang et al., 2016). In brief, 1 g ground expandable graphite was dissolved into 150 ml concentrated sulfuric acid in a flask. Then, 40 g $KMnO_4$ was gradually added under strong stirring overnight. The flask was transferred to an oil bath heated to 60°C and maintained for 6 h with strong mechanical stirring. Afterward, the mixture was poured into 1 L of Deionized (DI) water followed by 40 ml of 30% H_2O_2. The GO sheets were purified by dialysis until the pH was around 7. The solution was lyophilized for 3 days to acquire a brown foam and stored at −4°C until further use.

Preparation of polydopamine-capped reduced graphene oxide (rGO/PDA)

A total of 50 mg of GO foam and 50 mg of dopamine hydrochloride were dissolved into 150 ml of Tris-Cl buffer solution (pH = 8.5) with vigorous stirring at 60°C for 24 h rGO/PDA was collected after centrifugation and washed using DI water three times. The solution was lyophilized for 3 days, generating a black foam and stored at −4°C until further use.

Synthesis of the adhesive double network hydrogel

1.5 g sodium alginate (SA) and 0.2 g ionic cross-linker $CaSO_4$, were dissolved in 100 ml DI water and stirred overnight until a clear solution was obtained. Then, 2 g acrylamide (AM) and rGO/PDA foam were dissolved into 10 ml of the above solution together with 0.01 g N,N-methylenebisacrylamide and 0.02 g ammonium persulfate. This solution was stirred until homogeneous. Finally, 10 μl tetramethylethylenediamine (TEMED), was added for polymerization. The hydrogels were sealed for 24 h to avoid water loss.

Characterization and performance of the adhesive double network hydrogel

Scanning electron microscopy (SEM, JEOL JSM-6390F) was used to characterize the morphology and microstructures of the adhesive hydrogel. The chemical composition of rGO/PDA hydrogels was confirmed by Fourier transform infrared 371 spectroscopy (FTIR; Vertex 70 Hyperion 1000). The mechanical property was measured by testing equipment (MTS Alliance RT-5) at a constant speed of 30 mm min^{-1} for strain loading.

Tissue adhesive strength

The tissue adhesive strength of hydrogels was investigated by using a universal testing machine (MTS Alliance RT-5). Fresh porcine skins were purchased from the supermarket and cleaned using tissue paper. The adhesive hydrogel was applied onto porcine skins and pressed using two glass sheets for 1 min. The sizes of contact areas were around 1 cm*1 cm. The adhesive strength was measured by equipping the UTM with a load cell of 100 N at a speed of 30 mm min^{-1}. Each experiment was repeated three times.

Animals

Ten-week-old Sprague Dawley (SD) rats fed with a high-fat diet (21% fat, 0.15% cholesterol) were purchased from the laboratory animal center of Shanghai Ninth People's Hospital, Shanghai Jiao Tong University School of Medicine. Animal procedures were performed following the Guidelines for Care and Use of Laboratory Animals of Shanghai Jiao Tong University School of Medicine with the approval of the Animal Ethics Committee of Shanghai Ninth People's Hospital, Shanghai Jiao Tong University School of Medicine.

Isolation, culture, and identification of adipose-derived stem cells

The adipose tissue of the axilla and inguinal region of 10-week-old SD rats was isolated and ADSCs were obtained as previously described (Bhattacharjee et al., 2022). ADSCs were incubated with low glucose (5.5 mM) Dulbecco's modified Eagle's medium (DMEM) supplemented with 10% fetal bovine serum (FBS) and 1% streptomycin/penicillin. The culture environment was set at 37°C, with 5% CO_2. ADSCs from the third to fifth generation (P3-P5) were used in subsequent experiments. The ADSCs phenotype was confirmed by flow cytometry (Beckman Coulter, Fullerton, CA, United States). Briefly, cells were washed with PBS, detached with trypsin, and incubated with phycoerythrin-conjugated CD29, CD90, CD105, CD34, CD45 and CD31. Isotype antibodies were applied as negative controls.

Construction of Netrin-1-modified adipose-derived stem cells

Adenovirus purchased from Hanbio Biotechnology (Shanghai, China) was used to transfect Netrin-1 into ADSCs as previously described (Zhang et al., 2018). Briefly, HEK293 cells were used to generate the recombinant adenoviral vector green fluorescent protein (GFP)-Netrin-1 which was confirmed by RT-qPCR. GFP-Netrin-1 adenoviral vector was co-cultured with rat ADSCs at the multiplicity of infection (MOI) of 500 for 48 h. An inverted fluorescence microscope (Olympus IX81, Tokyo, Japan) was used to confirm the green fluorescence in transfected ADSCs, and the expression of Netrin-1 was detected by Western blotting and RT-qPCR, as previously described (Zhang et al., 2018).

Viability assay of Netrin-1-modified adipose-derived stem cells cultured on adhesive double network hydrogel

To confirm the biosafety of our developed adhesive DN hydrogel, the proliferation and apoptosis of N-ADSCs were evaluated. Briefly, the adhesive DN hydrogel was seeded into a 96-well plate with 100 μl DMEM per well. The experimental group N-ADSCs (2×10^3/well) was plated onto the adhesive DN hydrogel, while the control group consisted of the same number of N-ADSCs added in a well that did not contain the hydrogel. DMEM was changed every other day.

A cell counting kit-8 (CCK-8; Abcam, Cambridge, UK) was used to assess the cytotoxicity of the adhesive DN hydrogel. Briefly, 10 μl/well CCK-8 solution was added on days 1, 3 and 5 and incubated for 2 h at 37°C. The optical density (OD) at 450 nm wavelength was recorded using a microplate spectrophotometer (Varioskan; Thermo Fisher Scientific, Eugene, OR, United States).

For the apoptosis assay, N-ADSCs seeded with or without hydrogels were cultured for 48 h and the Annexin V-FITC/PI apoptosis detection kit (Abcam, Cambridge, United Kingdom) was used. Cells were analyzed using flow cytometry to detect the apoptosis ratio as previously mentioned (Zhang et al., 2018).

Macrophage culture and polarization assay of macrophages co-cultured with Netrin-1-modified adipose-derived stem cells

The mouse macrophage cell line Raw264.7 was purchased from Sangon Biotech (Shanghai) Co., Ltd. and cultured in high-glucose DMEM supplemented with 10% FBS. Immunofluorescence and flow cytometry were used to detect the macrophage-specific antibody CD68 (Abcam, United Kingdom).

To assess the effect of ADSCs on macrophage polarization, Raw 264.7 cells (5×10^5 cells) and N-ADSCs (10^5 cells) were co-cultured in six-well transwell plates for 24 h as previously described (Yu et al., 2022). DMEM was used as a control. RT-qPCR was performed to examine the expression of Arginase-1 (Arg-1) and Interleukin 10 (IL-10) as polarization markers of M2 macrophages, while Interleukin 6 (IL-6), Tumor Necrosis Factor (TNF-α) were used as polarization markers of M1 macrophages. Then, 100 ng/ml lipopolysaccharide (LPS) was added for 4 h to stimulate Raw 264.7 cells—equal volumes of N-ADSC conditioned medium and DMEM were added into the wells. The expression of M2 macrophage marker CD206 (Abcam, United Kingdom) and M1 macrophage marker CD86 were quantified by flow cytometry and immunofluorescence to confirm the M1/M2 phenotype under a pro-inflammatory environment.

Animal model and surgical procedures

The rat carotid artery guidewire injury model was established as described previously (Liang et al., 2019). Briefly, eighteen specific pathogen-free (SPF) male 10-week-old SD rats fed with a high-fat diet (21% fat, 0.15% cholesterol) were maintained at a constant temperature of 25°C for 1 week. First, rats were injected with 0.1 mg/100 g body weight of anticoagulant sodium heparin through the tail vein. Then, rats were anesthetized using 3% isoflurane and maintained under anesthesia using isoflurane plus 0.3% sodium pentobarbital (1 ml/100 g) i.p. The 18 rats were randomly divided into 3 groups: carotid artery wire injury control group, adhesive DN hydrogel group and N-ADSC + adhesive DN hydrogel group. For the control group, the skin was incised and the carotid artery was exposed and isolated. The left external carotid artery was incised, a 0.83 mm guidewire was inserted to the proximal end for about 1 cm, and the carotid endothelium was damaged by f5 gentle rotations of the wire. The vascular incision was closed with 8-0 sutures, the skin was closed with 3-0 silk sutures and sterilized with benzalkonium chloride. For the adhesive DN hydrogel group, a 1 × 1 cm adhesive DN hydrogel was wrapped around the damaged artery after the vascular incision was sutured, and 100 μl of DMEM was injected into the hydrogel with a syringe. For the N-ADSC + adhesive DN hydrogel group, 10^6 N-ADSCs were diluted in 100 μl of DMEM and injected into the inner layer of hydrogel. After surgery animals were heated in an incubator and maintained a constant body temperature until recovery from anesthesia.

Histological analysis

Rats were sacrificed 14 days after surgery, and the bilateral carotid arteries were isolated and processed for immunofluorescence staining. The integrity of the endothelium was analyzed by staining CD31 (Abcam, United Kingdom) and α-SMA (Abcam, United Kingdom). To further assess the distribution of M1 and M2 macrophages, macrophages were stained with F4/80 (Abcam, United Kingdom), M1 macrophages were stained with iNOS (Abcam, United Kingdom) and M2 macrophages were stained with CD206 (Abcam, United Kingdom). Nuclei were stained with 6-dimercapto-2-phenylindole (DAPI) (DAKO, USA). A Zeiss LSM 510 META immunofluorescence microscope (Carl-Zeiss-Strasse, Oberkochen, Germany) was used to observe and capture images. Carotid arteries were also paraffin-embedded and hematoxylin/eosin (HE) staining was performed. The ImageJ Pro Plus software (NIH, Bethesda, MD) was used to analyze the thickness of the carotid intima. In addition, the heart, liver, spleen, lung and kidney of rats were stained with HE to analyze the toxicity of the adhesive DN hydrogel to major organs.

Statistical analysis

All quantitative data are presented as mean ± standard deviation (SD). Student's *t*-test or one-way analysis of variance (ANOVA) was applied to compare differences between groups. $p < 0.05$ was defined as statistically significant. All experiments were repeated 3 times in each group.

Results

Morphology and physical properties of adhesive double network hydrogels

The fabrication process of the adhesive DN hydrogel was schematically shown in Figure 1. Dopamine was intercalated and self-polymerized among GO sheets. The pace between GO sheets was limited, leading to a low volume of oxygen which hinders the overoxidation of PDA and maintains the massive free catechol groups to mimic the natural structures of mussels (Jin et al., 2021). FTIR was used to investigate the chemical structure of rGO/PDA (Figure 2A). Compared to GO, the peak intensity of rGO/PDA at 1,729 cm^{-1} was decreased which illustrates the reduction of GO by dopamine (Pandey et al., 2018). Furthermore, there was an obvious peak at 1,360 cm^{-1}, which was affirmed as a C–N stretching vibration (Wan et al., 2017). Besides, rGO had fewer hydrophilic functional groups due to poor water solubility. As shown in Supplementary Figure S1, rGO/PDA was precipitated. Thus, the successful immobilization of PDA onto GO sheets by self-polymerization of dopamine was confirmed. The super mechanical performance of adhesive DN hydrogels was also investigated, as shown in Figure 2B. The ultimate tensile strength increased from 38.41 to 68.74 kPa, and the elongation at the break doubles enhanced from 91.82% to 269.32% in the DN hydrogel when compared to a single network (SN) PAM hydrogel. In addition, rGO/PDA proved to be an excellent reinforcing agent in the hydrogel matrix since it increased the elastic modulus from 39.31 ± 2.92 to 87.69 ± 2.92 kPa compared with the PAM/CA hydrogel. A similar elastic modulus to that of the arterial wall was shown to avoid local inflammatory responses caused by force mismatch at the interface between the scaffold and the tissue (Gulino et al., 2019).

Meanwhile, the morphology of the adhesive DN hydrogel was evaluated by SEM. As shown in Figure 2C, the adhesive DN hydrogel exhibited multiple porous structures which were vital for nutrient diffusion. The average pore size was around 113 ± 59 μm, with 70% porosity, which is suitable for cell retention and delivery (Eke et al., 2017). The adhesive capacity of the hydrogel was an important factor for long-term treatment and hemostasis. As depicted in Figure 2D, higher concentrations of rGO/PDA increased the adhesive strength of hydrogels, showing that hydrogel adhesiveness can be adjusted by varying the mass ratio of rGO/PDA. Compared with previous reports (Han et al., 2018; Hong et al., 2019), our hydrogel maintained an excellent adhesion to porcine skin (49.32 ± 5.48 kPa at 5 mg/ml) owing to the high binding affinity to diverse functional groups of peptides and proteins on the tissue surface (Ryu, et al., 2018). Altogether, the adhesive DN hydrogel could effectively bind to surrounding tissues and potentially maintain stem cell delivery *in vivo*.

Characterization of adipose-derived stem cells and Netrin-1-modified adipose-derived stem cells

ADSCs were successfully isolated from inguinal and axillary adipose tissue of rats, and cultured until passages P3-P5. ADSCs demonstrated a typical spindle-like appearance (Figure 3A). Flow cytometric analysis showed that stem cell surface antigens CD29, CD90, and CD105 were positively expressed in ADSCs, while CD34, CD45, and the endothelial cell surface antigen CD31 were not expressed (Figure 3C). These are typical identification features of ADSCs.

The NTN-1 gene was successfully transfected into ADSCs using GFP-labeled adenovirus (Figure 3B). Adenoviruses have the advantages of low pathogenicity, no integration into the genome, high titer, and long gene expression duration (Zhang et al., 2018), which were ideal for our objectives. Western blotting and RT-qPCR were conducted and the results indicated that the expression of

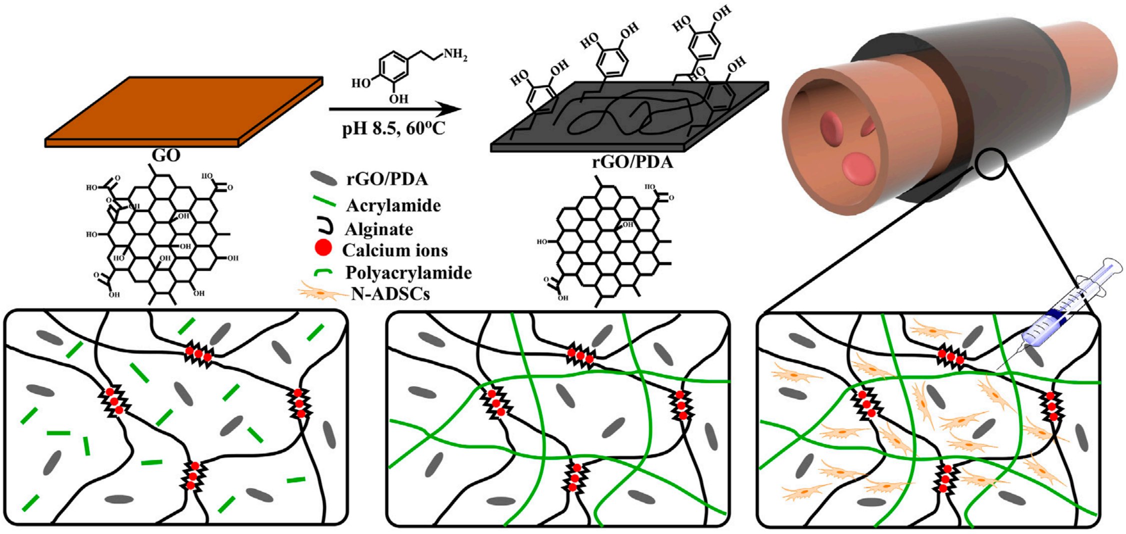

FIGURE 1
Schematics and fabrication process of the N-ADSC-loaded adhesive DN hydrogel. **(A)** Dopamine molecules were attached to graphene oxide (GO) sheets. **(B)** PDA chains were formed and GO was reduced. **(C)** The adhesive hydrogel was wrapped around an artery for repair. **(D,E)** Structure and polymerization process of the double network (DN) hydrogel. **(F)** N-ADSCs were injected into the hydrogel matrix. N-ADSCs, Netrin-1-modified adipose-derived stem cells.

Netrin-1 (RNA and protein) was significantly upregulated in N-ADSCs compared with ADSCs ($P< 0.001$). It was remarkable that ADSCs showed a low expression of Netrin-1, thus corroborating our strategy of transfecting Netrin-1 into ADSCs (Figures 3D,E).

The biocompatibility of adhesive double network hydrogels on Netrin-1-modified adipose-derived stem cells *in vitro*

The CCK-8 proliferation assay showed that there was no significant difference between N-ADSCs seeded on wells coated with or without adhesive DN hydrogels for up to 5 days ($p > 0.05$) (Figure 4A). Flow cytometry analysis demonstrated that the apoptosis rate of N-ADSCs was also not affected when cells were seeded onto adhesive DN hydrogels ($p > 0.05$) (Figures 4B,C). Taken together, these assays corroborate that the adhesive DN hydrogel exhibited low cytotoxicity to N-ADSCs, which indicates satisfying biocompatibility.

Characterization of macrophages and the effect of Netrin-1-modified adipose-derived stem cells on macrophage polarization *in vitro*

Immunofluorescence detection and flow cytometry showed that Raw264.7 macrophages were strongly positive for the macrophage-specific antibody CD68, which validated the purity of these cells (Supplementary Figures S2A,B). The co-culture system of N-ADSCs and macrophages allowed N-ADSCs to influence macrophages via a paracrine effect, which was reported to be the main effect of ADSCs after transplantation *in vivo* (Cai et al., 2020). After being co-cultured for 24 h, M2 markers Arg-1 and IL-10 were significantly up-regulated while M1 markers IL-6 and TNF-α were significantly downregulated in N-ADSCs-treated macrophages compared to DMEM-treated ones ($p < 0.05$) (Figure 5A). This indicates that under normal circumstances N-ADSCs significantly induce the M2 polarization of macrophages to decrease inflammation. Considering the pro-inflammatory microenvironment of carotid intima injury, LPS was added into the culture medium to mimic arterial inflammation, and results of flow cytometry (Figures 5B,C) and immunofluorescence (Figures 5D,E) experiments demonstrated that CD206 was significantly upregulated and CD86 was downregulated. This depicts an increase in M2 macrophages due to an M2 polarization or an M1-to-M2 phenotype transition induced by N-ADSCs.

The effect of N-ADSC-loaded adhesive double network hydrogels on macrophage polarization and intimal hyperplasia *in vivo*

The rat carotid artery guidewire/balloon injury model is acknowledged to mimic the carotid interventional injury that occurs in patients. Therefore, a guidewire was applied due to its

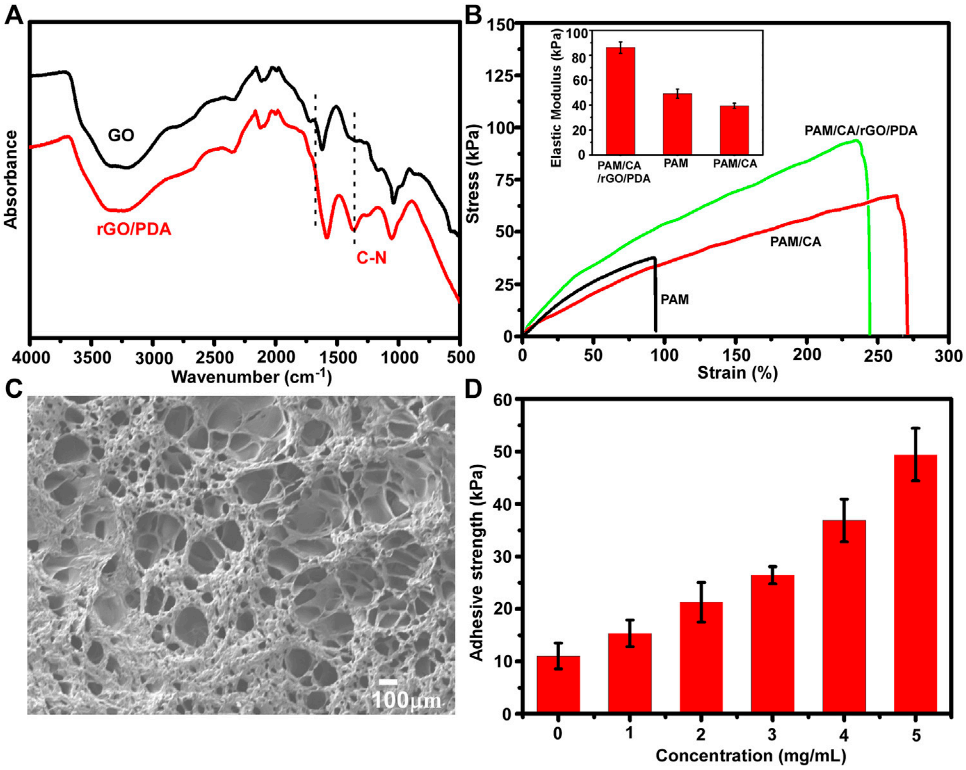

FIGURE 2
Characterization of the adhesive DN hydrogel. **(A)** FTIR spectra of dried GO and rGO/PDA. **(B)** Stress–strain curves of the DN hydrogel; insets show the elastic modulus. **(C)** SEM images of a dry adhesive DN hydrogel. **(D)** Adhesion strengths of the DN hydrogel onto porcine skin tissues with different concentrations of rGO/PDA.

small diameter that facilitates handling. Indeed, the thickness of both tunica neointima and tunica media was significantly reduced in N-ADSCs + adhesive DN hydrogel rats when compared to other groups. Moreover, the texture of the tunica media was smoother and more continuous in N-ADSCs + adhesive DN hydrogel rats (Figures 6A,E; Supplementary Figure S4), which indicates less damage to vascular endothelial cells, a lower proliferation of vascular smooth muscle cells and less macrophage infiltration. Besides, the integrity of the endothelium was partially restored in the N-ADSCs + adhesive DN hydrogel group when compared to that of the other two groups (Figures 6B,F). Immunofluorescence staining of CD206, iNOS, and F4/80 evidenced that N-ADSCs + adhesive DN hydrogel rats had more M2 and less M1 macrophages than the other two groups (Figures 6C,D,G,H). This suggests that a combination of N-ADSCs plus the adhesive DN hydrogel promoted the M2 polarization and inhibited the M1 polarization of macrophages, thus inhibiting inflammation. Taken together, the above results corroborated that the combination of N-ADSCs and the adhesive DN hydrogel reduced arterial inflammation and inhibited intimal hyperplasia after endovascular interventions *in vivo*.

The biocompatibility of N-ADSC-loaded adhesive double network hydrogels *in vivo*

Excellent biocompatibility is essential for a safe and qualified implantation material. To examine the *in vivo* biocompatibility of the N-ADSC-loaded adhesive DN hydrogel, major organs were collected and HE stained from rats subjected to surgery and treated with or without the N-ADSC-loaded adhesive DN hydrogel. There were no significant differences in the heart, liver, spleen, lung and kidney in terms of lesions, injuries or inflammation among groups (Figure 7). This testifies that the N-ADSC-loaded adhesive DN hydrogel had no biotoxicity and showed satisfying biocompatibility *in vivo*.

Discussion

We report a biocompatible slow-releasing system of N-ADSC-loaded adhesive DN hydrogel wrap which significantly promoted the M2 polarization of macrophages, reduced arterial inflammation, inhibited intimal and media hyperplasia, and improved the re-endothelialization in a rat

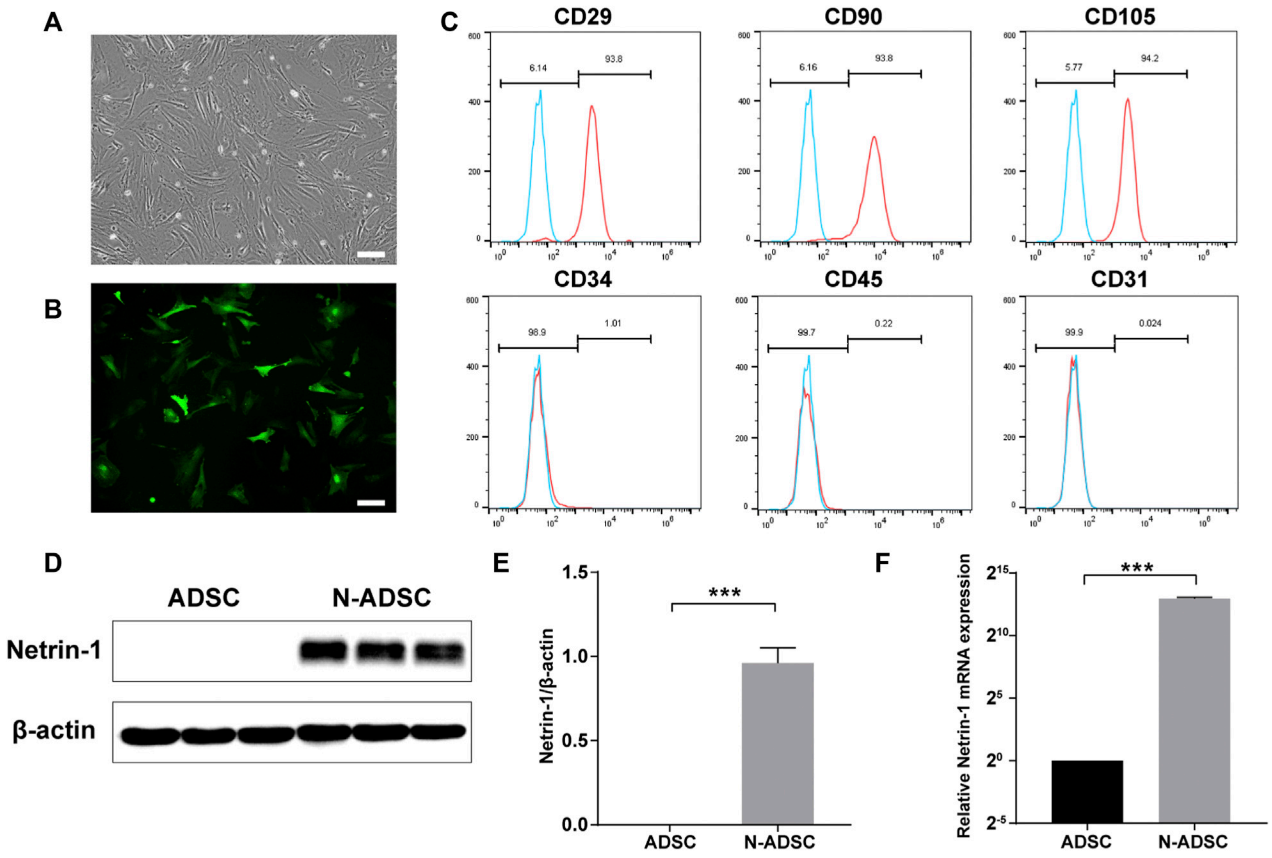

FIGURE 3
Characterization of ADSCs and N-ADSCs. **(A)** P3-ADSCs were examined under the microscope. **(B)** N-ADSCs were examined under a fluorescence microscope. **(C)** Identification of ADSC surface markers using flow cytometry. **(D,E)** Western blot and **(F)** RT-qPCR analyses proved the overexpression of Netrin-1 in the N-ADSCs. ***$p < 0.001$. Scale bar = 100 μm. P3, passage 3; N-ADSCs, Netrin-1-modified adipose-derived stem cells.

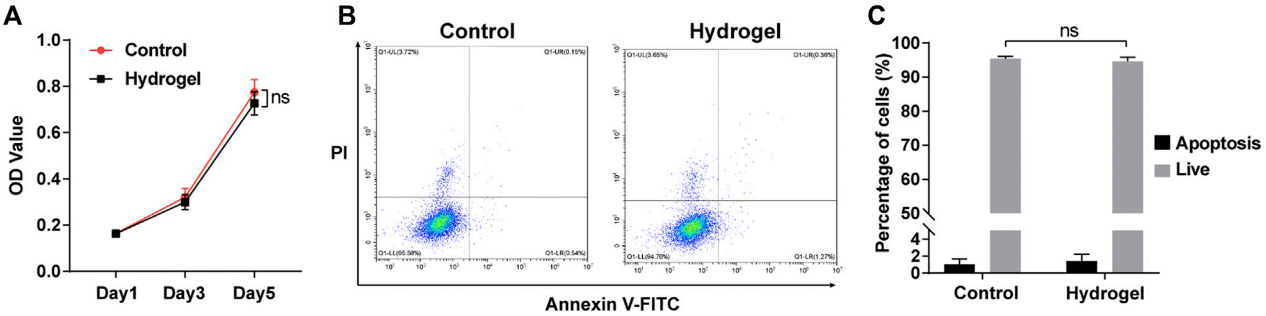

FIGURE 4
Biocompatibility of the adhesive DN hydrogel on N-ADSCs in vitro. **(A)** The CCK-8 proliferation assay of N-ADSCs seeded with or without the adhesive DN hydrogel. **(B,C)** Flowcytometry and statistical analysis of the apoptosis rate of N-ADSCs seeded with or without the adhesive DN hydrogel. ns, $p > 0.05$. N-ADSCs, Netrin-1-modified adipose-derived stem cells.

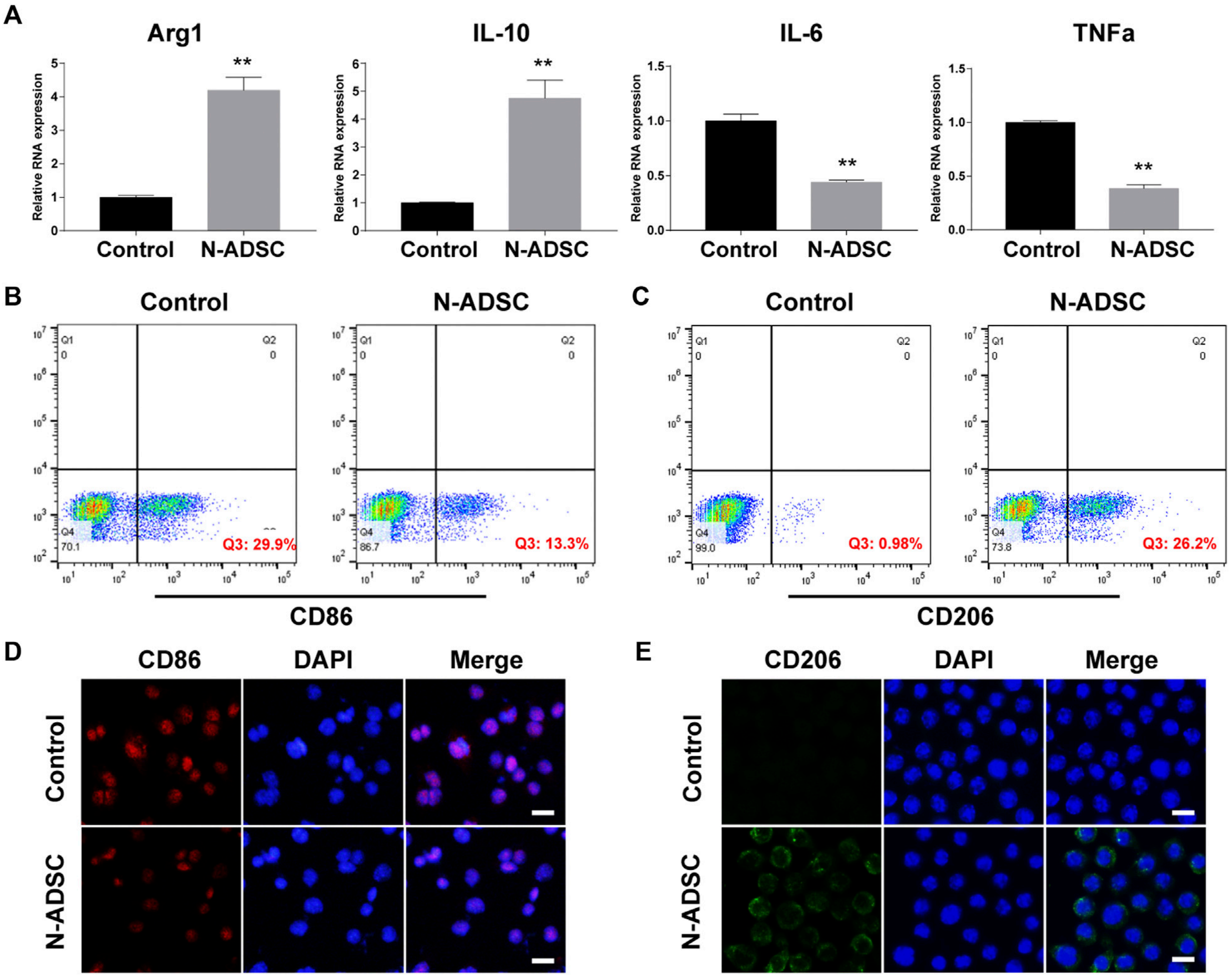

FIGURE 5
The effect of N-ADSCs on macrophage polarization in vitro. **(A)** RT-qPCR of Arg-1, IL-10, IL-6 and TNF-α from N-ADSCs-treated macrophages compared to DMEM-treated macrophages. **(B,C)** Addition of LPS and flow cytometry analysis of CD86 and CD206. **(D,E)** Immunofluorescence of CD86 and CD206. $^{**}p < 0.01$. Scale bar = 100 μm. N-ADSCs, Netrin-1-modified adipose-derived stem cells.

carotid intima injury model. Results of the present study provide a new strategy to treat arterial restenosis after endovascular interventions in clinical practice.

We designed a PAM/CA/rGO/PDA adhesive DN hydrogel that shows several advantages as a platform to load N-ADSCs. The rGO/PDA was inspired by the mussel adhesive mechanism and showed a high adhesiveness to tissue surfaces thus allowing the hydrogel to tightly wrap around damaged arteries for long-term treatment. Besides, rGO had three key functions in hydrogels: it prevented PDA overoxidation, enhanced the stiffness of the hydrogel and promoted the adhesion and growth of stem cells (Lee et al., 2011). The DN design of a PAM/CA hydrogel was endowed with suitable toughness and stretch ability because of effective energy dissipation (Nakayama et al., 2004). Meanwhile, the abundant porous structure of the DN hydrogel improved stem cell retention and sustainable delivery.

We obtained stable N-ADSCs overexpressing Netrin-1. Our previously published study (Zhang et al., 2018) found that Netrin-1 improved ADSCs proliferation, migration, adhesion, and inhibited apoptosis through the activation of the AKT/PI3K/eNOS signaling pathway, and secretion of VEGF, b-FGF, HGF, PDGF, EGF and IGF-1. Therefore, the overexpression of Netrin-1 improved the biological functions of ADSCs. At the same time, our present report shows that N-ADSCs expressed a large amount of Netrin-1, while the secreted Netrin-1 protein was shown to induce M2 macrophage polarization (Li et al., 2017) and attenuate the neointimal formation (Liu et al., 2017). Thus, N-ADSCs are key to induce the M2 polarization of macrophages and secrete anti-inflammation cytokines.

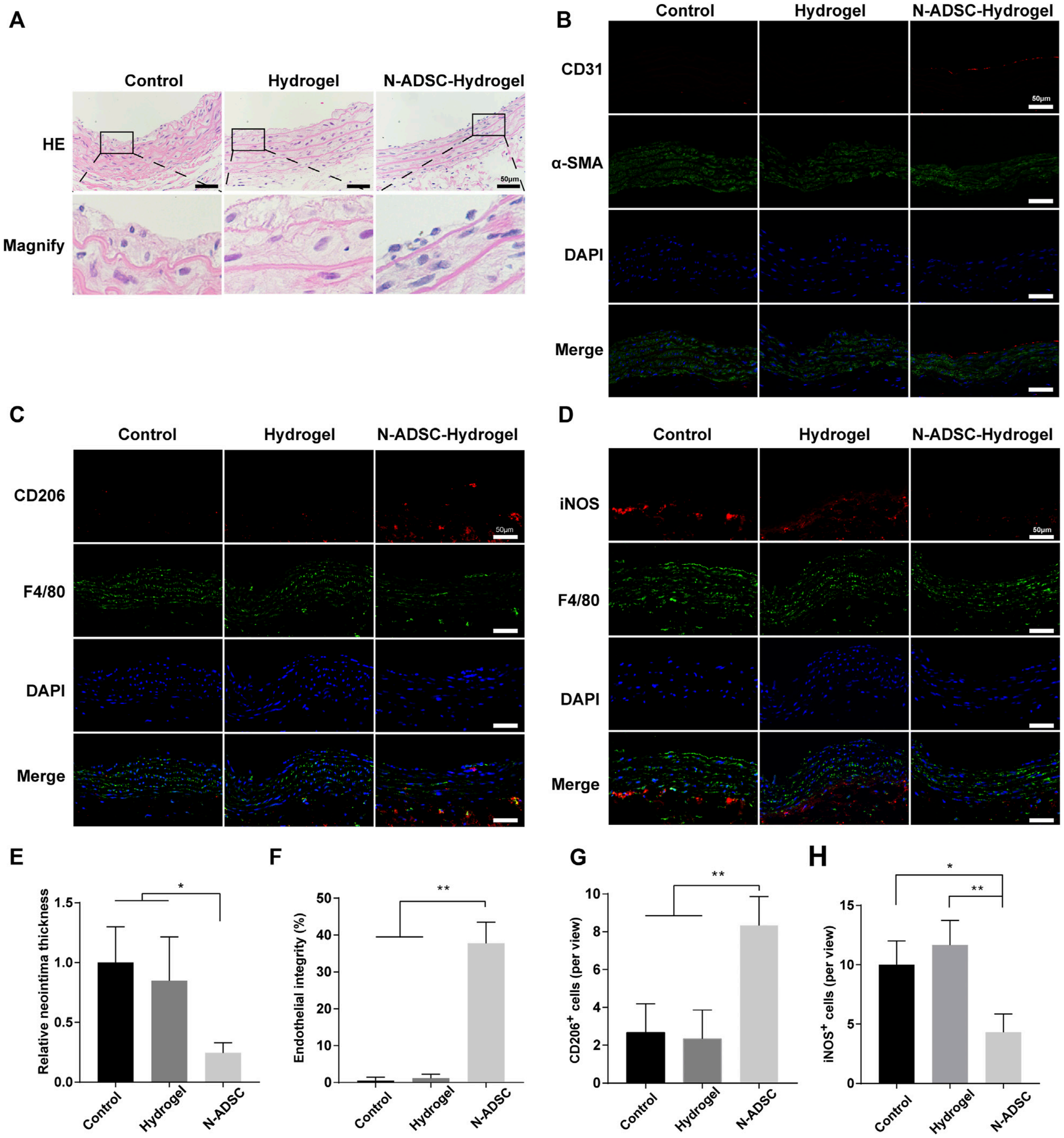

FIGURE 6
The effect of N-ADSC-loaded adhesive DN hydrogels on macrophage polarization and intimal hyperplasia *in vivo*. **(A,E)** HE staining and statistical analysis of the thickness of the carotid neointima. **(B,F)** Immunofluorescence staining of CD31 (red) and α-SMA (green) depicting endothelial integrity. **(C, G)** Immunofluorescence staining of CD206 (red) and F4/80 (green) and analysis of CD206+ cells. **(D,H)** Immunofluorescence staining of iNOS (red) and F4/80 (green) and analysis of iNOS + cells. $*p < 0.05$. $**p < 0.01$. Scale bar = 50 μm. N-ADSCs, Netrin-1-modified adipose-derived stem cells.

Currently, intensive research output has focused on perivascular drug delivery systems. Several approaches, such as targeted drugs, films/wraps, depot gels, meshes, rings, or micro/nanoparticles have been proposed. Many of these have shown promising efficacy and safety to alleviate intimal hyperplasia through the perivascular delivery of drugs (Lee

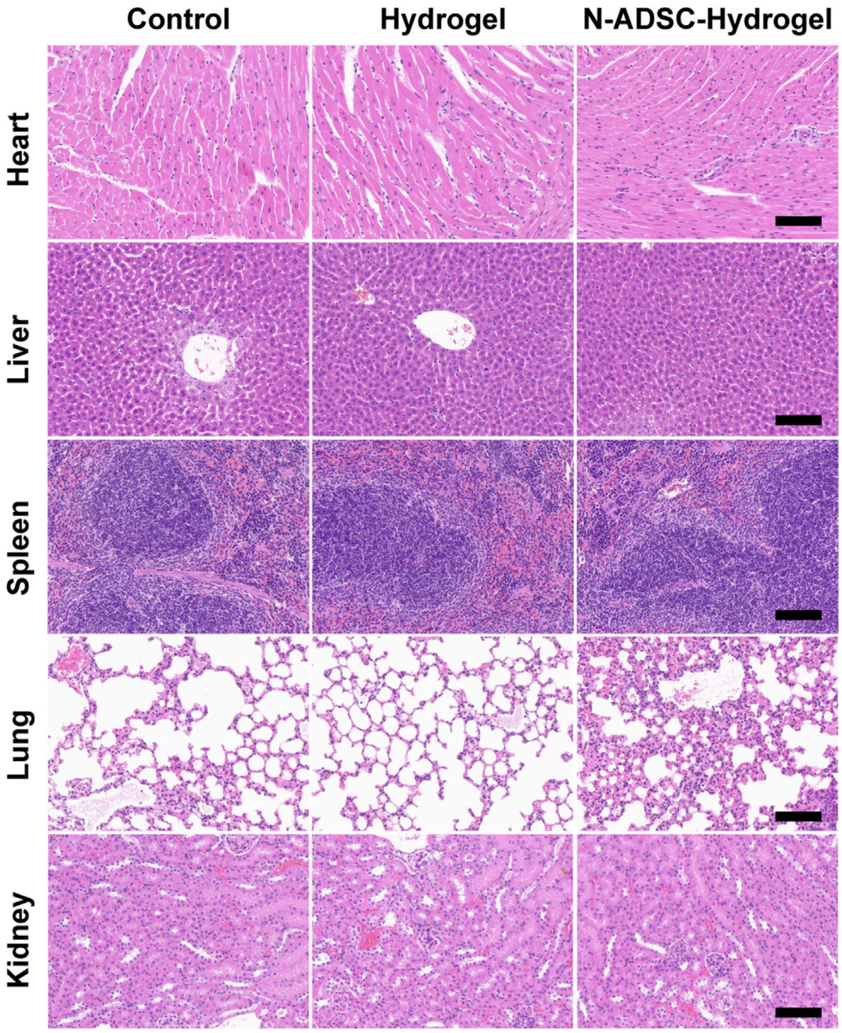

FIGURE 7
Biocompatibility of the N-ADSC-loaded adhesive DN hydrogel *in vivo*. HE staining of the heart, liver, spleen, lung and kidney from rats of the three experimental groups as detailed in Materials and Methods.

et al., 2017). Indeed, Christopher et al. used a micro-infusion catheter to inject adventitial drug into the vasculature and found that this approach was safe and feasible for adjunctive therapy in the femoropopliteal artery (Owens et al., 2014). Meanwhile, William et al. constructed a 30-day reabsorbable polymer-based bilayer wrap loaded with sunitinib for perivascular drug delivery (Sanders et al., 2012). In a rabbit carotid artery bypass model, Wu et al. (2018) constructed a resolvin D1-loaded perivascular Pluronic F127 gel to attenuate venous graft hyperplasia without biotoxicity. Warren et al. found that the injection of NAB-rapamycin into the tunica adventitia vasorum could inhibit medial proliferation and adventitial inflammation after balloon angioplasty in porcine arteries to reduce lumen stenosis (Gasper et al., 2013). However, these previous studies were focused on the perivascular delivery of antiproliferative drugs, which may be toxic to blood vessels and have a short drug half-life. Here we used N-ADSCs as a “drug.” Compared with pure Netrin-1 protein or other anti-proliferative drugs, N-ADSCs provide a “biological pump” that stably secrete Netrin-1 and other anti-inflammatory cytokines in large quantities. In parallel, the adhesive DN hydrogel served as an excellent three-dimensional scaffold and natural culture medium for N-ADSCs with strong adhesion to the surface of blood vessels, and controlled release and distribution of Netrin-1 and other cytokines into the vascular wall. These strategies synergized to create a slow-release mechanism to reduce intimal hyperplasia.

The premise of evaluating the effectiveness of a biomaterial is to first assess its biosafety. The biocompatibility and biodegradability of graphene-based materials are still controversial. Pinto et al. (2013) found a slight decrease in cell viability in bacteria and mammalian cells after exposure to graphene-based materials, while Park et al. (2014) found that graphene promoted mesenchymal stem cells differentiation into cardiomyocytes by enhancing the expression of extracellular matrix proteins. Previous studies have also shown that peroxidase secreted by activated immune cells such as neutrophils and eosinophils *in vivo* can biodegrade graphene (Kurapati et al., 2018). Therefore, we carefully evaluated the biocompatibility and toxicity of the adhesive DN hydrogel applied in this study. We showed no cytotoxicity *in vitro* as well as no deleterious effect on major organs *in vivo* upon the use of our developed DN hydrogel. Therefore, our adhesive DN hydrogel is a material with excellent biocompatibility and biodegradation.

Conclusion

In conclusion, the results of this study corroborate that the adhesive DN hydrogel wrap loaded with N-ADSCs can significantly reduce arterial inflammation, inhibit intimal hyperplasia and improve re-endothelialization. Hence, the slow-releasing system of N-ADSCs-loaded adhesive DN hydrogel wrap was safe and effective, thus being characterized as a promising and novel therapeutic approach to treat vascular restenosis after endovascular interventions.

Data availability statement

The raw data supporting the conclusion of this article will be made available by the authors, without undue reservation.

Ethics statement

The animal study was reviewed and approved by the Animal Ethics Committee of Shanghai Ninth People's Hospital, Shanghai Jiao Tong University School of Medicine.

Author contributions

XZ, DS, and YJ conceived and designed the study. ZP, JL, and QH performed the experiments, acquired, analyzed, or interpreted the data. XZ, YC, and YJ wrote the first draft of the manuscript. XZ, ZX, BL, JQ, WL, KY, DS, and XL reviewed and edited the manuscript. All authors reviewed and approved the submitted version.

Funding

This study was supported by the Shanghai Sailing Program (20YF1423800), National Natural Science Foundation of China (Nos. 82170509, 81971758, 81971712), Natural Science Foundation of Shanghai Science and Technology Committee (20ZR1431600), and the Project of Biobank (No. YBKB201913) from Shanghai Ninth People's Hospital, Shanghai Jiao Tong University School of Medicine. We acknowledge supports by the NSFC-RGC Joint Research Scheme (N_HKUST607/17), Mainland-Hong Kong Joint Funding Scheme (MHKJFS, MHP/046/20), the IER foundation (HT-JD-CXY-201907), "International Science and Technology Cooperation Projects" of Science and Technological Bureau of Guangzhou Huangpu District (2019GH06). We acknowledge the support of Guangdong Provincial Key Laboratory Program (2021B1212040001) from the Department of Science and Technology of Guangdong Province.

Acknowledgments

We sincerely thank M. D. Yining Wang for enlightening the discussion and providing help towards the completion of this study.

Conflict of interest

The authors declare that the research was conducted in the absence of any commercial or financial relationships that could be construed as a potential conflict of interest.

The handling editor, YQ, declared a shared parent affiliation with the authors XZ, YJ, HT, JL, ZP, QH, ZX, BL, JQ, WL, KY, and XL at the time of review.

Publisher's note

Supplementary material

The Supplementary Material for this article can be found online at: https://www.frontiersin.org/articles/10.3389/fbioe.2022.944435/full#supplementary-material

SUPPLEMENTARY FIGURE S1
Difference in water solubility of GO and rGO/PDA.

SUPPLEMENTARY FIGURE S2
Characterization of Raw264.7 cells. **(A)** Immunofluorescence of CD68. **(B)** Flow cytometry of CD68.

SUPPLEMENTARY FIGURE S3
Surgical operation and development of the rat model. **(A)** The N-ADSC-loaded adhesive DN hydrogel was successfully wrapped around the carotid artery of rats. **(B)** Rats were sacrificed 14 days after operation and bilateral carotid arteries were isolated.

SUPPLEMENTARY FIGURE S4
Relative media thickness, a supplement to Figure 6A. $^{*}p < 0.05$.

SUPPLEMENTARY FIGURE S5
Immunofluorescence staining of CD31 (red) and α-SMA (green) depicting endothelial integrity of control group (no injury and no treatment).

References

Adamiak, M., Cheng, G., Bobis-Wozowicz, S., Zhao, L., Kedracka-Krok, S., Samanta, A., et al. (2018). Induced pluripotent stem cell (iPSC)-Derived extracellular vesicles are safer and more effective for cardiac repair than iPSCs. *Circ. Res.* 122 (2), 296–309. doi:10.1161/CIRCRESAHA.117.311769

Bhattacharjee, M., Escobar Ivirico, J. L., Kan, H. M., Shah, S., Otsuka, T., Bordett, R., et al. (2022). Injectable amnion hydrogel-mediated delivery of adipose-derived stem cells for osteoarthritis treatment. *Proc. Natl. Acad. Sci. U. S. A.* 119 (4), e2120968119. doi:10.1073/pnas.2120968119

Cai, Y., Li, J., Jia, C., He, Y., and Deng, C. (2020). Therapeutic applications of adipose cell-free derivatives: a review. *Stem Cell Res. Ther.* 11 (1), 312. doi:10.1186/s13287-020-01831-3

Conte, M. S., Bradbury, A. W., Kolh, P., White, J. V., Dick, F., Fitridge, R., et al. (2019). Global vascular Guidelines on the management of chronic limb-threatening ischemia. *Eur. J. Vasc. Endovasc. Surg.* 58 (1S), S1–S109. doi:10.1016/j.ejvs.2019.05.006

Ding, Q., Liao, S. J., and Yu, J. (2014). Axon guidance factor netrin-1 and its receptors regulate angiogenesis after cerebral ischemia. *Neurosci. Bull.* 30 (4), 683–691. doi:10.1007/s12264-013-1441-9

Eke, G., Mangir, N., Hasirci, N., MacNeil, S., and Hasirci, V. (2017). Development of a UV crosslinked biodegradable hydrogel containing adipose derived stem cells to promote vascularization for skin wounds and tissue engineering. *Biomaterials* 129, 188–198. doi:10.1016/j.biomaterials.2017.03.021

Gasper, W. J., Jimenez, C. A., Walker, J., Conte, M. S., Seward, K., Owens, C. D., et al. (2013). Adventitial nab-rapamycin injection reduces porcine femoral artery luminal stenosis induced by balloon angioplasty via inhibition of medial proliferation and adventitial inflammation. *Circ. Cardiovasc. Interv.* 6 (6), 701–709. doi:10.1161/CIRCINTERVENTIONS.113.000195

Ghandforoushan, P., Golafshan, N., Babu Kadumudi, F., Castilho, M., Dolatshahi-Pirouz, A., Orive, G., et al. (2022). Injectable and adhesive hydrogels for dealing with wounds. *Expert Opin. Biol. Ther.* 22 (4), 519–533. doi:10.1080/14712598.2022.2008353

Gnecchi, M., Danieli, P., Malpasso, G., and Ciuffreda, M. C. (2016). Paracrine mechanisms of mesenchymal stem cells in tissue repair. *Methods Mol. Biol.* 1416, 123–146. doi:10.1007/978-1-4939-3584-0_7

Gu, Z., Huang, K., Luo, Y., Zhang, L., Kuang, T., Chen, Z., et al. (2018). Double network hydrogel for tissue engineering. *Wiley Interdiscip. Rev. Nanomed. Nanobiotechnol.* 10 (6), e1520. doi:10.1002/wnan.1520

Gulino, M., Kim, D., Pané, S., Santos, S. D., and Pêgo, A. P. (2019). Tissue response to neural implants: the use of model systems toward new design solutions of implantable microelectrodes. *Front. Neurosci.* 13, 689. doi:10.3389/fnins.2019.00689

Han, L., Lu, X., Liu, K., Wang, K., Fang, L., Weng, L. T., et al. (2017). Mussel-inspired adhesive and tough hydrogel based on nanoclay confined dopamine polymerization. *ACS Nano* 11 (3), 2561–2574. doi:10.1021/acsnano.6b05318

Han, L., Wang, M., Li, P., Gan, D., Yan, L., Xu, J., et al. (2018). Mussel-inspired tissue-adhesive hydrogel based on the polydopamine-chondroitin sulfate complex for growth-factor-free cartilage regeneration. *ACS Appl. Mat. Interfaces* 10 (33), 28015–28026. doi:10.1021/acsami.8b05314

He, X., Dong, Z., Cao, Y., Wang, H., Liu, S., Liao, L., et al. (2019). MSC-derived exosome promotes M2 polarization and enhances cutaneous wound healing. *Stem Cells Int.* 2019, 1–16. doi:10.1155/2019/7132708

Hong, Y., Zhou, F., Hua, Y., Zhang, X., Ni, C., Pan, D., et al. (2019). A strongly adhesive hemostatic hydrogel for the repair of arterial and heart bleeds. *Nat. Commun.* 10 (1), 2060. doi:10.1038/s41467-019-10004-7

Jin, X., Jiang, H., Zhang, Z., Yao, Y., Bao, X., Hu, Q., et al. (2021). Ultrastretchable, self-adhesive, strain-sensitive and self-healing GO@DA/Alginate/P(AAc-co-AAm) multifunctional hydrogels via mussel-inspired chemistry. *Carbohydr. Polym.* 254, 117316. doi:10.1016/j.carbpol.2020.117316

Kamann, S., Haase, T., Stolzenburg, N., Löchel, M., Peters, D., and Schnorr, J. (2019). Resveratrol-coated balloon catheters in porcine coronary and peripheral arteries. *Int. J. Mol. Sci.* 20 (9), 2285. doi:10.3390/ijms20092285

Krankenberg, H., Tübler, T., Ingwersen, M., Schlüter, M., Scheinert, D., Blessing, E., et al. (2015). Drug-coated balloon versus standard balloon for superficial femoral artery in-stent restenosis: the randomized femoral artery in-stent restenosis (FAIR) trial. *Circulation* 132 (23), 2230–2236. doi:10.1161/CIRCULATIONAHA.115.017364

Kurapati, R., Mukherjee, S. P., Martín, C., Bepete, G., Vázquez, E., Pénicaud, A., et al. (2018). Degradation of single-layer and few-layer graphene by neutrophil myeloperoxidase. *Angew. Chem. Int. Ed.* 57 (36), 11722–11727. doi:10.1002/anie.201806906

Lee, W. C., Lim, C. H., Shi, H., Tang, L. A., Wang, Y., Lim, C. T., et al. (2011). Origin of enhanced stem cell growth and differentiation on graphene and graphene oxide. *ACS Nano* 5 (9), 7334–7341. doi:10.1021/nn202190c

Lee, J., Kim, D. H., Lee, K. J., Seo, I. H., Park, S. H., Jang, E. H., et al. (2017). Transfer-molded wrappable microneedle meshes for perivascular drug delivery. *J. Control. Release* 268, 237–246. doi:10.1016/j.jconrel.2017.10.007

Li, Y., Wan, S., Liu, G., Cai, W., Huo, D., Li, G., et al. (2017). Netrin-1 promotes inflammation resolution to achieve endothelialization of small-diameter tissue engineering blood vessels by improving endothelial progenitor cells function *in situ*. *Adv. Sci. (Weinh)* 4 (12), 1700278. doi:10.1002/advs.201700278

Liang, J., Li, Q., Cai, W., Zhang, X., Yang, B., Li, X., et al. (2019). Inhibition of polycomb repressor complex 2 ameliorates neointimal hyperplasia by suppressing trimethylation of H3K27 in vascular smooth muscle cells. *Br. J. Pharmacol.* 176 (17), 3206–3219. doi:10.1111/bph.14754

Liu, N. M., Siu, K. L., Youn, J. Y., and Cai, H. (2017). Attenuation of neointimal formation with netrin-1 and netrin-1 preconditioned endothelial progenitor cells. *J. Mol. Med.* 95 (3), 335–348. doi:10.1007/s00109-016-1490-4

Nakayama, A., Kakugo, A., Gong, J. P., Osada, Y., Takai, M., Erata, T., et al. (2004). High mechanical strength double network hydrogel with bacterial cellulose. *Adv. Funct. Mat.* 14, 1124–1128. doi:10.1002/adfm.200305197

Owens, C. D., Gasper, W. J., Walker, J. P., Alley, H. F., Conte, M. S., Grenon, S. M., et al. (2014). Safety and feasibility of adjunctive dexamethasone infusion into the adventitia of the femoropopliteal artery following endovascular revascularization. *J. Vasc. Surg.* 59 (4), 1016–1024. doi:10.1016/j.jvs.2013.10.051

Pandey, N., Hakamivala, A., Xu, C., Hariharan, P., Radionov, B., Huang, Z., et al. (2018). Biodegradable nanoparticles enhanced adhesiveness of mussel-like hydrogels at tissue interface. *Adv. Healthc. Mat.* 7 (7), e1701069. doi:10.1002/adhm.201701069

Park, J., Park, S., Ryu, S., Bhang, S. H., Kim, J., Yoon, J. K., et al. (2014). Graphene-regulated cardiomyogenic differentiation process of mesenchymal stem cells by enhancing the expression of extracellular matrix proteins and cell signaling molecules. *Adv. Healthc. Mat.* 3 (2), 176–181. doi:10.1002/adhm.201300177

Pinto, A. M., Gonçalves, I. C., and Magalhães, F. D. (2013). Graphene-based materials biocompatibility: a review. *Colloids Surfaces B Biointerfaces* 111, 188–202. doi:10.1016/j.colsurfb.2013.05.022

Ranganathan, P. V., Jayakumar, and C., and Ramesh, G. (2013). Netrin-1-treated macrophages protect the kidney against ischemia-reperfusion injury and suppress inflammation by inducing M2 polarization. *Am. J. Physiol. Renal Physiol.* 304 (7), F948–F957. doi:10.1152/ajprenal.00580.2012

Razavi, M. K., Donohoe, D., D'Agostino, R. B., Jaff, M. R., and Adams, G.DANCE Investigators (2018). Adventitial drug delivery of dexamethasone to improve primary patency in the treatment of superficial femoral and popliteal artery disease: 12-Month results from the DANCE clinical trial. *JACC Cardiovasc. Interv.* 11 (10), 921–931. doi:10.1016/j.jcin.2017.12.015

Ryu, J. H., Messersmith, P. B., and Lee, H. (2018). Polydopamine surface chemistry: a decade of discovery. *ACS Appl. Mat. Interfaces* 10 (9), 7523–7540. doi:10.1021/acsami.7b19865

Sanders, W. G., Hogrebe, P. C., Grainger, D. W., Cheung, A. K., and Terry, C. M. (2012). A biodegradable perivascular wrap for controlled, local and directed drug delivery. *J. Control. Release* 161 (1), 81–89. doi:10.1016/j.jconrel.2012.04.029

Sinha, S. K., Miikeda, A., Fouladian, Z., Mehrabian, M., Edillor, C., Shih, D., et al. (2021). Local M-CSF (macrophage colony-stimulating factor) expression regulates macrophage proliferation and apoptosis in atherosclerosis. *Arterioscler. Thromb. Vasc. Biol.* 41 (1), 220–233. doi:10.1161/ATVBAHA.120.315255

Tabas, I., and Lichtman, A. H. (2017). Monocyte-Macrophages and T Cells in atherosclerosis. *Immunity* 47 (4), 621–634. doi:10.1016/j.immuni.2017.09.008

Vo, T. N., Kasper, F. K., and Mikos, A. G. (2012). Strategies for controlled delivery of growth factors and cells for bone regeneration. *Adv. Drug Deliv. Rev.* 64 (12), 1292–1309. doi:10.1016/j.addr.2012.01.016

Wan, Q., Liu, M., Xie, Y., Tian, J., Huang, Q., Deng, F., et al. (2017). Facile and highly efficient fabrication of graphene oxide-based polymer nanocomposites through mussel-inspired chemistry and their environmental pollutant removal application. *J. Mat. Sci.* 52, 504–518. doi:10.1007/s10853-016-0349-y

Wu, B., Werlin, E. C., Chen, M., Mottola, G., Chatterjee, A., Lance, K. D., et al. (2018). Perivascular delivery of resolvin D1 inhibits neointimal hyperplasia in a rabbit vein graft model. *J. Vasc. Surg.* 68 (6S), 188S–200S. doi:10.1016/j.jvs.2018.05.206

Xia, X., Hu, Z., Wang, S., and Yin, K. (2022). Netrin-1: an emerging player in inflammatory diseases. *Cytokine Growth Factor Rev.* 64, 46. doi:10.1016/j.cytogfr.2022.01.003

Yahagi, K., Otsuka, F., Sakakura, K., Sanchez, O. D., Kutys, R., Ladich, E., et al. (2014). Pathophysiology of superficial femoral artery in-stent restenosis. *J. Cardiovasc. Surg.* 55 (3), 307–323. doi:10.1016/j.cardfail.2014.04.015

Yan, W., Li, T., Yin, T., Hou, Z., Qu, K., Wang, N., et al. (2020). M2 macrophage-derived exosomes promote the c-KIT phenotype of vascular smooth muscle cells during vascular tissue repair after intravascular stent implantation. *Theranostics* 10 (23), 10712–10728. doi:10.7150/thno.46143

Yu, L., Shi, Q., Zhang, B., and Xu, J. (2022). Genetically modified mesenchymal stem cells promote spinal fusion through polarized macrophages. *Lab. Invest.* 102 (3), 312–319. doi:10.1038/s41374-021-00693-4

Zhang, X., Qin, J., Wang, X., Guo, X., Liu, J., Wang, X., et al. (2018). Netrin-1 improves adipose-derived stem cell proliferation, migration, and treatment effect in type 2 diabetic mice with sciatic denervation. *Stem Cell Res. Ther.* 9 (1), 285. doi:10.1186/s13287-018-1020-0

Zhang, X., Liu, J., Yang, X., He, G., Li, B., Qin, J., et al. (2019). $CuCo_2S_4$ nanocrystals as a nanoplatform for photothermal therapy of arterial inflammation. *Nanoscale* 11 (19), 9733–9742. doi:10.1039/c9nr00772e

Zhu, J., and Marchant, R. E. (2011). Design properties of hydrogel tissue-engineering scaffolds. *Expert Rev. Med. Devices* 8 (5), 607–626. doi:10.1586/erd.11.27

Zhuang, M., Ou, X., Dou, Y., Zhang, L., Zhang, Q., Wu, R., et al. (2016). Polymer-embedded fabrication of Co2P nanoparticles encapsulated in N, P-doped graphene for hydrogen generation. *Nano Lett.* 16 (7), 4691–4698. doi:10.1021/acs.nanolett.6b02203

Frontiers in Bioengineering and Biotechnology

TYPE Original Research
PUBLISHED 18 October 2022
DOI 10.3389/fbioe.2022.950970

OPEN ACCESS

EDITED BY
Yun Qian,
Shanghai Jiao Tong University, China

REVIEWED BY
Milad Kamkar,
University of British Columbia, Canada
Jie Wei,
East China University of Science and Technology, China

*CORRESPONDENCE
Tingting Ding,
dtt_kai@163.com
Xin Liu,
liuxin0556@163.com

†These authors have contributed equally to this work

SPECIALTY SECTION
This article was submitted to Biomaterials,
a section of the journal
Frontiers in Bioengineering and Biotechnology

RECEIVED 23 May 2022
ACCEPTED 04 October 2022
PUBLISHED 18 October 2022

CITATION
Mei N, Wu Y, Chen B, Zhuang T, Yu X, Sui B, Ding T and Liu X (2022), 3D-printed mesoporous bioactive glass/GelMA biomimetic scaffolds for osteogenic/cementogenic differentiation of periodontal ligament cells.
Front. Bioeng. Biotechnol. 10:950970.
doi: 10.3389/fbioe.2022.950970

3D-printed mesoporous bioactive glass/GelMA biomimetic scaffolds for osteogenic/cementogenic differentiation of periodontal ligament cells

Nianrou Mei[1†], Yiwen Wu[1†], Binglin Chen[1†], Tian Zhuang[1], Xinge Yu[2,3], Baiyan Sui[1], Tingting Ding[1*] and Xin Liu[1*]

[1]Department of Dental Materials, Shanghai Biomaterials Research & Testing Center, Shanghai Ninth People's Hospital, Shanghai Jiao Tong University School of Medicine, College of Stomatology, Shanghai Jiao Tong University, National Center for Stomatology, National Clinical Research Center for Oral Diseases, Shanghai Key Laboratory of Stomatology, Shanghai, China, [2]School and Hospital of Stomatology, Tongji University, Shanghai Engineering Research Center of Tooth Restoration and Regeneration, Shanghai, China, [3]Department of Oral and Cranio-maxillofacial Science, Shanghai Ninth People's Hospital, Shanghai Jiao Tong University School of Medicine, College of Stomatology, Shanghai Jiao Tong University, National Center for Stomatology, National Clinical Research Center for Oral Diseases, Shanghai Key Laboratory of Stomatology, Shanghai, China

Integrated regeneration of periodontal tissues remains a challenge in current clinical applications. Due to the tunable physical characteristics and the precise control of the scaffold microarchitecture, three-dimensionally (3D) printed gelatin methacryloyl (GelMA)-based scaffold has emerged as a promising strategy for periodontal tissue regeneration. However, the optimization of the printing biomaterial links the formulation and the relationship between the composition and structures of the printed scaffolds and their comprehensive properties (e.g. mechanical strength, degradation, and biological behaviors) remains unclear. Here, in this work, a novel mesoporous bioactive glass (BG)/GelMA biomimetic scaffold with a large pore size (~300 μm) was developed by extrusion-based 3D printing. Our results showed that the incorporation of mesoporous bioactive glass nanoparticles (BG NPs) significantly improved shape fidelity, surface roughness, and bioactivity of 3D-printed macroporous GelMA scaffolds, resulting in the enhanced effects on cell attachment and promoting osteogenic/cementogenic differentiation in human periodontal ligament cells. The excellent maintenance of the macropore structure, the visibly improved cells spreading, the release of bioactive ions (Si^{4+}, Ca^{2+}), the upregulation of gene expressions of osteogenesis and cementogensis, and the increase in alkaline phosphatase (ALP) activity and calcium nodules suggested that BG NPs could endow GelMA-based scaffolds with excellent structural stability and the ability to promote osteogenic/cementogenic differentiation. Our findings demonstrated the great potential of the newly formulated biomaterial inks and biomimetic BG/GelMA scaffolds for being used in periodontal tissue regeneration and provide important insights into the understanding of cell–scaffold interaction in promoting the regeneration of functional periodontal tissues.

KEYWORDS

biomimetic scaffolds, 3D printing, bioactive glass, GelMA, periodontal regeneration

1 Introduction

The average worldwide prevalence of severe periodontitis has been estimated to be 11%, including countries with relatively less emphasis on periodontal health care (Slots, 2017). For patients with severe periodontitis, the loss of periodontal bone tissue is irreversible. Current clinical approaches can only control the progression of periodontal disease and set back the destruction of the periodontal tissue, but can hardly regenerate the periodontal tissue, especially for those teeth with deep pockets. Up until now, severe periodontitis associated with deep intrabony defects is considered as a clinical challenge (Cortellini and Tonetti, 2015). As is well known, the key to overcoming the challenge is the tissue-engineering strategy, which creates replacement tissues using a combination of cells, scaffolds, and growth factors and promotes tissue regeneration (Iwata et al., 2014). However, owing to the complicated biological evaluation and the high cost of synthesis, the clinical translation of tissue-engineering products with seeding exogenous stem cells remains quite limited (Gao et al., 2021). Thus, it is of great importance to design and develop desirable cell-free scaffolds to stimulate endogenous regeneration for repairing periodontal soft/hard tissue defects.

To achieve successful tissue regeneration, implanted scaffolds need to have the capability to recapitulate the structural and compositional aspects of the tissue, which important for restoring tissue function (Jeon et al., 2014). Depending on the use of a singular homogeneous biomaterial or biphasic or multiphase heterogeneous biomaterials, scaffolds for tissue regeneration can be divided into single-phase, dual-phase, and multiphase (Deliormanlı and Atmaca, 2018). Due to the limitation of its structure and composition, single-phase scaffolds cannot meet the need for the simultaneous regeneration of multiple tissues (Gong Jinglei and Wang, 2021), while multiphase scaffolds can be composed of diverse materials or loaded with a variety of bioactive molecules to mimic the complex tissue structure or promote multiple tissue regeneration. In the repair of osteochondral defects, scaffold–cell constructs were specifically designed to mimic the physiological properties and structure of two different tissues (cartilage and bone) (Yousefi et al., 2015). This concept can be applied to periodontal tissue regeneration. For example, a multiphase polycaprolactone/hydroxyapatite scaffold with different pore/channel scales was fabricated using three-dimensional (3D) printing and was found to regenerate a periodontium complex by time-releasing various functional proteins such as amelogenin, connective tissue-growth factor, and bone morphogenetic protein-2 (Lee et al., 2014). Also, a porous tri-layered nanocomposite hydrogel scaffold composed of chitin-poly (Sowmya et al., 2017a) and nano-bioactive glass–ceramic with various functional proteins (i. g. cementum protein 1, fibroblast growth factor 2, and platelet-rich plasma-derived growth factors) was reported to promote cementogenic, fibrogenic, and osteogenic differentiations of human dental follicle stem cells (Sowmya et al., 2017b). However, in these studies, the integrated multiple-tissue regeneration largely depended on the delivery of various growth factors which would limit the long-term benefits and clinical translation because of their short effective half-life, low stability, and rapid inactivation under physiological conditions (Wang et al., 2017).

Among manufacturing technologies for scaffolds, 3D printing enabled precise control of the scaffold's microarchitecture, showing a promising prospect in realizing simultaneous integrated periodontal-tissue regeneration. Generally, 3D printing has a variety of methodologies, such as inkjet printing, laser-assisted 3D printing, extrusion, and so on which are suitable for various biomaterials and printing needs (Tao et al., 2019). In recent years, 3D-printed hydrogel-based scaffolds have attracted increasing attention for bone and cartilage-tissue regeneration because they can mimic the 3D microenvironment of the native extracellular matrix, provide a porous channel-rich structure to supply nutrients for cell growth and differentiation, and offer tunable geometric shapes to repair irregular bone defect (Gao et al., 2019; Luo et al., 2022). For 3D-printed hydrogel-based scaffolds, one of the most commonly used natural bioink is gelatin methacryloyl (GelMA), which is derived from a hydrolytic degradation of collagen (Janmaleki et al., 2020.). Currently, GelMA hydrogels have been widely used for various biomedical applications due to their suitable biological properties and tunable physical characteristics (Yue et al., 2015; Kamkar et al., 2021). It has been reported that GelMA hydrogels closely resemble some essential properties of native extracellular matrix (ECM) which allows cells to proliferate and spread in GelMA-based scaffolds (Alge and Anseth, 2013; Yue et al., 2015). Light crosslinking makes GelMA from liquid to gel with increasing mechanical strength and stability. Even so, applications of GelMA hydrogels are still limited due to the low mechanical strength and poor printability (Xiao et al., 2019). Furthermore, the pore size of scaffolds is also a critical

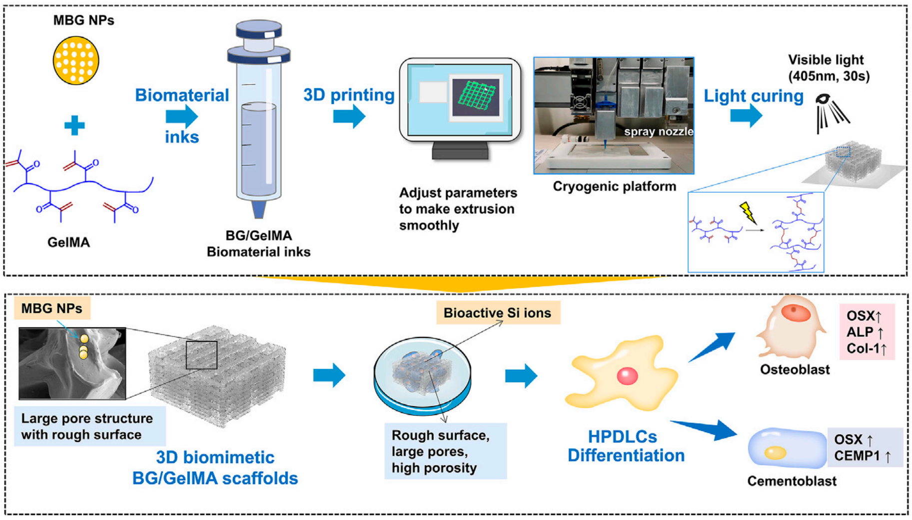

SCHEME 1
Schematic elucidating the 3D printing strategy of biomimetic scaffolds with BG/GelMA inks for osteogenic and cementogemic differentiation of human periodontal ligament cells (HPDLCs). Mesoporous bioactive glass nanoparticles: MBG NPs; Gelatin methacryloyl: (GelMA).

parameter that modulates cell biological behaviors including osteogenesis, chondrogenesis, and vascularization. It has been reported that scaffolds with large macropores (greater than 250 μm in diameter) facilitate the osteogenic differentiation of bone marrow mesenchymal stem cells and robust vascularization (Swanson et al., 2021). Thus, numerous efforts are devoted for improving the mechanical property and bioactivity of 3D-printed GelMA scaffolds by incorporating various inorganic nanomaterials (e.g. nanoclay, silica nanoparticles, hydroxyapatite nanoparticles, etc.) (Gao et al., 2021; Tavares et al., 2021). However, such 3D-printed GelMA multiphase scaffolds still present some challenges regarding the optimization of the printing biomaterial ink formulation and macropore structure. Moreover, the relationship between the composition and structures of the printed scaffolds and their comprehensive properties (e.g. mechanical strength, degradation, and biological behaviors) remains unclear. Among the most popular bioactive inorganic nanoparticles, bioactive glass nanoparticles (BG NPs), mainly comprised of SiO_2, CaO, and Na_2O, have been highlighted in bone regeneration due to their excellent osteoinductive capability, which can lead to the formation of a hydroxyapatite layer with a bond forming between the tissue and the material (Skallevold et al., 2019). However, bioactive glass has several limitations such as the difficulty of being processed into 3D scaffolds and a low-degradation rate which hardly matches the formation rate of new tissue (Rahaman et al., 2011). Herein, in this work, to mimic the organic component and 3D microenvironment of native ECM in the periodontal tissue, both gelatin and mesoporous BG NPs were selected for the biomaterial ink formulation due to gelatin derived from type I collagen and the osteoinductive activity of bioactive glass, and then a novel biomimetic BG/GelMA macroporous scaffold with a large pore size (~300 μm) was developed by 3D printing through controlling the amounts of BG NPs. With increasing mesoporous BG NPs incorporation, the 3D-printed GelMA hydrogel scaffold displayed higher structural stability, rougher surface, and better bioactivity, which is more suitable for cell attachment, spreading, and osteogenic/cementogenic differentiation in periodontal ligament cells (Scheme 1). The 3D-printed biomimetic bioactive glass/GelMA macroporous scaffolds show good shape fidelity, biocompatibility, and excellent osteogenesis/cementogensis ability, suggesting a promising material for integrated periodontal tissue regeneration.

2 Materials and methods

2.1 Synthesis and characterization of mesoporous BG NPs

Mesoporous BG NPs used in this study were prepared using a cetyl pyridine bromide (CPB) template method according to the previously published protocol (Sui et al., 2018). Briefly, 0.23 g NaOH and 1.0 g of polyvinylpyrrolidone (PVP) were dissolved in 120 ml ddH_2O. After stirring for 10 min, 1.4 g of CPB (Sigma-Aldrich, St. Louis, United States) was dissolved in the solution and stirred continuously for one

TABLE 1 The component of each group of biomaterial inks and scaffolds.

Biomaterial inks	Scaffolds	PBS (ml)	LAP(g)	GelMA (g)	BG NPs (g)
I	0% BG	20	0.05	2.0	0.00
II	1% BG	20	0.05	2.0	0.02
III	5% BG	20	0.05	2.0	0.10
IV	10% BG	20	0.05	2.0	0.20

PBS, phosphate buffer saline; GelMA, gelatin methacryloyl; BG, bioactive glass; LAP, Lithium phenyl-2,4,6-trimethylbenzoylphosphinate.

hour. Next, tetraethyl orthosilicate (TEOS), calcium nitrate tetrahydrate, and TEP (the molar ratio of Ca: P: Si = 15: 5: 80) were subsequently added and stirred for 24 h. The solution was collected and washed with ddH$_2$O three times and then sealed in Teflon-lined autoclaves at 80°C for 48 h. Finally, the dispersion was dried at 80°C for 12 h and calcined at 550°C for five hours to obtain mesoporous BG NPs.

The structure and morphology of the BG NP sample were characterized by high-resolution transmission electron microscopy (TEM, JEM-2100, JEOL), and the size distribution was calculated by using ImageJ analysis software (Media Cybernetics Inc., United States). The Brunauer–Emmett–Teller (BET) specific surface area and pore size distribution of MBG were determined using a micromeritics porosimeter (ASAP 2460, Micrometrics Instrument).

2.2 Preparation of biomaterial inks

Gelatin methacryloyl (GelMA) and photoinitiator LAP (phenyl-2,4,6-trimethylbenzoylphosphi-nate) were purchased from Suzhou Intelligent Manufacturing Research Institute (Suzhou, China). First, 20 mL phosphate buffer saline (PBS, HyClone, Logan, UT, United States) was added into a brown flask containing 0.05 g LAP powder to obtain 0.25% (w/v) LAP solution, and then it was sterilized by a syringe filter with a pore size of 0.22 μm (Merck Millipore, Billerica, MA, United States). Subsequently, as shown in Table 1, different ratios of BG NPs and 10% (w/v) of GelMA powder were added into four LAP solutions to prepare the biomaterial inks for the 3D-printed scaffolds, melted in a water bath (60°C, 30 min), and oscillated three times. The four kinds of biomaterial inks were named as 0% BG, 1% BG, 5% BG, and 10% BG with respect to the weight of GelMA (w/w).

2.3 Rheological characterization of biomaterial inks

Rheological properties of the biomaterial inks were performed by using a rheometer (Anton Paar MCR302, Austria) equipped with parallel plates with a diameter of 25 mm and a truncation gap distance of 2.6 mm. The linear viscoelastic range (LVR) was obtained from the single frequency amplitude sweep. To measure the viscosity, these inks were loaded with steady-rate sweeps within a shear rate range of 0.01–1,000 s^{-1}. To measure the storage modulus (G′) and loss modulus (G″), frequency sweep tests were conducted in the linear viscoelastic region at a strain of 1.0% according to previously reported methods (Gao et al., 2019; Schwab et al., 2020b). All experiments were performed in room temperature (RT = 25°C). Before the experiments, the biomaterial inks were cooled to 4 °C for 30 min to get the transformation from liquid to gel.

2.4 Preparation of biomimetic BG/GelMA scaffolds

The biomimetic BG/GelMA scaffolds were constructed by an extrusion-based 3D printer (Motor Assisted Microsyringe, Shanghai fuqifan Electromechanical Technology Co., Ltd., Shanghai, China). First of all, a parameter file was designed. The scaffold was designed as a 1×1 × 0.5 cm (long×wide×high) rectangle. The filament diameter was 400 μm and the filament space was 1.2 mm. The temperature of the bin and print plate were 20–25°C and 15°C, respectively. The moving speed of the nozzle (inner diameter: 400 μm) was 10 mm/s and the extrusion pressure was 0.3–0.6 MPa. Then, the photocurable crosslinked biomaterial inks were loaded into the printer and the program was started. During the printing process, the external computer transmitted the 3D model data of the scaffolds to the control system of the printer and drove the printing nozzle to move along the X–Y directions so that the ink could be stacked into the section of the model. After the printing of the section was completed, the nozzle was raised to the next section layer, and the printing process was repeated until the supported printing was completed. After printing, crosslinking curing was carried out under UV-lamp irradiation. The wavelength of the UV light was 405nm, the illumination intensity was 25 mW/cm^2, and the irradiation time was 50 s. The scaffolds were refrigerated in PBS and the scaffolds prepared with printing biomaterial inks of 0% BG, 1% BG, 5% BG, and 10% BG were labeled as scaffolds 0% BG, 1% BG, 5% BG, and 10% BG, respectively.

2.5 Morphological characterization of biomimetic BG/GelMA scaffolds

The morphological structure of the 3D-printed BG/GelMA scaffolds was observed from macro and micro perspectives. For gross observation, the length and height of the scaffolds were measured with a ruler and determined according to images taken by a camera. From a micro perspective, the morphology of scaffolds including the pore structure was visualized using scanning electron microscopy (SEM, Tescan Mira 3 XH, Czech Republic) and the incorporated mesoporous BG NPs were characterized by using an energy dispersive spectrometer (EDS, AZtec X-Max^{N} 80, United Kingdom).

The pore size and porosity were measured and calculated using the threshold method by using ImageJ (Media Cybernetics Inc., United States) analysis software (Grove and Jerram, 2011; Loh and Choong, 2013). Specifically, SEM images of the scaffolds were opened, the scale was adjusted, the image was cropped to make a rectangular section only comprising of the sample, it was converted to an 8-bit paletted file, the threshold tool was used to select the porous areas, and the particles tool was analyzed to get the pores' diameter. The displayed results were copied and analyzed in Excel (Microsoft, China) and Prism 9 (GraphPad Software, LLC. United States), respectively.

2.6 Thermal behavior and infrared analysis of biomimetic BG/GelMA scaffolds

The thermal stability of scaffolds was studied through thermogravimetric analysis (Netzsch STA 449 F3 Jupiter®, Germany) from room temperature to 700°C at a heating rate of 10°C/min under Ar flow.

The chemical compositions of the biomimetic BG/GelMA scaffolds were assayed by using (FTIR) Fourier transform infrared spectroscopy with KBr powder on a DTGS spectrometer (Thermo Scientific, United States). The samples were dried in constant temperature under 40 °C in an oven and crushed down. Spectra were recorded in the range of 500–4,000 cm^{-1} at 32 scans with a resolution of 4 cm^{-1}.

2.7 Mechanical property of biomimetic BG/GelMA scaffolds

The mechanical property of the 3D-printed BG/GelMA scaffolds was measured by performing a compression test using a universal testing system loaded on a microcomputer-controlled electronic universal material-testing machine (Shanghai Hengyi Precision Instrument Co., LTD, China) at a speed of 1 mm/min until above 90% deformation of the sample. The sample scaffolds were 10.0 mm×10.0 mm×5.0 mm (long × wide × height) with lattice structure (7 × 7, meaning 7 columns and 7 rows) with 0°, 90° stacking (12 layers). The compressive modulus was calculated by the slope of the linear region of the stress–strain curve, almost limited to 5%–20% of the strain. All samples were tested thrice.

2.8 Degradation property of biomimetic BG/GelMA scaffolds

The degradation property of the 3D-printed BG/GelMA scaffolds was evaluated using a gravimetric method. Firstly, the original weight M0 of all test samples was recorded. Secondly, under sterile operation, the test sample (N = 3) was completely immersed in PBS at a ratio of 1g: 30 ml within a sealed container and placed in a 37°C oven. At various time-points (1 day, 3 days, 7 days, 14 days, and 28 days), the test sample was weighted and recorded as M1. The degradation ratio was assessed by monitoring the weight changes of the scaffolds using the following equation:

$$\text{Degradation ratio}\,(\%) = (M0 - M1)/M0 \times 100\%$$

Moreover, the scaffolds were submerged in a solution of 1 mg/ml collagenase 2 solutions (ThermoFisher, Waltham, MA, United States) at a ratio of 1g: 10 ml. The degradation was carried out at 37°C and 100rpm in an oscillator. The original weight M0 of all test samples was recorded. The scaffolds were observed every 15 min and their wet weight was recorded as M2 at that time. The mass loss ratio was assessed by monitoring the weight changes of the scaffolds using the following equation:

$$\text{Mass loss ratio}\,(\%) = (M0 - M2)/M0 \times 100\%$$

2.9 Cell morphology on the surface of biomimetic BG/GelMA scaffolds

Human periodontal ligament cells (HPDLCs) were purchased from ScienCell Research Laboratories, Inc. (catalog #2630, Carlsbad, United States) and cultured in a cell medium (ScienCell, Carlsbad, United States) containing 2% fetal bovine serum (FBS, ScienCell, Carlsbad, United States), 1% penicillin/streptomycin solution (P/S, ScienCell, United States), and 1% growth supplement (ScienCell, Carlsbad, United States) in a humidified atmosphere of 5% CO_2 at 37°C. In detail, the BG/GelMA scaffolds were sterilized by ultraviolet light for 4 h and placed in a 24-well cell-culture plate. Subsequently, HPDLCs at a density of 2.0×10^5/ml were seeded on the surface of as-prepared scaffolds for 24h and then fixed in 2.5% glutaraldehyde (4°C) overnight. The cell morphology, adhesion, and growth on the surface of the scaffolds were observed by SEM (Tescan Mira 3 XH, Czech Republic).

TABLE 2 Primers used for real-time quantitative RT-PCR.

Target gene	Primer sequence	
	Forward	Reverse
OSX	CCTCTGCGGGACTCAACAAC	AGCCCATTAGTGCTTGTAAAGG
ALP	ACCACCACGAGAGTGAACCA	CGTTGTCTGAGTACCAGTCCC
Col-1α1	GTGCGATGACGTGATCTGTGA	CGGTGGTTTCTTGGTCGGT
CEMP-1	GGGCACATCAAGCACTGACAG	CCCTTAGGAAGTGGCTGTCCAG
GAPDH	ACAACTTTGGTATCGTGGAAGG	GCCATCACGCCACAGTTTC

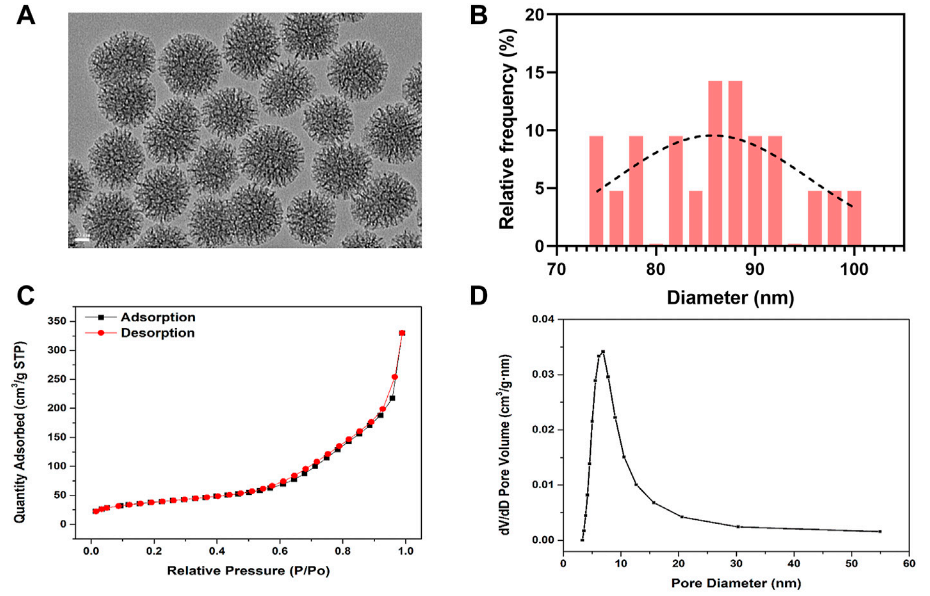

FIGURE 1
Characterization of mesoporous bioactive glass nanoparticles (BG NPs). **(A)** TEM images. Scale = 20 nm. **(B)** Particle-size analysis by ImageJ of mesoporous BG NPs. **(C)** Nitrogen adsorption–desorption isotherms and **(D)** Pore-size distribution of BG NPs.

2.10 Cell viability assay

The CellTiter 96® AQueous one solution assay (Promega, Madison, WI, United States) was used to evaluate the cell viability of HPDLCs cultured in the as-prepared BA/GelMA scaffolds for 3 days. Then, the HPDLCs cultured with different scaffolds were incubated with a cell medium containing 20% v/v of MTS (3-(4,5-dimethylthiazol-2-yl)-5-(3carboxymethoxyphenyl)-2-(4-sulfophenyl)-2H-tetrazolium). After 4 h, the supernatants were transferred to new 96-well plates and the absorbance at 490 nm was determined on a microplate reader (Multiskan GO, Thermo Scientific, MA, United States).

2.11 Inductively coupled plasma mass spectrometry (ICP-MS) analysis

To investigate whether the ion-release of biomimetic BG/GelMA scaffolds could promote osteogenic/cementogenic differentiation of HPDLCs, cells were cultured in the scaffolds 0% BG, 1% BG, 5% BG, and 10% BG for day 1 and day 7, respectively. Subsequently, the concentrations of Ca, Si, and P ions in the cell-culture medium extracts of as-prepared scaffolds were respectively measured by inductively coupled plasma mass spectrometry (ICP-MS) (Agilent7700s, Agilent Technologies Co. Ltd, United States). The number of replicates used in this experiment was three.

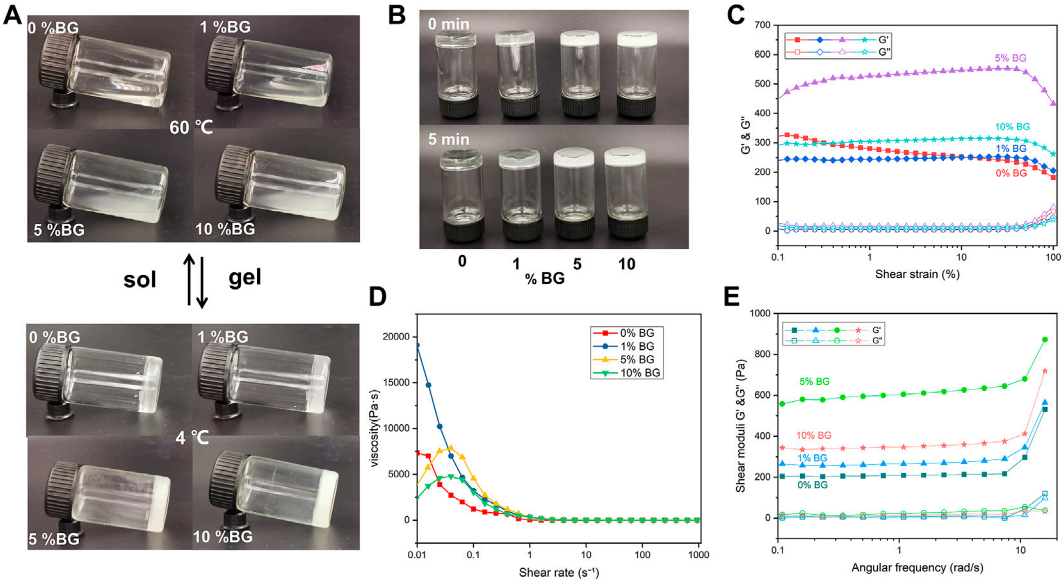

FIGURE 2
Rheological properties of the BG/GelMA biomaterial ink: flow behavior of 0%, 1%, 5%, and 10% BG **(A)** at 60 °C and 4 °C **(B)** after 0 min and 5 min **(C)** the elastic moduli (G′) and viscous moduli (G″) shear–strain; **(D)** the viscosity–shear rate; and **(E)** the shear moduli–angular frequency of the respective biomaterial inks. The 'sol' means the biomaterial inks went from liquid to gel and the 'gel' means from gel to liquid.

2.12 Alkaline phosphatase staining

ALP staining was performed using BCIP/NBT Alkaline Phosphatase Color Development Kit (Beyotime Biotechnology, Shanghai, China) to evaluate the osteogenesis differentiation of HPDLCs cultured in the as-prepared BG/GelMA scaffolds. In detail, HPDLCs were cultured in the scaffolds 0% BG, 1% BG, 5% BG, and 10% BG for day 7, 14, and 21, respectively. According to the requirements of the ALP kit, added 5 ml ALP color-developing buffer and 16.5 μl BCIP solution (300X), NBT solution (150x) 33 μL, and BCIP/NBT solution 5.05 ml into the test tube, in turn, was mixed to prepare BCIP/NBT dyeing working solution. After washing the scaffold samples (on day 7, 14, 21) with PBS, the washing solution was removed and added BCIP/NBT dyeing working solution to ensure that the samples can be fully covered, and then the scaffold samples were incubated in the dark for 5–30 min until the color developed to the expected depth. We removed the BCIP/NBT dyeing working solution, washed it with distilled water 1–2 times, stopped the color reaction, and the results of each group were observed and recorded.

2.13 Alizarin Red S staining

Alizarin Red S staining (Beyotime Biotechnology, Shanghai, China) was used to observe extracellular matrix calcification of HPDLCs cultured in the as-prepared BG/GelMA scaffolds. HPDLCs were inoculated with the scaffolds of each group for 21 days, washed with PBS, removed from the washing solution, added to the fixed solution for 20 min, and washed 3 times by PBS. According to the requirements of the kit, we added an appropriate amount of Alizarin Red S dyeing working solution to ensure that the sample can be fully covered, dyed at room temperature for 30 min, and the results of each group were observed after fully washing with distilled water. The results of each group were observed and recorded.

2.14 Real-time quantitative RT-PCR

The osteoblast/cementoblast-related gene transcription of Osterix (OSX), Cementum protein-1 (CEMP-1), ALP and type I collagen (Col-1a1) was detected by real-time quantitative reverse transcriptase–polymerase chain reaction (qRT-PCR). Briefly, HPDLCs were cultured in the scaffolds 0% BG, 1% BG, 5% BG, and 10% BG for 7 days, and the total RNA of HPDLCs was extracted using the RNeasy® Mini kit (QIAGEN, Germany). Complementary DNA (cDNA) was synthesized from the total RNA using the PrimeScript RT Reagent Kit (TaKaRa, Japan) according to the manufacturer's instructions. qPCR was performed by using a LightCycler® System (Roche Diagnostics, United States) using TB Green Premix Ex Taq II (Tli RNaseH Plus) (TaKaRa, Japan). The housekeeping gene GAPDH was used to normalize the results. The primer sequences used in this study are listed in Table 2.

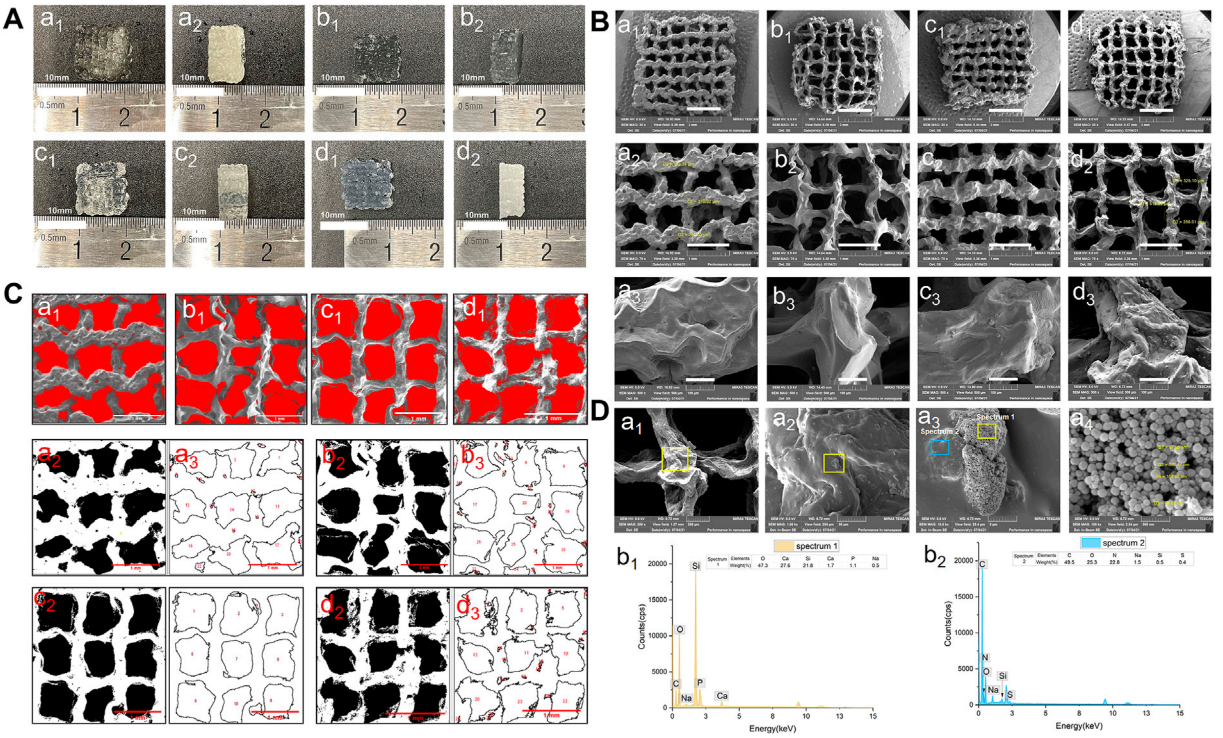

FIGURE 3
Morphology of 3D-printed mesoporous BG/GelMA macropore scaffolds. **(A)** Top and side-views of the macro morphology. a1–a2) 0% BG group; b1–b2) 1% BG group; c1–c2) 5% BG group; d1–d2) 10% BG group; **(B)** Representative scanning electron microscopic images at 30x, 75x, 500x magnification. a1–a3) 0% BG group; b1–b3) 1% BG group; c1–c3) 5% BG group; d1–d3) 10% BG group; **(C)** and pore sizes of scaffolds. a1–a3) 0% BG group; b1–b3) 1% BG group; c1–c3) 5% BG group; and d1–d3) 10% BG group; Note: all the darkest regions of the image became red; contours of the pores were traced and coded (from a2, a3 to d2,d3); **(D)** The representative SEM images of the 10% BG group scaffolds from a1) 200x; b1) 1.0kx; c1) 10.0kx to d1)100kx and SEM-energy-dispersive X-ray spectroscopy (EDS) analysis of two lumps in a3. b1) graph of EDS analysis of the yellow box area in panel a3; b2) graph of EDS analysis of the blue box area in panel a3.

2.15 Statistical analysis

All data are presented as the mean ± standard deviation. Statistical analysis was performed using the Prism 9 statistical software package (GraphPad Software, LLC. United States). An ordinary one-way analysis of variance (ANOVA) was performed, followed by Turkey's post hoc test to determine the differences between the scaffolds 0% BG, 1% BG, 5% BG, and 10% BG. In all cases, significance was asserted at $p < 0.05$.

3 Results

3.1 Characterization of the biomaterial BG/GelMA inks

3.1.1 Characterization of mesoporous bioactive glass nanoparticles

The morphology of BG NPs was characterized by transmission electron microscopy (van Haaften et al., 2019) (Figure 1A). BG NPs exhibits an obvious multi-generational hierarchical dendritic structure: inner mesoporous BG NPs exhibit hexagonal channels and external mesoporous BG NPs show radial channels, the mean particle size was measured as 85.97±7.60 nm (Figure 1B). We further confirmed the mesoporous structure of BG NPs by using the nitrogen sorption analysis. Figure 1C shows the N_2 adsorption–desorption of type IV isotherm and pore-size distribution for mesoporous BG NPs, which is a typical isotherm for mesoporous materials. Specifically, the specific surface area, pore volume, and pore size of mesoporous BG NPs are 134.84 m^2/g, 0.51 cm^3/g and 9.10 nm, respectively (Figure 1C,D).

3.1.2 Rheological properties of the biomaterial inks

To assess the printability of the biomaterial inks, rheological properties including viscosity, viscoelasticity, and shear-thinning were measured. As shown in Figures 2A,B the biomaterials inks (0% BG, 1% BG, 5% BG,

TABLE 3 Porosity and pore size analysis of 3D-printed BG/GelMA scaffolds.

Scaffolds		0% BG group	1% BG group	5% BG group	10% BG group
Porosity		43.252%	52.163%	55.03%	52.691%
Pore size (mm)	Mean	0.333	0.424	0.446	0.304
	SD	0.026	0.113	0.065	0.034

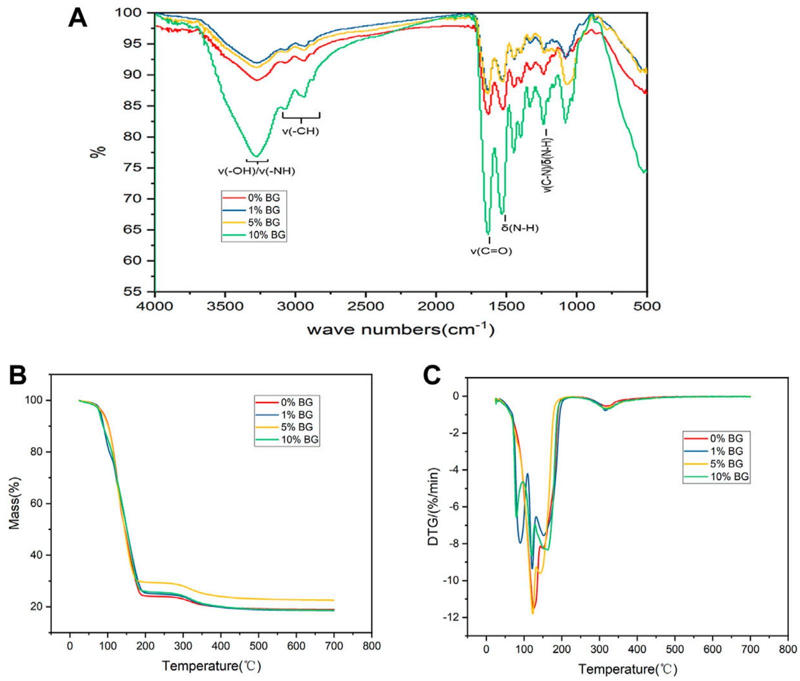

FIGURE 4
Characterization and thermal properties analysis of 3D-printed mesoporous BG/GelMA macropore scaffolds **(A)** FTIR spectra of BG/GelMA scaffolds with different mass ratios of BG NPs. The symbol 'ν' means stretching vibration while δ means bending vibration; **(B)** Thermogravimetric analysis (TGA); **(C)** Derived thermogravimetric (DTG) of scaffolds.

and 10% BG) showed different flow behaviors. Viscosity is the resistance of a fluid to flow. It has been observed that the viscosity of the 10% BG group is higher than that of the 0% BG group. Furthermore, the viscoelasticities of four biomaterial inks were measured within the linear viscoelastic region (LVR) *via* shear–strain sweeps, which can be described by the viscous components (storage modulus G′) and the elastic components (loss modulus G″). Figure 2C shows that the GelMA inks containing 1%–10% BG NPs have clearer linear-viscoelastic range (LVR), compared with the GelMA inks without BG NPs. Figure 2D shows that all the biomaterial inks have shear-thinning behavior with increasing shear rate, and the storage modulus of the GelMA inks containing BG NPs is higher than the loss modulus (Figure 2E), suggesting that BG NP incorporation could increase the stability of the GelMA inks.

3.2 Synthesis and characterization of the biomimetic BG/GelMA scaffolds

The lattice scaffold design (7 × 7, meaning 7 columns and 7 rows) with 0°, 90° stacking (12 layers), and 1.2 mm filament space were used to construct the 3D scaffolds with lateral and vertical interconnected pores. Four groups of biomaterial inks were successfully printed into 10.0 mm×10.0 mm×5.0 mm (long×wide×height) 3D porous scaffolds and the macro morphology of the scaffolds were shown in Figure 3A. All groups of BG/GelMA biomaterial inks were printed into integrated and structured scaffolds, while the obvious collapse on the bottom and twisted filaments were observed in the group of biomaterials without BG NPs. With the increase in the concentration of BG NPs, the BG/GelMA scaffolds (1% BG,

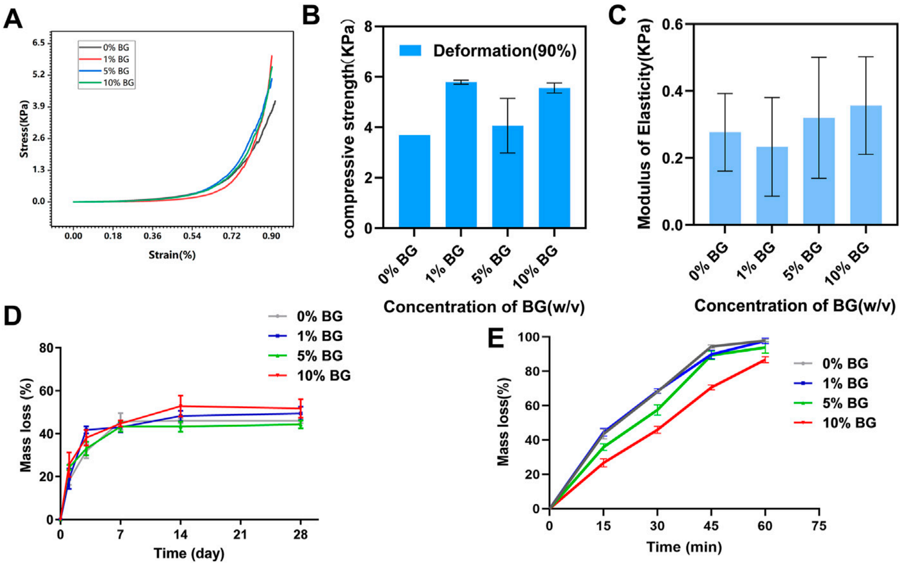

FIGURE 5
Mechanical and degradation properties of the biomimetic BG/GelMA scaffolds **(A)** Representative compressive stress–strain curve of the biomimetic BG/GelMA scaffolds. Grey: 0% BG group; Red: 1% BG group; Blue: 5% BG group; Green: 10% BG group; **(B)** Compressive strength of the scaffolds at the deformation of 90%; **(C)** Elastic modulus of the scaffolds. N = 3 samples per group; **(D)** *In vitro* degradation in PBS solution at 37°C and **(E)** enzymatic degradation of scaffolds 0% BG, 1% BG, 5% BG, and 10% BG. Grey: 0% BG group; Blue: 1% BG group; Green: 5% BG group; Red: 10% BG group; Data represent the mean ± SD, n = 3.

5% BG, and 10% BG) became more and more regular and uniform, and were less prone to collapse.

The SEM images of the BG/GelMA scaffolds were shown in Figure 3B. All four scaffolds had uniformly interconnected macropores (Figure 3B), indicating the use of the BA/GelMA biomaterial inks and the extrusion-based 3D printing technique which allowed for precise control of the pore size and structure. Furthermore, the mean pore sizes and porosities of the scaffolds of all groups were analyzed by ImageJ (Figure 3C) and summarized in Table 3. The porosity of the BG/GelMA scaffolds without BG NPs was 43.25%, while it became higher than 50% after the addition of BG NPs. Furthermore, the mean pore size of the BG/GelMA scaffolds increased from ~300 μm to ~400 μm by the incorporation of 1%–5% BG NPs, while decreasing to ~300 μm by the incorporation of 10% BG NPs.

By analyzing the SEM images, we observed that the surface of the BG/GelMA scaffolds without BG NPs was the smoothest. With the increase of BG NP content in the scaffold, the scaffolds' surface became coarser and coarser (Figures 3B,D). At high magnification, spherical nanoparticles embedded in the scaffolds were seen in the 10% BG group, with nanoparticle diameters around 90 nm (Figure 3D). Furthermore, a strong silicon (Si), calcium (Ca) and phosphate (P) peak in the EDS spectra confirmed that the BG NPs were successfully incorporated into the biomimetic BG/GelMA scaffolds by 3D printing (Figure 3D).

The FTIR spectra of the BG/GelMA scaffolds showed a sharp intense peak at 1640 cm^{-1} corresponding to C=O bonds, and two typical peaks at 1,530 cm^{-1} and 1,240 cm^{-1} related to N–H bending and C–N stretching plus N–H bending, respectively (Figure 4A). Moreover, a broad peak at 3,275 cm^{-1} representing the associated signal for the O-H and N-H groups and a band at 2,940 cm^{-1} representing the C-H stretching groups were also observed. Furthermore, the thermal degradation behavior of the four biomimetic BG/GelMA scaffolds was characterized by using TGA analysis. As shown in Figures 4B, C, the TGA curve showed that all scaffolds began to lose integrity between 80°C and 120°C, probably caused by the loss of water molecules. At temperatures above 150°C, the degradation of GelMA started and the residual mass for scaffold 0%BG, 1% BG, 5% BG, and 10% BG was 18.94%, 18.52%, 22.59%, and 18.61%, respectively, when heating temperature reached 700 °C.

3.3 Mechanical and degradational properties of the biomimetic BG/GelMA scaffolds

The compressive mechanical properties of the biomimetic BG/GelMA scaffolds were investigated to verify whether the mechanical properties of tissue engineering scaffold were able to maintain the structural stability when it was cultured *in vitro* or implanted *in vivo* (Wang et al., 2018). From the compressive stress–strain curve (Figure 5A), the trends in scaffolds 0% BG, 1% BG, 5% BG, and 10% BG were consistent and the inflection

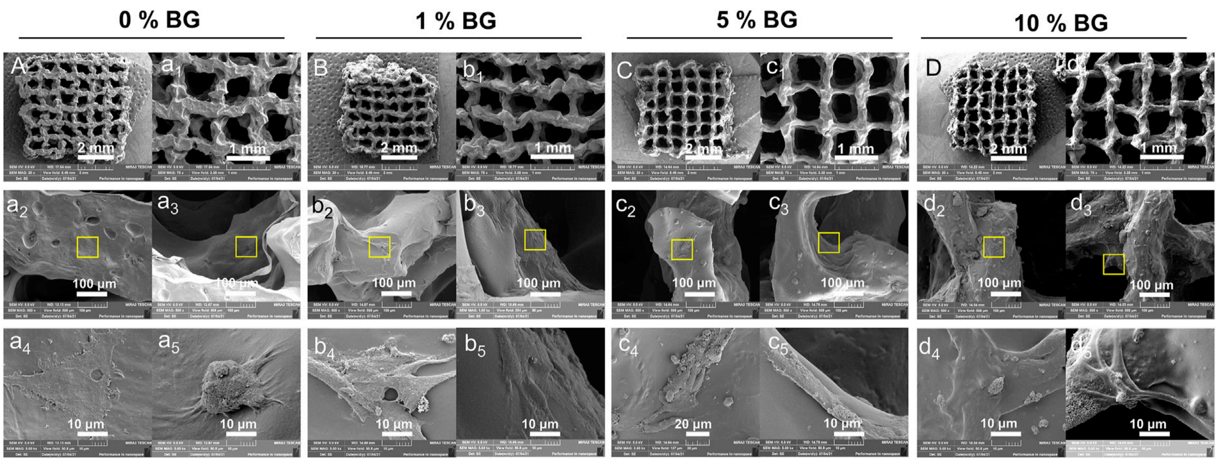

FIGURE 6
Cell morphology of HPDLCs in 3D-printed biomimetic BG/GelMA macropore scaffolds by SEM. Cells were cultured in scaffolds 0% BG, 1% BG, 5% BG, and 10% BG for 24 h **(A,B,C, and D)** SEM images of integral scaffolds with cells from scaffolds 0% BG, 1% BG, 5% BG, and 10% BG at 30x magnification. (a_1, b_1, c_1, and d_1) SEM images of partial scaffolds with cells from all groups at 75x magnification. (a_2, b_2, c_2, and d_2) SEM images of cells in the outer surface and (a_3, b_3, c_3, and d_3) inner pore surface of scaffolds at 500x magnification. (a_{4-5}, b_{4-5}, c_{4-5}, and d_{4-5}) Magnifying images of cells of the yellow box area at 5.0kx magnification. A/a_1-a_5) 0% BG group; B/b_1-b_5) 1% BG group; C/c_1-c_5) 5% BG group; and D/d_1-d_5) 10% BG group.

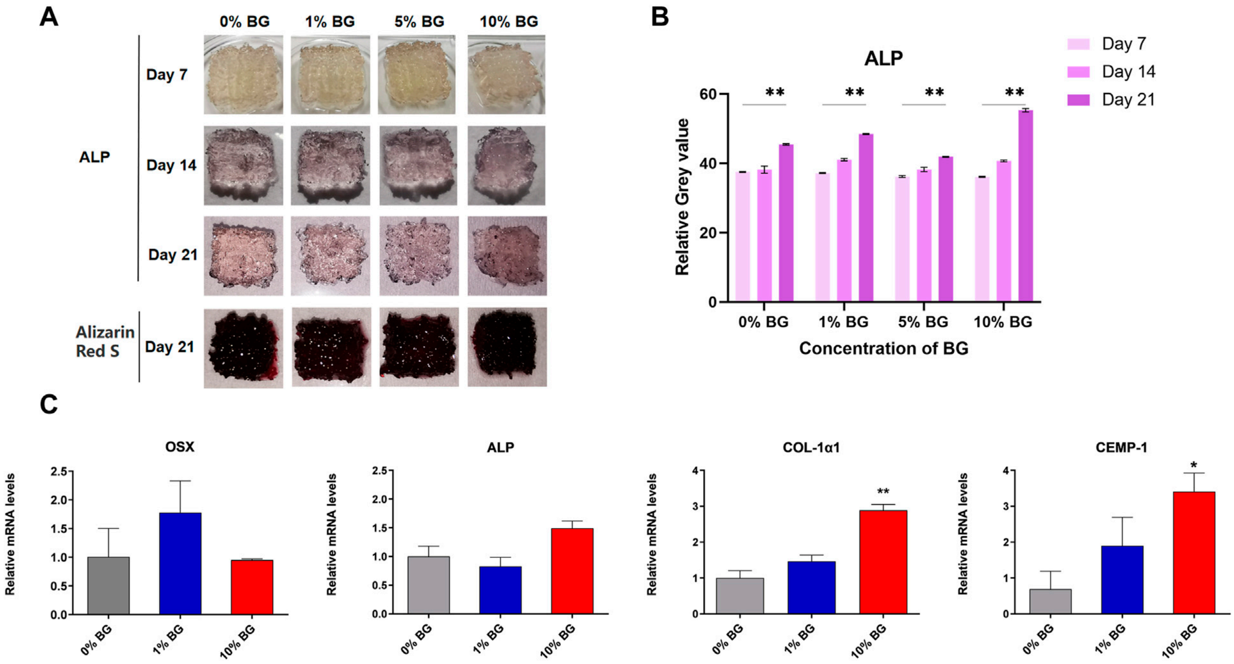

FIGURE 7
Osteogenic/cementogenic differentiation of HPDLCs on the biomimetic BG/GelMA scaffolds **(A)** Human periodontal ligament cells HPDLCs were cultured in macroporous BG/GelMA scaffolds *in vitro*. Alkaline phosphatase and alizarin red staining were performed every week. Photos of scaffolds on days 7, 14, and 21 were shown. **(B)** The Quantitative analysis of ALP staining. ****$p < 0.01$. n = 3 for each group. **(C)** The osteogenic and cementogenic quantification and gene expression of HPDLCs seeded on scaffolds 0% BG, 1% BG, and 10% BG for 7 days. n = 3 for each group. **$p < 0.01$, *$p < 0.05$.

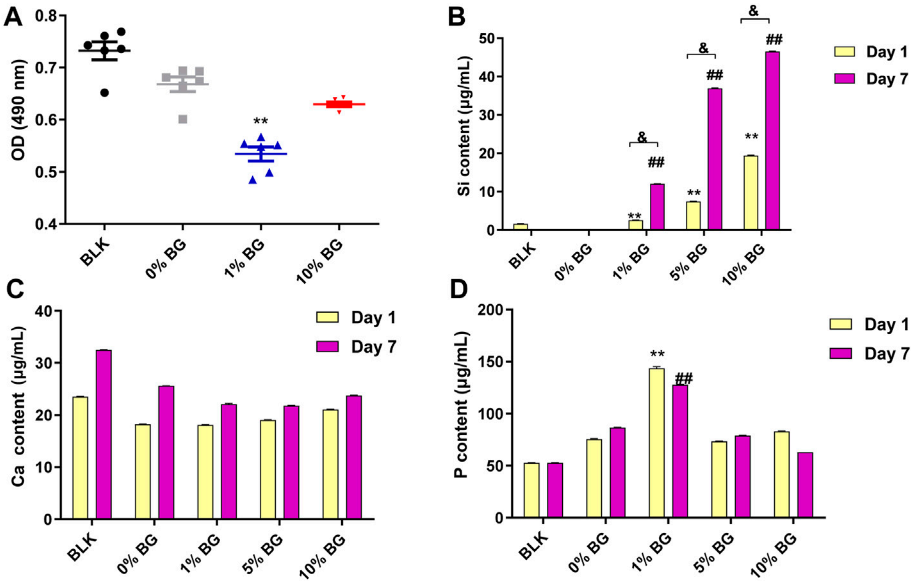

FIGURE 8
Cell viability of HPDLCs by using MTS assay and the ion release of the biomimetic BG/GelMA scaffolds by ICP-MS **(A)** The OD (490 nm) values in the BLK (Blank: flat plate) group and the scaffolds 0% BG, 1% BG, and 10% BG groups on day 3; The Ca ion release **(B)**, the Si ion release **(C)**, and the P ion release in the BLK group and the scaffold 0% BG, 1% BG, and 10% BG groups on day 1 and day 7. The data represent the mean ± SD, n = 3. **,##,& $p < 0.01$. MTS: (3-(4,5-dimethylthiazol-2-yl)-5-(3carboxymethoxyphenyl)-2-(4-sulfophenyl)-2H-tetrazolium).

points were all around 70% of the deformation. The mean compressive strength at 90% deformation of scaffolds 0% BG, 1% BG, 5% BG, and 10% BG were 3.679±0.001, 5.790±0.001, 4.065±0.001, and 5.556±0.001 KPa, respectively, and the moduli of elasticity were 0.277±0.116, 0.233±0.147, 0.320±0.181, and 0.357±0.146 KPa, respectively (Figures 5B,C). There was no significance in compressive strength and modulus elasticity between the scaffolds 0% BG, 1% BG, 5% BG, and 10% BG.

As displayed in Figure 5D, all scaffolds' mass loss and degradation increased with increase in time. Till 14 days, the curve of mass loss tended to be flat which meant that the degradation of the BG/GelMA scaffolds was brought into a steady state. After degradation for 28 days, the weight loss of all groups of scaffolds tended to be around 50%.

To further evaluate enzymatic degradability, the biomimetic BG/GelMA scaffolds were incubated in collagenase solutions for 15 min, 30 min, 45 min, and 60 min, and the degradation rates of the various scaffolds are shown in Figure 5E. Compared to various scaffolds in PBS, the degradation of four BG/GelMA scaffolds in collagenase solutions became faster and the curve of mass loss became steeper. Notably, after 60 min, the mass loss of scaffolds 0% BG, 1% BG, and 5% BG were all close to 100% except for scaffold 10% BG, which exhibited a slightly slower degradation rate, indicating that the degradation of BG/GelMA scaffolds could be delayed by the incorporation of BG NPs.

3.4 Cell adhesion and growth on the surface of the biomimetic BG/GelMA scaffolds

There were more and more HPDLCs adhering to the surface of scaffolds 0% BG, 1% BG, 5% BG, and 10% BG, and a large proportion of them aggregated around the coarse-faced mass composed of BG NPs under a high-power scanning electron microscope (Figure 6A). According to clumps with rough surfaces formed with inorganic particles at the macro level and the crude surface of BG nanospheres at the micro-level (Figures 3C, D), the adhesion of HPDLCs was promoted. Also, the cells grew flat and spread both on the scaffold surface and the inner region of the pores (Figure 6 a2, a3–d2, d3). BG particles could be seen on and around the cells, and the cells with BG particles around them stretched better (Figure 6 a4, a5–d4, d5).

3.5 Osteogenic/cementogenic differentiation of HPDLCs on the biomimetic BG/GelMA scaffolds

Alkaline phosphatase (ALP) and Alizarin Red staining results of scaffolds 0% BG, 1% BG, 5% BG, and 10% BG were shown in Figure 7A. It could be seen that the scaffolds of each group cultured with HPDLCs were stained, and the staining deepened with the increase of culture days, which was attributed to enhanced osteogenic differentiation. However, the difference between the scaffolds of different BG concentrations was not obvious under observation of the naked eye.

As shown in Figure 7C, the real-time PCR data showed that the scaffold 10%BG group exhibited the highest expression of osteogenesis and cementogenesis markers (Col-1α1 and CEMP-1) compared to those of scaffolds 0%BG and 1%BG on day 7 ($p < 0.01$). However, the expressions of OSX and ALP showed no significance between scaffolds 0% BG, 1% BG, and 10% BG. We suspected that it might be related to the regulatory mechanisms of different genes, which need further research.

The cell viability assay result is shown in Figure 8A. After 3 days of culture, a slight decrease in cell viability in both scaffold 1% BG and 10% BG group was observed compared to the scaffold 0% BG group, and the difference was statistically significant ($p < 0.01$), which revealed that the addition of BG had a negative effect on cell proliferation. However, as the concentration of BG increased, the cell viability was rising rather than falling.

The ion release of the biomimetic BG/GelMA scaffolds with different ratios of BG NPs was investigated by ICP-MS. The amount of silicon ions released from both scaffolds 1% BG and 10% BG was significantly increased in a time-dependent manner (Figure 8B). Scaffolds 10% BG exhibited the highest level of silicon ions release on day 1 and day 7 compared to other scaffolds ($p < 0.01$), which is attributed to the highest concentration of BG NPs. Additionally, in line with the degradation of the scaffolds, the release of silicon ions surged during the first week. No significance was observed in the calcium ion release (Figure 8C). As for phosphorus ions affected by PBS solutions, there is no clear pattern of release (Figure 8D).

4 Discussion

In this study, to stimulate endogenous periodontal tissue-regeneration, a novel biomimetic BG/GelMA scaffold with a large pore size and a rough surface was successfully developed by extrusion-based 3D bioprinting. Compared with solvent casting, gas forming, emulsification freeze-drying, and so on, the 3D-printing technique has distinctive advantages in flexibility and accurate control of the macrostructure and pore size (Turnbull et al., 2018). For the purpose of great shape fidelity of extrusion-based 3D-printed scaffolds, the printability of biomaterial inks, referring to the “suitable” extrudability, filament formation, and shape fidelity, is as essential as the design and characterization of biomaterial scaffolds (Gao et al., 2019) (Schwab et al., 2020a). Among biomaterial inks, GelMA shows great potential for extrusion 3D printing, which allows the preparation of hydrogel-based scaffolds with controllable shapes for repairing personalized and irregular periodontal defects. However, the high self-healing ability and the low mechanical strength of GelMA make it difficult for GelMA scaffolds to obtain macroporous structures with good shape fidelity (Liu et al., 2017). To overcome the limits of GelMA-based inks, in this work, the mesoporous BG NPs were incorporated into GelMA to prepare the BG/GelMA biomaterial inks and to improve the shape fidelity.

To investigate whether the mesoporous BG NPs improved the printability of the GelMA biomaterial inks, the critical parameters of rheological properties such as viscoelasticity and shear-thinning were measured. Generally, viscoelasticity displays viscous flow and elastic shape-retention of biomaterial inks, while shear-thinning means their viscosity decreases with increasing shear rate. Compared to the GelMA inks without BG NPs, both clearer line viscoelasticity and typical shear-thinning were observed in the GelMA biomaterials inks after incorporation of BG NPs from 1% to 10% (Figure 2). Our results demonstrated that the as-prepared BG/GelMA inks could be easily extruded from the nozzle due to the good shear-thinning property (Gao et al., 2019). Additionally, Figure 2D showed that the storage modulus (G') of the BG/GelMA biomaterial inks was higher than the loss modulus (G'') indicating that the incorporation of BG NPs could improve the shape fidelity of 3D-printed scaffolds (Kamkar et al., 2021, 2022).

Next, the stacking lattice scaffold (7×7) with 1.2 mm filament distance and 12 layers with a large porous structure (~300 μm of pore size) was designed for clinically relevant periodontal defect applications. By extrusion-based 3D printing, the resultant multilayered scaffold was about 10.0 mm×10.0 mm×5.0 mm and the pore size was ranged from 304 μm to 446 μm, which is defined as macropore (Figure 3). The 3D-printed GelMA scaffolds without BG NPs addition showed the bottom had collapsed, indicating poor filament support and stability. With the incorporation of BG NPs (scaffolds 1%BG, 5%BG, and 10% BG), there was less collapse in the scaffolds with higher porosity, suggesting that the addition of mesoporous BG NPs not only increased the printability of biomaterial inks and endowed the scaffolds with a stable macropore structure of good shape fidelity, but also lowered the self-healing degree of GelMA hydrogel inks to ensure the high porosity of scaffolds (Figure 3). Our results were consistent with previous studies showing incorporation of inorganic NPs such as nanoclay, and MXene Nanosheets/Gold NPs into the GelMA solutions could improve the shape fidelity and printability of GelMA inks (Boularaoui et al., 2021).

We further characterized the as-prepared BG/GelMA scaffolds by FTIR spectra. As shown in Figure 4A, the FTIR spectra of the BG/GelMA scaffolds showed typical peaks of gelatin as described for GelMA in previous studies (Rahali et al., 2017). Interestingly, in the GelMA scaffold with 10% BG, the intensity of the O-H groups and N-H amino band was obviously reduced, which is ascribable to the incorporation of BG NPs. Our results were consistent with other studies demonstrating that the incorporation of biphasic calcium phosphate NPs could cause the decrease in peak intensity of the O-H band and N-H amino band of GelMA hydrogels (Choi et al., 2021). Moreover, the thermal stability of the as-prepared BG/GelMA scaffolds was analyzed by using the

TGA method. It was observed that the incorporation of BG NPs did not significantly affect the thermal degradation behavior of the biomimetic Gel/MA scaffolds (Figures 4B,C).

It is well-recognized that the composition, structure (e.g. pore size, porosity), and properties (e.g. stiffness, compressive strength, elastic modulus, etc.) of biomaterial scaffolds are critical parameters affecting stem-cell fate and tissue regenerative outcomes (Swanson et al., 2021). An ideal 3D architecture of the scaffold should have an interconnected porous structure with high porosity to decrease the obstacles to the cell and nutrient migration (Turnbull et al., 2018), and the osteoblastic cell adhesion on biomaterials is an important event in initiating and regulating cell survival, migration, recruitment, and osteogenic differentiation (Chen et al., 2018). In this study, compared to the GelMA scaffold without BG NPs (Figure 6 a5), cell attachment and spreading were enhanced on scaffolds with BG incorporation, where cells inside the pore could also stretch (Figure 6 b5-d5). Most of the cells were always found to adhere to BG NP-doped rough surface (Figure 6D). The possible mechanism underlying better cell adhesion and spread in BG groups might be attributed to the rough surface modified by the bioactive glass (Figure 3D) and the highly connected and stable macroporous structure (Figure 3; Table 3). For the rough surface, several studies stated that roughness increased adhesion (Shapira and Halabi, 2009; Boyd et al., 2021). Furthermore, X. Shi et al. found that the topography itself was also important for cell adhesion on a rough protein-resistant surface (Shi et al., 2012). These research studies indicated that the effect of rough surfaces on cell adhesion should not be ignored.

Moreover, the construction of cell-living spaces by macropores in scaffolds is also essential for the establishment of cellular functions, such as cell growth, division, proliferation, and differentiation (Fan and Wang, 2017). The introduction of macroporous structures in scaffolds brings cell-adhesive surfaces and spaces, which is beneficial for cell adhesion, spreading, proliferation, and increased cell–cell contacts (Fan and Wang, 2017). Meanwhile, a porous structure may have offered a better environment for cell proliferation and albumin production through the enhanced mass transfer of nutrients, oxygen, and waste removal, which is essential for cell growth (Hwang et al., 2010) (Fan and Wang, 2015) (Turnbull et al., 2018). A recent study of developing biomaterial scaffolds to maintain the stemness of skeletal bone marrow mesenchymal stem cells (BMSC) gave evidence that different pore sizes had different regulatory effects on stem cell differentiation, where BMSC growing in large pores (>250 μm) have a trajectory toward osteogenic differentiation, while small pores (<125 μm) maintain stemness and prevent the differentiation of BMSC *in vivo* and *in vitro* (Swanson et al., 2021). Consistently, our results also confirmed that large pores greater than 250 μm in diameter could induce osteogenic differentiation of HPDLCs in all 3D-printed GelMA-based scaffold groups (Figure 7).

Although mechanical properties are also important parameters, the mechanical properties of the scaffolds in this study did not significantly improve (Figures 5A–C). Osteogenic and cementogenic differentiations of HPDLCs were demonstrated by alkaline phosphatase (ALP) and Alizarin Red staining as well as up-regulating gene expressions of *Col-1α1*, *ALP*, *CEMP-1*, and *OSX*. ALP has clear functions in the initial stages of cells' osteoblastic differentiation and growth-plate calcification, which is produced early in growth and is easily found on the surface of the cell and in matrix vesicles of all bones and calcifying cartilages (Vimalraj, 2020). Alizarin Red can chelate with calcium ions to form complexes that can be used to mark calcium nodules formed by osteogenesis differentiation of stem cells (Li et al., 2020) (Gregory et al., 2020). In this study, higher ALP staining of all the groups was remarkably exhibited on the 14th and 21st days compared to that on the 7th day, meaning a trajectory toward osteogenic differentiation from the 14th day (Figure 7A). The same, mineralized nodule formation was observed on the 21st day for all groups. Col-1α1, ALP, and OSX are all osteo-specific genes and are necessary for osteogenic and cementogenic differentiations (Nakashima et al., 2002; Chen et al., 2009). CEMP-1, as a marker protein for cementoblast-related cells, regulates cementogenic differentiation in stem cells (Komaki et al., 2012) (Sanz et al., 2021). Compared to the 3D-printed GelMA scaffold without BG NPs, a significant up-regulation in the gene expressions of Col-1α1 and CEMP-1 was observed in the scaffold 10% BG group, suggesting that the enhanced osteogenic and cementogenic differentiations in HPDLCs were more likely to be related to Si ions release during scaffold degradation (Figure 8B). The most mass loss occurs (Figure 5D) and relatively rapid Si ions release from the scaffold 10% BG group during the first week (Figure 8B). The osteogenic effect induced by Si ions was observed in some previous studies (Odatsu et al., 2015). Silicon ions, as ionic products from bioactive glass degradation, could facilitate the induction of collagen type 1 (Col(I)α1, Col(I)α2) synthesis, and in turn, enhance the expression of downstream markers such as alkaline phosphatase (ALP), Runx2, and osteocalcin (OCN) during osteoblast differentiation (Varanasi et al., 2009; Varanasi et al., 2012; Saffarian Tousi et al., 2013). In a word, BG NPs could contribute to the enhancement of HPDLCs' osteogenic differentiation by releasing inorganic bioactive ions with the help of macroporous structures, rough surface, and GelMA components.

5 Conclusion

In summary, we successfully developed a novel mesoporous bioactive glass (BG)/GelMA biomimetic scaffold with a large pore size (~300 μm) by 3D printing. Our results showed that the incorporation of mesoporous BG NPs significantly improved shape fidelity, surface roughness, and bioactivity of 3D-printed macropore GelMA scaffolds, resulting in the enhanced effects on cell attachment and spreading and promoting osteogenic/cementogenic differentiation in periodontal ligament cells, evidenced by the excellent maintenance of the macropore structure, the visibly improved cell-spreading, the release of bioactive ions (e.g. Si^{4+}, Ca^{2+}), the up-regulation of gene expressions of osteogenesis and cementogensis, the increase in ALP activity and calcium nodules, suggesting that BG NPs could endow GelMA-based scaffold with excellent structural stability and the ability to promote osteogenic/cementogenic differentiation. Our findings demonstrated the great potential of the newly formulated biomaterial inks and biomimetic BG/GelMA scaffolds for being used in periodontal tissue regeneration and provide important insights into the understanding of cell–scaffold interaction in promoting regeneration of functional periodontal tissues.

Data availability statement

The original contributions presented in the study are included in the article/supplementary material, further inquiries can be directed to the corresponding authors.

Author contributions

NM (conceptualization, methodology, investigation, and writing the original draft); YW (methodology, investigation, and formal analysis); BC (methodology, writing the original draft); TZ: (conceptualization, investigation); BS (investigation, formal analysis); TD (investigation, formal analysis, and supervision); XL (conceptualization, supervision, resources, investigation, writing–review & editing, and project administration). All authors contributed to the manuscript and approved the submitted version.

Funding

This work was supported by the 14th " College Students' Innovative Training Plan Program of Shanghai Jiao Tong University School of Medicine " Research (project number: 1420Y510), National Natural Science Foundation of China (NO. 82271024). Science and Technology Commission of Shanghai Municipality (22DZ2201300, 19DZ2203900, 21DZ2291700), Discipline fund KQXJXK2021 from Ninth People's Hospital, Shanghai Jiao Tong University School of Medicine, and College of Stomatology, Shanghai Jiao Tong University, Innovative research team of high-level local universities in Shanghai, Oral and maxillofacial regeneration and functional restoration SHSMU-ZLCX20212400.

Acknowledgments

The authors thank Lin Kaili for his help with the 3D printing of GelMA-based scaffolds.

Conflict of interest

The remaining authors declare that the research was conducted in the absence of any commercial or financial relationships that could be construed as a potential conflict of interest.

The handling editor, YQ, declared a shared parent affiliation with the authors NM, YW, BC, TZ, BS, TD, XL at the time of review.

Publisher's note

References

Alge, D. L., and Anseth, K. S. (2013). Lighting the way. *Nat. Mat.* 12 (11), 950–952. doi:10.1038/nmat3794

Boularaoui, S., Shanti, A., Lanotte, M., Luo, S., Bawazir, S., Lee, S., et al. (2021). Nanocomposite conductive bioinks based on low-concentration GelMA and MXene nanosheets/gold nanoparticles providing enhanced printability of functional skeletal muscle tissues. *ACS Biomater. Sci. Eng.* 7 (12), 5810–5822. doi:10.1021/acsbiomaterials.1c01193

Boyd, J. D., Stromberg, A. J., Miller, C. S., and Grady, M. E. (2021). Biofilm and cell adhesion strength on dental implant surfaces via the laser spallation technique. *Dent. Mat.* 37 (1), 48–59. doi:10.1016/j.dental.2020.10.013

Chen, S., Gluhak-Heinrich, J., Wang, Y. H., Wu, Y. M., Chuang, H. H., Chen, L., et al. (2009). Runx2, osx, and dspp in tooth development. *J. Dent. Res.* 88 (10), 904–909. doi:10.1177/0022034509342873

Chen, S., Guo, Y., Liu, R., Wu, S., Fang, J., Huang, B., et al. (2018). Tuning surface properties of bone biomaterials to manipulate osteoblastic cell adhesion and the signaling pathways for the enhancement of early osseointegration. *Colloids Surfaces B Biointerfaces* 164, 58–69. doi:10.1016/j.colsurfb.2018.01.022

Choi, J.-B., Kim, Y.-K., Byeon, S.-M., Park, J.-E., Bae, T.-S., Jang, Y.-S., et al. (2021). Fabrication and characterization of biodegradable gelatin methacrylate/biphasic calcium phosphate composite hydrogel for bone tissue engineering. *Nanomater. (Basel, Switz.* 11 (3), 617. doi:10.3390/nano11030617

Cortellini, P., and Tonetti, M. S. (2015). Clinical concepts for regenerative therapy in intrabony defects. *Periodontol.* 68 (1), 282–307. doi:10.1111/prd.12048

Deliormanlı, A. M., and Atmaca, H. (2018). Biological response of osteoblastic and chondrogenic cells to graphene-containing PCL/bioactive glass bilayered scaffolds for osteochondral tissue engineering applications. *Appl. Biochem. Biotechnol.* 186 (4), 972–989. doi:10.1007/s12010-018-2758-7

Fan, C., and Wang, D.-A. (2015). Effects of permeability and living space on cell fate and neo-tissue development in hydrogel-based scaffolds: A study with cartilaginous model. *Macromol. Biosci.* 15 (4), 535–545. doi:10.1002/mabi.201400453

Fan, C., and Wang, D.-A. (2017). Macroporous hydrogel scaffolds for three-dimensional cell culture and tissue engineering. *Tissue Eng. Part B Rev.* 23 (5), 451–461. doi:10.1089/ten.TEB.2016.0465

Gao, J., Ding, X., Yu, X., Chen, X., Zhang, X., Cui, S., et al. (2021). Cell-free bilayered porous scaffolds for osteochondral regeneration fabricated by continuous 3D-printing using nascent physical hydrogel as ink. *Adv. Healthc. Mat.* 10 (3), e2001404. doi:10.1002/adhm.202001404

Gao, Q., Niu, X., Shao, L., Zhou, L., Lin, Z., Sun, A., et al. (2019). 3D printing of complex GelMA-based scaffolds with nanoclay. *Biofabrication* 11 (3), 035006. doi:10.1088/1758-5090/ab0cf6

Gong Jinglei, H. Y., and Wang, J. (2021). Research progress on multiphasic scaffold in periodontal regeneration. *Int. J. Stomatol.* 48 (5), 563–569. doi:10.7518/gjkq.2021101

Gregory, C. A., McNeill, E. P., and Pan, S. (2020). "Chapter 2 - preparation of osteogenic matrices from cultured cells," in *Methods in cell biology*. Editors D. Caballero, S. C. Kundu, and R. L. Reis (Academic Press), 15–43.

Grove, C., and Jerram, D. A. (2011). jPOR: An ImageJ macro to quantify total optical porosity from blue-stained thin sections. *Comput. Geosciences* 37 (11), 1850–1859. doi:10.1016/j.cageo.2011.03.002

Hwang, C. M., Sant, S., Masaeli, M., Kachouie, N. N., Zamanian, B., Lee, S.-H., et al. (2010). Fabrication of three-dimensional porous cell-laden hydrogel for tissue engineering. *Biofabrication* 2 (3), 035003. doi:10.1088/1758-5082/2/3/035003

Iwata, T., Yamato, M., Ishikawa, I., Ando, T., and Okano, T. (2014). Tissue engineering in periodontal tissue. *Anat. Rec. Hob.* 297 (1), 16–25. doi:10.1002/ar.22812

Janmaleki, M., Liu, J., Kamkar, M., Azarmanesh, M., Sundararaj, U., and Nezhad, A. S. (2020). Role of temperature on bio-printability of gelatin methacryloyl bioink in two-step cross-linking strategy for tissue engineering applications. *Biomed. Mat.* 16 (1), 015021. doi:10.1088/1748-605X/abbcc9

Jeon, J. E., Vaquette, C., Klein, T. J., and Hutmacher, D. W. (2014). Perspectives in multiphasic osteochondral tissue engineering. *Anat. Rec. Hob.* 297 (1), 26–35. doi:10.1002/ar.22795

Kamkar, M., Janmaleki, M., Erfanian, E., Sanati-Nezhad, A., and Sundararaj, U. (2022). Covalently cross-linked hydrogels: Mechanisms of nonlinear viscoelasticity. *Can. J. Chem. Eng.* n/a. doi:10.1002/cjce.24388

Kamkar, M., Janmaleki, M., Erfanian, E., Sanati-Nezhad, A., and Sundararaj, U. (2021). Viscoelastic behavior of covalently crosslinked hydrogels under large shear deformations: An approach to eliminate wall slip. *Phys. Fluids* 33 (4), 041702. doi:10.1063/5.0046801

Komaki, M., Iwasaki, K., Arzate, H., Narayanan, A. S., Izumi, Y., and Morita, I. (2012). Cementum protein 1 (CEMP1) induces a cementoblastic phenotype and reduces osteoblastic differentiation in periodontal ligament cells. *J. Cell. Physiol.* 227 (2), 649–657. doi:10.1002/jcp.22770

Lee, C. H., Hajibandeh, J., Suzuki, T., Fan, A., Shang, P., and Mao, J. J. (2014). Three-dimensional printed multiphase scaffolds for regeneration of periodontium complex. *Tissue Eng. Part A* 20 (7-8), 1342–1351. doi:10.1089/ten.TEA.2013.0386

Li, B., Qin, K., Wang, B., Liu, B., Yu, W., Li, Z., et al. (2020). Crocin promotes osteogenesis differentiation of bone marrow mesenchymal stem cells. *Vitro Cell. Dev. Biol. -Animal.* 56 (8), 680–688. doi:10.1007/s11626-020-00487-w

Loh, Q. L., and Choong, C. (2013). Three-dimensional scaffolds for tissue engineering applications: Role of porosity and pore size. *Tissue Eng. Part B Rev.* 19 (6), 485–502. doi:10.1089/ten.TEB.2012.0437

Luo, Y., Zhang, T., and Lin, X. (2022). 3D printed hydrogel scaffolds with macro pores and interconnected microchannel networks for tissue engineering vascularization. *Chem. Eng. J.* 430, 132926. doi:10.1016/j.cej.2021.132926

Nakashima, K., Zhou, X., Kunkel, G., Zhang, Z., Deng, J. M., Behringer, R. R., et al. (2002). The novel zinc finger-containing transcription factor osterix is required for osteoblast differentiation and bone formation. *Cell* 108 (1), 17–29. doi:10.1016/s0092-8674(01)00622-5

Odatsu, T., Azimaie, T., Velten, M. F., Vu, M., Lyles, M. B., Kim, H. K., et al. (2015). Human periosteum cell osteogenic differentiation enhanced by ionic silicon release from porous amorphous silica fibrous scaffolds. *J. Biomed. Mat. Res. A* 103 (8), 2797–2806. doi:10.1002/jbm.a.35412

Rahali, K., Ben Messaoud, G., Kahn, C. J. F., Sanchez-Gonzalez, L., Kaci, M., Cleymand, F., et al. (2017). Synthesis and characterization of nanofunctionalized gelatin methacrylate hydrogels. *Int. J. Mol. Sci.* 18 (12), 2675. doi:10.3390/ijms18122675

Rahaman, M. N., Day, D. E., Bal, B. S., Fu, Q., Jung, S. B., Bonewald, L. F., et al. (2011). Bioactive glass in tissue engineering. *Acta Biomater.* 7 (6), 2355–2373. doi:10.1016/j.actbio.2011.03.016

Saffarian Tousi, N., Velten, M. F., Bishop, T. J., Leong, K. K., Barkhordar, N. S., Marshall, G. W., et al. (2013). Combinatorial effect of Si4+, Ca2+, and Mg2+ released from bioactive glasses on osteoblast osteocalcin expression and biomineralization. *Mater. Sci. Eng. C* 33 (5), 2757–2765. doi:10.1016/j.msec.2013.02.044

Sanz, J. L., López-García, S., Lozano, A., Pecci-Lloret, M. P., Llena, C., Guerrero-Gironés, J., et al. (2021). Microstructural composition, ion release, and bioactive potential of new premixed calcium silicate-based endodontic sealers indicated for warm vertical compaction technique. *Clin. Oral Investig.* 25 (3), 1451–1462. doi:10.1007/s00784-020-03453-8

Schwab, A., Levato, R., D'Este, M., Piluso, S., Eglin, D., and Malda, J. (2020a). Printability and shape fidelity of bioinks in 3D bioprinting. *Chem. Rev.* 120 (19), 11028–11055. doi:10.1021/acs.chemrev.0c00084

Schwab, A., Levato, R., D'Este, M., Piluso, S., Eglin, D., and Malda, J. (2020b). Printability and shape fidelity of bioinks in 3D bioprinting. *Chem. Rev.* 120 (19), 11028–11055. doi:10.1021/acs.chemrev.0c00084

Shapira, L., and Halabi, A. (2009). Behavior of two osteoblast-like cell lines cultured on machined or rough titanium surfaces. *Clin. Oral Implants Res.* 20 (1), 50–55. doi:10.1111/j.1600-0501.2008.01594.x

Shi, X., Wang, Y., Li, D., Yuan, L., Zhou, F., Wang, Y., et al. (2012). Cell adhesion on a POEGMA-modified topographical surface. *Langmuir* 28 (49), 17011–17018. doi:10.1021/la303042d

Skallevold, H. E., Rokaya, D., Khurshid, Z., and Zafar, M. S. (2019). Bioactive glass applications in dentistry. *Int. J. Mol. Sci.* 20 (23), 5960. doi:10.3390/ijms20235960

Slots, J. (2017). Periodontitis: Facts, fallacies and the future. *Periodontol.* 75 (1), 7–23. doi:10.1111/prd.12221

Sowmya, S., Mony, U., Jayachandran, P., Reshma, S., Kumar, R. A., Arzate, H., et al. (2017a). Tri-layered nanocomposite hydrogel scaffold for the concurrent regeneration of cementum, periodontal ligament, and alveolar bone. *Adv. Healthc. Mat.* 6 (7), 1601251. doi:10.1002/adhm.201601251

Sowmya, S., Mony, U., Jayachandran, P., Reshma, S., Kumar, R. A., Arzate, H., et al. (2017b). Tri-layered nanocomposite hydrogel scaffold for the concurrent regeneration of cementum, periodontal ligament, and alveolar bone. *Adv. Healthc. Mat.* 6 (7), 1601251. doi:10.1002/adhm.201601251

Sui, B., Liu, X., and Sun, J. (2018). Dual-functional dendritic mesoporous bioactive glass nanospheres for calcium influx-mediated specific tumor suppression and controlled drug delivery *in vivo*. *ACS Appl. Mat. Interfaces* 10 (28), 23548–23559. doi:10.1021/acsami.8b05616

Swanson, W. B., Omi, M., Zhang, Z., Nam, H. K., Jung, Y., Wang, G., et al. (2021). Macropore design of tissue engineering scaffolds regulates mesenchymal stem cell differentiation fate. *Biomaterials* 272, 120769. doi:10.1016/j.biomaterials.2021.120769

Tao, O., Kort-Mascort, J., Lin, Y., Pham, H. M., Charbonneau, A. M., ElKashty, O. A., et al. (2019). The applications of 3D printing for craniofacial tissue engineering. *Micromachines* 10 (7), 480. doi:10.3390/mi10070480

Tavares, M. T., Gaspar, V. M., Monteiro, M. V., S Farinha, J. P., Baleizão, C., and Mano, J. F. (2021). GelMA/bioactive silica nanocomposite bioinks for stem cell osteogenic differentiation. *Biofabrication* 13 (3), 035012. doi:10.1088/1758-5090/abdc86

Turnbull, G., Clarke, J., Picard, F., Riches, P., Jia, L., Han, F., et al. (2018). 3D bioactive composite scaffolds for bone tissue engineering. *Bioact. Mater.* 3 (3), 278–314. doi:10.1016/j.bioactmat.2017.10.001

van Haaften, E. E., Duijvelshoff, R., Ippel, B. D., Söntjens, S. H. M., van Houtem, M. H. C. J., Janssen, H. M., et al. (2019). The degradation and performance of electrospun supramolecular vascular scaffolds examined upon *in vitro* enzymatic exposure. *Acta Biomater.* 92, 48–59. doi:10.1016/j.actbio.2019.05.037

Varanasi, V. G., Leong, K. K., Dominia, L. M., Jue, S. M., Loomer, P. M., and Marshall, G. W. (2012). Si and Ca individually and combinatorially target enhanced MC3T3-E1 subclone 4 early osteogenic marker expression. *J. Oral Implantol.* 38 (4), 325–336. doi:10.1563/AAID-JOI-D-11-00108

Varanasi, V. G., Saiz, E., Loomer, P. M., Ancheta, B., Uritani, N., Ho, S. P., et al. (2009). Enhanced osteocalcin expression by osteoblast-like cells (MC3T3-E1) exposed to bioactive coating glass (SiO2-CaO-P2O5-MgO-K2O-Na2O system) ions. *Acta Biomater.* 5 (9), 3536–3547. doi:10.1016/j.actbio.2009.05.035

Vimalraj, S. (2020). Alkaline phosphatase: Structure, expression and its function in bone mineralization. *Gene* 754, 144855. doi:10.1016/j.gene.2020.144855

Wang, W., Nie, W., Liu, D., Du, H., Zhou, X., Chen, L., et al. (2018). Macroporous nanofibrous vascular scaffold with improved biodegradability and smooth muscle cells infiltration prepared by dual phase separation technique. *Int. J. Nanomedicine* 13, 7003–7018. doi:10.2147/IJN.S183463

Wang, Z., Wang, Z., Lu, W. W., Zhen, W., Yang, D., and Peng, S. (2017). Novel biomaterial strategies for controlled growth factor delivery for biomedical applications. *NPG Asia Mat.* 9 (10), e435. doi:10.1038/am.2017.171

Xiao, S., Zhao, T., Wang, J., Wang, C., Du, J., Ying, L., et al. (2019). Gelatin methacrylate (GelMA)-Based hydrogels for cell transplantation: An effective strategy for tissue engineering. *Stem Cell Rev. Rep.* 15 (5), 664–679. doi:10.1007/s12015-019-09893-4

Yousefi, A.-M., Hoque, M. E., Prasad, R. G. S. V., and Uth, N. (2015). Current strategies in multiphasic scaffold design for osteochondral tissue engineering: A review. *J. Biomed. Mat. Res. A* 103 (7), 2460–2481. doi:10.1002/jbm.a.35356

Yue, K., Trujillo-de Santiago, G., Alvarez, M. M., Tamayol, A., Annabi, N., and Khademhosseini, A. (2015). Synthesis, properties, and biomedical applications of gelatin methacryloyl (GelMA) hydrogels. *Biomaterials* 73, 254–271. doi:10.1016/j.biomaterials.2015.08.045

Advantages of publishing in Frontiers

OPEN ACCESS
Articles are free to read
for greatest visibility
and readership

FAST PUBLICATION
Around 90 days
from submission
to decision

HIGH QUALITY PEER-REVIEW
Rigorous, collaborative,
and constructive
peer-review

TRANSPARENT PEER-REVIEW
Editors and reviewers
acknowledged by name
on published articles

Frontiers
Avenue du Tribunal-Fédéral 34
1005 Lausanne | Switzerland

Visit us: www.frontiersin.org
Contact us: frontiersin.org/about/contact

REPRODUCIBILITY OF RESEARCH
Support open data
and methods to enhance
research reproducibility

DIGITAL PUBLISHING
Articles designed
for optimal readership
across devices

FOLLOW US
@frontiersin

IMPACT METRICS
Advanced article metrics
track visibility across
digital media

EXTENSIVE PROMOTION
Marketing
and promotion
of impactful research

LOOP RESEARCH NETWORK
Our network
increases your
article's readership